uOttawa

L'Université canadienne
Canada's university

FACULTÉ DES ÉTUDES SUPÉRIEURES ET POSTOCTORALES

uOttawa

L'Université canadienne
Canada's university

FACULTY OF GRADUATE AND POSDOCTORAL STUDIES

Cornelis Johannes Lissenberg
AUTEUR DE LA THÈSE / AUTHOR OF THESIS

Ph.D. (Earth Sciences)
GRADE / DEGREE

Department of Earth Sciences
FACULTÉ, ÉCOLE, DÉPARTEMENT / FACULTY, SCHOOL, DEPARTMENT

The Origin and Tectonic Evolution of the Annieopsquotch Ophiolite Belt, Newfoundland Appalachians

TITRE DE LA THÈSE / TITLE OF THESIS

Cees van Staal
DIRECTEUR (DIRECTRICE) DE LA THÈSE / THESIS SUPERVISOR

CO-DIRECTEUR (CO-DIRECTRICE) DE LA THÈSE / THESIS CO-SUPERVISOR

EXAMINATEURS (EXAMINATRICES) DE LA THÈSE / THESIS EXAMINERS

Jean Bédard

Keith Benn

Robert Berman

Henry Dick

Gary W. Slater
LE DOYEN DE LA FACULTÉ DES ÉTUDES SUPÉRIEURES ET POSTDOCTORALES /
DEAN OF THE FACULTY OF GRADUATE AND POSTDOCORAL STUDIES

THE ORIGIN AND TECTONIC EVOLUTION OF THE ANNIEOPSQUOTCH OPHIOLITE BELT, NEWFOUNDLAND APPALACHIANS

Cornelis Johannes Lissenberg

Thesis submitted to the
Faculty of Graduate and Postdoctoral Studies
In partial fulfillment of the requirements
For the Ph.D. degree in Earth Sciences

Department of Earth Sciences
University of Ottawa
and
Ottawa-Carleton Geoscience Centre

Your file Votre référence
ISBN: 0-494-10986-6
Our file Notre référence
ISBN: 0-494-10986-6

Table of Contents

List of Figures

List of Tables

Abstract

The Annieopsquotch Accretionary Tract comprises a series of arc-back arc complexes and ophiolites that formed in Iapetus Ocean and were accreted to the composite Laurentian margin, providing a unique view of tectonic processes operating during the Ordovician Taconic orogeny. The Annieopsquotch ophiolite belt, the oldest and structurally highest complex, preserves three magmatic episodes, and formed during initiation of west-directed subduction. It thus records the formation of the subduction zone that was responsible for formation of the units preserved in the Annieopsquotch Accretionary Tract. The Annieopsquotch ophiolite belt was accreted to the Laurentian margin prior to 470 Ma along the sinistral-oblique Lloyds River Fault Zone. The Lloyds River Fault Zone was intruded syn-kinematically by two plutonic suites (464-459 Ma), which triggered renewed deformation at high temperatures, illustrating that a positive feedback between deformation and magmatism facilitates the transfer of oceanic complexes to continental margins. Age constraints indicate that the majority of the Annieopsquotch Accretionary Tract was accreted 5 to 10 Ma after formation of the units, illustrating that complexities of accretionary tectonics in Iapetus were similar to those in Mesozoic to recent accretionary orogens. In contrast to other accretionary orogens, the role of fore-arc accretion was limited, whereas recycled continental basement played an important role. Syn-kinematic plutons tapped not only a sub-arc mantle source, but also a lithospheric mantle and crustal source, leading to isotopically evolved signatures.

The majority of the gabbro zone of the Annieopsquotch ophiolite is composed of gabbroic cumulates with paleohorizontal intrusive contacts. These contacts have finer grain sizes and comb structures (crescumulates), suggesting they are sills. The parental magmas of cumulates in the sills had compositions very similar to the overlying sheeted dykes and basalts, and generally become more evolved up-section, indicating that magma evolution in the Annieopsquotch ophiolite was dominated by fractionation in lower crustal conduits. The parental magmas of the gabbros, sheeted dykes, and basalts preserve a similar, wide range of compositions, indicating that aggregation, homogenization, and fractionation in an axial melt lens was inefficient. Lower crustal accretion was thus dominated by intrusion of melts from below, rather than remobilization of cumulates from above.

Acknowledgements

First and foremost, my thanks are extended to my supervisors, Cees van Staal and Jean Bédard. Cees gave me the opportunity to take on this challenge, and encouraged me to follow my interests wherever they took me. His stimulating supervision, comments and vision were of great benefit to this study. Jean helped me realize the wealth of information recorded in ophiolitic lower crust, and made me appreciate working with cumulate rocks. Without his input, I would not have ventured into the field of ophiolite genesis and mid-ocean ridge processes.

Research presented in this this thesis is part of the Geological Survey of Canada Targeted Geoscience Initiative "Red Indian Line", and my results would have meant little without those of my collaborators, Alexandre Zagorevski, Joe Whalen, Sally Pehrsson, Arjan Brem, Neil Rogers, and Pablo Valverde-Vaquero. Extensive discussions with them, especially Alexandre Zagorevski, have greatly improved the results. Vicki McNicoll's enthusiastic involvement has given this project an extra dimension that proved to be crucial. I thank the field assistants who assisted me during the two summers in the Newfoundland wilderness, David Portsmouth and Max McGillen, as well as Michiel van Noorden and Sander Boutsma, who were involved in mapping the King George IV ophiolite.

Katherine Venance is acknowledged for helping with the microprobe analyses. Analytical work at the Geological Survey of Canada was assisted by Julie Peressini, Diane Bellerive, and Carole Lafontaine (geochronology) and Pat Hunt (SEM). Discussion about Ar/Ar geochronology with Mike Villeneuve and geothermobarometry with Rob Berman are greatly appreciated. George Mrazek is thanked for preparing high-quality thin sections whenever necessary, and Helene de Gouffe for administrative support. I gratefully acknowledge Lise Maisonneuve's efforts to obtain scholarships.

This research was funded by a fellowship from the Faculty of Graduate and Postdoctoral Studies of the University of Ottawa to the author and a Natural Sciences and Engineering Research Council grant to C. van Staal. Field work was supported by the Geological Survey of Canada.

Several people have contributed to this work on a personal level. First, my parents are gratefully acknowledged for the support they have provided throughout the years. Maggie Currie and Alexandre Zagorevski are thanked for sharing the office, and Kristal Dubois, Paul Ferguson, Guillaume Girouard, Janet Kingsley, and Andre Koladich for the many Friday nights. Finally, my deepest gratitude is extended to Geraldine van Kleef, who gave me the freedom to pursue this study, and was always a source of love, support, and inspiration.

Statement of Contributions

This study has benefited from the use of data collected by colleagues from the Red Indian Line Targeted Geoscience Initiative. Alexandre Zagorevski provided some of the geochemical and Nd-isotopic analyses used in Chapters 3 and 5 (samples starting with VL01A and VL02A), and Joe Whalen provided some of the geochemical and Nd-isotopic analyses used in Chapter 3 (samples starting with WXNF).

The U/Pb and Ar/Ar ages presented in Chapter 5 and Appendix 1 have been obtained in collaboration with the Geological Survey of Canada Geochronology Laboratory under the guidance of Vicki McNicoll. Zircons and titanites for U/Pb TIMS analysis were hand-picked, grouped into different morphological fractions, air abraded and weighed by the author. Exception is sample VL01A258, which was handled by Alexandre Zagorevski. Dissolution and TIMS analyses were performed by staff of the Geochronology Laboratory. Grains for SHRIMP II analysis were selected by the author. Mounting of grains for SHRIMP II analysis was done by staff of the Geochronology laboratory. Imaging of these grains was done by Vicki McNicoll and the author, and SHRIMP II analysis by Vicki McNicoll. Vicki McNicoll calculated ages for all samples. Hornblende for Ar/Ar analysis was hand-picked by the author. Analysis was done by Geochronology Laboratory staff, and age calculation by Vicki McNicoll and Mike Villeneuve. Geochronology analytical procedures were described by Vicki McNicoll.

Microprobe analyses of targets selected by the author were performed by Katherine Venance at the Geological Survey of Canada. Geochemical analyses and most Nd-isotopic analyses were done at commercial laboratories. Remaining Nd-isotopic analyses were done at the isotope laboratory at Carleton University (Ottawa) under the supervision of Brian Cousens. Dissolution and separation was done by the author, and analysis by Alexandre Zagorevski.

Modeling of parental magma compositions of cumulates was greatly facilitated by spreadsheets provided by Jean Bédard. In addition, Dr. Bédard calculated a scheme to correct for trapped liquid shift in these calculations.

Parts of sections 5.3 to 5.5 have been written in collaboration with Alexandre Zagorevski.

CHAPTER I
Introduction

1.1. Background

While oceanic spreading ridges are responsible for formation of nearly two-thirds of the Earth's crust, and are major sites of thermal and chemical exchange between the mantle, crust, and hydrosphere, understanding of processes involved in crustal accretion at spreading ridges remains limited. This is largely due to the limited exposure of *in-situ* oceanic crust and difficulties in drilling large sections of lower crust. Geophysical investigations have provided important information regarding the physical and thermal structure of oceanic crust, as well as the distribution of melt below spreading centers (e.g., Sinton and Detrick, 1992). However, geophysical studies fail to constrain the dynamic processes that govern crustal accretion. Studies of *in-situ* oceanic crust formed at mid-ocean ridges have greatly contributed to knowledge about spreading ridge processes (e.g., Natland and Dick, 2001; Coogan et al., 2002a), but are limited to locations where extended crustal sections are exposed as a result of tectonic processes. Much information regarding spreading ridge processes has therefore been derived from the study of ophiolites, which are easily accessible and commonly expose complete three-dimensional sections of oceanic lithosphere.

A subject of particular debate concerns the magma plumbing system at mid-ocean ridges. Fractionation of mantle-derived melts is a fundamental process that has important implications for the geochemical evolution of mid-ocean ridge basalts and the structural and thermal evolution of oceanic lithosphere. However, it is uncertain where fractionation of mantle-derived melts occurs, and as a result the formation of the lower oceanic crust is poorly understood. Lower crustal processes are particularly difficult to study since *in-situ* lower oceanic crust is rarely exposed, and the interpretation of geochemistry of cumulates, which form the vast majority of lower oceanic crust, is not straightforward. The number of ophiolites for which detailed lower crustal relationships and geochemistry are available is very limited (e.g., Oman, Bay of Islands, and Troodos; Boudier et al., 1996; Bédard et al., 2000a; Coogan et al., 2003).

In addition to their importance for reconstruction of physical and chemical processes at spreading centers, ophiolites are important components of orogenic belts. While generally volumetrically limited, they commonly represent the vestiges of former oceanic basins, and as such contain key information for paleogeographic and tectonic reconstructions of the orogen. Most well-studies ophiolites occur as relatively large, coherent sheets emplaced over continental passive margin sequences. However, a significant number of ophiolites occur in accretionary complexes, commonly associated with relics of arc sequences and associated sediments. Such accretionary complexes mark the transfer of material from the oceanic realm to continental margins, and thus contribute significantly to continental growth (e.g., Sengör and Natal'in, 1996). Commonly, these accretionary complexes contain abundant sediments, leading to widespread occurrence of mélange, and mafic complexes are generally dismembered. As a result, it is often difficult to reconstruct original relationships and accretionary histories.

This study presents the results from a comprehensive investigation into the Annieopsquotch ophiolite belt and related rocks (Newfoundland Appalachians) as part of the Targeted Geoscience Initiative "Red Indian Line" of the Geological Survey of Canada. The Annieopsquotch ophiolite belt extends for >200 km, and comprises three well-exposed, nearly complete ophiolites (the Annieopsquotch, King George IV, and Star Lake ophiolites). The Annieopsquotch ophiolite belt is part of the Annieopsquotch Accretionary Tract, which formed as a result of accretion of several arc-back arc complexes and ophiolites to the composite Laurentian margin during the Ordovician Taconic orogeny. The Annieopsquotch Accretionary Tract is nearly devoid of sediments, and the various complexes are well preserved, allowing for a detailed reconstruction of its tectonic history. The Annieopsquotch Accretionary Tract thus presents a unique opportunity to study both spreading ridge processes and the processes involved in accretionary tectonics.

1.2. Objectives

The objective of this thesis is threefold:

1. To establish the field- and geochemical relationships in the lower crust of the Annieopsquotch ophiolite in order to reconstruct processes involved in oceanic lower crustal accretion;
2. To determine the origin and tectonic evolution of the Annieopsquotch ophiolite belt, and its implication for the tectonic evolution of the Newfoundland Appalachians;
3. To reconstruct the time scales and processes by which oceanic complexes are transferred from the oceanic domain to continental margins.

1.3. Thesis organization

This thesis is subdivided into 7 chapters. The first and second provide a general introduction and an overview of the geology of the study area, respectively. Subsequent chapters address the extent and origin of the Annieopsquotch ophiolite belt (Chapter 3), its implications for lower crustal accretion at oceanic spreading ridges (Chapter 4), the assembly of the Annieopsquotch Accretionary Tract (Chapter 5), and the structural history of the Lloyds River Fault Zone (Chapter 6). Finally, Chapter 7 summarizes the conclusions of this study. Chapters 3-6 were prepared as manuscripts for submission to peer-reviewed journals, and as a result they show some overlap, particularly regarding the regional geology.

CHAPTER II
Geological Framework

2.1. Newfoundland Appalachians

The Appalachian-Caledonide mountain chain results from Cambrian to Permian convergence and collision between Laurentia and several Gondwanan continents and microcontinents (e.g. Baltica, Ganderia, Avalonia), leading to closure of the Iapetus and Rheic oceans (Wilson, 1966; Williams, 1979; Williams and Hatcher, 1983; van Staal et al., 1998). The Newfoundland Appalachians preserve the early record of convergence (Cambrian-Ordovician) exceptionally well due to good exposure and limited late-orogenic tectonic overprint and cover sequences. As a result, the geology of Newfoundland has been, and continues to be, instrumental in the development of tectonic models for the evolution of the Appalachians and orogenic belts in general.

The Newfoundland Appalachians have been subdivided into four zones with distinct tectonostratigraphic characteristics. From west to east, these are the Humber, Dunnage, Gander, and Avalon zones (Williams, 1979; Fig. 2.1). The Humber Zone represents Laurentian Grenville basement and its allochtonous to para-autochtonous passive margin cover. Rocks formed within the oceanic realm of Iapetus are preserved in the Dunnage Zone, and are the focus of this thesis. The Dunnage Zone has been subdivided into the peri-Laurentian Notre Dame and Dashwoods subzones, and the Exploits Subzone, which mainly has a peri-Gondwanan provenance (Williams et al., 1988; Fig. 2.1). The two subzones are separated by the fundamental suture zone of the Newfoundland Appalachians, the Red Indian Line (Williams et al., 1988; van Staal et al., 1998). The Gander and Avalon zones preserve the remnants of peri-Gondwanan continental blocks.

Both the Notre Dame and Dashwoods subzones are dominated by granitoid arc plutons and associated volcanic rocks, ophiolites, and dominantly mafic arc-back arc complexes (Fig. 2.2). The Dashwoods Subzone generally exposes a deeper crustal level than the Notre Dame Subzone (e.g., the amphibolite to granulite-facies Cormacks Lake Complex; Pehrsson et al., 2003), and has a larger sedimentary component, but both subzones share a common Ordovician tectonic history (e.g., Pehrsson et al., 2003). Most arc plutons and volcanics belong to the Late Cambrian to Silurian Notre Dame Arc (e.g., Whalen et al., 1987, 1997). Geochemical and isotopic data, as well as inherited zircons, suggest the arc was built on Laurentian continental basement (Whalen et al., 1997). The Notre Dame Arc was active in three distinct pulses (c. 488-480 Ma, 468-456 Ma, and 445-425 Ma; van Staal et al., 2003; Whalen et al., 2003). Ophiolites occur in three distinct belts (Fig. 2.2): the Lushs Bight and Baie Verte oceanic tracts, which overlie metasedimentary rocks of the Notre Dame and Humber (sub)zones, respectively (e.g., Swinden et al., 1997; van Staal et al., 2003), and the Annieopsquotch ophiolite belt (Annieopsquotch ophiolite belt; Dunning and Chorlton, 1985). The Annieopsquotch ophiolite belt, along with most mafic arc-back arc complexes, occurs in a linear belt along the eastern boundary of the Notre Dame Subzone. Together, these rocks are referred to as the Annieopsquotch Accretionary Tract (van Staal et al., 1998).

The Lushs Bight oceanic tract formed in the Cambrian during the early stages of east-directed subduction in Iapetus (Fig. 2.3a; van Staal et al., 1998, 2004). Tectonic emplacement of Lushs Bight and correlative ophiolitic rocks occurred in the Late Cambrian (Swinden et al., 1997), immediately preceding metamorphism and Early Tremadoc (c. 488 Ma; Dubé et al., 1996) magmatism associated with the Notre Dame Arc (Fig. 2.3b). However, the Humber zone records the persistence of passive margin sedimentation until c. 475 Ma (Waldron and van Staal, 2001). This disparity in tectonic histories suggests the basement to the Notre Dame Arc and Lushs Bight oceanic tract was a microcontinent, referred to as Dashwoods, which was separated from the Laurentian margin by an oceanic basin termed the Humber Seaway (Fig. 2.3; Waldron and van Staal, 2001). Closure of the Humber Seaway occurred by east-directed subduction underneath the Dashwoods microcontinent in the early Ordovician, and led to the first pulse of Notre Dame Arc magmatism (Fig. 2.3b). Subduction led to collision between the Dashwoods microcontinent and the Laurentian margin by at least 475 Ma (Waldron and van Staal, 2001; Fig. 2.3c). This collision may have triggered convergence in the lapetus Ocean to the east, leading to the formation of a west-dipping subduction zone to the east of the Dashwoods microcontinent (Fig. 2.3c; see Chapter 3). This subduction zone was responsible for formation of the ophiolites and arc-back arc complexes that were to become the Annieopsquotch Accretionary Tract (Fig. 2.3d; Chapter 5).

2.2. The Annieopsquotch Accretionary Tract

The Annieopsquotch Accretionary Tract represents the easternmost (i.e. most outboard) unit of the Notre Dame Subzone, and is the focus of this study. The Annieopsquotch Accretionary Tract has a structural thickness of 8-15 km, and forms an east-vergent thrust stack comprised of ophiolites and arc-back arc complexes that is bounded by the Lloyds River Fault Zone to the west and the Red Indian Line to the east (Fig. 2.2). On the Lithoprobe seismic reflection profile, which runs through the study area, the Annieopsquotch Accretionary Tract appears as c. 5-12 km thick, c. 30° northwest-dipping package, that extends underneath the Dashwoods microcontinent to c. 25 km depth (van der Velden et al., 2004). In its original definition, it comprised the Annieopsquotch ophiolite belt (Annieopsquotch ophiolite belt), the ophiolitic Skidder Basalt and arc volcanic rocks of the Buchans-Robert's arm belt (van Staal et al., 1998). New mapping and geochemical, isotopic, and geochronological data within the framework of the Targeted Geoscience Initiative "Red Indian Line" have led to recognition of new units and redefinition of existing units within the Annieopsquotch Accretionary Tract (Zagorevski et al., subm.; this study). The Annieopsquotch Accretionary Tract is now subdivided into four units. The uppermost unit is the Annieopsquotch ophiolite belt, and is the main subject of the thesis. Structurally underneath the Annieopsquotch ophiolite belt are the ophiolitic Lloyds River Complex, the Buchans Group, and the Red Indian Lake Group. These structural panels are separated by northwest-dipping amphibolite- to (sub) greenschist-grade shear zones, and the rocks in these panels become progressively younger to the east (Chapter 5; Zagorevski et al., 2003).

The Annieopsquotch ophiolite belt (c. 481-478 Ma; Dunning and Krogh, 1985) has been described previously by Dunning (1984, 1987) and Dunning and Chorlton (1985), who concluded it comprised a piece of normal oceanic crust formed in lapetus and emplaced onto the Laurentian margin. In contrast, new data presented in Chapter 3 suggest the Annieopsquotch ophiolite belt formed during initiation of west-directed subduction outboard of the Dashwoods microcontinent (Fig. 2.3). The structurally underlying ophiolitic, previously unrecognized Lloyds River Complex, the age and geochemical signature of which is distinct from the Annieopsquotch ophiolite belt, formed at c. 473 Ma in a back arc setting to the Buchans arc (Zagorevski et al., subm.). The Buchans Group (473 Ma) is preserved structurally underneath the Lloyds River Complex, and comprises mafic and felsic tholeiitic and calc-alkaline arc volcanic and volcaniclastic rocks, and associated sediments (Dunning et al., 1987; Zagorevski et al., subm.). ε_{Nd} values as low as –10 (Swinden et al., 1997), as well as inherited zircon (Zagorevski et al., subm.) suggest the Buchans arc was underlain by continental basement. This has led to a model in which the Buchans arc formed on a continental sliver that originated along the eastern margin of the Dashwoods microcontinent and was subsequently emplaced to the east (i.e. outboard) of the Annieopsquotch ophiolite belt and Lloyds River Complex by trench-parallel transport as a fore-arc sliver (Fig. 2.3d; Zagorevski et al., subm.) The structurally lowest unit of the Annieopsquotch Accretionary Tract, the Red Indian Lake Group (c. 464 Ma; Zagorevski et al., subm.), comprises a series of mafic and felsic volcanic and volcaniclastic rocks and subordinate sediments, as well as a dismembered ophiolite. The volcanic rocks progress upward from island arc tholeiite to calc-alkaline basalt, and have inherited zircons and negative ε_{Nd} values (as low as –7.7), indicative of continental basement (Zagorevski et al., subm.). The Red Indian Lake group is interpreted to have formed by rifting of the Buchans arc in response to slab rollback of the west-dipping subduction zone. This yielded a back arc basin (the dismembered Skidder ophiolite) and younger continentally floored arc (Fig. 2.3d; Zagorevski et al., subm.). Formation of the Red Indian Lake Group coincides with the second magmatic plulse of the Notre Dame Arc; hence the second pulse of the Notre Dame Arc is unrelated to the west-directed subduction. The remarkable volume of magma generated during this phase of the Notre Dame Arc, combined with geochemical evidence for the presence of both arc- and non-arc magmas, indicate it rather formed as a result of slab-break off of the oceanic portion of the Laurentian plate (Fig. 2.3d; van Staal et al., 2003; Whalen et al., 2003).

Accretion of all units of the Annieopsquotch Accretionary Tract to the Dashwoods microcontinent was achieved by at least the Upper Caradoc-Ashgill (c. 450 Ma), when sediments overlying the Peri-Gondwanan Victoria Lake Supergroup, east of the Red Indian Line, started to receive Laurentian detritus (e.g., McNicoll et al., 2001), signaling juxtaposition of the Victoria Lake Supergoup with the composite Laurentian margin.

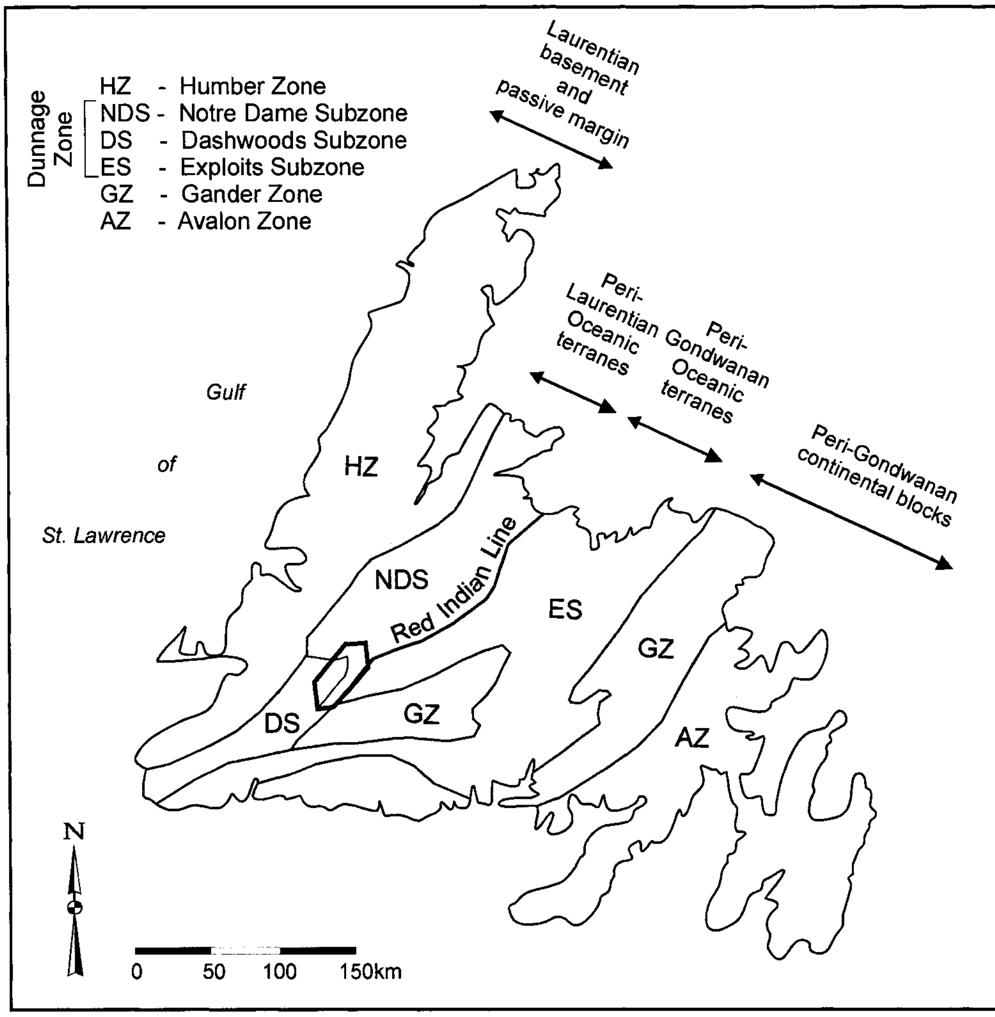

Figure 2.1: Tectonostratigraphic zones of the Newfoundland Appalachians, modified from Williams et al. (1988) and Williams (1995). Polygon marks location of study area.

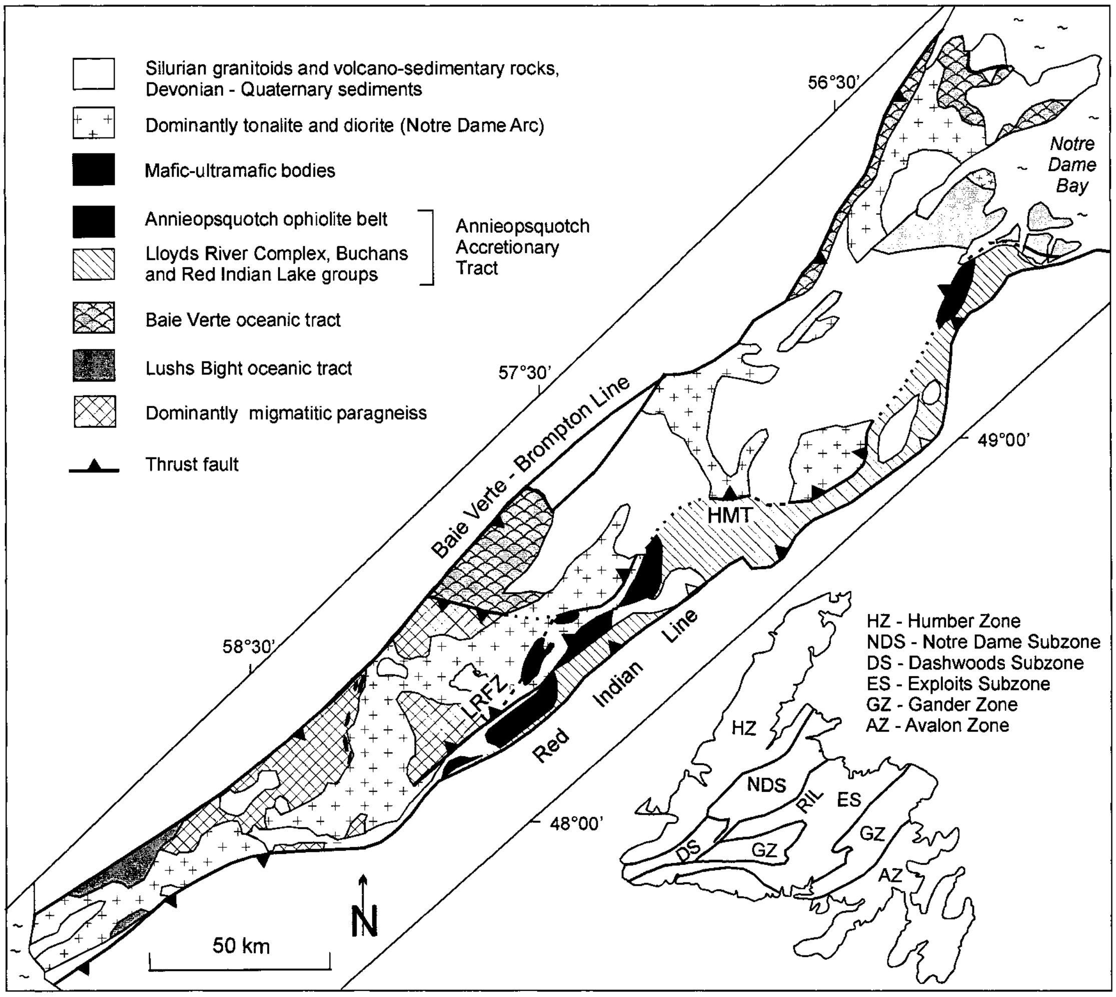

Figure 2.2: Generalized geology of the Notre Dame and Dashwoods subzones. Modified from Colman-Sadd et al. (1991), Lissenberg et al. (in press) and van Staal et al. (in press a,b,c). HMT=Hungry Mountain Thrust; LRFZ=Lloyds River Fault Zone; RIL=Red Indian Line.

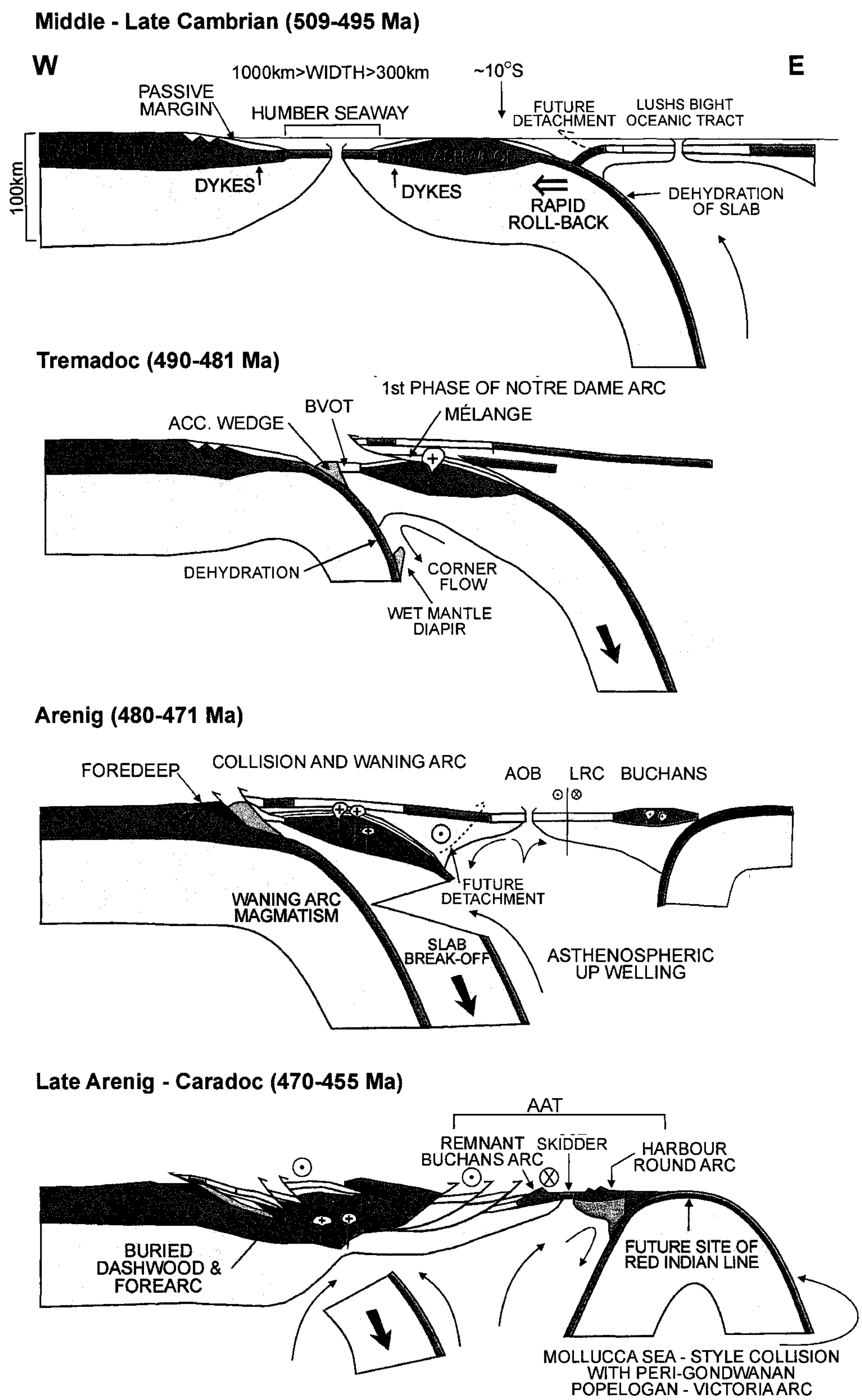

Figure 2.3: Schematic tectonic history of the peri-Laurentian portion of the Newfoundland Appalachians, modified from van Staal et al. (2004). AAT=Anniepsquotch Accretionary Tract; AOB=Annieopsquotch ophiolite belt; BVOT=Baie Verte oceanic tract; LRC=Lloyds River Complex. Pink, green, and blue colours represent continental crust, oceanic crust, and lithospheric mantle, respectively.

CHAPTER III

Geochemical constraints on the origin of the Annieopsquotch ophiolite belt, Newfoundland Appalachians

3.1. Introduction

Ophiolites are relics of oceanic lithosphere that commonly delineate suture zones between former oceanic or continental terranes. Their origin and tectonic evolution thus impose important constraints on tectonic reconstructions of orogens. The Appalachian-Caledonian orogen results from the Paleozoic closure of Iapetus Ocean, which led to the assembly of Laurentia with a number of intra-oceanic and continental arcs, basins, and microcontinents (Williams, 1979; van Staal et al., 1998). The Annieopsquotch ophiolite belt occupies a key position in the Newfoundland Appalachians because it is situated close to the main Iapetus suture zone. It is the largest and structurally highest belt in a series of accreted ophiolites and arc-back arc complexes termed the Annieopsquotch Accretionary Tract (Fig. 3.1; van Staal et al., 1998; Chapter 5). This accretionary tract marks an important episode of generation and accretion of intra-oceanic complexes to the Laurentian margin, and represents a period of major ocean closure and continental growth (Chapter 5). However, its tectonic evolution has hitherto been poorly constrained due to limited field, geochemical, and geochronological data.

Recent reevaluation of the Annieopsquotch Accretionary Tract has shown that the units within the Annieopsquotch Accretionary Tract become progressively younger to the east, indicating they formed above a retreating west-dipping subduction zone (Zagorevski et al., 2003; Chapter 5). The Annieopsquotch ophiolite belt holds the key to the early evolution of this subduction zone as it is the oldest and structurally highest component of the Annieopsquotch Accretionary Tract.

Previous geochemical results appeared to indicate that lavas and dykes from the Annieopsquotch ophiolite belt had normal mid-ocean ridge basalt (NMORB) chemistry (Dunning, 1987; Swinden et al., 1997). Consequently, van Staal et al. (1998) suggested the Annieopsquotch ophiolite belt represented pieces of Iapetus oceanic lithosphere scraped-off during west-directed subduction underneath the Laurentian margin. This chapter presents new geochemical and regional tectonic data that result from a comprehensive study of the Annieopsquotch ophiolite belt, and provides more rigorous constraints on its origin. I argue that the Annieopsquotch ophiolite belt formed during the initiation of west-directed subduction near Laurentia prior to 480 Ma, and records a complex history of supra-subduction zone (SSZ) opening and closure prior to accretion to the Laurentian margin. This constrains the age of formation and the early evolution of a west-dipping peri-Laurentian subduction zone, providing an important step in understanding the evolution of the Annieopsquotch Accretionary Tract and the peri-Laurentian portion of Iapetus.

3.2. Geological framework

The Newfoundland Appalachians have been subdivided in several tectonostratigraphic zones (Williams, 1979; Fig. 3.1), that represent, from west to east, Laurentian Grenville basement and passive margin cover (Humber Zone), rocks formed in the oceanic realm of Iapetus (Dunnage Zone), and peri-Gondwanan continental blocks (Gander and Avalon zones). Peri-Laurentian rocks in the Dunnage Zone define the Notre Dame and Dashwoods subzones, and are separated from peri-

Gondwanan rocks of the Exploits Subzone by the fundamental suture zone of the Newfoundland Appalachians, the Red Indian Line (Williams et al., 1988; Williams, 1995).

On the Laurentian side of the Red Indian Line is a series of east-vergent thrust slices containing 480-464 Ma ophiolites and arc-back arc complexes (Annieopsquotch ophiolite belt, Dunning and Chorlton, 1985; Lloyds River complex, Buchans Group and Red Indian Lake Group, Zagorevski et al., 2003; Fig. 3.1). The structural collage of the complexes display the characteristic architecture of an accretionary complex, and are collectively referred to as the Annieopsquotch Accretionary Tract (van Staal et al., 1998; Chapter 5). Recent work has shown that these complexes young eastwards (480-464 Ma; Dunning and Krogh, 1985; Zagorevski et al., 2003), suggestive of formation above a west-dipping subduction zone (Zagorevski et al., 2003; Chapter 5).

In southwest Newfoundland the Annieopsquotch Accretionary Tract is bounded to the northwest by the Lloyds River Fault Zone, which comprises three shear zones (Fig. 3.1; the southeastern, central, and northwestern shear zones, Chapter 6). This fault system separates the Annieopsquotch Accretionary Tract to the east from a peri-Laurentian microcontinent called Dashwoods, which was separated from Laurentia by an oceanic basin termed the Humber Seaway during the Cambrian-Early Ordovician (Waldron and van Staal, 2001). The earliest record of orogenic activity in the Dashwoods microcontinent is the Upper Cambrian (<501 Ma; Szybinski, 1995; Swinden et al., 1997) obduction of the Lower to Middle Cambrian Lushs Bight oceanic tract (508-501 Ma; Elliott et al., 1991; Szybinski, 1995; Kurth et al., 1998). The Lushs Bight oceanic tract was emplaced by attempted subduction of Dashwoods in an east-dipping subduction zone (van Staal et al., 1998). Obduction was followed by closure of the Humber Seaway by east-directed subduction underneath the Dashwoods microcontinent, and led to (1) formation of the SSZ the Baie Verte oceanic tract at 489-484 Ma (Dunning and Krogh, 1985; Cawood et al., 1996; Kurth et al., 1998); (2) formation of a continental arc (the Notre Dame Arc) on the Dashwoods microcontinent (Whalen et al., 1997; van Staal et al., 2003); (3) collision between the Dashwoods microcontinent and Laurentia by at least 475 Ma and the obduction of the Baie Verte oceanic tract onto the Laurentian margin (Waldron and van Staal, 2001).

The Annieopsquotch ophiolite belt contrasts with the Lushs Bight and Baie Verte ophiolite belts; it is younger (481-478 Ma; Dunning and Krogh, 1985), and was thrust underneath the Dashwoods microcontinent, rather than obducted onto Dashwoods or the Laurentian margin (van Staal et al., 1998; Chapter 6). The Annieopsquotch ophiolite belt comprises three main ophiolitic massifs, the Annieopsquotch, Star Lake, and King George IV ophiolites (Fig. 3.1). The ophiolite massifs are nearly continuous, and are separated by gabbroic to granitic plutons that contain ophiolitic enclaves. The Long Range ophiolitic complex, which occurs 70 km southwest of the King George IV ophiolite, was originally included in the Annieopsquotch ophiolite belt by Dunning and Chorlton (1985). However, the Long Range complex is older than the Annieopsquotch ophiolite belt and was obducted onto the Dashwoods microcontinent prior to intrusion of the Cape Ray granodiorite (488 Ma; Dubé et al., 1996), suggesting a closer link with the Lushs Bight oceanic tract. In addition, ultramafic and several layered gabbroic bodies within the northern Dashwoods Subzone have been considered to form part of the Annieopsquotch ophiolite belt (Dunning and Chorlton, 1985). I have examined these bodies, and, based on geochronological, lithological, and structural data, concluded that the majority is unrelated to the Annieopsquotch ophiolite belt (see Appendix 1). Several mafic- and ultramafic fragments that occur along strike of the Annieopsquotch ophiolite belt to the northeast (e.g., Hall Hill complex; Bostock, 1988; Hungry Mountain complex; Whalen et al.,

1997) have a similar tectonic setting and age of (479 Ma for the Hall Hill complex; Dunning et al., 1987), and are considered to be part of the Annieopsquotch ophiolite belt. The Annieopsquotch ophiolite belt thus extends for c. 200 km from southwest Newfoundland to Notre Dame Bay on Newfoundland's north coast (Fig. 3.1).

Structural and geochronological data imply that the Annieopsquotch ophiolite belt was thrust northwestward underneath the Dashwoods microcontinent and its Notre Dame Arc prior to 470 Ma along the sinistral oblique Lloyds River Fault Zone (Chapter 6). This is consistent with seismic reflection data, which suggests the Annieopsquotch ophiolite belt forms a thrust slice that extends to at least 15 km depth and structurally underlies the Dashwoods microcontinent (van der Velden et al., 2004). Similar kinematic histories have also been documented along the northeastern extension of the Lloyds River Fault Zone, the Hungry Mountain thrust (Calon and Green, 1987; Thurlow et al., 1992; Fig. 3.1). Underthrusting was accompanied by amphibolite-facies metamorphism along the Lloyds River Fault Zone, but the interior of the ophiolite massifs generally retained most of their original igneous mineralogy (Dunning, 1987; Chapter 4). The Annieopsquotch ophiolite belt is separated from younger units of the Annieopsquotch Accretionary Tract to the east by the Otter Brook Shear Zone. The change in orientation of the ophiolite pseudostratigraphy from the King George IV ophiolite, through Annieopsquotch to the Star Lake ophiolite, suggests that the Annieopsquotch ophiolite belt was deformed into large doubly-plunging folds prior to the final movement accommodated by the Lloyds River Fault Zone and the Otter Brook Shear Zone (Fig. 3.1).

In current tectonic models for the Newfoundland Appalachians, the Annieopsquotch ophiolite belt is regarded either as relic of normal Iapetus oceanic crust scraped off during west-directed subduction underneath the composite Laurentian margin (van Staal et al., 1998), or as having formed in a back-arc basin behind the continental Buchans arc or its oceanic extension (Swinden et al., 1997). In this chapter I present field and geochemical data that bear on this topic.

3.3. The Annieopsquotch ophiolite belt

The Annieopsquotch ophiolite is the biggest (25 x 8 km) and best-exposed ophiolite of the Annieopsquotch ophiolite belt, and will be used as a template for the entire belt. It preserves a steeply southeast-dipping (c. 70°), fault-bounded section through 5.5 km of oceanic crust, with 3-3.5 km of gabbroic rocks (olivine gabbros and gabbros), 1.5-2 km of sheeted dykes and at least 500 m of pillow basalts. Pegmatitic pods and trondhjemitic bodies occur locally throughout the gabbroic zone. Hydrothermal metamorphism increases in intensity up-section. Narrow, greenschist-facies mylonitic zones occur locally, but do not appear to have seriously disrupted the ophiolite pseudostratigraphy. The base of the ophiolite is faulted and intruded by numerous Ordovician mafic-intermediate and Silurian felsic plutonic rocks, and the lowermost crust and mantle are not exposed except for a few isolated ultramafic enclaves in the Middle Ordovician tonalites that intruded the Annieopsquotch ophiolite belt.

The gabbro zone of the Annieopsquotch ophiolite is subdivided into 3 parts (Chapter 4). The lowermost 500 m of the exposed section comprises coarse-grained gabbros, olivine gabbros, and subordinate Fe-rich pyroxenites that contain abundant decimeter- to decameter-sized enclaves of layered troctolite, olivine gabbro, and subordinate anorthosite (Fig. 3.2a). Layering in the troctolites is locally isoclinally folded and anorthositic layers are commonly boudinaged, suggesting high-temperature deformation. Modal grading is commonly preserved, however, and layer thicknesses vary from a few cm to 1 m. The dips of layering and foliation in the troctolites are dominantly paleo-vertical, sub-parallel to the strike and dip of the sheeted dykes (Dunning, 1987). The troctolite enclaves are extensively veined and replaced by the gabbroic rocks (Fig. 3.2b). The veins show no evidence of a penetrative high-temperature deformation event, and the surrounding gabbros are generally massive and lack fabrics. These field relationships imply that an early troctolite-forming phase was deformed, and then intruded by a second gabbro-forming magmatic phase. Fine-grained dykes that crosscut both the troctolites and gabbros form a minor component (<5%) of this subzone.

Troctolites have variable proportions of plagioclase (20-90%), but rocks with around 60% plagioclase (An_{80}- An_{90}) and 40% Ol (Fo_{82} - Fo_{84}) are particularly abundant. Olivine is 0.5 - 3 mm, sub- to euhedral, and variably serpentinized. Plagioclase is subhedral, 1 - 6 mm sized, and is locally recrystallized into polygonal aggregates. In rocks thought to be free from superimposed metasomatic effects (see below), clinopyroxene is rare (0-10%), occurring as sub- euhedral ca. 2 - 7 mm sized oikocrysts and 0.5 – 1 mm sized crystals interstitial to plagioclase. Troctolites have adcumulate textures, and commonly exhibit well-defined, layer-parallel shape-preferred orientations defined by plagioclase laths and, locally, elongated olivines. Olivine is variably serpentinized, and is locally surrounded by coronas of pale green amphibole. Plagioclase is partly sericitized.

Clinopyroxene modes generally increase towards the host gabbros, elevated olivine contents occur in the gabbros immediately surrounding the enclaves, and pyroxenites develop at some troctolite-gabbro contacts. In addition, the gabbros immediately surrounding the troctolites contain up to 20% orthopyroxene and are rich in Fe-Ti oxides. These relationships suggest that the troctolites reacted with the magmas from which the gabbros crystallized. In these transitional samples, clinopyroxene occurs in a diversity of habits, including anhedral to subhedral grains, oikocrysts, and perfectly euhedral prisms (generally 5 mm, up to12 mm). Orthopyroxene occurs as 2-3 mm sized subhedral crystals, as rims and exsolutions on and within clinopyroxene.

Host gabbros of the troctolitic enclaves are generally massive, and have variable olivine contents (0-20%). They are characterized by subhedral 1-5 mm sized plagioclase laths and 2-7 mm sized an- to subhedral clinopyroxene with sub-ophitic to ophitic textures. Olivine occurs as 0.5-2 mm sized anhedral grains. Domains characterized by weak hydrothermal overprints still show partial to complete serpentinization of olivine. In more altered zones, clinopyroxene and rims of plagioclase are replaced by aggregates of fine-grained green amphibole.

Overlying the troctolite-bearing level is 1.5 km of gabbros and olivine gabbros that make up 5-30 m thick sills. These rocks are described in detail in Chapter 4. The gabbroic sills are generally medium- to coarse-grained, but commonly have fine-gained upper and lower margins. Sill contacts are locally marked by downward growing dendritic plagioclase and clinopyroxene up to 10 cm in length. The gabbros are massive to layered, with layering defined by subtle variations in modal content of olivine, plagioclase, and clinopyroxene on a centimeter to decameter scale. Crosscutting fine-grained diabase dykes, locally with chilled margins, are rare at this level (5%). The gabbros are cumulates dominated by plagioclase (An_{55} – An_{74}) and clinopyroxene (En_{41-50} Wo_{38-46} Fs_{8-24}), with minor olivine (Fo_{64} – Fo_{68}), and rarely have a shape-preferred orientation. Ophitic and sub-ophitic textures are common, and crescumulate textures have been observed locally. Brown amphibole and oxides fill interstices. Trace element modeling results suggest that many of these gabbros contain high fractions of trapped melt (15-25%; Chapter 4). Hydrothermal metamorphic overprints are variably developed, and are commonly related to veins and cracks. In general, alteration becomes more pervasive up-section. It is characterized by extensive replacement of clinopyroxene by green amphibole, and growth of small amphibole grains along grain boundaries and cracks in plagioclase. Sericitization of plagioclase and formation of epidote occur only in the most altered samples.

The upper 500 m of the gabbroic zone is composed of texturally heterogeneous gabbros with liquid-like compositions (Chapter 4). These gabbros generally have a higher content of Fe-Ti oxides than is typical of underlying gabbros. Pegmatitic gabbro pods, some of which grade into hornblende gabbro, occur locally (Dunning, 1987). In some locations, gabbro pods grade into diabase, suggesting this level is the root zone of the sheeted dykes (Dunning, 1987). These relationships, and data presented in Chapter 4, suggest that this level is essentially composed of frozen melts, and preserves relics of the axial melt lens of the spreading ridge. Within this level, the proportion of crosscutting dykes increases upwards as the sheeted dyke complex is approached. The gabbros are characterized by subhedral 2-5 mm sized plagioclase laths and 0.5-7 mm sized anhedral clinpyroxene with subophitic textures. Locally, clinopyroxene occurs interstitially between plagioclase. Fe-Ti oxides occur as irregularly shaped grains that appear to have overgrown and partly replaced plagioclase and clinopyroxene. Clinopyroxene is completely replaced by aggregates of small green amphibole. These aggregates also replace plagioclase along grain boundaries and cracks, but plagioclase otherwise remains relatively unaffected by hydrothermal metamorphism. Epidote-filled cracks dissect the gabbros.

Trondhjemite bodies form about 1% of the gabbro zone, and are concentrated near its top. They generally occur as intrusion breccia matrices, although locally they form the cores of pegmatitic gabbro pods (Dunning, 1987). In many cases, the trondhjemites are spatially associated with putative paleo-normal faults (Dunning, 1984). These faults are represented by poorly exposed narrow zones of cataclasites and mylonitic rocks.

The sheeted dyke complex consists of subparallel diabasic dykes with widths typically 1-10 m at its base, and 0.5-3 m higher up in the section (Dunning, 1987). Dykes range from aphanitic to medium grained, and may have subophitic to diabasic textures, with nearly equal amounts of clinopyroxene and plagioclase. Oxides may be abundant (up to 20%). Dykes are commonly plagioclase-phyric (generally <5%, locally 10%), rarely plagioclase + clinopyroxene-phyric. Pillow lavas (0.2-1 m) are commonly aphyric, but may contain a few percent plagioclase phenocrysts (Dunning, 1987). The lavas are cut by abundant dykes, and locally contain interpillow jasper. Dykes and basalts are generally pervasively altered, with complete replacement of clinopyroxene by amphibole and partial replacement of plagioclase by sericite, chlorite, and epidote.

The 25 x 7 km sized Star Lake ophiolite massif exposes a shallowly north to northeast-dipping, tectonically bounded section through gabbros and sheeted dykes (Fig. 3.1). Basalts are present to the northeast of the sheeted dykes, and were considered to be part of the ophiolite by Whalen (1993). However, recent mapping and geochemical data suggest they form part of the structurally underlying Lloyds River Complex, which comprises a 473 Ma arc-back arc sequence (Chapter 5). The thickness of the Star Lake ophiolite units is uncertain. The lowermost part of the gabbro zone of Star Lake, like Annieopsquotch, also contains abundant troctolitic enclaves, suggesting it preserves a similar section. The fault-bounded, 12 x 5 km, King George IV ophiolite comprises similar gabbros, sheeted dykes, and basalts of uncertain thickness. The ophiolite pseudostratigraphy and pillow tops indicate that the King George IV ophiolite youngs towards the west with a dip of >60°.

The Hungry Mountain complex of the Notre Dame Arc is dominated by diorites and tonalites that contain abundant mafic-ultramafic fragments, which were interpreted by Whalen et al. (1997) to be correlative to the Annieopsquotch ophiolite. The Hall Hill complex was described in detail by Bostock (1988), and comprises a 25 x 5 km sized fault-bounded block of variably metamorphosed gabbros, plagiogranite, and basalts, cut by diabase dykes (Bostock, 1988). It is situated on the north coast of Newfoundland immediately southeast of the Lobster Cove fault (Fig. 3.1).

3.4. Whole-rock geochemistry

3.4.1. Sampling and analytical techniques

We analyzed major and trace elements for 78 samples of troctolites, gabbros, sheeted dykes, and lavas from the Annieopsquotch ophiolite, 15 samples from the Star Lake ophiolite, and 4 from the King George IV ophiolite. Data are listed in Table 3.1, with the exception of data of gabbros and some of the crosscutting dykes of the Annieopsquotch ophiolite, which are given in Chapter 4 (Table 4.1). Details on the different procedures, as well as detection limits, can be found in Appendix II and Rogers (2004).

3.4.2. Element mobility

Hydrothermal ocean floor metamorphism and subsequent accretion-related metamorphism has affected the Annieopsquotch ophiolite belt to various degrees. The distribution of hydrous assemblages is thought to predominantly reflect ocean floor processes, but mineral equilibria were probably partly reset during the amphibolite-facies metamorphism which accompanied accretion of the Annieopsquotch ophiolite belt to the Dashwoods microcontinent. The effect of these metamorphic episodes on the geochemistry of the samples is evaluated by plotting various elements against the immobile incompatible element zirconium, which is also an index of fractionation. The sheeted dykes show good correlations against Zr for all elements but Rb and Cs; Ba, Pb, Sr, and K (with the exception of two samples) also show reasonable correlations. The dominantly magmatic abundance patterns are consistent with the low LOI (average 1.2%). Basalts show greater element mobility than dykes, concurrent with an increase in LOI (average 2.1%). Some basalts have increased contents of SiO_2 and Na_2O, while some CaO has been removed. Sr, Ba, and Cs were mobile in most samples. Abundances of K_2O and Rb are low (<0.1% and 0.1-2 ppm, respectively) in almost all samples, likely indicating removal of these elements. Al_2O_3 shows a broad correlation with Zr, suggesting limited mobility, and Pb correlates well with Zr for all but the most altered samples. Nonetheless, despite the relatively consistent behaviour of the LILE, I mostly use immobile trace elements (REE, HFSE) for the paleo-tectonic interpretation of the gabbros, sheeted dykes, and basalts. Element abundances in troctolites are inferred to be almost entirely magmatic in origin.

3.4.3. Troctolites, Annieopsquotch ophiolite

The troctolites have high Mg# = 0.81-0.85 (Mg# = Mg/(Mg+Fe^{2+}), assuming Fe^{3+}/Fe^{2+} = 0.1) and show major element chemical patterns dominated by accumulation of plagioclase and olivine. Incompatible trace element abundances are low (e.g., chondrite normalized Yb_N = 0.4-0.8; normalization values of Sun and McDonough, 1989), whereas compatible elements such as Ni are high (Table 3.1). They also have strong positive Eu anomalies (Eu/Eu* = 3.31-4.19), reflecting their plagioclase-cumulate nature. The REE patterns are flat, LILE (Cs, Rb, K, Sr, Pb) are strongly enriched, and HFSE contents are low (mostly below detection limit; Fig. 3.3a,b).

In order to evaluate the origin of the troctolite substrate, I calculated the compositions of the magmas that generated the Annieopsquotch troctolites using the method of Bédard (1994). This method calculates the liquid in equilibrium with a given cumulus assemblage by combining whole rock geochemical analyses with an updated, parameterized partition coefficient dataset (Bédard, 2004). Trapped melt was modeled as a phase with D=1 for all elements under the assumption that was in equilibrium with the cumulus phases, and calculations were repeated with different amounts of trapped melt. The modes of the samples were estimated from thin section, augmented by CIPW modes, but have little effect on the calculated melt composition (Bédard, 1994). Partition coefficients were calculated for each phase in each sample based on mineral compositions determined by electron microprobe. The use of a trapped melt fraction in equilibrium with the cumulus crystals assumes that (see also Bédard, 1994) (1) the trapped melt remained in contact with the main melt resevoir during growth of the cumulus crystals and their adcumulus overgrowths (see Wager et al., 1960), and (2) that no late-stage percolation of trapped melt (more evolved or more primitive than the equilibrium trapped melt) occurred. Equilibrium between the trapped melt and cumulus crystals is supported by the absence of prominent compositional zoning in the Annieopsquotch cumulates, which would be expected had more primitive or more evolved melt percolated the cumulate pile.

The composition of the model melts for different amounts of assumed trapped melt are listed in Table 3.2 and illustrated in Figure 4. The melts that generated the troctolites were clearly more depleted in incompatible elements than NMORB, with flat REE patterns, and U-shaped extended-REE plots with enrichment in LILE. Assuming 10% trapped melt, the TiO_2 contents of the model liquids are low (c. 0.3%), whereas Cr and Ni contents are high (c. 600 ppm and c.100-300 ppm, respectively). The low REE and HFSE contents and high compatible element contents signal melting of a refractory source, which is typical of boninites (e.g., Crawford et al., 1989). The model liquids correspond reasonably well with boninites from the Betts Cove ophiolite (Fig. 3.4; Bédard, 1999), suggesting that the troctolite substrate formed from boninite-like magmas. The plagioclase-rich nature of the troctolites is enigmatic, but may indicate that the parental magmas, if indeed boninitic, were of the high-calcium type, which is the least depleted of the boninitic subtypes (Crawford et al., 1989). The Mg# of the parental melt was 61-58, as calculated from olivine analyses using an olivine-liquid partition coefficient of 0.3 (Roeder and Emslie, 1970), and neglecting the trapped melt effect (Barnes, 1986). This is in the lower range of typical boninites (e.g., Crawford et al., 1989), suggesting that the parental magmas were evolved, which may in part account for the abundance of plagioclase. Plagioclase phenocrysts have been described in similarly evolved high-calcium boninites from Tonga (Mg# 57-63; Falloon and Crawford, 1991), the New Hebrides arc (Mg# 60-70; Monzier et al., 1993), and the Izu-Bonin-Mariana fore-arc (Mg# 55; Meijer, 1980; Hickey and Frey, 1982). In these suites, plagioclase phenocrysts are associated with clinopyroxene, orthopyroxene and olivine.

We note that the high Cs content of the model liquids (3.2-10.5 ppm assuming 10% trapped melt; Fig. 3.4), which reflects the high Cs content of the whole rock analyses (0.39-1.32 ppm) probably does not reflect the original magmatic abundance of this element. Its concentration far exceeds that in any Tertiary-recent boninite. The same may hold for Rb and K in samples VL01J035b and VL02J310A and P in samples VL02J309B and VL02J310a. Unrealistically high Cs (and locally Ba, K, and P) contents in some troctolites suggest that (1) the trapped melt was evolved, having concentrations of these elements that exceed concentrations in equilibrium with the cumulus phases, or (2) LILE were introduced by an external agent, possibly a melt or hydrous fluid associated with the intrusion and crystallization of the gabbros, or a post-magmatic hydrous fluid responsible for serpentinization.

3.4.4. The gabbro-sheeted dyke-basalt sequence, Annieopsquotch ophiolite

The basaltic sheeted dykes and pillow lavas of the Annieopsquotch ophiolite belt define a typical tholeiitic differentation trend with increasing Fe-content during differentiation, consistent with low-pressure fractionation of olivine, plagioclase, and clinopyroxene. The basaltic Annieopsquotch ophiolite belt dykes and lavas have a wide compositional range, with MgO 4.45-9.55 %, SiO_2 45.3-53.3%, Mg# 0.42-0.72, and TiO_2 0.36-1.95%. Three chemical groups have been recognized based primarily on the degree of LREE depletion (La/Sm) and the extent of Nb depletion (Fig. 3.5). Differences between these groups are also reflected in contrasting Mg# and TiO_2 contents (Table 3.1).

The first group comprises nearly all of the sheeted dykes and basaltic lavas, as well as some dykes that crosscut the gabbro zone, and is characterized by LREE depletion slightly stronger than NMORB (NMORB normalized La/Sm = 0.59–1.35, av. = 0.81) and low Nb contents (Fig. 3.5). It has average SiO_2 and TiO_2 contents of 49.2% and 1.25%, respectively, and an average Mg# of 0.56. Trace element patterns resemble MORB overall, but negative anomalies for Nb, Zr, and Ti are apparent, and dykes show enrichment in K, Ba, and, in some samples, Pb and Sr (Fig. 3.3c-d). These features are ubiquitous in intraoceanic arcs, which result from melting of a mantle source triggered by the release of hydrous fluids from the subducting slab and/or metasomatized mantle (e.g., Tatsumi et al., 1986). Trace element and isotopic evidence indicates that, in primitive island arc tholeiites, the depleted mantle wedge imparts the LREE depletion signature, while the slab-derived fluids carry LILE (Cs, Ba, Rb, K, Pb, Sr) into the sub-arc mantle, enriching the arc source in these components (e.g., Pearce, 1983; Tatsumi et al., 1986; Saunders et al., 1991; Hawkesworth et al., 1991; Class et al., 2000). Depletion in HFSE (Ti, Nb, Zr, Ta) may result from residual phases within the mantle source and/or subducting slab (rutile, titanite: e.g., Saunders et al., 1991; Brenan et al., 1994), a solubility effect in the fluids released from the slab (e.g., Keppler, 1996), or interaction of rising magmas with the mantle (Kelemen et al., 1990). The HFSE depletion and enrichment in LILE of the Annieopsquotch tholeiites thus suggest that the spreading center at which the ophiolites formed was situated near a subduction zone, or tapped a source previously enriched by subduction zone processes. A suprasubduction zone (SSZ) setting is consistent with the similarity between the Annieopsquotch tholeiites and basalts from the Lau back arc basin (Fig. 3.3c-d), which have been interpreted to be melts of a depleted MORB-like mantle, but with a distinct subduction zone component (low HFSE and enriched LILE) derived from the associated Lau remnant arc and active Tofua arc (Hawkins and Allan, 1994).

The second group is found only among the basaltic lavas, and is particularly abundant near the stratigraphic top of the extrusive section. It has higher average SiO_2 (50.5%) and TiO_2 (1.43%) contents and lower average Mg# (0.52) than Group 1, and shows NMORB-like LREE depletion and Nb contents (Fig. 3.5). These basalts exhibit only small Nb, Zr, and Ti anomalies (Fig. 3.3e-f), suggesting they have a NMORB-like source, with only a minor SSZ signature.

The third group comprises dykes that crosscut the gabbros, lavas, and sheeted dykes. They are characterized by strong LREE depletion relative to NMORB (average La/Sm_N = 0.45), low incompatible element contents (average TiO_2 = 0.98%; average Nb_N =0.18) and high Mg# (0.53-0.72, average 0.63). Their trace element patterns show variable Nb, Ti, and Zr anomalies (Fig. 3.3g-h), and the samples have variable HREE contents for a given Mg#. The low but variable incompatible element contents and strong LREE depletion suggest these dykes are generated by variable degrees of partial melting of a depleted source, and the preservation of dykes with Mg# of 0.72 suggest some of them have experienced little fractionation since leaving their mantle source. Based on their occurrence throughout the ophiolite pseudostratigraphy, their primitive nature, low incompatible element contents and the magnitude of geochemical variation, I interpret these dykes to be off-axis intrusions that sampled the last, most depleted increments of melt from the melting column. This interpretation is supported by the fact that most of these dykes are markedly fresher than their host rocks. It is also consistent with off-axis lava compositions from the East Pacific Rise, which are more primitive than NMORB, and have lower incompatible element contents (Reynolds and Langmuir, 2000).

Annieopsquotch gabbros have high Mg# (0.53-0.81, average 0.71) and low TiO_2 contents (average 0.49%). The low incompatible element contents indicate that most are cumulates, with the exception of sample VL02J341A, which comes from the uppermost part of the gabbro zone. Their trace element patterns show marked negative Nb, Ti and Zr anomalies, as well as enrichment in Pb, suggesting they may have crystallized from melts similar to Group 1 basalts (Fig. 3.3i-j). The parental magmas of gabbroic cumulates, modeled in a similar fashion as for the troctolites, have compositions indistinguishable from Group 1 dykes and basalts, suggesting these gabbros, dykes and basaltic lavas are consanguineous (Chapter 4). Two samples (VL02J326b and VL01J339a) have negligible Zr and Ti anomalies, and a small Nb anomaly, and may have crystallized from melts with Group 2-like compositions.

3.4.5. The Star Lake and King George IV ophiolites

In order to evaluate the along-strike variety in magma compositions in the Annieopsquotch ophiolite belt, I compare the chemistry of the Annieopsquotch ophiolite, presented above, with the chemistry of the other major components of the belt (Star Lake, King George IV).

The majority of samples from the Star Lake and King George IV ophiolites follow trends very similar to Group 1 of the Annieopsquotch ophiolite. Dykes and basalts from King George IV and Star Lake are indistinguishable from the Annieopsquotch dykes and basaltic lavas (Figs. 3.6a-b, g-h); they too are MORB-like, LREE depleted, and characterized by HFSE depletion, and so are interpreted also to have formed in a SSZ setting. Star Lake ophiolite gabbros are generally depleted in LREE, Zr and Ti, and enriched in LILE. They have the same composition as gabbros from the Annieopsquotch ophiolite (Fig. 3.6c-d), which are cumulates complementary to the melt compositions preserved in the sheeted dykes and basaltic lavas (Chapter 4). Like those from Annieopsquotch, troctolites from the Star Lake ophiolite show strong REE-HFSE depletion, and enrichment in Cs, Ba, K, Sr and Pb (Fig. 3.6c,d). In contrast, the Fo content of olivine in Star Lake troctolites (average 81.8) is slightly lower than that in Annieopsquotch troctolites (83.1), whereas absolute REE contents are slightly higher (Fig. 3.6c-d). These data are compatible with three hypotheses, which are not mutually exclusive. The Star Lake ophiolite troctolites may have: 1) accumulated from a slightly more differentiated version of the same melt which generated the troctolites in the Annieopsquotch ophiolite; 2) formed from a somewhat less depleted source; 3) retained a larger fraction of trapped melt. These data suggest the majority of the Star Lake and King George IV ophiolites formed from magmas very similar, if not identical, to those from which the Annieopsquotch ophiolite formed.

A group of five gabbroic samples that occur in the upper level of the gabbro zone of the main Star Lake massif, as well as in a smaller ophiolitic body just to the west of it (Fig. 3.1), have trace element patterns that deviate from the MORB-like patterns of the Annieopsquotch gabbros. The age relationships between these anomalous gabbros and the tholeiitic gabbros are unclear. The anomalous gabbros are dominated by clinopyroxene and plagioclase, with, in two samples, olivine (15%) and orthopyroxene (5%). These rocks have a mesocumulate texture, with intercumulus amphibole, suggesting the magma was hydrous. They have SiO_2 44.9-48.5%, TiO_2 0.12-0.15%, Mg# 0.77-0.80 and positive Eu anomalies (1.4-2.1), reflecting their cumulate nature. One of these anomalous gabbros (VL02J380a) has lower SiO_2 (41%), and high FeO and TiO_2 contents (16.3% and 1.24%, respectively), suggesting accumulation of Fe-Ti oxides. Trace element patterns are characterized by low HREE abundances, significantly lower than the gabbros from the Annieopsquotch ophiolite, and enrichment in LREE (i.e. high La/Nd), which is not observed anywhere within the Annieopsquotch ophiolite (Fig. 3.6e-f). The Mg# of the parental melt was 0.45, as calculated from olivine and orthopyroxene compositions using Fe/Mg partition coefficients of 0.30 and 0.27, respectively, and neglecting the trapped melt effect (Barnes, 1986). The relatively low Mg# of the parental melt and accumulation of Fe-Ti oxides in sample VL02J380A, suggest the melt was quite evolved. The presence of orthopyroxene as a cumulus phase suggests the parental melt was SiO_2 saturated. For reasonable assumed trapped melt fractions, estimated from the change in LREE slope and LILE contents during modeling, calculated parental melts of the olivine gabbros are markedly more depleted than Annieopsquotch sheeted dykes and basalts with similar Mg# (Table 3.2; Fig. 3.7); and calculated melt TiO_2 contents (around 0.5%) are much lower than would be expected from evolved MORB-like magmas. Thus despite their fractionated nature, incompatible element abundances of the model parental melts are very low, suggesting the melts from which they evolved were extremely depleted, and may have been similar to the boninitic magmas that generated the troctolites. A boninitic parent is consistent with the observed enrichment in LREE, with the SiO_2 saturation indicated by the presence of orthopyroxene, and with the hydrous nature of the melt suggested by the presence of intercumulus amphibole. The similarity in degree of depletion, measured by the HREE content, between the calculated melt and evolved boninites from the Tonga ridge (Mg# 47; Falloon and Crawford, 1991) supports this interpretation (Fig. 3.7). Interestingly, the evolved boninite from Tonga is olivine-plagioclase-orthopyroxene-clinopyroxene phyric (Falloon and Crawford, 1991), which corresponds to the cumulus phases in the modeled Star Lake olivine gabbro. If the Star Lake olivine gabbros were indeed generated from a boninitic melt, this suggests a genetic link with the troctolites that occur within the lowermost part of the Annieopsquotch and Star Lake gabbro zone, although a stronger enrichment in LREE and steeper slope in the MREE indicates the melts which generated the olivine gabbros were different from those that generated the troctolites. Possibly, these rocks represent a higher-level relict of a boninitic substrate that formed the basement to the SSZ sequence?

3.5. Discussion

The geochemical similarity of the tholeiitic sequences of the Annieopsquotch, Star Lake and King George IV ophiolites, as well as the occurrence of troctolite enclaves in the lower part of the gabbro zone of both the Star Lake and Annieopsquotch ophiolites, supports previous interpretations that the Annieopsquotch ophiolite belt represents a single piece of oceanic lithosphere (Dunning and Chorlton, 1985; Dunning, 1987). Data presented herein show that the Annieopsquotch ophiolite belt comprised three distinct magma series. The first phase encompassed the formation of a boninitic substrate or basement, represented by the troctolitic enclaves in the gabbros of the Annieopsquotch and Star Lake ophiolites. The Star Lake gabbros that appear to have crystallized from an evolved boninitic melt may also have formed during this phase, although relationships are not clear from field evidence. The boninitic phase was followed by tholeiitic gabbros, sheeted dykes, and lavas, which dominate the Annieopsquotch, Star Lake, and King George IV ophiolites. The tholeiitic magmas initially had a strong SSZ geochemical signature (Group 1), which became less pronounced with time (Group 2). The age-gap between the boninitic and tholeiitic series is not constrained. Finally, depleted tholeiitic off-axis dykes cut the entire sequence.

3.5.1. Model for Generation of the Annieopsquotch ophiolite belt

Any model for generation of the Annieopsquotch ophiolite belt has to account for the following: 1) an early phase of boninitic magmatism; 2) a main phase of rapid seafloor-spreading tapping mantle enriched by subduction zone processes; 3) accretion to the Dashwoods microcontinent within 10 Ma after formation of the tholeiite sequence; 4) a lower-plate setting during accretion to the Dashwoods microcontinent. An additional constraint is provided by the fact that the Annieopsquotch ophiolite belt is the oldest unit preserved within the Annieopsquotch Accretionary Tract, and is juxtaposed with the Dashwoods microcontinent. Thus there is no record of preexisting intra-oceanic units within the peri-Laurentian portion of Iapetus that may have contributed to formation of (part of) the Annieopsquotch ophiolite belt.

The depleted nature of boninites (high MgO, Ni, Cr, low Al_2O_3, TiO_2, HREE) is widely interpreted to result from melting of a refractory mantle wedge, from which melts had previously been extracted. This source is enriched by a LILE-rich hydrous fluid, and possibly by a LREE rich melt, commonly interpreted to be derived from the subducting slab and/or overlying sediments (e.g., Crawford et al., 1989; Sobolev and Danyushevsky, 1994; Bédard, 1999). The temperatures required for melting refractory mantle to produce boninites (1100° - 1550°C: Crawford et al., 1989; Sobolev and Danyushevsky, 1994) are higher than those expected in a typical sub-arc mantle wedge, and three end member processes have been proposed to explain the elevated mantle temperatures. The first involves introduction of a heat source into "normal" sub-arc mantle wedge, by subduction of a spreading ridge (Crawford et al., 1989) or propagation of a spreading center into an arc or fore-arc (e.g., Tonga: Falloon and Crawford, 1991; New Hebrides: Monzier et al., 1993). The second process invokes rapid upwelling of mantle in response to extension induced by arc or fore-arc rifting rifting (Crawford et al., 1981; Hickey and Frey, 1982; Bédard et al., 1998) or the initiation of subduction (e.g., Izu-Bonin-Mariana fore-arc; Stern and Bloomer, 1992; Pearce et al., 1992). The third process involves a high geothermal gradient caused by the presence of a mantle plume (Macpherson and Hall, 2001).

Whereas I cannot rule out the possibility that there was influence of a mantle plume, no evidence exists within the Annieopsquotch ophiolite belt of an OIB-like geochemical signature. I therefore infer a plume was not the primary cause of boninite generation in the Annieopsquotch ophiolite belt. In addition, as mentioned above, there is no record of an intra-oceanic arc of the appropriate age and structural position associated with the Annieopsquotch ophiolite belt. The absence of an associated intra-oceanic arc indicates the boninitic magmas did not form by arc or fore-arc rifting or propagation of a spreading center into an arc.

The Annieopsquotch ophiolite belt is bounded by the Early Ordovician (488-480 Ma; van Staal et al., 2003) continental Notre Dame Arc and its Dashwoods basement on the northwestern side and the younger Lloyds River complex and Buchans arc (473 Ma; Dunning et al., 1987; Zagorevski et al., 2003) on the southeastern. The Buchans arc is built on attenuated continental crust (Zagorevski et al., 2003), suggesting that the Buchans arc, like the Notre Dame Arc, was built on a rifted piece of Laurentian crust. This raises the possibility that the Annieopsquotch ophiolite belt may have been generated in a peri-continental intra-arc rift basin separating the Buchans and Notre Dame arcs (cf. Swinden et al., 1997). In such a scenario the boninites could have been generated in the early stages of arc rifting by decompression melting of a mantle source that was already depleted in HFSE and HREE and enriched in LILE and LREE due to the generation of Notre Dame Arc magmas. The tholeiites could then have formed by subsequent upwelling of less depleted mantle as the extension proceeded, with the magma supply increasing to the point where it kept pace with the rate of opening. However, three lines of arguments indicate this scenario is unlikely. First, boninites have not been observed in young oceanic basins that formed by rifting of continental arcs, such as the Japan Sea, the Bransfield Strait, the Gulf of California and the Sarmiento complex. The earliest magmas formed in these basins are typically tholeiitic basalts with suprasubduction zone signatures, which are quickly followed by MORB-like lavas (e.g., Saunders et al., 1982; Alabaster and Story, 1990; Keller et al., 2002). Second, there is a remarkable scarcity of clastic sedimentary rocks within the Annieopsquotch Accretionary Tract, and the Annieopsquotch ophiolite belt in particular, contrary to what would be expected within an immature rift separating two continental blocks (e.g., Gulf of California; Saunders et al., 1982). Third, Nd isotopic data for the Annieopsquotch ophiolite belt suggest it is very juvenile (ε_{Nd}=7.6-8.3; Swinden et al., 1997), inconsistent with a crustal contribution. The only remaining possibility to explain the absence of an associated intra-oceanic arc is a scenario in which the Annieopsquotch ophiolite belt formed during initiation of subduction. This is similar to the Izu-Bonin-Mariana fore-arc, where the early stage of subduction was characterized by widespread boninitic magmatism (200 km wide) in a strongly extensional environment interpreted to result from rollback of the old Pacific plate in the early stages of subduction (Stern and Bloomer, 1992). Hall et al. (2003) showed that after a finite amount of convergence (100 km), the buoyancy-related force of the sinking slab leads to a period of rapid rollback, with extension rates in the overriding plate of 10 cm/yr. Rapid extension allows for the ascent of mantle to shallow levels, leading to the high geothermal gradient required for boninite genesis. In this scenario, decompression melting of the mantle, as well as contact melting of the overlying depleted mantle, aided by slab-derived fluids, would have yielded the boninites.

Using the Izu-Bonin-Mariana forearc as an analogy, I envisage the following evolution of the Annieopsquotch ophiolite belt (Fig. 3.8). Subduction would have initiated outboard of the Dashwoods microcontinent, perhaps as a result of a plate reorganization following initial collision between Laurentian promontories and the Dashwoods microcontinent. Sedimentological evidence suggests the collision was underway at least by the Middle Arenig (475 Ma; see Waldron and van Staal, 2001), which coincides with a marked gap in arc magmatism in the Dashwoods microcontinent (van Staal et al., 2003). Subduction likely initiated along a preexisting weak zone in the crust. Little is known about the spreading history of Iapetus, although the presence of peri-Laurentian microcontinents (e.g., Dashwoods) suggests the presence of abandoned spreading centers and associated transform faults near the Laurentian margin (Müller et al., 2001). Such zones of weakness may have been reactivated during subduction initiation. Given that Laurentia separated from west Gondwana at 570 Ma (Cawood et al., 2001), the oceanic lithosphere immediately outboard of the Dashwoods microcontinent was likely rather cool at the time of subduction initiation, with a lithospheric thickness approaching 95 km (Richardson et al., 1995). The lithospheric mantle was probably already depleted after the extraction of Iapetus oceanic crust from it.

Subduction initiation caused early extension in the overriding plate, leading to stretching and eventual break-up (Fig. 3.8). Melt production during stretching and initial break-up was probably minor, due to a low geothermal gradient and absence of fluids derived from the subducting slab. Once started, rollback proceeds extremely fast, leading to very quick influx of hot mantle from below (Hall et al., 2003). After 60 km of subduction of the downgoing plate, the more fertile asthenospheric mantle would have ascended to 50 km depth, assuming the amount of upwelling is more or less equal with the amount of mantle displaced by rollback. At this stage, boninitic magmas would have formed when the depleted mantle reached a level where it was fluxed with fluids derived from the subducted slab (Fig. 3.8b). These magmas generated crust now preserved as the Annieopsquotch and Star Lake troctolites, and some gabbros. Associated volcanic rocks have not been observed; I speculate that they have been tectonically removed during rollback-induced extension of the boninitic substrate, possibly by low-angle detachment faulting similar to that occurring along mid-ocean ridges (e.g., Karson, 1999). Subduction initiation and boninite genesis must have occurred prior to 480 Ma, the age of the tholeiitic sequence (Dunning and Krogh, 1985), but the time interval between the boninitic and tholeiitic phases is uncertain.

As extension proceeds, fertile mantle may decompress enough to initiate melting (e.g., Pearce & Parkinson, 1993), an effect that would be amplified if the rising fertile mantle enters the region of the mantle wedge that is fluxed by fluids expelled from the subducting slab (Fig. 3.8c). In the Annieopsquotch ophiolite belt, this process may have yielded tholeiitic SSZ magmas at 481-478 Ma, which generated the dominant gabbro-sheeted dyke-basaltic lava sequence. Rapid extension was accompanied by a robust supply of magma and led to seafloor spreading. Extension may have contributed to break-up of the boninitic substrate, producing the current configuration of isolated troctolitic enclaves within the gabbros. Continued spreading may have removed the spreading axis from the vicinity of the subducting slab and its derived fluids, leading to more MORB-like compositions at the top of the extrusive section. This is analogous to the rapid transition from SSZ to MORB-like compositions during formation of back arcs (e.g., Ewart et al., 1994).

As the convergence rate and subduction angle stabilize, a true magmatic arc may form after 15 Ma (Stern and Bloomer, 1992). In contrast, the absence of andesites and dacites suggests that the Annieopsquotch ophiolite belt never reached the stage of a true magmatic arc. Instead, arc magmatism was localized outboard of the Annieopsquotch ophiolite belt forming the Buchans arc on a piece of Dashwoods basement which is interpreted to have been emplaced by trench-parallel transport (Zagorevski et al., 2003; Fig. 3.8d).

3.5.2. Implications for tectonic evolution of the Newfoundland Appalachians

Structural relationships in the Lloyds River Fault Zone, which separates the Annieopsquotch ophiolite belt from the remnants of the Dashwoods microcontinent, suggest the Annieopsquotch ophiolite belt was thrust underneath Dashwoods (Fig. 3.1; Chapter 6). The fact that similar structural relationships occur in related segments along strike for at least 200 km (Dean and Strong, 1977; Calon and Green, 1987; Thurlow et al., 1992), and that the Lloyds River Fault zone extends to 15 km depth (van der Velden et al., 2004), together indicate the Annieopsquotch ophiolite belt occupied a lower plate setting during accretion to the Dashwoods microcontinent. Thus after its formation the Annieopsquotch ophiolite belt was transferred from an upper to a lower plate setting (Fig. 3.8). Moreover, age data indicate arc-back arc complexes of the Annieopsquotch Accretionary Tract, to the southeast of the Annieopsquotch ophiolite belt, become progressively younger to the east (Zagorevski et al., 2003). These relationships suggest that the subduction zone in which the Annieopsquotch ophiolite belt was formed dipped to the west. After generation of the Annieopsquotch ophiolite belt during initiation of subduction, west-directed subduction thus continued, with the overlying arc remaining in extension during most of its history. This episode was marked by important strike-slip movements, leading to trench-parallel transport of the basement to the Buchans arc (Zagorevski et al., 2003). In addition, accretion of the various units of the Annieopsquotch Accretionary Tract to the Dashwoods microcontinent involved a sinistral strike-slip component (Chapter 6). This suggests that both subduction and subsequent accretion were oblique. I note, however, that strike slip processes cannot have been responsible for the occurrence of the two distinct units (boninites and tholeiites) within the Annieopsquotch ophiolite belt, e.g. by initiating spreading in a previously generated boninitic crust formed by arc-related processes (arc rifting, propoagation of a spreading center into an arc), as such older units do not exist.

3.6. Conclusions

Field and geochemical data from the Annieopsquotch ophiolitic belt show that all of the different massifs have similar compositions and record similar magmatic histories, and likely constitute a single accreted oceanic terrane. Field relationships imply that the Annieopsquotch ophiolite belt was generated in three phases. The first phase, of unknown age, encompasses troctolites and olivine gabbros formed from boninitic melts. The absence of an associated coeval intra-oceanic arc suggests the boninites were generated during initiation of subduction outboard of the Dashwoods microcontinent by shallow melting of a previously depleted mantle source. Subduction likely initiated in response to the collision between the Dashwoods microcontinent and the Laurentian margin. The second magmatic phase comprises the tholeiitic SSZ gabbro-sheeted dyke-basalt sequence formed at 480 Ma, followed by the final magmatic episode represented by off-axis dykes that cut the entire ophiolite. This model differs significantly from existing tectonic models for the Newfoundland Appalachians, where the Annieopsquotch ophiolite belt is interpreted as scraped-off NMORB Iapetus oceanic crust (van Staal et al., 1998), or as back-arc basin crust (Swinden et al., 1997). These data constrain the timing of initiation of west-directed subduction outboard of the composite Laurentian margin. This subduction zone was responsible for formation of the entire Annieopsquotch Accretionary Tract, and thus played a significant role in Early Ordovician Appalachian orogenesis.

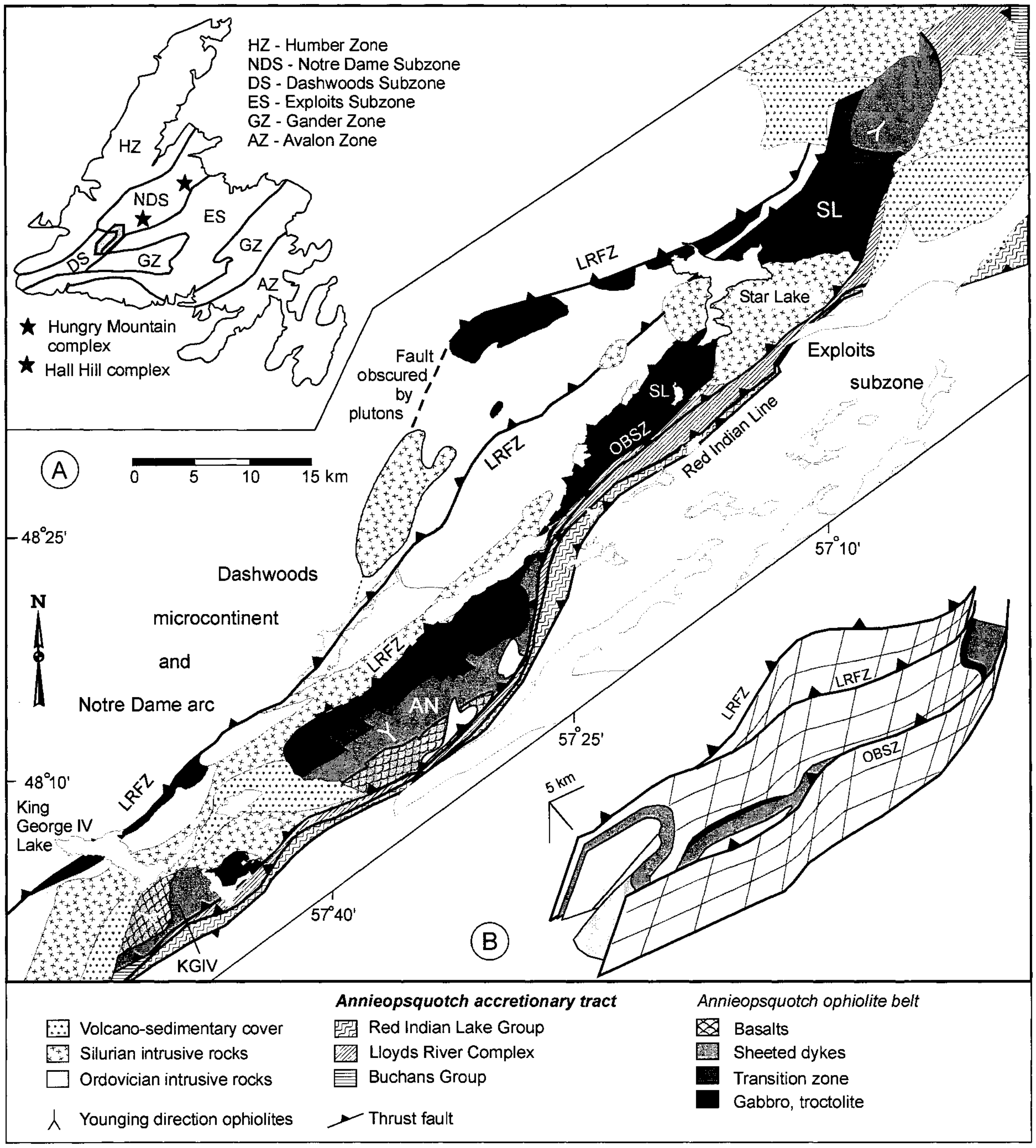

Figure 3.1: (a) Geological map of the Annieopsquotch Accretionary Tract, showing the regional relationships and stratigraphic units of the Annieopsquotch (AN), Star Lake (SL) and King George IV (KGIV) ophiolites. Inset shows location, tectonostratigraphic zones of the Newfoundland Appalachians, as well as the locations of the Hungry Mountain and Hall Hill complexes. OBSZ=Otter Brook Shear Zone. Modified from Lissenberg et al. (in press) and van Staal et al. (in press a,b,c). (b) Schematic block diagram illustrating the structure of the main components of the Annieopsquotch ophiolite belt, ignoring Middle Ordovician-Silurian intrusions and cover sequences. Plunge of folds is estimated from dip of ophiolite pseudostratigraphy. Contacts between gabbro zone and transition zone, transition zone and sheeted dykes, and sheeted dykes and basalts are dark grey, grey and light grey, respectively.

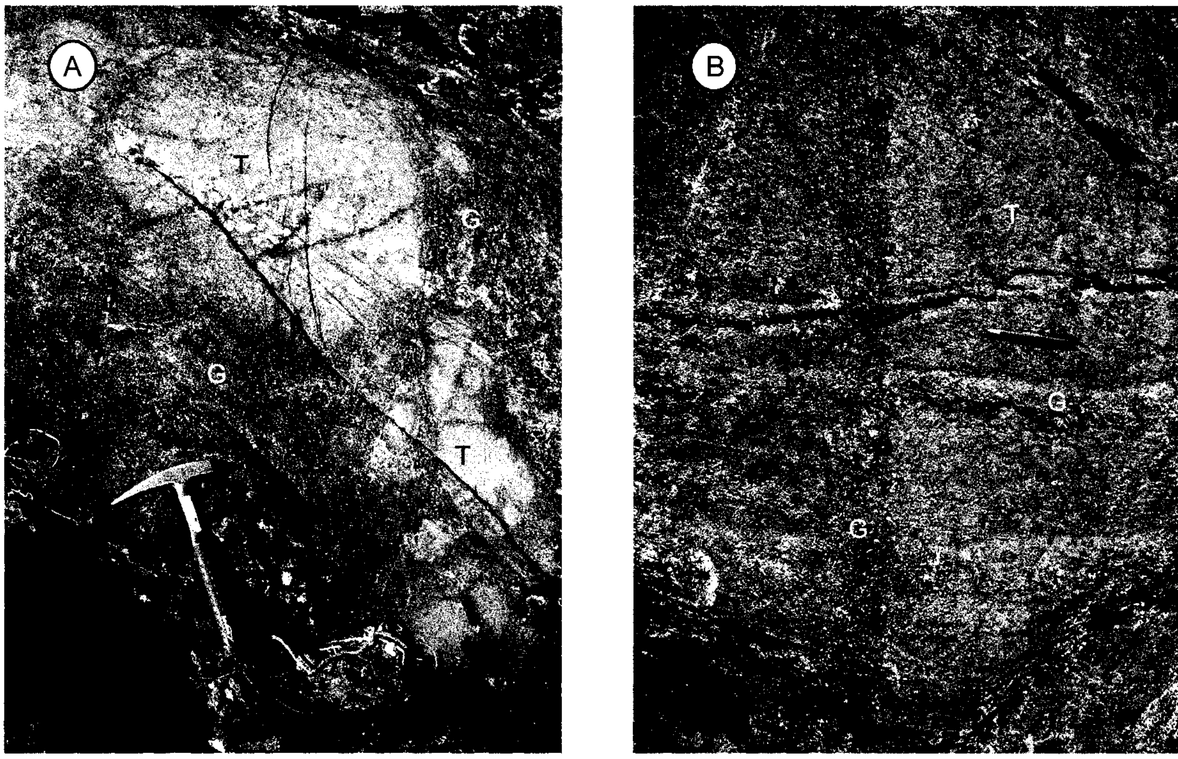

Figure 3.2: Field relationships between troctolites and gabbros in the Annieopsquotch ophiolite. (a) Fine-grained troctolite (T) forms decameter-sized enclaves within invading medium-grained gabbro (G). Hammer for scale is 30 cm long. (b) Medium-grained, layered troctolite enclave (T) is cut by numerous medium- to coarse-grained olivine gabbro and gabbro veins (G; vertical and horizontal in photo). Pen for scale (15 cm long) is parallel to layering in troctolite.

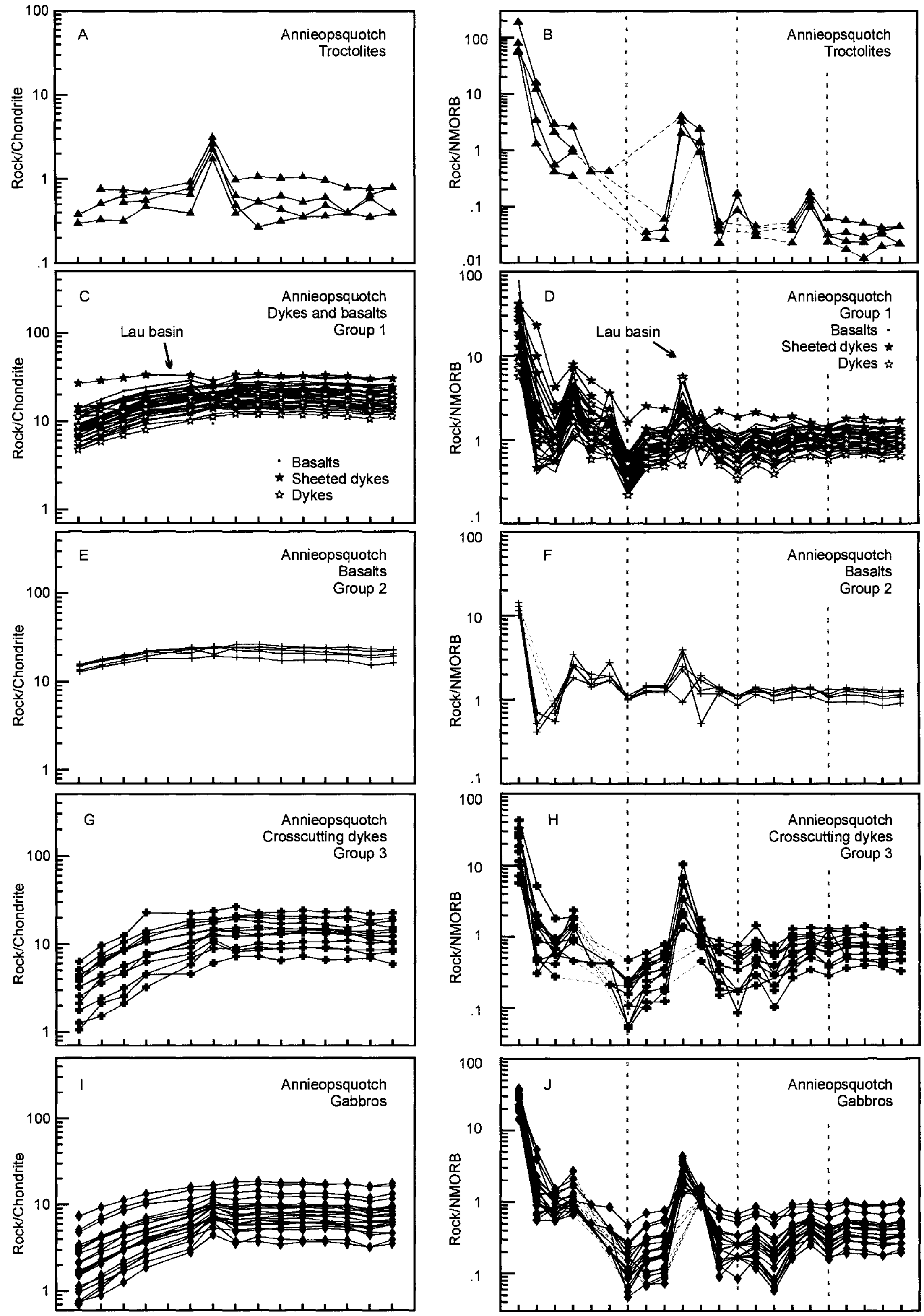

Figure 3.3: Whole rock geochemical data of the Annieopsquotch ophiolite. (a-b) troctolites; (c-d) sheeted dykes and basalts (Group 1); (e-f) basalts (Group 2); (g-h) Crosscutting dykes (Group 3); (i-j) gabbros. Note the very depleted nature of the troctolites, and relative depletion in Nb, Ti and Zr of sheeted dykes and basalts. Grey fields outline the composition of basalts from the Lau basin (Hergt et al., 1994 a, b). Normalizing values from Sun and McDonough (1989).

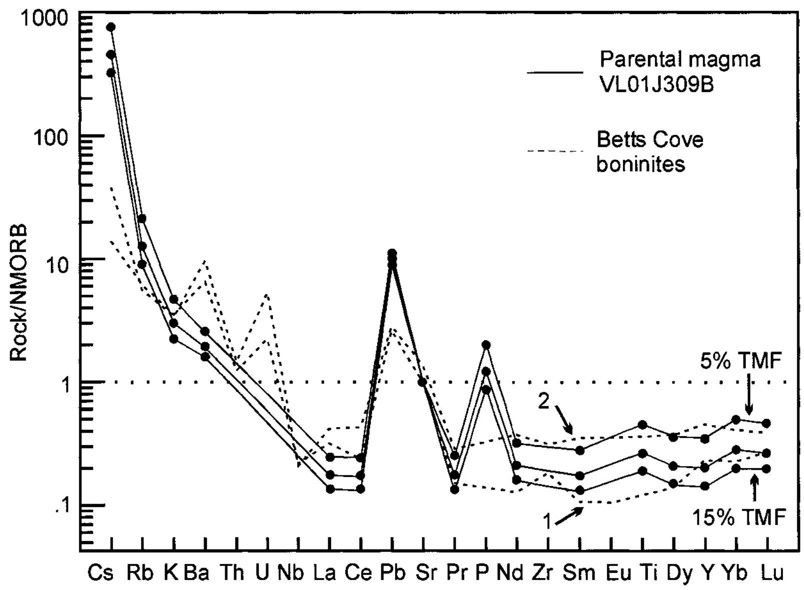

Figure 3.4: Modeled composition of the parental magma of troctolite VL01J309B for different assumed trapped melt fractions (5, 10 and 15%). Dashed lines are average compositions of low-Ti (1) and intermediate-Ti (2) boninites from the Betts Cove ophiolite (Bédard et al., 2000b). Note the similarity between the model composition and the boninites. Normalizing values from Sun and McDonough (1989).

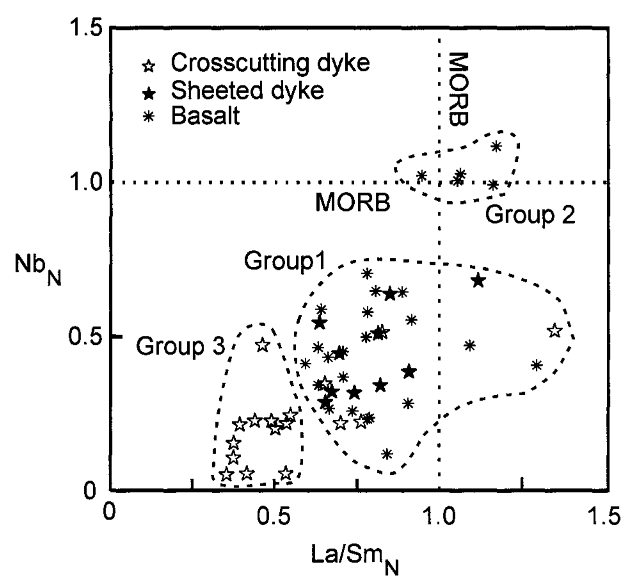

Figure 3.5: La/Sm$_N$ vs. Nb$_N$ of Annieopsquotch sheeted dykes, basalts and dykes crosscutting the ophiolite pseudostratigraphy. Annieopsquotch rocks can be subdivided into 3 chemically distinct groups based on the degree of LREE- and Nb depletion.

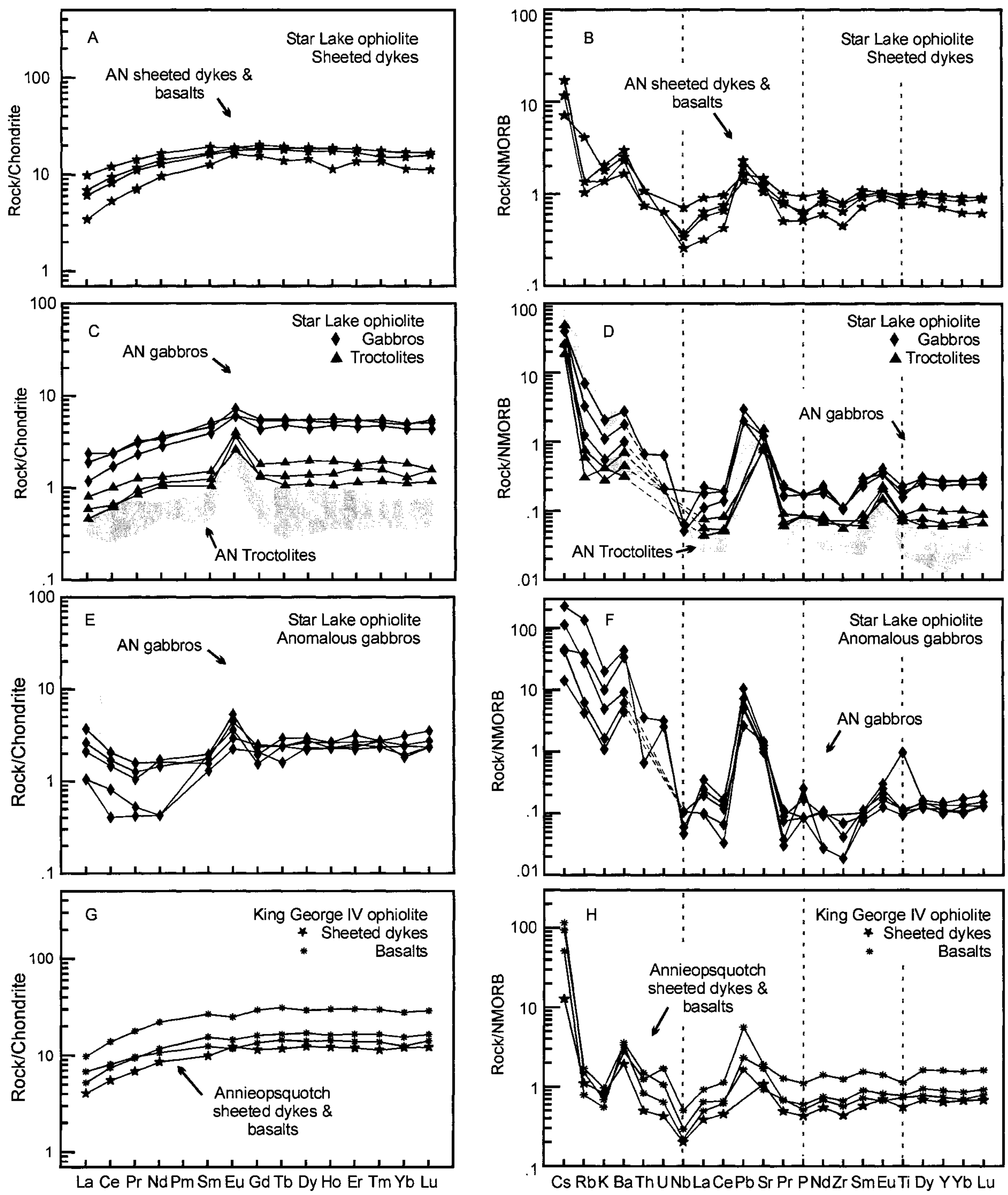

Figure 3.6: Comparison between trace element patterns of the Annnieopsquotch, Star Lake and King George IV ophiolites. (a-b) Sheeted dykes from the Star Lake ophiolite; (c-d) Gabbros and troctolites from the Star Lake ophiolite; (e-f) Anomalous gabbros from from the Star Lake ophiolite; (g-h) Sheeted dykes and basalts from the King George IV ophiolite. Normalizing values from Sun and McDonough (1989).

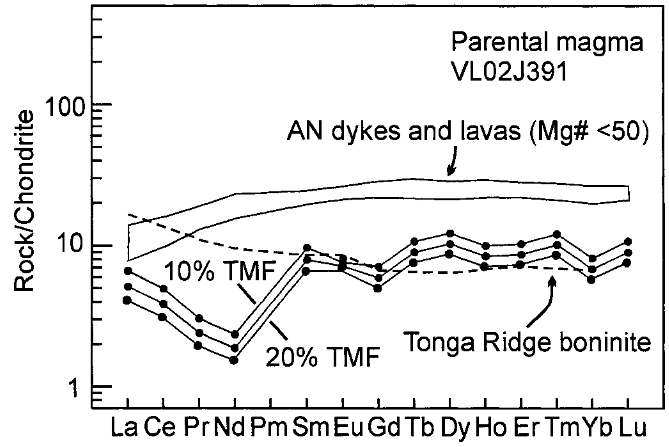

Figure 3.7: Modeled parental magmas of anomalous olivine gabbro VL02J391 from the Star Lake ophiolite for 10%, 15% and 20% trapped melt (see text for details), compared with evolved boninitic rocks from the Tonga Ridge (Mg# 47; Falloon and Crawford, 1991). Note the similarity in degree of depletion (i.e. HREE contents) between the SL parental magmas and the evolved boninites. Normalizing values from Sun and McDonough (1989).

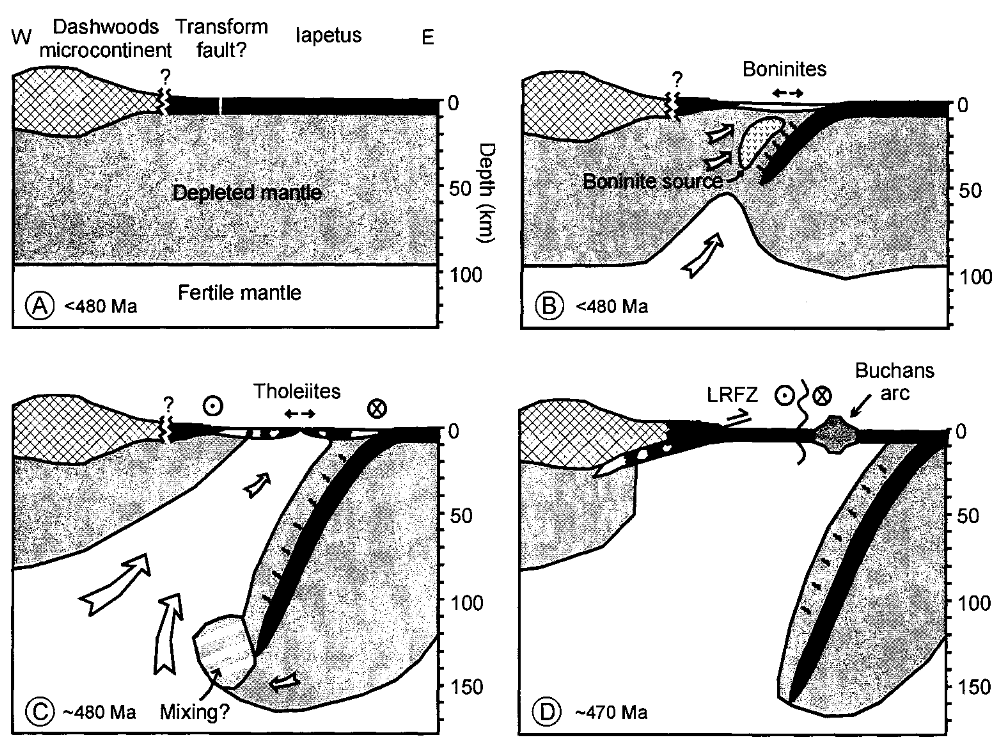

Figure 3.8: Model for generation of the Annieopsquotch ophiolite belt. Initiation of west-dipping subduction outboard of the Dashwoods microcontinent leads to extension in the upper plate, and upwelling of mantle already depleted by the generation of oceanic crust. Aided by fluids expelled from the downgoing plate, the depleted mantle melts at shallow levels yielding boninites. Continuing rollback causes upwelling of a fertile mantle diapir, which, in the presence of slab-derived fluids, melts to yield SSZ tholeiites. These form the gabbro-sheeted dyke-basalt sequence as a spreading center rifts the boninitic substrate. Finally, the Annieopsquotch ophiolite belt is thrust beneath the Dashwoods microcontinent. LRFZ=Lloyds River Fault Zone.

Table 3.1: Whole-rock geochemical data of the Annieopsquotch ophiolite belt

sample[1]	1J035b	1J35c	2J309b	2J310a	1J177b	1J181a	1J188	1J189	1J190	1J191	1J192	1J193
Ophiolite	AN	AN	AN	AN	AN	AN	AN	AN	AN	AN	AN	AN
Lithology	Troctolite	Troctolite	Troctolite	Troctolite	Sheeted dyke	Sheeted dyke	Sheeted dyke	Sheeted dyke	Sheeted dyke	Sheeted dyke	Sheeted dyke	Sheeted dyke
UTM x[2]	447956	447956	447871	447899	464470	459907	456008	456411	456345	456158	456034	455871
UTM y	5348318	5348318	5348194	5348092	5359115	5358064	5349897	5349630	5349588	5349364	5349225	5349006
SiO_2	43.01	41.28	40.63	45.19	50.10	48.51	49.06	48.43	51.82	53.29	49.13	48.04
TiO_2	0.03	0.04	0.04	0.08	1.65	1.20	1.01	0.90	1.12	1.81	1.46	1.14
Al_2O_3	28.32	19.58	15.99	25.64	14.95	16.73	15.99	17.05	15.52	15.17	15.43	15.90
Fe_2O_3*	2.44	5.30	8.53	3.96	14.11	10.40	10.90	10.33	11.34	13.13	13.03	11.06
MnO	0.04	0.09	0.12	0.06	0.19	0.19	0.19	0.17	0.18	0.15	0.22	0.19
MgO	5.39	16.01	21.60	7.70	5.61	8.12	8.08	7.66	6.06	4.45	7.10	7.34
CaO	16.17	11.36	8.36	13.94	9.73	11.42	11.89	13.02	9.98	8.39	11.36	11.52
Na_2O	1.41	0.91	0.66	1.65	3.36	2.54	2.13	1.79	3.67	3.28	2.29	2.39
K_2O	0.21	0.04	0.03	0.15	0.09	0.19	0.07	0.04	0.09	0.31	0.07	0.08
P_2O_5	b.d.	b.d.	0.02	0.01	0.12	0.09	0.07	0.05	0.11	0.22	0.09	0.08
LOI	2.66	3.94	4.39	1.62	0.56	0.74	0.94	0.78	0.96	0.39	0.77	1.25
Total	99.68	98.55	100.48	100.06	100.48	100.14	100.34	100.22	100.85	100.58	100.96	98.99
Trace elements (ppm)												
Ba	16.5	5.9	2.2	6.6	25.8	23.2	14.9	6.7	45.2	50.3	14.9	19.5
Cr	56	268	310	220	69	401	329	330	>500	41	190	306
Cs	1.32	0.56	0.39	0.41	0.06	0.25	0.09	0.07	0.23	0.29	0.12	0.13
Hf	b.d.	b.d.	b.d.	b.d.	2.44	2.01	1.49	1.30	2.32	3.81	2.17	1.95
Nb	b.d.	b.d.	b.d.	b.d.	1.49	1.19	0.90	0.75	1.59	3.74	1.27	0.67
Ni	158	516	665	244	41	158	120	100	35	32	77	105
Pb	1.23	0.62	1.00	b.d.	0.24	0.68	0.24	0.29	0.64	0.68	0.75	0.27
Rb	8.84	1.9	0.73	6.78	0.47	5.54	0.99	0.47	1.24	12.86	0.63	1.51
Sc	2.2	7.7	4.6	5.6	41.4	34.9	39.0	40.1	41.5	35.1	42.1	39.8
Sr	218	127	84	125	109	97	101	73	164	146	94	100
Th	0.05	b.d.	b.d.	b.d.	0.26	0.16	0.20	0.09	0.40	0.61	0.10	0.11
U	0.02	b.d.	b.d.	b.d.	0.08	0.07	0.05	0.03	0.11	0.17	0.04	0.03
V	9	22	20	35	530	261	286	261	335	322	394	306
Y	0.34	0.8	0.65	1.42	39.98	30.00	25.09	22.27	30.50	51.52	34.34	27.96
Zr	b.d.	b.d.	b.d.	b.d.	83.10	65.87	51.24	36.75	73.60	135.95	69.02	59.02
La	b.d.	b.d.	0.07	0.09	2.94	2.16	1.88	1.23	3.42	6.38	1.85	1.61
Ce	b.d.	0.46	0.20	0.31	9.01	6.80	5.84	4.12	9.42	17.75	6.48	5.52
Pr	0.05	0.07	0.03	0.06	1.67	1.25	1.04	0.78	1.57	2.94	1.31	1.10
Nd	0.26	0.33	0.22	0.33	9.52	7.52	6.08	4.72	8.67	15.74	8.00	6.59
Sm	0.12	0.1	0.06	0.14	3.64	2.79	2.18	1.92	3.22	5.05	3.06	2.59
Eu	0.15	0.13	0.10	0.18	1.45	1.12	0.94	0.83	1.17	1.65	1.22	1.10
Gd	0.10	0.13	0.08	0.20	5.15	4.16	3.55	2.98	4.31	6.90	4.63	3.84
Tb	0.01	0.02	0.02	0.04	0.95	0.71	0.62	0.54	0.77	1.27	0.86	0.73
Dy	0.08	0.16	0.11	0.26	6.39	4.91	4.07	3.63	4.99	8.20	5.75	4.84
Ho	0.02	0.03	0.02	0.06	1.46	1.08	0.92	0.83	1.12	1.83	1.32	1.07
Er	0.06	0.1	0.08	0.16	4.35	3.18	2.72	2.47	3.37	5.54	3.91	3.27
Tm	0.01	0.01	0.01	0.02	0.66	0.46	0.38	0.37	0.50	0.82	0.58	0.50
Yb	0.06	0.11	0.10	0.13	4.06	2.94	2.48	2.41	3.33	5.16	3.68	3.22
Lu	0.01	0.02	0.01	0.02	0.61	0.46	0.39	0.35	0.50	0.77	0.57	0.50
Mg#[3]	0.83	0.84	0.85	0.81	0.46	0.63	0.62	0.62	0.54	0.42	0.54	0.59

[1]Prefix VL0 has been omitted from all samples; [2]UTM in NAD83, zone 21; [3]Mg# = $Mg/(Mg+Fe^{2+})$ assuming $Fe^{3+}/Fe^{2+}=0.1$;
b.d. = below detection limit

Table 3.1 (continued)

sample	1J194	1J196b	1J177a	2A228b	1J195	1J196a	1J199a	1J205a	1A167b	*1A260*	1A105b	*1A048*	1A211
Ophiolite	AN	AN	AN	AN	AN	AN	AN	AN	AN	AN	AN	AN	AN
Lithology	Sheeted dyke	Sheeted dyke	Sheeted dyke	SSZ Basalt	SSZ Basalt	SSZ Basalt	SSZ Basalt	SSZ Basalt	SSZ Basalt	SSZ Basalt	SSZ Basalt	SSZ Basalt	SSZ Basalt
UTM x	455599	455619	464470	463483	455720	455619	454388	455164	450771	458836	455174	462974	453255
UTM y	5348700	5348407	5359115	5359321	5348477	5348407	5347672	5347338	5344879	5348483	5347352	5352999	5345045
SiO_2	48.38	47.45	49.47	50.52	49.29	49.25	49.60	48.81	49.03	47.59	48.79	48.30	49.52
TiO_2	0.98	1.05	1.44	1.61	0.93	0.73	1.04	1.37	1.70	1.16	1.34	1.27	0.93
Al_2O_3	16.00	15.88	15.26	14.57	17.16	17.14	17.26	14.28	14.66	14.91	13.75	13.64	15.04
Fe_2O_3*	11.04	11.53	12.63	13.43	11.51	10.52	10.85	11.91	14.42	11.19	15.57	13.58	9.44
MnO	0.20	0.21	0.20	0.16	0.18	0.19	0.19	0.21	0.32	0.17	0.28	0.18	0.16
MgO	8.34	8.60	6.85	5.70	5.77	5.98	6.10	6.15	6.44	6.54	6.78	6.91	6.96
CaO	11.53	10.65	10.94	9.95	11.52	12.08	10.53	9.82	7.47	12.55	9.51	11.32	8.68
Na_2O	2.00	2.56	2.72	3.38	3.04	3.06	3.48	4.43	4.46	2.85	3.29	2.42	5.35
K_2O	0.07	0.04	0.16	0.13	0.08	0.07	0.05	0.04	0.04	0.04	0.05	0.10	0.07
P_2O_5	0.06	0.07	0.07	0.14	0.06	0.05	0.07	0.09	0.11	0.08	0.09	0.08	0.08
LOI	2.06	2.64	1.03	0.72	1.19	1.37	1.47	3.56	2.45	2.70	2.02	2.00	4.40
Total	100.66	100.68	100.77	100.37	100.73	100.44	100.62	100.66	101.09	99.84	101.47	99.84	100.63
Trace elements (ppm)													
Ba	20.6	20.3	26.1	30.4	25.1	26.3	15.4	16.4	11.0	23.0	22.7	35.0	25.4
Cr	311	259	206	99	188	209	201	257	19	260	200	171	357
Cs	0.18	0.07	0.20	0.14	0.14	0.05	0.06	0.09	0.08	0.05	0.14	0.40	0.19
Hf	1.46	1.56	2.18	2.50	1.50	1.14	1.64	2.20	2.71	2.20	1.99	1.10	1.41
Nb	0.74	0.80	1.04	1.50	0.62	0.54	1.16	1.08	1.51	1.10	1.01	0.60	0.95
Ni	125	113	66	45	64	79	65	95	30	42	83	22	142
Pb	0.34	0.73	0.61	0.40	0.24	0.28	0.38	0.28	0.88	0.50	0.73	0.20	0.49
Rb	1.36	0.26	3.50	1.16	1.48	1.10	0.68	0.24	b.d.	0.25	b.d.	2.30	0.65
Sc	40.1	45.2	42.2	42.2	37.7	34.4	37.9	40.8	44.3	36.0	37.0	37.0	35.4
Sr	102	153	98	108	210	178	170	122	130	184	140	85	94
Th	0.13	0.16	0.15	0.27	0.09	0.09	0.12	0.12	0.20	0.20	0.10	0.10	0.28
U	0.04	0.05	0.05	0.07	0.19	0.06	0.04	0.05	0.08	0.05	0.05	0.05	0.07
V	290	295	474	358	283	243	268	320	441	282	286	342	244
Y	21.68	25.08	34.92	39.72	26.08	19.85	25.48	33.75	40.54	27.10	33.20	30.30	20.67
Zr	44.43	51.17	65.72	79.60	46.34	37.47	53.54	68.71	88.19	47.80	63.23	49.40	49.21
La	1.53	1.81	2.13	3.08	1.52	1.19	1.76	1.86	2.86	2.70	1.84	1.40	2.67
Ce	4.88	5.77	7.02	9.50	5.02	3.98	5.64	6.47	9.27	8.70	6.05	4.00	7.21
Pr	0.94	1.07	1.36	1.76	0.94	0.74	1.04	1.31	1.74	1.26	1.23	0.86	1.22
Nd	5.53	6.01	7.99	10.24	5.52	4.32	5.90	7.96	9.91	7.90	7.25	5.80	6.28
Sm	2.17	2.32	3.22	3.65	2.40	1.60	2.38	3.09	3.73	2.60	2.92	2.00	2.17
Eu	0.88	0.81	1.17	1.47	1.10	0.70	1.01	1.24	1.50	1.00	1.25	0.82	0.91
Gd	3.09	3.45	4.57	5.61	3.29	2.63	3.41	4.86	5.52	3.87	4.48	3.50	2.94
Tb	0.57	0.62	0.87	1.03	0.62	0.48	0.65	0.87	1.05	0.71	0.81	0.68	0.55
Dy	3.76	4.08	5.75	6.86	4.11	3.20	4.21	5.48	7.00	4.29	5.46	4.69	3.46
Ho	0.84	0.90	1.29	1.48	0.97	0.73	0.93	1.25	1.60	0.93	1.22	1.05	0.81
Er	2.41	2.67	3.72	4.54	2.82	2.10	2.75	3.78	4.44	2.74	3.60	3.02	2.18
Tm	0.37	0.41	0.58	0.67	0.43	0.32	0.41	0.55	0.68	0.42	0.53	0.53	0.34
Yb	2.29	2.53	3.60	4.37	2.68	2.01	2.53	3.66	4.17	2.97	3.31	3.30	2.08
Lu	0.38	0.39	0.57	0.66	0.42	0.31	0.38	0.56	0.67	0.43	0.53	0.60	0.34
Mg#	0.62	0.62	0.54	0.48	0.52	0.55	0.55	0.53	0.49	0.56	0.49	0.53	0.62

Table 3.1 (continued)

sample	1A164b	1A100	1J203	1A238	1A197	1A266	1J198	2A031b	1J200a	1A103	1A104	1J201
Ophiolite	AN	AN	AN	AN	AN	AN	AN	AN	AN	AN	AN	AN
Lithology	SSZ Basalt	SSZ Basalt	SSZ Basalt	SSZ Basalt	SSZ Basalt	SSZ Basalt	SSZ Basalt	SSZ Basalt	SSZ Basalt	SSZ Basalt	MORB-like Basalt	MORB-like Basalt
UTM x	451523	455767	454757	456264	453750	459545	454822	464245	454456	455496	455211	454583
UTM y	5345001	5347572	5347733	5346557	5345885	5349781	5347768	5354895	5347738	5347546	5347393	5347865
SiO_2	50.98	50.07	48.19	48.42	50.49	48.70	47.75	48.28	47.46	48.90	48.68	49.94
TiO_2	1.95	1.92	1.61	1.31	1.29	1.43	1.29	0.97	0.80	1.34	1.68	1.50
Al_2O_3	13.60	14.11	14.50	15.22	13.98	15.05	16.08	15.45	18.49	14.77	13.69	14.51
Fe_2O_3*	13.72	15.33	13.03	12.14	13.33	13.17	12.34	10.64	10.25	13.99	15.25	13.46
MnO	0.24	0.32	0.19	0.20	0.26	0.22	0.23	0.19	0.20	0.27	0.22	0.20
MgO	7.05	7.13	7.21	7.26	7.32	7.37	7.47	7.49	7.90	8.02	6.64	6.31
CaO	5.97	7.11	10.58	11.17	5.65	11.67	11.18	11.33	10.88	6.64	6.64	8.90
Na_2O	5.22	4.18	3.25	2.43	4.82	2.24	2.20	3.60	2.42	4.13	4.55	4.05
K_2O	0.04	0.05	0.07	0.13	0.05	0.06	0.03	0.05	0.04	0.04	0.07	0.07
P_2O_5	0.13	0.13	0.09	0.08	0.09	0.09	0.09	0.08	0.05	0.09	0.13	0.13
LOI	2.34	0.98	2.08	2.55	3.68	0.85	1.58	2.36	2.18	2.95	2.26	1.26
Total	101.23	101.36	100.80	100.91	100.95	100.84	100.26	100.52	100.69	101.14	99.81	100.31
Trace elements (ppm)												
Ba	6.8	16.1	12.4	41.0	14.0	14.6	8.7	27.9	8.1	16.2	11.5	16.7
Cr	144	32	142	211	23	181	207	207	269	247	180	162
Cs	0.56	0.13	0.13	0.16	0.25	0.10	0.10	0.09	0.09	0.10	0.09	0.10
Hf	3.15	3.30	2.46	1.77	1.91	2.12	2.09	1.40	1.32	2.68	2.72	2.83
Nb	1.37	1.64	0.96	0.80	0.86	1.05	1.35	0.66	0.55	1.29	2.38	2.34
Ni	59	29	74	80	37	76	90	105	94	116	72	55
Pb	0.91	0.29	0.58	1.14	0.64	0.31	0.22	0.70	0.14	0.65	1.04	1.17
Rb	0.25	0.22	0.30	2.90	0.26	0.84	0.32	0.31	0.37	0.34	b.d.	0.29
Sc	48.8	42.8	42.8	43.0	39.2	42.6	42.3	39.0	38.9	40.9	40.3	38.8
Sr	45	107	109	96	47	87	89	160	159	131	47	117
Th	0.21	0.26	0.12	0.09	0.16	0.13	0.14	0.14	0.10	0.17	0.18	0.24
U	0.09	0.08	0.04	0.03	0.10	0.04	0.04	0.07	0.09	0.06	0.08	0.09
V	430	475	416	323	308	339	322	281	238	280	298	311
Y	44.51	45.92	36.88	30.54	30.42	33.18	33.10	24.89	20.91	36.88	35.85	37.01
Zr	99.73	103.65	74.04	55.93	60.02	66.64	68.59	50.10	39.80	86.63	91.02	95.37
La	2.51	3.31	1.93	1.61	1.85	1.98	2.20	1.84	1.37	3.01	3.20	3.71
Ce	8.87	10.91	6.76	5.71	6.17	6.78	7.19	5.54	4.40	8.02	9.41	10.96
Pr	1.73	2.08	1.34	1.14	1.19	1.30	1.35	0.95	0.82	1.63	1.65	1.87
Nd	10.01	11.40	8.47	6.62	6.90	7.57	8.08	5.70	4.86	8.87	9.01	10.29
Sm	4.11	4.46	3.42	2.67	2.75	2.94	2.96	2.14	1.83	3.46	3.56	3.70
Eu	0.92	1.44	1.39	1.10	1.07	1.25	1.15	0.92	0.82	1.01	1.17	1.36
Gd	6.09	6.23	5.30	4.08	4.05	4.48	4.44	3.28	2.81	5.04	5.02	5.41
Tb	1.18	1.20	0.97	0.78	0.78	0.86	0.82	0.61	0.53	0.91	0.91	0.98
Dy	7.97	7.87	6.30	5.07	5.21	5.63	5.41	4.07	3.44	6.02	6.04	6.36
Ho	1.82	1.81	1.44	1.19	1.19	1.30	1.21	0.90	0.76	1.32	1.36	1.37
Er	5.20	4.97	4.30	3.28	3.29	3.64	3.55	2.76	2.26	3.84	3.87	3.98
Tm	0.80	0.80	0.64	0.50	0.51	0.56	0.52	0.36	0.36	0.58	0.58	0.62
Yb	4.97	4.95	4.24	3.13	3.24	3.55	3.33	2.72	2.17	3.70	3.73	3.98
Lu	0.81	0.80	0.66	0.50	0.53	0.56	0.50	0.38	0.34	0.59	0.57	0.58
Mg#	0.53	0.50	0.55	0.57	0.54	0.55	0.57	0.61	0.63	0.56	0.49	0.51

Table 3.1 (continued)

sample	1J204a	1J204b	1J205b	1J054b	1J056d	1J063a	1J065c	1J199b	1J200b	1J202	*2J308*	2J315c
Ophiolite	AN	AN	AN	AN	AN	AN	AN	AN	AN	AN	AN	AN
Lithology	MORB-like Basalt	MORB-like Basalt	MORB-like Basalt	Cross-cutting dyke	Cross-cutting dyke	Cross-cutting dyke	Cross-cutting dyke	Cross-cutting dyke	Cross-cutting dyke	Cross-cutting dyke	Cross-cutting dyke	Cross-cutting dyke
UTM x	454951	454951	455164	456398	456621	448841	448583	454388	454456	454692	447970	447440
UTM y	5347446	5347446	5347338	5354259	5357789	5344158	5345186	5347672	5347738	5347724	5348189	5345777
SiO_2	51.02	52.09	50.89	45.28	48.88	47.45	47.41	47.71	48.12	51.89	48.08	47.68
TiO_2	1.18	1.42	1.36	1.62	0.91	0.75	0.76	1.20	0.52	0.48	0.36	1.59
Al_2O_3	13.25	13.51	14.15	14.56	15.86	16.83	16.61	15.63	15.77	14.64	16.71	13.73
Fe_2O_3*	12.85	12.39	12.03	14.46	10.48	9.80	9.80	11.67	9.70	9.38	7.92	14.84
MnO	0.19	0.16	0.20	0.19	0.18	0.16	0.16	0.19	0.17	0.16	0.14	0.22
MgO	6.71	6.33	5.94	8.57	9.05	8.99	8.90	8.30	9.55	7.35	9.25	7.81
CaO	9.18	9.04	9.79	13.84	12.40	12.90	12.89	11.80	12.98	11.86	14.94	11.57
Na_2O	4.09	4.52	4.36	1.65	2.12	1.80	1.82	1.97	1.49	3.66	1.28	2.59
K_2O	0.05	0.06	0.04	0.05	0.07	0.02	0.04	0.04	0.05	0.05	0.13	0.06
P_2O_5	0.10	0.12	0.12	b.d.	0.05	0.04	0.04	0.07	0.02	0.02	0.02	0.09
LOI	1.45	1.12	2.08	0.79	0.82	1.42	1.42	1.90	1.81	1.74	1.10	0.70
Total	100.07	100.76	100.96	101.01	100.81	100.16	99.84	100.49	100.18	101.22	99.99	100.92
Trace elements (ppm)												
Ba	15.8	16.3	21.7	8.6	9.2	b.d.	5.5	b.d.	b.d.	14.9	12.0	11.1
Cr	248	225	239	104	279	434	439	248	429	341	322	93
Cs	0.07	0.08	0.10	0.19	0.04	0.23	0.20	0.07	0.17	0.08	0.30	0.11
Hf	2.00	2.40	2.32	0.26	1.37	0.99	0.98	1.91	0.60	0.71	0.25	0.90
Nb	2.31	2.39	2.60	0.12	0.51	0.47	0.53	0.53	0.13	0.13	0.25	0.36
Ni	76	86	86	79	116	157	151	148	153	124	18	55
Pb	0.68	0.28	0.74	1.02	0.42	b.d.	b.d.	0.66	b.d.	1.02	1.60	3.10
Rb	b.d.	0.23	0.39	1.12	0.87	0.28	0.78	0.26	1.10	0.53	2.90	0.47
Sc	37.2	37.4	37.2	55.8	42.1	37.1	36.2	39.4	38.7	31.1	39.0	>50
Sr	106	175	153	88	90	68	66	69	41	156	113	119
Th	0.18	0.17	0.21	b.d.	0.05	b.d.	b.d.	0.05	b.d.	b.d.	b.d.	b.d.
U	0.13	0.08	0.09	b.d.	0.02	0.01	0.02	0.02	0.01	0.02	b.d.	0.01
V	274	319	319	734	241	219	225	291	233	190	177	396
Y	26.38	33.49	31.20	13.08	22.85	20.23	20.22	29.34	16.25	13.08	11.10	28.88
Zr	71.72	82.95	81.96	b.d.	45.14	28.89	29.31	56.02	15.16	21.85	7.60	21.20
La	3.07	3.55	3.60	0.30	1.02	0.77	0.77	1.20	0.42	0.60	0.25	0.94
Ce	9.00	10.56	10.38	0.93	3.99	2.63	2.71	4.73	1.46	2.21	1.30	3.63
Pr	1.54	1.81	1.76	0.20	0.82	0.54	0.53	1.01	0.30	0.46	0.24	0.81
Nd	8.43	10.22	9.77	1.51	5.04	3.40	3.46	6.52	2.14	2.91	2.10	5.53
Sm	2.78	3.51	3.23	0.89	2.00	1.61	1.65	2.86	1.06	1.18	0.70	2.62
Eu	1.12	1.43	1.44	0.60	0.85	0.72	0.74	1.12	0.51	0.65	0.35	1.07
Gd	3.85	4.98	4.62	1.67	2.90	2.53	2.52	4.20	1.86	1.76	1.48	4.29
Tb	0.68	0.86	0.82	0.32	0.55	0.47	0.48	0.75	0.38	0.34	0.27	0.81
Dy	4.34	5.76	5.23	2.27	3.83	3.28	3.36	4.97	2.56	2.24	1.65	5.27
Ho	0.98	1.24	1.17	0.51	0.84	0.76	0.77	1.10	0.60	0.51	0.41	1.17
Er	2.91	3.55	3.34	1.49	2.34	2.17	2.23	3.34	1.75	1.52	1.09	3.35
Tm	0.43	0.52	0.51	0.22	0.36	0.33	0.34	0.52	0.28	0.22	0.17	0.49
Yb	2.59	3.34	3.16	1.30	2.22	2.12	2.10	3.16	1.75	1.46	1.18	2.89
Lu	0.41	0.52	0.49	0.21	0.35	0.31	0.31	0.50	0.27	0.22	0.15	0.47
Mg#	0.53	0.53	0.52	0.56	0.65	0.67	0.66	0.61	0.68	0.63	0.72	0.53

Table 3.1 (continued)

sample	2J318	2J319	2J326c	2J341c	2J335a	2J375a	2J375b	2J370b	2J335d	2J373	2J334c
Ophiolite	AN	AN	AN	AN	SL	SL	SL	SL	SL	SL	SL
Lithology	Cross-cutting dyke	Cross-cutting dyke	Cross-cutting dyke	Cross-cutting dyke	Troctolite	Troctolite	Troctolite	Gabbro	Gabbro	Gabbro	Gabbro
UTM x	447510	447239	448207	447964	483907	484014	484014	485169	485742	483907	459859
UTM y	5346085	5345849	5346760	5345489	5383239	5384685	5384685	5385153	5384684	5383239	5376247
SiO_2	48.37	48.50	48.46	48.61	44.90	43.35	46.18	47.08	47.33	47.97	48.51
TiO_2	0.97	1.05	1.65	0.90	0.11	0.09	0.10	0.24	0.20	0.29	0.15
Al_2O_3	15.65	15.00	14.12	16.18	19.40	17.63	28.84	19.22	16.97	17.22	16.17
Fe_2O_3*	10.78	11.34	13.74	9.97	6.65	7.44	2.12	5.7	6.07	7.55	6.79
MnO	0.16	0.18	0.21	0.16	0.10	0.11	0.04	0.11	0.11	0.13	0.14
MgO	8.66	8.41	7.01	8.66	15.50	17.06	3.52	9.32	10.99	9.58	11.03
CaO	12.48	12.76	11.41	13.13	11.51	11.31	16.25	15.05	15.34	13.71	13.66
Na_2O	1.86	1.89	2.28	1.72	1.30	1.07	1.72	1.47	1.1	1.77	1.16
K_2O	0.06	0.06	0.03	0.05	0.02	0.03	0.03	0.08	0.04	0.15	0.73
P_2O_5	0.06	0.01	0.09	0.06	0.01	0.01	0.01	0.02	0.02	0.02	0.01
LOI	0.70	0.70	0.80	0.70	0.83	2.38	1.16	1.75	1.66	1.71	1.77
Total	99.82	99.95	99.84	100.22	100.44	100.65	100.06	100.11	99.9	100.19	100.17
Trace elements (ppm)											
Ba	9.0	6.0	8.0	2.9	2.8	2.0	4.4	11.2	6.3	17.5	213.4
Cr	328	226	123	382	312	680	489	310	279	465	227
Cs	0.05	0.05	0.05	0.13	0.34	0.13	0.18	0.28	0.18	0.28	0.32
Hf	1.00	0.80	1.70	1.20	0.10	0.10	b.d.	0.30	0.30	0.30	0.20
Nb	0.50	0.25	1.10	0.57	b.d.	b.d.	b.d.	0.12	b.d.	0.15	0.11
Ni	59	45	30	124	538	598	122	133	137	143	89
Pb	0.60	2.00	0.40	b.d.	b.d.	b.d.	b.d.	0.60	0.60	0.90	2.20
Rb	0.80	1.10	0.25	0.17	0.33	0.17	0.42	1.84	0.70	3.93	21.54
Sc	35.0	41.0	40.0	31.6	12.6	15.0	9.2	32.2	39.5	33.7	48.5
Sr	73	92	96	78	68	75	137	110	71	111	114
Th	b.d.	b.d.	b.d.	b.d.	b.d.	b.d.	b.d.	b.d.	b.d.	0.08	0.43
U	b.d.	b.d.	b.d.	0.02	b.d.	b.d.	b.d.	0.01	0.01	0.03	0.15
V	297	347	392	246	57	56	37	122	124	138	151
Y	28.80	21.00	39.20	22.09	2.75	1.85	1.66	6.51	7.38	7.77	3.83
Zr	39.40	13.00	41.10	39.90	4.10	b.d.	b.d.	8.30	7.90	8.00	5.20
La	0.90	0.50	1.50	1.06	0.19	0.11	0.14	0.28	0.45	0.56	0.88
Ce	4.30	2.60	5.90	3.80	0.62	0.38	0.40	1.05	1.45	1.46	1.26
Pr	0.83	0.43	1.18	0.80	0.12	0.09	0.08	0.22	0.31	0.29	0.15
Nd	6.10	3.70	10.60	4.97	0.61	0.53	0.49	1.32	1.56	1.69	0.76
Sm	2.40	1.40	3.40	2.03	0.23	0.19	0.16	0.60	0.78	0.70	0.24
Eu	1.00	0.83	1.37	0.86	0.23	0.15	0.21	0.35	0.35	0.42	0.17
Gd	3.98	2.82	5.49	3.13	0.37	0.28	0.27	0.89	1.10	1.14	0.51
Tb	0.67	0.47	0.84	0.59	0.07	0.05	0.04	0.18	0.20	0.21	0.09
Dy	4.34	3.51	5.92	3.79	0.50	0.35	0.28	1.12	1.40	1.35	0.67
Ho	0.99	0.81	1.36	0.85	0.11	0.08	0.06	0.27	0.32	0.29	0.15
Er	2.77	2.42	3.84	2.50	0.30	0.27	0.19	0.76	0.89	0.91	0.44
Tm	0.39	0.34	0.61	0.36	0.05	0.04	0.03	0.12	0.14	0.13	0.07
Yb	2.90	1.95	3.75	2.38	0.31	0.22	0.19	0.74	0.85	0.83	0.42
Lu	0.39	0.26	0.57	0.37	0.04	0.04	0.03	0.11	0.13	0.14	0.07
Mg#	0.64	0.62	0.53	0.65	0.84	0.83	0.78	0.78	0.80	0.73	0.78

Table 3.1 (continued)

sample	*2J380a*	2J387	*2J391*	*2J392*	1J209a	*2J393*	2J411a	2J411b	1A112b	2A010b	2A019	10081
Ophiolite	SL	SL	SL	SL	SL	SL	SL	SL	KGIV	KGIV	KGIV	KGIV
Lithology	Gabbro	Gabbro	Gabbro	Gabbro	Sheeted dyke	Sheeted dyke	Sheeted dyke	Sheeted dyke	Basalt	Basalt	Basalt	Sheeted dyke
UTM x	488056	487361	489099	489240	492722	489991	492426	492426	437696	439662	437979	440800
UTM y	5390420	5386304	5389582	5389567	5394620	5389428	5394801	5394801	5334147	5336422	5333899	5337911
SiO_2	40.80	44.90	46.68	46.35	48.57	47.25	48.16	47.94	50.30	48.82	49.39	48.08
TiO_2	1.24	0.14	0.14	0.12	1.16	0.97	1.24	1.079	0.93	0.98	1.43	0.70
Al_2O_3	15.35	21.25	15.41	14.29	15.86	16.58	16.24	16.13	14.92	15.64	15.66	19.01
Fe_2O_3*	19.97	5.91	7.67	8.34	11.77	10.38	11.14	10.56	11.63	10.16	11.51	8.63
MnO	0.20	0.10	0.13	0.14	0.20	0.17	0.19	0.177	0.21	0.18	0.16	0.14
MgO	7.20	10.65	11.61	12.46	8.35	9.22	8.37	8.73	8.95	8.63	6.52	7.90
CaO	12.32	11.61	16.15	15.97	11.78	12.14	11.40	11.93	5.67	11.63	8.74	13.28
Na_2O	0.79	1.12	0.54	0.49	2.36	1.89	2.65	2.32	5.19	2.68	3.65	1.82
K_2O	0.36	1.46	0.12	0.08	0.10	0.13	0.15	0.1	0.04	0.07	0.05	0.06
P_2O_5	0.01	0.02	0.03	0.01	0.07	0.06	0.11	0.076	0.06	0.07	0.13	0.05
LOI	1.60	3.07	1.30	1.50	0.76	1.10	1.06	1.2	3.38	1.73	3.20	1.16
Total	99.85	100.31	99.88	99.87	100.97	99.96	100.78	100.33	101.28	100.67	100.52	100.83
Trace elements (ppm)												
Ba	58.0	276.1	39.0	28.0	10.4	16.0	18.9	14.5	22.6	21.2	17.6	12.2
Cr	7	364	547	650	304	294	290	347	369	366	250	308
Cs	0.80	1.61	0.30	0.10	0.12	0.05	0.12	0.082	0.36	0.66	0.82	0.09
Hf	0.25	0.10	0.25	0.25	1.78	1.40	1.80	1.6	1.36	1.50	2.90	1.06
Nb	0.25	0.14	0.25	0.25	0.87	0.60	1.66	0.8	0.68	0.51	1.17	0.47
Ni	0	292	95	163	118	53	133	144	170	143	106	128
Pb	0.80	3.20	1.60	1.50	0.42	0.70	0.50	0.60	0.50	0.70	1.70	n.d.
Rb	15.70	76.28	3.50	2.40	0.76	2.30	0.76	0.58	0.44	0.95	0.84	0.62
Sc	49.0	18.0	45.0	48.0	43.2	35.0	42.7	39.8	40.8	41.7	41.8	32.1
Sr	130	131	102	89	111	116	134	95	83	153	172	98
Th	b.d.	0.08	b.d.	b.d.	0.09	b.d.	0.13	0.09	0.18	0.10	0.15	0.06
U	b.d.	0.12	b.d.	b.d.	0.03	b.d.	b.d.	0.03	0.05	0.03	0.08	0.02
V	893	64	164	147	305	252	315	270	272	282	315	208
Y	4.20	3.26	3.20	2.80	27.40	19.80	27.36	24.64	20.68	25.08	44.94	17.87
Zr	3.10	b.d.	1.40	1.40	58.30	33.40	59.70	47.9	41.98	49.40	93.00	32.30
La	0.50	0.62	0.25	0.25	1.61	0.80	2.28	1.42	1.62	1.24	2.32	0.96
Ce	0.90	1.04	0.50	0.25	5.67	3.20	7.28	4.94	4.95	4.60	8.50	3.39
Pr	0.10	0.12	0.05	0.04	1.09	0.67	1.33	1.03	0.92	0.89	1.69	0.65
Nd	0.80	0.68	0.20	0.20	6.50	4.40	7.62	5.89	4.98	5.48	10.35	3.99
Sm	0.30	0.27	0.30	0.20	2.51	1.90	2.90	2.43	1.90	2.37	4.10	1.51
Eu	0.31	0.26	0.21	0.13	1.08	0.92	1.07	1.01	0.68	0.84	1.45	0.71
Gd	0.40	0.49	0.32	0.43	3.73	3.14	4.08	3.7	2.77	3.31	6.08	2.35
Tb	0.11	0.09	0.09	0.06	0.68	0.51	0.71	0.67	0.54	0.62	1.17	0.44
Dy	0.75	0.56	0.71	0.59	4.73	3.59	4.60	4.31	3.55	4.33	7.43	3.13
Ho	0.15	0.13	0.13	0.13	1.04	0.63	1.02	0.98	0.81	0.92	1.71	0.69
Er	0.53	0.37	0.39	0.42	2.98	2.21	2.99	2.75	2.30	2.76	5.03	1.98
Tm	0.07	0.06	0.07	0.06	0.44	0.34	0.44	0.38	0.35	0.42	0.76	0.29
Yb	0.53	0.33	0.31	0.41	2.80	1.90	2.84	2.53	2.12	2.62	4.75	2.05
Lu	0.09	0.06	0.06	0.06	0.42	0.28	0.42	0.40	0.36	0.42	0.74	0.31
Mg#	0.44	0.80	0.77	0.77	0.61	0.66	0.62	0.62	0.63	0.65	0.55	0.67

Table 3.2: Modeled trace element compositions (ppm) of parental magmas of troctolites from the Annieopsquotch ophiolite and anomalous gabbros from the Star Lake ophiolite

Sample	VL01J35c			VL01J35b			VL02J310a			VL02J309b			VL02J391			VL02J392		
Unit	Troctolite AN			Troctolite AN			Troctolite AN			Troctolite AN			Gabbro SL			Gabbro SL		
TMF[1] (%)	5	10	15	5	10	15	15	10	5	15	10	5	10	15	20	10	15	20
K	3918	2490	1825	17579	11800	8880	6339	8379	12354	1344	1811	2776	7783	5649	4434	5061	3676	2894
P	b.d.	b.d.	b.d.	b.d.	b.d.	b.d.	336	459	722	455	633	1042	995	728	574	169	123	97
Ti	2976	1945	1445	1982	1349	1022	2895	4064	6819	1457	2052	3465	3756	3146	2706	3326	2797	2403
Ba	44	33	26	98	77	63	25	31	39	10	12	16	256	196	158	184	140	113
Co	59	57	55	50	48	46	41	39	37	50	48	47	53	54	55	42	41	40
Cr	467	572	739	92	113	145	737	819	920	645	686	733	174	181	188	214	227	239
Cs	8.2	4.8	3.4	17.4	10.5	7.6	2.31	3.20	5.21	2.27	3.18	5.30	2.5	1.8	1.4	0.8	0.6	0.4
Cu	247	235	224	70	67	65	87	90	94	86	90	94	186	177	169	213	202	192
Ga	7.6	7.6	7.6	7.7	7.7	7.7	8.87	8.80	8.73	6.28	6.22	6.16	9.3	9.3	9.3	10.1	10.2	10.2
Hf	b.d.	b.d.	b.d.	b.d.	b.d.	b.d.	b.d.	b.d.	b.d.	b.d.	b.d.	b.d.	1.55	1.20	0.98	1.58	1.22	1.00
Nb	b.d.	b.d.	b.d.	b.d.	b.d.	b.d.	b.d.	b.d.	b.d.	b.d.	b.d.	b.d.	2.40	1.62	1.23	2.39	1.62	1.23
Ni	327	306	288	298	276	260	126	113	102	152	144	137	37	39	41	39	38	38
Pb	2.2	1.9	1.7	3.2	2.9	2.7	b.d.	b.d.	b.d.	2.7	3.0	3.4	6.1	5.2	4.6	6.0	5.1	4.5
Rb	34	18	12	152	82	56	43	62	113	5	7	12	32	22	17	21	14	11
Sc	16	22	35	3	4	6	27	35	48	19	23	30	15	16	16	18	18	19
Sr	138	136	134	170	168	167	98	98	98	88	88	89	151	146	142	147	142	137
Ta	2.70	1.42	0.97	2.66	1.41	0.96	0.70	1.01	1.84	0.74	1.07	1.89	0.45	0.31	0.24	0.42	0.30	0.23
Th	b.d.	b.d.	b.d.	0.92	0.48	0.33	b.d.	b.d.	b.d.	b.d.	b.d.	b.d.	b.d.	b.d.	b.d.	b.d.	b.d.	b.d.
U	b.d.	b.d.	b.d.	0.33	0.18	0.13	b.d.	b.d.	b.d.	b.d.	b.d.	b.d.	b.d.	b.d.	b.d.	b.d.	b.d.	b.d.
V	88	95	103	31	33	36	184	242	353	93	119	163	120	121	123	117	119	122
Y	10.36	6.71	4.96	3.91	2.64	1.99	8.66	12.38	21.65	3.97	5.67	9.92	13.97	11.76	10.15	12.82	10.73	9.22
Zn	78	70	63	79	64	54	55	58	62	67	69	71	28	26	24	26	25	24
Zr	b.d.	b.d.	b.d.	b.d.	b.d.	b.d.	b.d.	b.d.	b.d.	b.d.	b.d.	b.d.	11.2	8.1	6.3	11.0	7.9	6.2
La	b.d.	b.d.	b.d.	b.d.	b.d.	b.d.	0.39	0.49	0.66	0.34	0.44	0.62	1.58	1.22	0.99	1.66	1.26	1.02
Ce	4.17	2.94	2.27	b.d.	b.d.	b.d.	1.39	1.75	2.39	0.99	1.29	1.84	3.03	2.36	1.94	1.59	1.23	1.00
Pr	0.66	0.46	0.36	0.39	0.29	0.23	0.28	0.36	0.50	0.17	0.23	0.33	0.29	0.23	0.19	0.24	0.19	0.16
Nd	3.30	2.28	1.74	2.15	1.57	1.23	1.61	2.09	2.99	1.16	1.54	2.32	1.10	0.88	0.73	1.16	0.91	0.76
Sm	1.11	0.75	0.56	1.12	0.80	0.62	0.75	1.00	1.53	0.34	0.46	0.74	1.49	1.22	1.03	1.05	0.85	0.71
Eu	1.00	0.86	0.75	0.89	0.79	0.71	0.27	0.29	0.30	0.18	0.20	0.21	0.44	0.42	0.39	0.30	0.28	0.27
Gd	1.57	1.03	0.77	1.03	0.72	0.55	1.13	1.56	2.55	0.47	0.66	1.11	1.47	1.22	1.05	2.08	1.72	1.47
Tb	0.25	0.16	0.12	0.11	0.07	0.06	0.25	0.35	0.58	0.11	0.15	0.26	0.40	0.34	0.29	0.28	0.23	0.20
Dy	2.04	1.33	0.99	0.90	0.61	0.46	1.54	2.18	3.77	0.67	0.95	1.66	3.12	2.62	2.26	2.72	2.27	1.95
Ho	0.39	0.25	0.19	0.23	0.16	0.12	0.34	0.48	0.85	0.15	0.21	0.37	0.57	0.48	0.41	0.59	0.50	0.43
Er	1.32	0.85	0.63	0.72	0.48	0.36	0.97	1.39	2.49	0.49	0.70	1.24	1.71	1.44	1.24	1.92	1.61	1.38
Tm	0.13	0.09	0.06	0.12	0.08	0.06	0.15	0.22	0.39	0.08	0.11	0.20	0.31	0.26	0.22	0.28	0.23	0.20
Yb	1.48	0.94	0.69	0.76	0.49	0.37	0.82	1.18	2.14	0.61	0.87	1.53	1.39	1.16	1.00	1.90	1.59	1.36
Lu	0.20	0.13	0.09	0.13	0.08	0.06	0.15	0.22	0.40	0.09	0.12	0.21	0.27	0.23	0.20	0.28	0.23	0.20

[1]TMF = trapped melt fraction used in modeling; b.d.= below detection limit; AN=Annieopsquotch; SL=Star Lake

CHAPTER IV

The structure and geochemistry of the gabbro zone of the Annieopsquotch ophiolite, Newfoundland: Implications for lower crustal accretion at spreading ridges

4.1. Introduction

Over the last few decades, the architecture of oceanic spreading ridges has received increasing attention. In contrast to the large magma chambers (30 x 5 km) that were proposed in the ophiolite-derived models of the 1970's and early 1980's (e.g., Pallister and Hopson, 1981; Smewing, 1981), modern seismic data rule out the presence of large, long-lived magma bodies beneath mid-ocean ridges. Fast-spreading ridges appear to have a thin, laterally continuous axial magma lens, whereas slow-spreading ridges appear to have no steady-state axial melt lens (Vera et al., 1990; Sinton and Detrick, 1992; Kent et al., 1993). However, geochemical data from both slow- and fast-spreading ridges require significant fractional crystallization of MORB magmas (e.g., Sinton and Detrick, 1992), which raises the question of where fractionation occurs, and about the role played by the axial melt lens in the evolution of ridge basalts. These questions are of fundamental importance for our understanding of the structural, compositional and thermal evolution of oceanic crust.

This chapter presents field observations and geochemical data and models from the lower crust of the Annieopsquotch ophiolite, southwest Newfoundland (Canada). I will show that sill intrusion was by far the most important lower crustal accretion process at this oceanic spreading center, and that most of the geochemical evolution seen in the lavas can be attributed to fractionation within these sills. By analogy, this suggests that the oceanic lower crust may be formed largely by intrusions from below, rather than by subsidence of material crystallized within a high-level axial magma lens.

4.2. The Annieopsquotch ophiolite

The Annieopsquotch ophiolite (481-478 Ma; Dunning and Krogh, 1985) is part of the Annieopsquotch ophiolite belt (Annieopsquotch ophiolite belt; Chapter 3), which is situated immediately to the west of the main Iapetus suture zone, known as the Red Indian Line in Newfoundland (Fig. 4.1). Within the Appalachian tectonostratigraphic framework, the Annieopsquotch ophiolite belt is part of the Notre Dame Subzone, which comprises rocks of peri-Laurentian affinity that originated within the oceanic realm of the Iapetus Ocean (Williams, 1995). Prior to 470 Ma, the Annieopsquotch ophiolite was juxtaposed against the Dashwoods Block, which is interpreted as a detached fragment of Laurentian continental crust (Waldron and van Staal, 2001; Chapter 5). Due to its behavior as a relatively rigid block, the tectonism and metamorphism associated with accretion of the Annieopsquotch ophiolite did not produce penetrative intra-ophiolitic metamorphic fabrics, but led to the formation of amphibolitic high-strain zones along its northwestern margin (Fig. 4.1), and partial reequilibration of hydrous mineral assemblages formed during seafloor alteration.

The Annieopsquotch ophiolite comprises a well-exposed, steeply tilted section, with stratigraphic units striking NE-SW, and generally dipping c. 50°-70° to the southeast (Dunning, 1984; this study). Poorly exposed, discrete NW-trending breaks in the stratigraphy suggest the presence of faults, but these show only minor displacements. The presence of dykes and late-stage differentiates of Annieopsquotch magmatic affinity intruding into and crosscutting shear zones and hydrothermal veins, allow us to interpret many of the structures, textures, and most hydrous assemblages observed within the ophiolite as original, spreading center-related features (Dunning, 1984; this study). The base of the lower crust is tectonically bounded, and Moho or mantle rocks are not preserved. The lowest exposed part of the ophiolite is dominated by medium- to coarse-grained olivine gabbros and gabbros, which grade upward into well-developed sheeted dykes and pillow basalts (Fig. 4.1). Within the lowermost 480 m of the exposed crustal section, heterogeneous gabbros and subordinate pyroxenites contain abundant troctolite enclaves, which are extensively veined by the intrusive gabbros. Trace element modeling shows that the troctolites had boninite-like parental magmas (Chapter 1), indicating that they originally formed part of a supra-subduction zone basement. Most gabbros, fine-grained dykes and lavas formed from tholeiitic magmas with a distinct arc signature. Consequently, I interpret the entire ophiolite to have formed in a supra-subduction zone setting (Chapter 3).

4.3. Fast or slow spreading?

Drilling and submersible studies of *in-situ* oceanic crust have revealed significant differences in structure between fast-, slow- and ultra-slow-spreading ridges (Dick et al., 2003). Crustal structure appears to depend largely on the supply of magma relative to the amount of extension (Karson, 1998). If a robust supply of magma to the spreading center is maintained, magmatic accretion keeps pace with extension, generally leading to a thick, continuous, coherent stratigraphy and little or no internal deformation. In contrast, the lack of a continuous melt supply at slow-spreading ridges leads to amagmatic or tectonic extension (e.g., Harper, 1985), characterized by normal faults, large-scale detachment faults, block rotation, tilting of units, and the formation of core-complexes that expose the lower crust and mantle on the seafloor (for a review see Lagabrielle et al., 1998). Solid-state deformation of lower crustal rocks is typically extensive, with the common occurrence of mylonitic gabbros (e.g., Cannat et al., 1991).

The major lithostratigraphic units of the Annieopsquotch ophiolite are well developed, with >2.7 km of cumulate gabbros, ~1.5 km of sheeted dykes, and >500 m of lavas. The top of the pillow basalt unit is a younger thrust fault. Units are laterally continuous, and have a fairly consistent orientation and thickness (Fig. 4.1). Most dykes in the sheeted complex have angles of 70 to 90° with the gabbro-dyke boundary (average 81°; Fig. 1), although smaller angles have also been observed in some cases. The uniform strike of the dykes, and their near-perpendicular orientation to major lithostratigraphic unit boundaries, suggests that crustal block rotations were of minor extent. Notably, the rotation of dykes in the Annieopsquotch ophiolite is less than that observed at the fast-spreading East Pacific Rise and the intermediate-spreading Juan de Fuca ridge (Karson et al., 2002ab). Some unit boundaries are offset by small (generally <1 m wide), poorly exposed faults, that are oriented parallel to the sheeted dykes. The fault offsets cannot be determined accurately, since their true sense of motion is unknown, but limited throws of tens of meters to a maximum of a kilometer are inferred from the location of unit boundary offsets (Fig. 4.1). Where exposed, these faults are marked by cataclasites and/or sheared rocks with dominantly greenschist-facies assemblages, and probably represent small normal faults developed near the spreading axis, similar to those occurring at the East Pacific Rise (Karson et al., 2002a; Bohnenstiehl and Carbotte, 2001). This is consistent with the intrusion of late stage differentiates with Annieopsquotch magmatic affinities into some of these faults (Fig. 4.1). Away from the faults, the rocks display little evidence of deformation and most gabbros have cumulus and (sub-)ophitic textures with little or no sign of intracrystalline strain. Small-scale (c.10 cm wide) shear zones of amphibolite to greenschist grade are scattered throughout the gabbro zone, but form only a minor component (<2%). The limited evidence for deformation in the Annieopsquotch ophiolite contrasts with slow-spreading ridges and some ophiolites, where sheared gabbros may form a significant part of the lower crust (Cannat et al., 1991; Bédard, 1990, 1993). No fault talus is observed in the Annieopsquotch ophiolite, and there is no evidence for seafloor exposure of sheeted dykes or gabbros. The thickness and continuity of the gabbros and sheeted dykes, the small throws of spreading-related faults, and the limited amount of early block rotation allowed by the field data, are consistent with a robust magma supply for the Annieopsquotch ophiolite spreading center, with only limited amagmatic extension. I therefore interpret the Annieopsquotch ophiolite to have formed at an intermediate- to fast-spreading ridge.

4.4. Models for crustal accretion at fast spreading ridges

Over the last fifteen years, it has become apparent that large-scale melt-filled magma chambers as originally envisaged from early ophiolite studies are not present at any of the spreading centers investigated to date. In contrast, seismic reflection data of the fast-spreading East Pacific Rise has revealed the presence of a small, but continuous, axial melt lens, overlying a low velocity zone interpreted to represent a crystal mush. The axial melt lens is c. 0.25-2 km wide and few tens to few hundreds meters thick, and is situated near the base of the sheeted dyke complex (4, 5, 23). The axial melt lens is segmented along-axis into 2-4 km long melt pockets separated by 15-20 km long mush zones (Singh et al., 1998). The low velocity zone extends from c. 1.5 km below the seafloor to the Moho, and is estimated to have a melt percentage varying from a few to c. 18% (Harding et al., 1989; Vera et al., 1990; Sinton and Detrick, 1992; Crawford et al., 1999; Crawford and Webb, 2002). Seafloor compliance and seismic tomography data indicate the low velocity zone is 2-7 km wide at its top, and 7-8 km wide at deeper crustal levels (Crawford and Webb, 2002; Dunn et al., 2000). It should be emphasized that from seismic and compliance data it is not clear whether melt in the low velocity zone is distributed along grain boundaries or whether it occurs in small melt bodies (Crawford et al., 1999; Crawford and Webb, 2002). In addition to the axial melt lens, seismic reflection and seafloor compliance studies have revealed the presence of a second zone of melt enrichment, located at the Moho (Garmany, 1989; Crawford et al., 1999; Dunn et al., 2000; Crawford and Webb, 2002). The Moho melt lens is estimated to be ~50-200 m thick, less than 2 km wide, and appears to be discontinuous along axis (Crawford and Webb, 2002).

The role that the small axial melt lens plays in crustal formation has been a matter of considerable debate. There are two competing end-member models; the gabbro glacier and the sheeted sill model. The gabbro glacier model (e.g., Henstock et al., 1993; Phipps Morgan and Chen, 1993; Quick and Denlinger, 1993) infers that the axial melt lens plays a major role in the formation of the lower crust. Here, partial crystallization within the axial melt lens is followed by subsidence and outward flow of a crystal mush (the gabbro glacier). This requires extensive ductile deformation within the low velocity zone. Evidence for magmatic deformation has indeed been observed in the gabbros of the Semail ophiolite (Benn and Allard, 1989; Nicolas, 1989), and it has been argued that

that the crystal flow process could explain the observed steepening of the magmatic layering (Quick and Denlinger, 1993).

In contrast to the gabbro glacier model, the sheeted sill model proposes that magma from the mantle may directly intrude and fractionate to form the lower crust, which implies a more limited role for the axial melt lens. These models are mostly based on field studies in Newfoundland and Oman. Bédard (1990, 1993) and Bédard et al. (1996) described intrusive contacts marked by the occurrence of host rock xenoliths, the formation of reaction rims and hybrid rocks in the Bay of Islands ophiolite, and concluded its lower crust formed essentially by syn-extensional intrusion of sills. Boudier et al. (1996) and Kelemen et al. (1997a) interpreted the layered gabbros from the Semail ophiolite, which generally form the lower two thirds of the gabbro section (Nicolas et al., 2000), as having formed from sills. This interpretation is based on a close resemblance of lower crustal layered units to gabbroic sills that intrude the Moho transition zone. In support, Kelemen et al. (1997a) argued that it is unlikely that lower crustal cumulate layers would be preserved if they were subjected to the large strains required by the gabbro glacier model.

The East Pacific Rise section at Hess Deep preserves evidence for gabbro formation from both the top and bottom, but the relative importance each process remains uncertain (Coogan et al., 2002a). The presence of primitive cumulus minerals deep in the section of the East Pacific Rise indicates *in-situ* crystallization, since signatures of primitive melts are unlikely to be preserved in cumulates formed within a well-homogenized axial melt lens (Coogan et al., 2002b). However, accretion from the top is implied by the presence high in the Hess Deep section of cumulus crystals generated by primitive melts (Natland and Dick, 1996; Coogan et al., 2002a), and the observation that the sheeted dykes and basalts at the East Pacific Rise and in Oman are more evolved than the parental melts of the high level gabbros (Coogan et al., 2002ab).

In the next section, I will present observations from the Annieopsquotch ophiolite that bear on these models of lower oceanic crustal accretion.

4.5. Structure of the Annieopsquotch gabbro zone

The Annieopsquotch gabbro zone has a minimum stratigraphic thickness of 2.7 km, since its base is tectonically bounded. This study focuses on a 2.5 km thick section on the southwestern side of the Annieopsquotch ophiolite, which extends from the lowest exposed part of the gabbros to the sheeted dyke complex (Fig. 4.1). The pseudostratigraphy of the lower crust of the Annieopsquotch ophiolite is illustrated in Fig. 4.2. It can be divided into three levels. The lowest of these (c. 480 m thick) is characterized by gabbroic and minor pyroxenitic rocks that enclose, invade and replace abundant (~15 %) troctolite enclaves, which typically range in size from 0.5 m to tens of meters. Upwards, the proportion of these enclaves decreases markedly and only gabbros and subordinate olivine gabbros occur within the middle level (480-2100 m). The highest level (c. 2100-2500 m) of the gabbro zone is composed of texturally heterogeneous gabbros that typically have a higher content of Fe-Ti oxides than the underlying gabbros. Dunning (1984) observed gabbro pods grading into diabase, and interpreted the upper gabbros as the root zone of the sheeted dykes. Based on the oxide content, its stratigraphic position, and the presence of diabasic-textured pods, I suspect that this level is essentially composed of frozen melts and preserves relics of an axial melt lens.

Dykes, usually with well-developed chilled margins, occur throughout the gabbro zone. Crosscutting dykes generally form <5% of the lower and middle levels, whereas within the upper level the proportion of crosscutting dykes progressively increases up section to c. 50%, thus marking the boundary with the transition zone (Fig. 4.1). The transition zone is constituted of equal proportions of sheeted dyke and gabbro septa, and grades up into the sheeted dyke complex.

4.5.1. Contact and field relationships

We will concentrate on the core of the gabbro zone (c. 1.6 km), where sill-like intrusive bodies can best be observed. Although contacts are locally very complex and diffuse, differences in grain size, texture, and/or contrasting modal mineralogy generally enable the determination of individual intrusive units (Fig. 4.3). Individual gabbroic bodies may be fine- to medium-grained or coarse-grained (Fig. 4.3a-c), and are generally about 10-30 m thick, although the lateral extent of individual bodies is uncertain due to limited outcrop size and the diffuse nature of many sill contacts. In general, fine- to medium-grained gabbro intruded coarser-grained gabbro, although the opposite has also been observed (Fig. 4.3a). Finer grain sizes at the margins of the gabbro bodies are common, and may represent 'chilled margins' (see Fig. 4.3b). Away from the contact zones, fine- to medium-grained gabbro generally coarsens, and eventually becomes indistinguishable from the coarse-grained gabbro sills. Most contacts are planar, with a mean strike of 083° and dip of 58° throughout the section; an orientation that is subparallel to the contact between the gabbro zone and the sheeted dykes (strike 060°, dip 50-70°). Vein-like apophyses (c. 20 cm) may branch off from the upper contacts of larger gabbroic bodies (Fig. 4.3a). These veins are typically sub-parallel to the main contacts, and may show inward growth structures from both sides (Fig. 4.3c). The local presence of crescumulate zones, up to 2 m in thickness and consisting of 5-10 cm long dendritic plagioclase and clinopyroxene growing down from the upper contacts of sills (Fig. 4.3d), imply cooling from the top down. Comb structures observed in other sills indicate that, at least locally, cooling was both from the top and the bottom. The orientation and planar character of these gabbroic bodies, the presence of upper chilled margins and vein-like apophyses, and of downwardly-growing crescumulate zones, are compelling evidence that these bodies represent intra-plutonic sills.

The overall medium to coarse grain size of these bodies and the generally diffuse nature of the contacts suggest that the entire zone was still hot when most sills were emplaced. Some sills show modal igneous layering parallel to the sill contacts. Locally, coarse-grained crosscutting channels have been observed that appear to feed laterally into sills (Fig. 4.4). These feeder channels have contacts reminiscent of the diffuse sill contacts, and may have formed in an early stage when the host was only partially solidified. Discrete, fine-grained crosscutting dykes with chilled margins are also common. The geochemistry of some of these is not significantly different from typical sheeted dyke or lava compositions (see below), and they may represent melts that escaped underlying sills in a later stage, when part of the sill complex had already cooled significantly.

4.5.2. Petrography

Gabbroic rocks from the lower gabbroic levels of the Annieopsquotch ophiolite are generally composed of 40-60% plagioclase ($An_{55\text{-}74}$) and 30-50% clinopyroxene ($En_{41\text{-}50}$ $Wo_{38\text{-}46}$ $Fs_{8\text{-}24}$) (Fig. 5). Olivine ($Fo_{64\text{-}68}$) is a minor constituent (1-10%) in about half the samples throughout the entire section, but tends to be more abundant (10-30%) in rocks from the lowest 1000 m of the section. Most gabbros have subophitic to ophitic textures, with some samples containing poikilitic clinopyroxene. The common occurrence of large subhedral plagioclase laths indicates that plagioclase is the dominant cumulate phase, with clinopyroxene both cumulus and intercumulus (Fig. 4.5). Plagioclase laths commonly show lenticular deformation twins, are locally kinked and occasionally display microstructures typical of grain boundary migration. However, despite the evidence for intracrystalline strain, the gabbros rarely show any fabric, suggesting that they generally experienced low strain. Only a few gabbros have a weak shape-preferred orientation of subparallel plagioclase laths. Minor Fe-Ti-oxides are nearly ubiquitous, forming ~5% of the gabbros from the upper level, and constitute up to 20% of the crosscutting dykes. Brown hornblende (1-4%) occurs in about half of the gabbros as rims on clinopyroxene and interstitial grains with oxides (Fig. 4.5). Apatite is present as accessory phase in one sample, where it occurs between cumulus plagioclase as euhedral crystals associated with brown amphibole.

Widespread secondary minerals were initially related largely to seafloor and oceanic hydrothermal metamorphism, but were probably partially reequilibrated during accretion-related amphibolite-facies metamorphism. The intensity of the seafloor hydrothermalism is irregularly distributed, but is generally pervasive in the uppermost part of the gabbro zone, and decreases to 50–80 % below this level. The rocks in the lowest 1000 m are generally fresher (0-20% replacement). Clinopyroxene is replaced by green hornblende, indicative of hydrothermal alteration at amphibolite-facies conditions. When preserved, clinopyroxene commonly shows exsolved oxides along cleavage planes. Plagioclase generally remains quite fresh, is commonly turbid due to the inclusion of extremely small oxides, and is commonly black in hand specimen. In the more intensely altered samples it is replaced by green amphibole along grain boundaries and cracks. Fresh olivine is rare, shows incipient alteration to magnetite + colorless amphibole and is surrounded by alteration coronas of radiating green amphibole when adjacent to plagioclase. Alteration can be extremely heterogeneous on the scale of a thin section, being preferentially developed adjacent to amphibole-filled veinlets. Pervasive lower temperature assemblages are not encountered in the gabbros, although a few epidote veins are present.

4.6. Gabbro geochemistry

4.6.1 Geochemical characteristics

25 samples (20 gabbroic rocks and 5 crosscutting dykes) from the gabbro zone have been analyzed for major and trace elements (Table 4.1). Analytical methods and precision are described in Appendix II and Rogers (2004). All gabbros analyzed, with the exception of sample VL02J341A, are cumulates, based on their high Mg# (65-81, average 72), positive Eu anomalies (0.97-1.83, average 1.26), and low incompatible element contents (e.g., TiO_2; 0.22-1.04, average 0.44). This is consistent with their cumulate textures (Figs. 4.5 & 4.6). There is no chemical distinction between the coarse- and medium-grained gabbros. The minimum Mg# reached at a given level decreases with stratigraphic height, and both minimum and maximum TiO_2 contents show an overall increase with height. This suggests that the magmas from which the cumulates formed became more evolved up section. The highest gabbro sampled (VL02J341A), which is from the relic axial melt lens, is also the most evolved and enriched gabbro (Fig. 4.6). This is clearly shown by its high TiO_2 and FeO contents when compared to the other gabbro analyses. The absence of an Eu anomaly and the similarity of trace and major element contents between the high-level gabbro (VL02J341A) and the dykes and basalts, implies that this gabbro is essentially a slowly cooled liquid, supporting the axial melt lens

hypothesis for its origin. The dykes that cut the gabbros (Table 4.1 and Figs. 4.6 & 4.8) have compositions indistinguishable from the sheeted dykes and lavas, which indicates that they probably represent a late stage of the axial sequence. Their composition contrasts with more primitive Annieopsquotch dykes with distinctly stronger LREE depletion and lower incompatible element contents that I interpret as off-axis intrusions (Chapter 3).

4.6.2. Parental liquid composition

In order to understand the origin and evolution of the sills, and their role in fractionation and crustal accretion, some estimate of the composition of the magma from which the cumulates formed is required. Model liquid compositions were calculated following the method of Bédard (1994), which calculates the melt in equilibrium with a given cumulus assemblage from whole-rock geochemical data using partition coefficients (Table 4.2). The mineral mode was estimated from thin sections, and I used an updated, parameterized partition coefficient dataset (Bédard, in press and in prep.). The trapped melt fraction was modeled as a phase with partition coefficient of 1 for all elements, and calculations were repeated for different trapped melt fractions. Constraints on the magnitude of the trapped melt fraction come from changes in model liquid trace element patterns (e.g., excessively high LILE contents at low trapped melt fraction, strong LREE depletion at high trapped melt fraction). In addition, I used the method of Natland et al. (1991) as an independent way to estimate the trapped melt fraction. For plausible trapped melt proportions, calculated liquid compositions correspond extremely well with the analysed dykes and basalts (Fig. 4.7), consistent with the hypothesis that the cumulates were generated by melts very similar to the dykes and basalts, and suggesting that the sill complex was generated on-axis as part of the same sequence as the dykes and basalts.

There is an overall increase in minimum and maximum concentration of incompatible elements up section (Fig. 4.8), which, together with decrease of bulk Mg# (Fig. 4.6), suggests that the magmas in the sills become more evolved up section. Dykes from within the gabbro zone have compositions similar to the model liquids, which may indicate that the dykes sample liquids parental to the gabbros, i.e., that they represent liquids expelled from sills occurring deeper in the section. The most evolved model liquid occurs just above the 2000 m level, where the sill complex gives way to non-cumulate gabbros, and is somewhat more evolved than the most differentiated lavas and dykes. The sole sample of the relic axial melt lens (VL02J341A), modeled as a liquid with 15% plagioclase phenocrysts, has a composition slightly more evolved than average upper crust.

The trapped melt fraction of the cumulates ranges from 4% to 30%, with the majority between 15% and 25% (Fig. 4.8). There is no clear trend of trapped melt fraction with stratigraphic height, but the average trapped melt fraction in the lower half of the section is lower (15%) than that in the upper half (21%). The trapped melt fraction of the Annieopsquotch gabbros are significantly higher than those obtained for the East Pacific Rise (average 4.4%; Natland and Dick, 1996) and Bay of Islands gabbros (<10%; Bédard et al., 2003).

4.7. Discussion

The structure of the gabbros of the Annieopsquotch ophiolite shows that a significant part of the lower crust produced at fast-spreading centers may consist of sills that crystallized *in-situ*, rather than remobilized cumulates from the axial melt lens, and as such provides strong support for the sheeted sill model. In particular, sills in the Annieopsquotch ophiolite are seen to occur to much higher levels (c. 400 m below the sheeted dykes), than has been observed in other ophiolites. There are numerous arguments supporting the interpretation that the Annieopsquotch sills formed at the spreading axis, rather than as off-axis intrusions into preexisting crust. Firstly, the cumulates within the sills crystallized from melts similar to the sheeted dykes and basalts (Figs. 2.7 & 2.8). Mass balance requires a significant volume of liquid to form these cumulates, and, given the chemical similarity, it is likely that the sheeted dykes and pillow basalts represent the liquids expelled from this crustal conduit system. Secondly, the dykes crosscutting the gabbroic sills are geochemically indistinguishable from the sheeted dykes and pillow basalts, suggesting an overall consanguineous relationship.

The sill complex was emplaced into an older substrate represented by the troctolite enclaves. The chaotic nature of this lower level, and the observation that the sill complex is developed immediately above the last of the troctolite enclaves, indicates that the enclaves inhibited sill formation. The chemical composition of the bulk tholeiitic Annieopsquotch crust is too evolved to be in equilibrium with the mantle (Fig. 4.6). This suggests that the missing section of lower crust, from below the enclaves, is dominated by primitive mafic-ultramafic cumulates and that this part of the crust acted as a fractionation filter, similar to the exposed lower crust. I therefore speculate that sills may have also been present at the deeper lower crustal levels.

4.7.1. Model for sill-dominated crustal accretion

The chemical data presented above support the field evidence for the formation of the Annieopsquotch gabbros as a ridge-related sill complex. The wide compositional variability of the gabbros, within the section as a whole and in individual outcrops, does not seem consistent with an origin from a well-mixed axial melt lens. Nor is the overall upward trend towards more evolved compositions in the Annieopsquotch cumulates. The virtual absence of the syn-magmatic and high-temperature plastic deformation fabrics is also inconsistent with the gabbro glacier model. Furthermore, the presence of cumulates derived from evolved melts in the lower crust, located well below the level of the axial melt lens, as well as the presence of both evolved and primitive crosscutting dykes, indicate that the bulk of crystal fractionation took place below the level of the axial melt lens. Additional fractionation increments within the axial melt lens are not required by the data, as the liquid compositions calculated from the gabbros in the sills have the same compositional range as the sheeted dykes and lavas.

We propose a model in which individual sill-like intrusions formed by the injection of magma from below (Fig. 4.9). In some cases the magma may have been derived directly from the mantle (primary melts), but more commonly it appears to have already experienced some degree of intra-conduit fractionation prior to emplacement into the sills I have studied. After partial crystallization in the sill-like conduits, the variably evolved residual melt was expelled to form either new, more evolved sills higher up in the crust, or to feed the axial melt lens and/or upper crustal dykes and lavas. Such processes are expected to generate a gabbro zone that grades to more evolved compositions up section, although sills at each level may record any stage of differentiation. Finer-grained dykes cutting the sills may have tapped melts expelled from deeper sills formed in the late stages of crustal accretion. I note that the presence of primitive magmas at high crustal levels need not indicate a minor role for lower crustal sills (cf. Coogan et al., 2002b), as they could conceivably represent localized emplacement of less-fractionated magmas. Neither does this require extensive fractionation within the axial melt lens, since primitive melts (MgO>11.5%) are added to the upper crust in the Annieopsquotch ophiolite (Dunning, 1984). The geochemical data thus support the interpretation for the formation of the gabbros as a sheeted sill complex, with significant chemical evolution by intra-conduit fractional crystallization, and eventual removal of the fractionated magmas through diffuse channels and, at a later stage, as discrete dykes. Such a model (Fig. 4.9) is similar to that proposed for the Bay of Islands complex (Bédard, 1993), and the Semail ophiolite (Kelemen et al., 1997; Korenaga and Kelemen, 1997; Kelemen and Aharonov, 1998).

The formation of sills in the lower ophiolitic and oceanic crust may be favoured by the presence of permeability barriers, such as the Moho. Magmas rising from the mantle tend to pond, and form melt-rich zones at or near the Moho. The build up of fluid pressure within this melt body will cause brittle failure within the low velocity zone, allowing melts to enter the lower crust in narrow melt-filled conduits (Korenaga and Kelemen, 1997; Kelemen and Aharonov, 1998). Ahead of such propagating fractures a tensional stress operates parallel to the fracture, that is likely to exceed the tensile strength of the rocks whenever a mechanical discontinuity, such as a cumulate layer or a preexisting sill, is encountered (the Cook-Gordon mechanism; Cook and Gordon, 1964), thus leading to the formation of a horizontal melt filled fracture. Once such a melt rich zone has been established it would likely act as a trap for subsequent batches of ascending magma and trigger sill development (cf. Bédard and Hébert, 1996; Kelemen and Aharonov, 1998). This mode of sill formation within the lower oceanic crust is analogous to the emplacement mechanism invoked for granites in continental crust (Clemens and Mawer, 1992). Although buoyancy is an important force for fracture propagation, it appears not to be a dominant factor in magma emplacement within the low velocity zone, since gabbroic sills intrude at levels far below their horizon of neutral buoyancy, which is estimated to lie between 1 and 3 km below the seafloor (Ryan, 1994).

4.7.2. The role of the axial melt lens

An axial melt lens is expected to collect and aggregate the melts expelled from lower crustal sills. Given its proximity to the efficiently cooled upper crust, the axial melt lens is also expected to crystallize in part, yielding high-level cumulates and quasi-liquid gabbros. The complexities of the processes occurring within the axial melt lens and the underlying rocks (mixing of extremely evolved magmas with primitive magmas, melt percolation, mineral reequilibration; e.g., Natland and Dick, 1996) preclude the drawing of detailed conclusions from the limited data on axial melt lens-type rocks I have from the Annieopsquotch ophiolite. However, comparing the rocks below the axial melt lens (i.e. the sill complex) with those above the axial melt lens (the sheeted dykes and basalts) allows us to extract some general implications about the role of the axial melt lens.

The variety in the observed compositions of lavas and sheeted dykes, ranging from primitive dykes and basalts (MgO >11.5% and >8.9%, respectively; Dunning, 1984) to evolved dykes (trondhjemitic), suggest that aggregation and homogenization within the Annieopsquotch axial melt lens was not very efficient (Figs. 4.6 & 4.8), since even highly evolved melts that occur in small quantities (Fig. 4.1) were able to erupt without significant modification in an axial melt lens. The fact that the basalts and dykes record the same compositional range as model liquids from the cumulate sills, suggests that melts expelled from the sills erupted without having fractionated significantly within the axial melt lens afterwards (Fig. 4.7). A similar conclusion was reached by Einaudi et al.

(2003), who show that the upper lava sequence in Wadi Shaffan of the Semail ophiolite is in equilibrium with the lower gabbros, and consequently interpret the lavas as having formed from the lower crustal gabbro sills without having resided in the axial melt lens. The limited amount of mixing within the axial melt lens indicated by the Annieopsquotch data suggests that magmatic cycles at this level occurred on a short time scale, and that the axial melt lens drained effectively into the overlying sheeted dykes and basalts. In such a scenario, short residence times of melts in the axial melt lens precluded significant aggregation and homogenization. This is consistent with the observed segmentation of the axial melt lens into 2-4 km long melt pockets and 15-20 km mush zones, which suggests parts of the lens are periodically supplied with melt before eruption, cooling and partial crystallization (Singh et al., 1998). In an alternative scenario, melts from the wide lower and middle crustal low velocity zone (c. 5 km) may reach the upper crust by using pathways outboard of a narrow axial melt lens (0.25-2 km). Using the structure of the Annieopsquotch crust as a guide, it appears unlikely that all of the melt expelled from the highest-level sills would have been trapped in an axial melt lens. A small proportion of the melt from the sills may have erupted 1-2 kilometer off-axis, contributing to off-axis thickening of seismic layer 2a, similar to that observed at the East Pacific Rise (Christeson et al., 1996). Such off-axis events may be preserved within the Annieopsquotch ophiolite as dykes crosscutting the fossil axial melt lens level (Fig. 4.2).

4.7.3. Melt extraction

The extraction of the interstitial liquids from the Annieopsquotch gabbroic cumulates was not very efficient, as shown by the high trapped melt fraction (15-25 %) obtained for many samples. This contrasts with the East Pacific Rise case, where compaction within the cumulate pile, aided by pressure solution, is thought to have led to the formation of adcumulates with low residual porosities (Natland and Dick, 1996). In the Bay of Islands complex and at Hole 735b it has been suggested that melt expulsion was assisted by shear deformation, leading to significantly lower residual porosities, typically <10% (Natland and Dick, 2001; Bédard et al., 2003). The higher residual porosities of Annieopsquotch gabbros, and the apparent absence of deformation, together suggest limited compaction, possibly as a result of the restricted size of the sills. The lower trapped melt fraction obtained from gabbros in the bottom half of the exposed Annieopsquotch crust is consistent with more extensive extraction of interstitial melt as a result of a downward increase in the lithostatic load.

In the Annieopsquotch ophiolite, the presence of crosscutting dykes and discordant feeder channels within some of the gabbroic sills implies that hydrofracturing was an important process in the transportation of residual melts from the sills to the upper crust, as was proposed for the Semail gabbros (Korenaga and Kelemen, 1997). Hydrofracturing may be the result of a build-up of magma pressure within the sills, related to the impermeable nature of overlying rocks (Kelemen and Aharonov, 1998). Alternatively, it may simply be a response to the overall tensional strain accompanying seafloor spreading.

4.7.4. Heat removal

The removal of latent heat released during sill crystallization from the lower crust has been regarded as a problem with the sheeted sill model, since thermal models indicate that conductive heat loss is insufficient, and hydrothermal cooling is assumed to be restricted to the upper part of the crust (<600°C; e.g., Quick and Denlinger, 1993; Chen, 2001). Based on these assumptions, it has been suggested that no more than 10% crystallization from the melt lens at the Moho can take place in the lower crust, since the release of latent heat would increase the size of the Moho melt lens (Chen, 2001).

In the Annieopsquotch gabbro zone, evidence for hydrothermal alteration is widespread. Alteration veins are cut by dykes, indicating that hydrothermal alteration was, at least in part, coeval with magmatism. Numerous other studies have demonstrated that hydrothermal alteration can occur at high temperatures deep in the lower crust (e.g., >700°C at Hess Deep (Manning et al., 1996); up to 1000°C in Oman (Nicolas et al., 2003)). Recently, Koepke et al. (2004a) showed experimentally that the "interstitial" pargasite-orthopyroxene-plagioclase assemblages, which are common in oceanic and ophiolitic gabbros, may form by water-saturated melting of MORB. In addition, these experiments indicated that hydrous melting at temperatures of 900-940°C may yield plagiogranites (Koepke et al., 2004b). If interaction between fluid and rock occurs above the stability limit of hornblende (c. 900-950°C), then metamorphic assemblages will be 'granulitic' and may be nearly indistinguishable from typical cumulate assemblages (e.g., Bird et al., 1988). Oxygen isotope signatures may be the only clear evidence of interaction with seawater in such rocks (e.g., Stakes et al., 1992; Lécuyer and Reynard, 1996). This suggests that hydrothermal alteration may be more widespread and might start at higher temperatures than is recorded by alteration assemblages (McCollom and Shock, 1998). There is thus abundant evidence for hydrothermal cooling at temperatures well in excess of the 600°C threshold used in the thermal model of Chen (2001). More recent models, which incorporate more realistic geological constraints (e.g., hydrothermal cooling up to higher temperatures, petrological variation throughout the lower crust), indicate that lower crust dominated by sheeted sills can indeed cool effectively (Cherkaoui et al., 2003; MacLennan et al., 2004).

We conclude that the latent heat argument does not in itself refute the sheeted sill model. However, it should be noted that the exact mechanisms of hydrothermal cooling within the Annieopsquotch ophiolite remain enigmatic. The "chilled margins" and the dendritic feldspar and pyroxene indicate sills intruded into crust that was already solidified and somewhat cooled. This is hard to reconcile with the presence of a steady state axial melt lens and underlying low velocity zone that is entirely composed of crystal mush, since the hydrothermal fluids required for cooling are not expected to penetrate far into a mush zone. A possible solution to the problem lies in the episodic nature of both sill formation and hydrothermal alteration. Episodic, high temperature hydrothermal cooling is efficient along the steep sides of the low velocity zone, where isotherms are nearly vertical (Dunn et al., 2000; Nicolas et al., 2003). Possibly, sills intrude into the periphery of the low velocity zone, followed by an episode of hydrothermal cooling. This scenario allows for dynamic interaction between intruding magmas and hydrothermal fluids. It is clear that a detailed study is required to elucidate the mechanisms of cooling of a sheeted sill complex, in particular the relationship between the magma plumbing system and the hydrothermal cooling system.

4.8. Conclusions

The internal structure of rocks from the gabbro zone of the Annieopsquotch ophiolite shows that the lower ophiolitic crust is dominated by 10-30m thick sills, which can be recognized to within 400 m of the sheeted dyke complex. In the lowermost exposed crust, however, the presence of numerous relict troctolite enclaves appears to have interfered with the formation of a well-developed sheeted sill complex. The sills are composed of gabbroic cumulates whose calculated parental magmas generally become more evolved upwards, and exhibit compositions very similar to those of the overlying basaltic sheeted dykes and lavas. These data lead to a model where mantle derived magmas intrude into and fractionate within a crustal sill complex (Fig. 9). Fractionated melts are expelled through dyke- or channel-like conduits, and then move up-section where they may: 1) form new sills; 2) pond at the gabbro/sheeted dyke interface to form a quasi-axial melt lens; or 3) erupt at the surface. The evidence from the Annieopsquotch ophiolite implies that a persistent axial melt lens was not a significant site for aggregation, homogenization and differentiation of mantle-derived melts. Rather, it seems as though most of the fractional crystallization in the system occurred within the intra-crustal sill complex, and that this intra-conduit differentiation dominates the compositional evolution of the lavas. If sill complexes also characterize some types of mid-ocean ridges, then they may play an important role in MORB evolution. I realize that a single, unifying model for crustal accretion at fast-spreading mid-ocean ridges is unrealistic, and that the relative importance of different processes probably varies from ridge to ridge. Nonetheless, the evidence from the Annieopsquotch ophiolite shows that sill emplacement can be a fundamental process in the accretion of the lower oceanic crust.

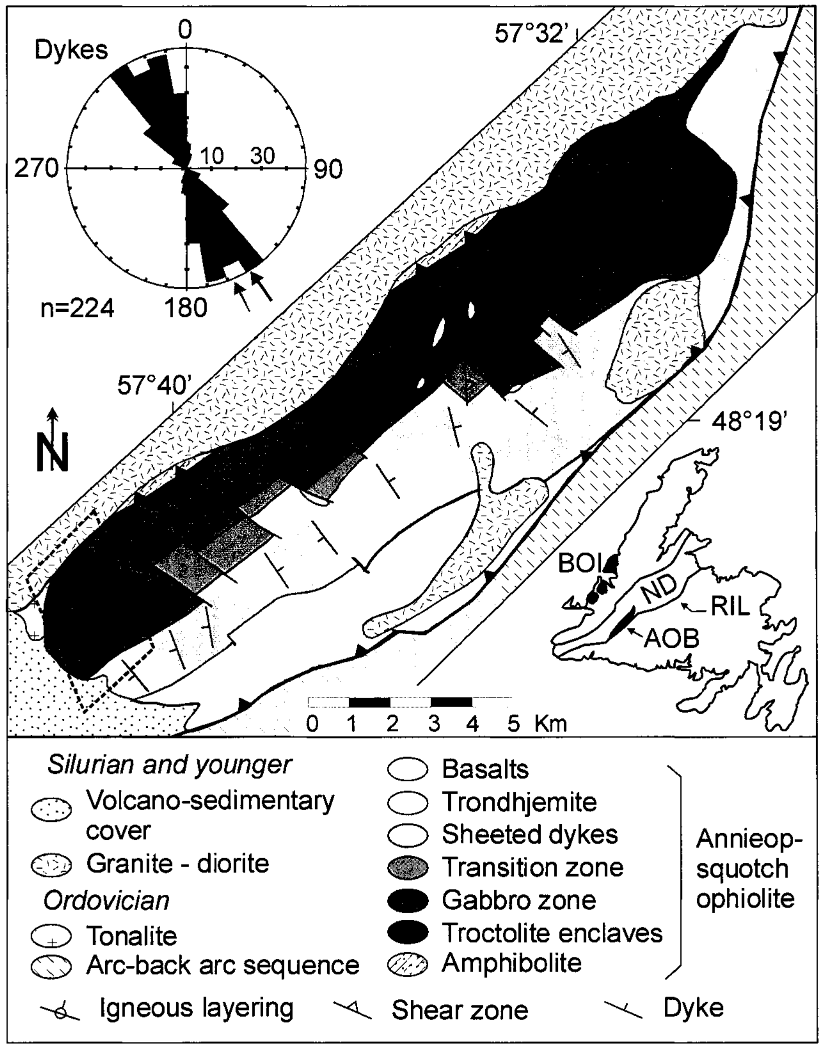

Figure 4.1: Geological map of the Annieopsquotch ophiolite and surrounding rocks of the Notre Dame Subzone of the Newfoundland Appalachians, modified from van Staal et al. (in press). Inset shows location of the Annieopsquotch ophiolite belt (AOB) within the Notre Dame subzone (ND), as well as the location of the Bay of Island ophiolite (BOI). Rose diagram shows the orientation of sheeted dykes (data from Dunning, 1984). The average dyke orientation (grey arrow) makes an angle of 9° with the pole of the gabbro-dyke boundary (black arrow), and the vast majority is within 20°. Dashed box shows location of section described in this chapter. RIL=Red Indian Line.

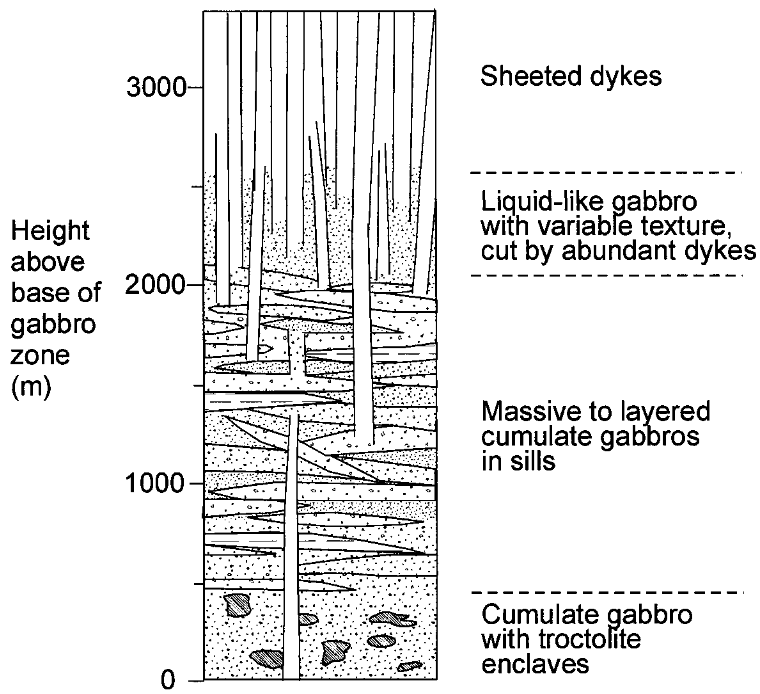

Figure 4.2: Schematic pseudostratigraphy of the lower crust of the southwestern end of the Annieopsquotch ophiolite

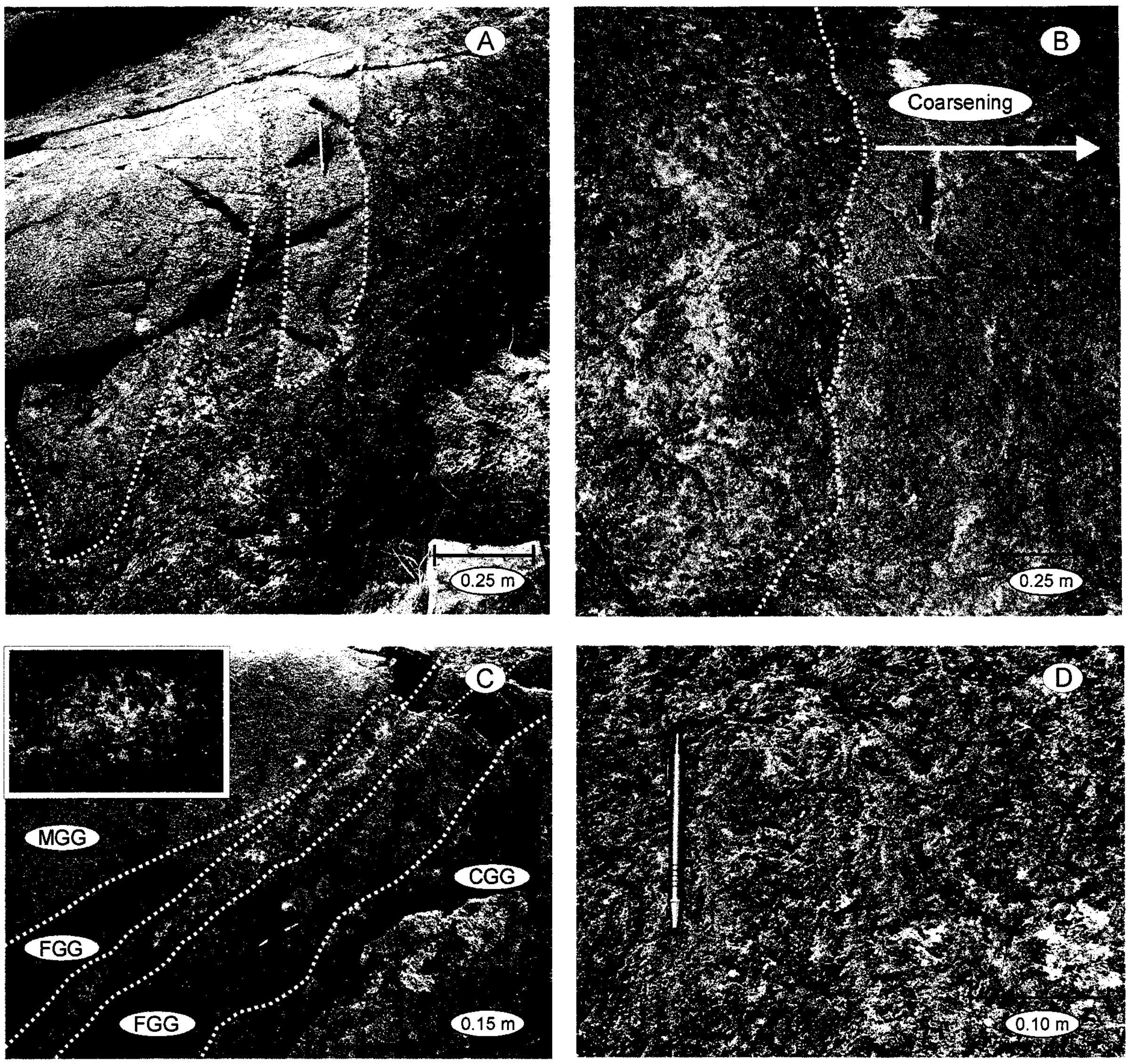

Figure 4.3: Field photographs illustrating the appearance of intrusive contacts within the Annieopsquotch ophiolite. (a) Coarse-grained gabbro (right) cuts fine- to medium-grained gabbro (left). Note that coarse veins issue from the main body of the gabbro, and that the intrusive gabbro does not display any grain size reduction towards the contact, suggesting that the fine- to medium-grained gabbro was still hot when it was intruded. View to the SW. (b) Fine- to medium-grained gabbro (right) intruded coarse-grained gabbro (left). Note that, away from the contact, the gabbro on the right gradually increases in grain size from fine- to medium-grained. (c) Fine-grained gabbro (FGG) intruded along the contact of a coarse- and medium-grained gabbro (CGG and MGG), and is itself cut by a gabbroic vein. Clinopyroxene crystals grow inwards from both walls of the gabbro vein, forming a comb structure, and give way to a plagioclase rich center (see inset), indicating cooling from both top and bottom. Vertical face, view towards the SW. (d) 5-10 cm long dendritic plagioclase and clinopyroxene growing down from a sill contact (above field of view), suggesting cooling of the sill occurred from the top down.

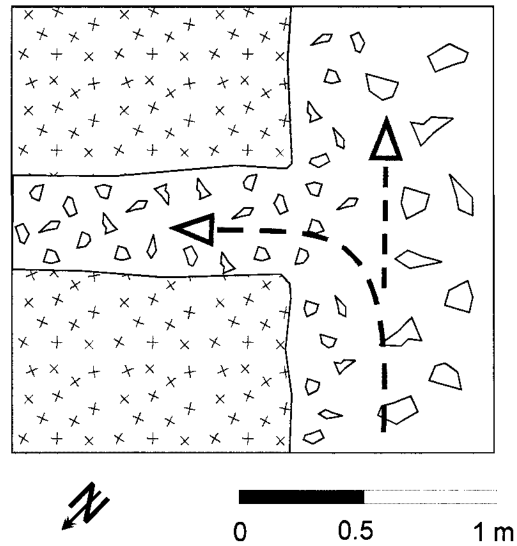

Figure 4.4: Sketch of discordant gabbo body (white), composed of coarse-grained anorthositic matrix with clinopyroxene clots, that cuts medium-grained gabbro (grey). The discordant body is subparallel to the sheeted dykes, and feeds a small, finer-grained sill. The discordant body is interpreted to be a melt channel that transports melt from lower crustal sills upward, feeding sills laterally. The coarse grain size suggests that the channel formed at near-solidus temperature.

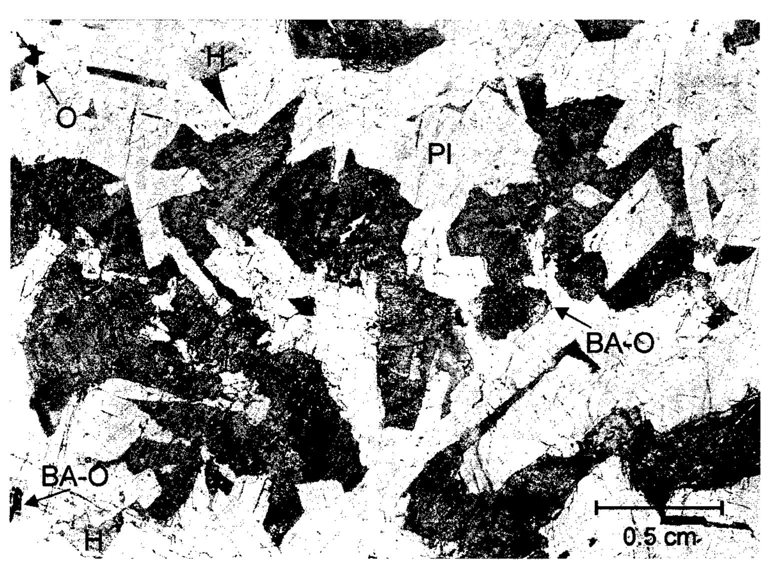

Figure 4.5: Photomicrograph of a typical coarse-grained Annieopsquotch gabbro. Note the large subhedral cumulus plagioclase laths (pale grey - Pl) and cumulus clinopyroxene (dark grey - Cpx). Minor brown amphibole (BA) rims clinopyroxene, and occupies interstices in association with oxides (O). Clinopyroxene is dark due to very fine-grained exsolved oxides, and is locally replaced by green hornblende (H). Plagioclase is turbid due to inclusion of micron-scale oxides. The gabbro is unfoliated. Plane polarized light.

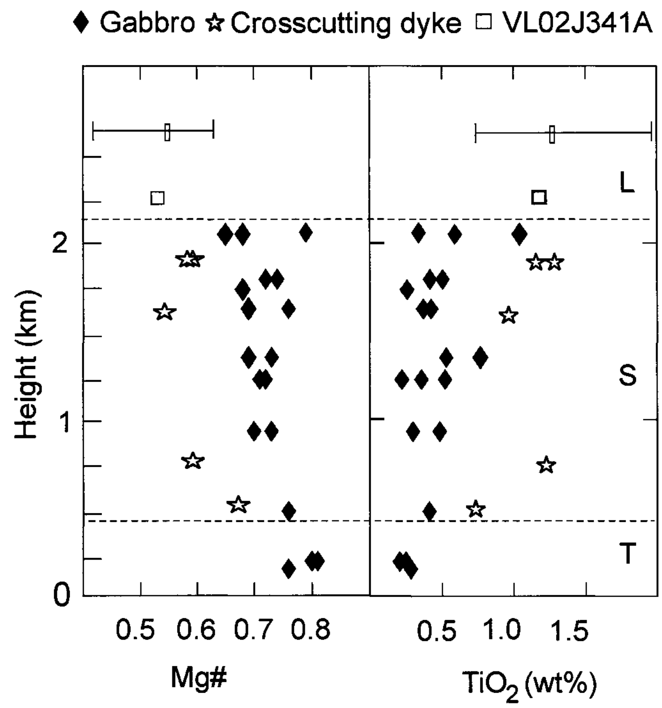

Figure 4.6: Variation of Mg# and TiO_2 of Annieopsquotch gabbros and crosscutting dykes with height above the exposed base of the gabbro zone. The bar indicates the range observed in the sheeted dykes and basalts, with the average marked by the rectangle. Mg# = Mg/Mg+Fe^{2+}, calculated using Fe^{3+}/Fe^{2+}=0.1. T=troctolite-bearing level; S=Sill complex; L=level with liquid-like gabbros.

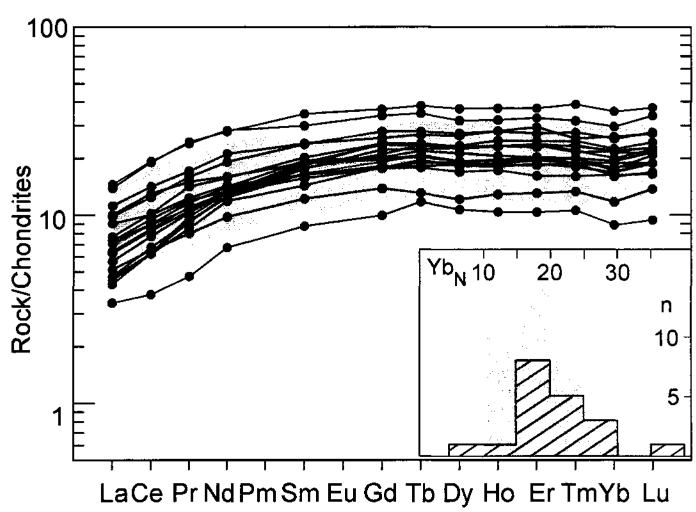

Figure 4.7: REE patterns of the modeled parental magmas of the cumulate gabbros (black, solid circles) compared with those of sheeted dykes and basalts (grey field). Note that both have similar patterns and span a similar compositional range. Histogram illustrates the similarity in REE of model liquids (hatched) and sheeted dykes and basalts (grey). Normalizing values from Sun and McDonough (1989).

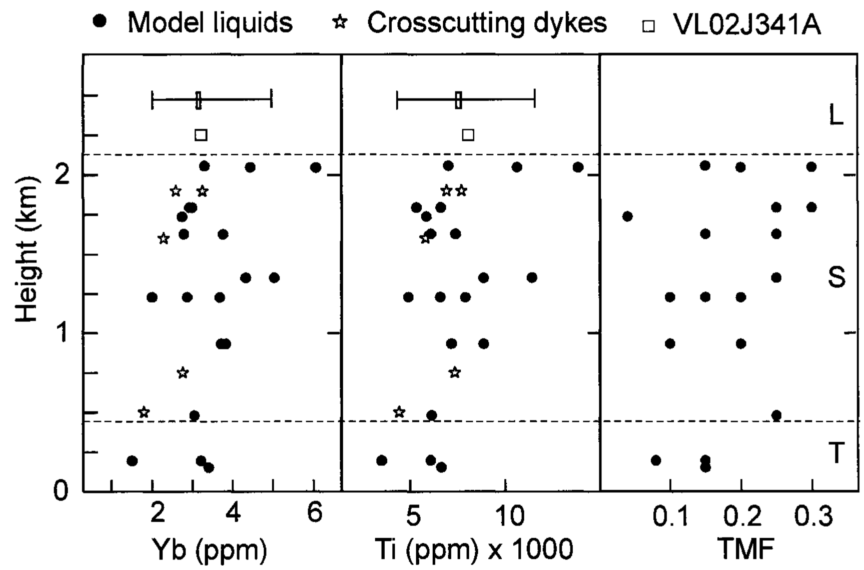

Figure 4.8: Variation of Ti and Yb in model liquids and crosscutting dykes with stratigraphic height above the exposed base of the gabbro zone. Trapped melt fractions of the cumulates are indicated in the third column. The bar shows the Ti and Yb range observed in the sheeted dykes and basalts, with the average marked by the rectangle. T=troctolite-bearing level; S=Sill complex; L=level with liquid-like gabbros.

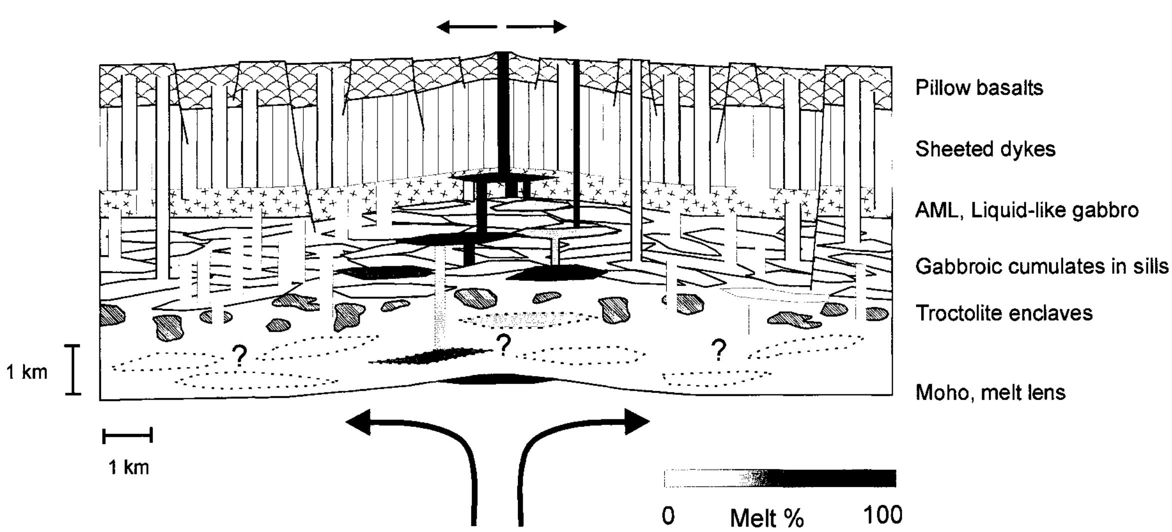

Figure 4.9: Schematic model for accretion of the Annieopsquotch ophiolite. Note that sills are not to scale. Melt ponded at the Moho feeds lower crustal sills, where magmas fractionate to different extents, before moving up section to: 1) form higher-level, more evolved sills, 2) feed into an axial melt lens immediately below the sheeted dyke complex, or 3) to erupt. The lower ~1300 m of the section is not exposed at Annieopsquotch, but is tentatively interpreted to comprise sills as well.

Table 4.1: Whole-rock geochemical data of the gabbro zone of the Annieopsquotch ophiolite

sample[1]	2J310c	2Jdm5	2Jdm8	2J423	2J426a	2J426b	2J328a	2J328b	2J328c	2J326a	2J326b	2J317a
Lithology	Ol-gabbro	Gabbro	Ol-gabbro	Gabbro	Gabbro	Ol-gabbro	Ol-gabbro	Gabbro	Ol-gabbro	Ol-gabbro	Gabbro	Gabbro
Heigth[2]	153	196	196	480	933	933	1228	1228	1228	1352	1352	1628
UTM x[3]	447899	447938	447938	447806	447835	447835	447480	447480	447480	448207	448207	447450
UTM y	5348092	5348130	5348130	5347628	5347077	5347077	5346503	5346503	5346503	5346760	5346760	5345982
SiO_2	48.46	48.36	48.43	48.51	49.50	48.67	47.41	49.91	45.98	49.95	48.21	47.97
TiO_2	0.29	0.20	0.25	0.41	0.48	0.30	0.35	0.52	0.22	0.52	0.76	0.36
Al_2O_3	16.97	16.18	16.73	16.44	14.78	15.99	18.67	15.36	18.60	16.67	16.51	16.86
Fe_2O_3*	7.04	5.95	5.76	6.42	9.02	8.05	7.63	7.74	9.21	7.00	9.01	7.22
MnO	0.13	0.13	0.11	0.13	0.17	0.15	0.13	0.15	0.14	0.12	0.15	0.13
MgO	10.05	10.81	11.00	9.39	9.58	9.78	9.00	8.98	10.23	8.60	9.32	10.21
CaO	15.46	15.12	15.33	15.51	13.90	14.57	13.43	13.88	11.10	13.63	12.75	13.96
Na_2O	1.71	1.38	1.54	1.72	2.06	1.76	1.87	2.36	2.30	2.51	2.24	1.83
K_2O	0.04	0.11	0.06	0.05	0.07	0.04	0.05	0.06	0.08	0.07	0.10	0.05
P_2O_5	0.02	0.02	0.03	0.03	0.03	0.01	0.02	0.03	0.02	0.04	0.06	0.02
LOI	0.29	1.62	0.69	1.35	0.80	0.87	1.26	1.05	1.98	1.31	1.20	1.24
Total	100.58	99.95	100.04	100.02	100.44	100.26	99.91	100.09	99.94	100.51	100.39	99.95
Trace elements (ppm)												
Ba	5.0	13.2	6.9	6.2	5.3	6.6	6.8	5.7	7.5	8.3	10.5	4.8
Cr	719	363	545	295	155	349	398	230	384	420	390	450
Cs	0.16	0.20	0.26	0.23	0.13	0.21	0.19	0.16	0.27	0.13	0.13	0.15
Hf	0.30	0.20	0.20	0.50	0.50	0.20	0.40	0.50	0.20	0.70	1.30	0.50
Nb	b.d.	0.11	b.d.	0.21	0.20	b.d.	0.15	0.26	b.d.	0.36	0.60	0.13
Ni	148	135	175	108	96	113	141	83	213	100	129	113
Pb	b.d.	1.20	b.d.	1.10	0.50	b.d.	0.60	0.60	0.40	0.80	1.00	0.50
Rb	0.88	2.99	2.21	0.81	1.06	0.60	0.65	0.39	1.26	0.99	0.68	0.56
Sc	42.6	49.1	50.0	49.7	48.5	45.6	33.4	>50	23.5	45.4	38.7	43.0
Sr	91	104	98	110	93	104	107	97	115	104	95	107
Th	b.d.	b.d.	b.d.	b.d.	b.d.	b.d.	b.d.	b.d.	b.d.	b.d.	b.d.	b.d.
U	b.d.	0.02	b.d.	0.01	0.01	b.d.	b.d.	0.01	b.d.	0.02	0.02	0.01
V	153	152	156	193	243	180	142	214	97	206	222	162
Y	8.97	5.89	7.62	11.27	12.34	9.04	9.15	13.66	5.20	15.18	19.76	10.06
Zr	9.00	4.30	5.70	13.60	11.80	6.20	11.40	15.00	5.00	20.70	44.80	12.10
La	0.25	0.18	0.17	0.36	0.38	0.18	0.40	0.51	0.23	0.81	1.14	0.37
Ce	0.94	0.55	0.65	1.27	1.36	0.71	1.41	1.83	0.79	2.66	4.01	1.34
Pr	0.21	0.12	0.17	0.28	0.29	0.17	0.29	0.42	0.16	0.53	0.80	0.29
Nd	1.38	0.87	1.20	1.97	1.87	1.22	1.69	2.42	1.02	3.17	4.76	1.84
Sm	0.68	0.43	0.65	0.84	0.93	0.65	0.76	1.14	0.47	1.31	1.77	0.83
Eu	0.39	0.26	0.31	0.47	0.54	0.42	0.44	0.57	0.36	0.58	0.78	0.41
Gd	1.20	0.73	1.04	1.49	1.61	1.25	1.20	1.97	0.78	2.09	2.82	1.39
Tb	0.22	0.16	0.20	0.29	0.29	0.23	0.25	0.37	0.14	0.38	0.54	0.26
Dy	1.55	1.02	1.31	2.02	2.01	1.51	1.59	2.45	0.88	2.53	3.38	1.74
Ho	0.35	0.22	0.29	0.43	0.48	0.35	0.35	0.55	0.21	0.58	0.76	0.40
Er	1.05	0.65	0.89	1.26	1.38	1.02	1.06	1.58	0.62	1.62	2.25	1.08
Tm	0.15	0.10	0.13	0.20	0.21	0.14	0.15	0.25	0.09	0.25	0.33	0.16
Yb	0.89	0.55	0.82	1.23	1.26	0.94	0.95	1.49	0.55	1.52	2.04	1.08
Lu	0.15	0.09	0.12	0.19	0.20	0.15	0.16	0.21	0.10	0.24	0.34	0.16
Mg#[4]	0.76	0.80	0.81	0.76	0.70	0.73	0.72	0.72	0.71	0.73	0.69	0.76

Notes:

[1]Prefix VL0 has been omitted from all samples

[2]Height above base of gabbro zone (m)

[3]UTM in NAD83, zone 21

[4]Mg# = Mg / Mg+Fe^{2+} assuming Fe^{3+}/Fe^{2+}= 0.1;

b.d. = below detection limit

Table 4.1 (continued)

sample	2J317b	2J316	2J314a	2J314b	2J339a	2J339b	2J340b	2J341a	1J046c	1J047d	1J049c	1J056e	1J056f
Lithology	Ol-gabbro	Gabbro	Gabbro	Gabbro	Ol-gabbro	Gabbro	Gabbro	Gabbro	Dyke	Dyke	Dyke	Dyke	Dyke
Heigth	1628	1737	1795	1795	2050	2050	2059	2253	AN	AN	AN	AN	AN
UTM x	447450	447576	447199	447199	447695	447695	448011	447964	449576	460688	459863	456621	456621
UTM y	5345982	5345923	5345629	5345629	5345593	5345593	5345763	5345489	5348776	5357054	5355418	5357789	5357789
SiO_2	50.37	46.43	51.04	49.98	47.89	47.80	49.10	50.02	49.26	49.60	51.00	49.84	48.76
TiO_2	0.42	0.26	0.41	0.50	1.02	0.58	0.33	1.16	1.23	0.74	0.97	1.29	1.16
Al_2O_3	17.66	16.88	16.52	15.64	13.85	19.78	16.83	17.04	15.68	16.59	16.64	15.85	16.22
Fe_2O_3*	7.51	10.17	6.47	7.91	11.87	7.47	5.83	10.78	11.70	9.11	11.76	11.68	11.84
MnO	0.14	0.18	0.13	0.15	0.19	0.13	0.11	0.15	0.20	0.12	0.19	0.17	0.18
MgO	7.58	10.08	8.27	9.25	10.13	7.39	10.27	5.62	7.78	8.41	6.32	7.28	7.67
CaO	12.92	13.16	13.77	13.45	11.47	13.86	13.77	11.58	11.84	13.00	10.82	11.42	11.70
Na_2O	2.85	1.80	2.73	2.20	2.19	1.92	2.02	3.00	2.64	2.01	2.68	2.76	2.54
K_2O	0.04	0.09	0.06	0.05	0.06	0.06	0.10	0.09	0.07	0.06	0.09	0.09	0.09
P_2O_5	0.03	0.02	0.03	0.03	0.07	0.04	0.03	0.08	0.08	0.04	0.09	0.08	0.06
LOI	0.68	1.28	0.80	0.82	1.63	0.95	1.80	0.67	0.66	0.62	0.57	0.39	0.88
Total	100.25	100.40	100.27	100.03	100.43	100.08	100.25	100.24	101.16	100.31	101.14	100.85	101.10
Trace elements (ppm)													
Ba	4.2	5.7	6.6	7.5	5.1	5.7	17.0	11.1	15.1	10.2	31.7	10.3	10.4
Cr	178	285	118	125	211	413	223	97	269	325	139	261	284
Cs	0.13	0.13	0.10	0.10	0.14	0.10	0.22	0.25	0.05	0.04	0.06	0.05	0.05
Hf	0.50	0.20	0.50	0.60	1.20	0.70	0.50	1.40	1.87	0.95	1.44	1.84	1.43
Nb	0.20	b.d.	0.46	0.54	0.64	0.27	0.25	1.10	1.20	0.52	1.21	0.81	0.51
Ni	65	132	73	81	129	128	122	45	73	112	54	94	97
Pb	b.d.	1.30	b.d.	b.d.	0.70	0.60	0.70	0.40	1.69	1.56	0.15	0.37	b.d.
Rb	0.31	0.74	0.37	0.51	0.32	0.50	2.27	1.09	0.51	0.56	0.59	0.73	0.68
Sc	41.6	37.1	>50	>50	42.1	32.0	35.4	36.4	43.5	41.4	43.4	40.6	42.5
Sr	108	127	103	92	79	95	137	145	119	108	138	100	90
Th	b.d.	b.d.	0.11	b.d.	0.06	b.d.	b.d.	0.11	0.13	0.16	0.32	0.11	0.07
U	0.01	b.d.	0.02	0.02	0.02	0.01	0.01	0.04	0.04	0.03	0.10	0.04	0.03
V	183	139	219	233	270	178	143	322	293	250	316	325	331
Y	11.60	7.36	14.35	13.62	24.20	13.00	9.23	25.40	28.58	18.73	23.58	30.65	24.24
Zr	13.80	4.80	15.90	15.80	36.60	23.30	14.00	46.90	61.77	29.09	49.42	59.24	47.31
La	0.50	0.27	0.75	0.65	1.21	0.76	0.41	1.75	2.09	1.13	2.69	1.80	1.37
Ce	1.71	0.87	2.64	2.08	4.40	2.53	1.37	5.74	6.79	3.60	7.39	6.31	4.60
Pr	0.34	0.19	0.51	0.41	0.90	0.49	0.29	1.06	1.27	0.66	1.24	1.21	0.88
Nd	2.17	1.24	2.84	2.35	5.19	3.04	1.74	6.26	7.15	3.74	6.40	7.38	5.28
Sm	0.94	0.58	1.25	1.11	2.26	1.20	0.84	2.45	2.66	1.56	2.10	2.90	2.06
Eu	0.55	0.46	0.58	0.55	0.87	0.64	0.42	0.97	1.13	0.65	0.95	1.16	0.95
Gd	1.51	1.01	1.90	1.81	3.37	1.80	1.23	3.78	3.97	2.51	3.16	4.05	3.18
Tb	0.31	0.19	0.38	0.37	0.65	0.34	0.25	0.70	0.73	0.45	0.59	0.77	0.58
Dy	2.05	1.38	2.44	2.29	4.30	2.34	1.63	4.56	4.78	3.04	3.83	5.18	4.09
Ho	0.46	0.31	0.55	0.53	0.97	0.55	0.35	1.02	1.01	0.67	0.86	1.16	0.92
Er	1.36	0.94	1.63	1.50	2.81	1.68	1.00	2.89	2.96	1.95	2.46	3.37	2.62
Tm	0.20	0.14	0.25	0.24	0.45	0.22	0.15	0.44	0.43	0.29	0.37	0.52	0.39
Yb	1.27	0.76	1.45	1.35	2.73	1.49	0.95	2.78	2.76	1.82	2.28	3.26	2.59
Lu	0.20	0.12	0.25	0.22	0.42	0.23	0.15	0.45	0.45	0.29	0.36	0.51	0.38
Mg#	0.69	0.68	0.74	0.72	0.65	0.68	0.79	0.53	0.59	0.67	0.54	0.58	0.59

Table 4.2: Model composition of parental melts of Annieopsquotch gabbros (ppm)

sample[1]	310c	dm5	dm8	423	426a	426b	328a	328b	328c	326a	326b
Height[2]	153	196	196	480	933	933	1228	1228	1228	1352	1352
K	1740	5145	4241	1457	2342	2369	2221	2093	4567	1867	2843
P	340	361	887	365	437	413	405	559	416	519	810
Ti	6657	3511	6096	6144	8884	7184	6602	7912	4923	8885	11431
Ba	19.8	61.1	40.3	18.3	16.1	33.5	28.0	18.7	34.1	19.5	28.9
Cr	334	91	169	100	63	111	118	60	120	215	132
Cs	0.95	1.19	2.63	0.86	0.56	1.73	1.10	0.72	2.19	0.45	0.48
Hf	1.46	0.77	1.18	1.52	1.88	1.13	1.65	1.63	1.06	2.32	3.94
Nb	0.29	0.70	0.52	0.82	0.96	0.42	0.95	1.24	0.41	1.38	2.32
Ni	56	283	102	232	58	53	272	162	210	201	264
Pb	0.53	3.75	0.67	2.42	1.11	0.63	1.63	1.51	1.14	1.41	2.10
Rb	5.48	19.16	24.75	3.15	5.00	5.39	4.11	1.86	11.39	3.75	2.62
Sc	16.3	9.4	12.1	13.0	15.7	12.5	7.6	10.6	5.7	18.2	10.1
Sr	87	129	107	104	75	108	106	95	103	66	80
Th	b.d.	b.d.	0.34	b.d.	b.d.	b.d.	b.d.	b.d.	b.d.	b.d.	b.d.
U	b.d.	0.10	b.d.	0.03	0.04	b.d.	b.d.	0.06	b.d.	0.06	0.06
V	159	85	112	137	212	132	93	123	69	211	158
Y	33.45	15.62	28.71	27.19	36.41	34.36	26.62	32.69	18.11	41.73	47.42
Zr	50.84	21.82	47.51	47.92	51.18	46.29	60.02	60.97	35.86	75.58	157.35
La	1.12	0.81	1.07	1.11	1.35	1.02	1.73	1.82	1.22	2.33	3.45
Ce	4.14	2.32	3.85	3.82	4.73	3.85	5.84	6.25	3.99	7.62	11.86
Pr	0.89	0.45	0.93	0.81	0.98	0.88	1.14	1.35	0.76	1.52	2.29
Nd	5.80	3.14	6.13	5.54	6.20	5.91	6.25	7.37	4.57	8.97	13.20
Sm	2.71	1.34	2.88	2.20	2.92	2.81	2.51	3.10	1.87	3.65	4.59
Eu	0.73	0.49	0.63	0.75	0.93	0.84	0.78	1.03	0.67	0.85	1.25
Gd	4.58	2.05	4.17	3.70	4.86	4.99	3.66	4.93	2.85	5.73	6.95
Tb	0.84	0.44	0.76	0.71	0.87	0.88	0.73	0.90	0.49	1.04	1.30
Dy	5.79	2.72	4.94	4.88	5.95	5.74	4.64	5.89	3.08	6.93	8.11
Ho	1.31	0.59	1.11	1.04	1.41	1.32	1.03	1.32	0.73	1.58	1.82
Er	3.94	1.72	3.37	3.05	4.10	3.90	3.10	3.80	2.16	4.50	5.44
Tm	0.56	0.27	0.48	0.48	0.63	0.55	0.46	0.60	0.34	0.70	0.81
Yb	3.41	1.51	3.22	3.05	3.83	3.71	2.87	3.68	2.00	4.33	5.04
Lu	0.57	0.24	0.48	0.48	0.62	0.58	0.48	0.54	0.35	0.70	0.86
TMF[3]	0.15	0.15	0.08	0.25	0.20	0.10	0.15	0.20	0.10	0.25	0.25

[1]Prefix VL02J has been omitted from all samples;

[2]Height above base of gabbro zone (m);

[3]TMF = Trapped melt fraction (see text for details)

Table 4.2 (continued)

sample[1]	317a	317b	316	314a	314b	339a	339b	340b	341a
Height[2]	1628	1628	1737	1795	1795	2050	2050	2059	2253
K	2167	1081	9911	1816	1237	2044	1508	4100	866
P	457	430	631	458	425	692	908	551	396
Ti	6100	7402	5864	5345	6620	10652	13862	7032	8112
Ba	18.8	10.3	44.7	21.0	18.8	13.4	18.1	58.5	12.4
Cr	138	86	66	27	40	74	177	88	112
Cs	0.88	0.46	2.24	0.36	0.30	0.43	0.46	1.24	0.29
Hf	1.81	1.70	1.23	1.34	1.56	3.18	2.60	2.27	1.63
Nb	0.81	0.77	0.93	1.79	1.76	2.09	1.30	1.57	1.28
Ni	161	39	271	135	158	223	361	290	51
Pb	1.29	0.38	5.21	0.53	0.41	1.45	1.30	1.58	0.43
Rb	3.51	1.17	15.43	1.44	1.65	1.04	2.39	14.08	1.26
Sc	7.6	19.2	6.6	9.1	12.9	11.0	9.7	10.7	42.1
Sr	99	75	146	133	85	78	78	103	123
Th	b.d.	b.d.	b.d.	0.11	b.d.	0.20	b.d.	b.d.	0.11
U	0.04	0.03	b.d.	0.09	0.05	0.07	0.07	0.07	0.05
V	110	182	75	107	154	195	160	122	374
Y	24.91	33.39	25.17	28.85	28.78	52.49	37.46	30.69	29.43
Zr	56.24	51.05	51.97	52.57	46.99	109.46	100.51	77.44	54.50
La	1.52	1.49	2.14	2.38	1.75	3.30	2.66	1.67	1.99
Ce	5.19	5.08	6.15	7.96	5.46	11.70	8.67	5.48	6.55
Pr	1.05	1.00	1.17	1.43	1.03	2.33	1.63	1.11	1.22
Nd	6.14	6.39	6.72	7.49	5.77	12.97	9.89	6.58	7.17
Sm	2.41	2.73	2.51	2.91	2.54	5.30	3.69	2.99	2.82
Eu	0.68	0.88	0.97	1.09	0.88	1.34	0.98	0.69	1.01
Gd	3.64	4.33	3.75	4.04	3.94	7.52	5.29	4.17	4.36
Tb	0.67	0.88	0.68	0.78	0.78	1.43	1.00	0.82	0.81
Dy	4.32	5.90	4.76	4.94	4.86	9.35	6.73	5.43	5.27
Ho	0.98	1.31	1.06	1.10	1.11	2.10	1.59	1.17	1.19
Er	2.68	3.96	3.23	3.28	3.19	6.12	4.87	3.36	3.36
Tm	0.41	0.59	0.48	0.51	0.51	0.99	0.65	0.51	0.51
Yb	2.78	3.76	2.74	2.99	2.92	6.06	4.44	3.30	3.23
Lu	0.42	0.58	0.43	0.53	0.48	0.95	0.69	0.55	0.52
TMF[3]	0.15	0.25	0.04	0.25	0.30	0.30	0.20	0.15	n/a

CHAPTER V

Assembly of the Annieopsquotch Accretionary Tract, Newfoundland Appalachians: Age- and geodynamic constraints from syn-kinematic intrusions

5.1. Introduction

The Annieopsquotch Accretionary Tract is a well-preserved Ordovician accretionary complex that occurs along the fundamental suture formed by the Ordovician-Silurian closure of the Iapetus Ocean, the Red Indian Line (Williams et al., 1988; van Staal et al., 1998). It comprises several fault-bounded, west-dipping slices of dominantly mafic arc-back arc complexes and ophiolites that formed in the upper plate above a west-dipping subducting slab and have been transferred from their original intra-oceanic setting to the peri-Laurentian Dashwoods microcontinent by underplating. Detailed mapping, in collaboration with extensive geochemistry and high-precision U-Pb and $^{40}Ar/^{39}Ar$ geochronology, have provided a tightly constrained geological framework for the Annieopsquotch Accretionary Tract, making it one of the best-documented examples of an Early Paleozoic accretionary complex. The Annieopsquotch Accretionary Tract thus provides a unique opportunity to study the processes involved in accretionary tectonics, and to evaluate the differences and similarities between Paleozoic and Mesozoic-Cenozoic accretionary orogeny. Of particular interest are the relative contributions of oceanic material and recycled continental crust and the sources involved in magmatism in accretionary tracts. These issues remain a subject of intense research and debate, particularly because of the role accretionary complexes play in continental growth (e.g., Sengör and Natal'in, 1996; Xiao et al., 2003).

In this chapter, I describe the results of $^{40}Ar/^{39}Ar$ geochronology of the shear zones that separate different units of the Annieopsquotch Accretionary Tract, and U/Pb geochronology and geochemistry of the plutons that intrude these shear zones. These data provide age constraints on juxtaposition of the different components of the Annieopsquotch Accretionary Tract, and constrain the geodynamic evolution of the Annieopsquotch Accretionary Tract. Linking the tectonic and magmatic events of the Annieopsquotch Accretionary Tract with those that took place in the adjacent Dashwoods microcontinent provides constraints on the overall tectonic evolution of the peri-Laurentian portion of the Newfoundland Appalachians during the Early to Late Ordovician Taconic orogeny (Williams and Hatcher 1983). I will demonstrate that: (1) the majority of the Annieopsquotch Accretionary Tract was accreted to Dashwoods by 468 Ma, indicating that accretion occurred within 5-10 Ma after formation of the units; (2) the Annieopsquotch Accretionary Tract comprises an important component of recycled continental crust in addition to accreted oceanic crust, and sediments are notably absent; (3) plutons intruding the Annieopsquotch Accretionary Tract tapped variable sources (sub-arc mantle, lithospheric mantle, crust); (4) magmatism in the Annieopsquotch Accretionary Tract is related to the adjacent Notre Dame Arc, but is chemically more primitive owing to intrusion into thin, predominantly mafic crust of the Annieopsquotch Accretionary Tract and ascent along shear zones.

5.2. Regional geology

The Newfoundland Appalachians result from the closure of the Iapetus Ocean, which resulted in juxtaposition of Laurentia with several peri-Gondwanan continental blocks. Rocks formed within the oceanic realm of Iapetus are preserved in Newfoundland's Dunnage Zone (Williams, 1979). The Dunnage Zone has been subdivided into the peri-Laurentian Notre Dame and Dashwoods subzones, and the Exploits Subzone, which mainly has a peri-Gondwanan provenance (Williams et al., 1988; Williams, 1995; Fig. 5.1). The Notre Dame and Dashwoods subzones are separated from peri-Gondwanan rocks of the Exploits Subzone by the Red Indian Line (Williams et al., 1988; van Staal et al., 1998). Both the Notre Dame and Dashwoods subzones are dominated by granitoid arc plutons and associated volcanic rocks of the Notre Dame Arc (e.g., Whalen et al., 1987, 1997), ophiolites, and dominantly mafic arc-back arc complexes. Magmatism in the Notre Dame Arc was episodic, with major pulses in the Tremadoc, Llanvirn-Caradoc, and Ashgill-Wenlock (van Staal et al., 2003; Whalen et al., 2003). Ophiolites occur in three distinct belts: the Lushs Bight and Baie Verte oceanic tracts, which overlie metasedimentary rocks of the Notre Dame and Humber (sub)zones, respectively (e.g., Swinden et al., 1997), and the Annieopsquotch ophiolite belt (Annieopsquotch ophiolite belt; Chapter 3). The Annieopsquotch ophiolite belt, along with most mafic arc-back arc complexes, occurs in a linear belt along the eastern margin of the Notre Dame Subzone. Together, these rocks are referred to as the Annieopsquotch Accretionary Tract (van Staal et al., 1998). The Dashwoods Subzone generally exposes a deeper crustal level than the Notre Dame Subzone and has a larger sedimentary component (e.g., the amphibolite to granulite-facies Cormacks Lake Complex; Pehrsson et al., 2003), but both share a common Ordovician tectonic history (Pehrsson et al., 2003).

It has been inferred on the basis of isotopic and geochronological studies (e.g., Swinden et al., 1997; Whalen et al., 1997), combined with tectonic relationships, that both subzones are underlain by thinned continental crust, which is interpreted as a ribbon-shaped microcontinent, referred to as Dashwoods, that rifted-off of the Laurentian margin during the Early Cambrian (Waldron and van Staal, 2001). During the Cambrian to Early Ordovician the Dashwoods microcontinent was separated from Laurentia by the Humber Seaway. The Humber Seaway was closed by east-directed subduction underneath the Dashwoods microcontinent in the Tremadoc, leading to the first magmatic phase of the Notre Dame Arc, and ended with the collision between Laurentia and the Dashwoods microcontinent by at least 475 Ma (Waldron and van Staal, 2001). This collision is thought to have resulted in slab break-off of the oceanic portion of the Laurentian slab, generating the second pulse of Notre Dame arc magmatism (van Staal et al., 2003; Whalen et al., 2003), and initiated convergence to the east (i.e. outboard) of the Dashwoods microcontinent, leading to the formation of a west-dipping subduction zone that was responsible for formation of the units now preserved within the Annieopquotch Accretionary Tract (Chapter 3).

5.3. The Annieopsquotch Accretionary Tract

The Annieopsquotch Accretionary Tract is the easternmost unit of the Notre Dame Subzone, and is defined as a complex east-vergent thrust stack of ophiolites and arc-back arc complexes that is bounded by the Lloyds River Fault Zone (Lloyds River Fault Zone; Chapter 6) and Hungry Mountain Thrust to the west and by the Red Indian Line to the east (Fig. 5.1; van Staal et al., 1998). Each thrust slice becomes progressively younger to the east (Thurlow et al., 1992; Zagorevski et al., subm.), suggesting sequential accretion to the Dashwoods microcontinent (van Staal et al., 1998). Sedimentary rocks are scarce within the Annieopsquotch Accretionary Tract, allowing detailed reconstruction of the relationships between the various mafic oceanic complexes. The different components of the Annieopsquotch Accretionary Tract are mainly separated by northwest-dipping, amphibolite- to sub-greenschist-grade shear zones, which in many places have been intruded by plutonic rocks during assembly of the tract. Most of these shear zones are thought to be Ordovician in age, although some of them accommodated out of sequence movement (e.g., Thurlow et al., 1992) or Silurian reactivation (Zagorevski and van Staal, 2002). The Annieopsquotch Accretionary Tract has a structural thickness varying from 8 to 15 km, and comprises, from top to bottom, the Annieopsquotch ophiolite belt (Chapter 3), the younger Lloyds River Complex ophiolitic sliver (defined below), the mature arc volcanic sequence of the Buchans Group (Swinden et al., 1997), and the younger immature arc-back arc succession of the Red Indian Lake Group (Fig. 5.2; Zagorevski et al., subm.). In addition, the Annieopsquotch Accretionary Tract contains a suite of syn-kinematic plutonic and syn-orogenic volcanic and associated metasedimentary rocks, termed the Otter Pond Complex (Figs. 5.1 & 5.2; defined below). The limited structural thickness of the tract suggests parts of the units are currently missing. This likely resulted from strike slip movements that accompanied accretion of the Annieopsquotch Accretionary Tract (Chapter 6; Zagorevski and van Staal, 2002), and possibly from subduction of some elements or parts thereof.

The Annieopsquotch ophiolite belt (481-478 Ma; Dunning and Krogh, 1985) is defined as a band of ophiolite complexes and fragments that extends for c. 200 km along the eastern margin of the Notre Dame Subzone (Fig. 5.1; Chapter 3). Its main components are the Annieopsquotch, Star Lake and King George IV ophiolites, all of which lack the mantle section and lowermost crust, but are otherwise intact (Fig. 5.1). Correlative ophiolitic fragments occur along strike within the Hungry Mountain Complex (Whalen et al., 1997), and on the north coast of Newfoundland within the Hall Hill Complex (Bostock, 1988). The ophiolite belt records early boninitic magmatism followed by a tholeiitic phase, and is interpreted to have formed during initiation of west-directed subduction outboard of the Dashwoods microcontinent following the Dashwoods-Laurentia collision (Chapter 3). The Annieopsquotch ophiolite belt is separated from the Dashwoods microcontinent by the Lloyds River Fault Zone. The Lloyds River Fault Zone is marked by highly strained amphibolites, separated by lenticular bodies of less deformed plutonic rocks, and comprises three major northwest-dipping shear zones (the northwestern, central and southeastern shear zones; Figs. 5.1, 5.2, 5.3a). The three shear zones are characterized by predominantly steeply northwest-dipping foliations with moderately (40-60°) north to northeast-dipping lineations, and record sinistral oblique underthrusting of the Annieopsquotch ophiolite belt beneath the Dashwoods microcontinent (Chapter 6). This is consistent with the sense of motion observed in amphibolite-facies mylonites that define the Hungry Mountain Thrust, the equivalent of the Lloyds River Fault Zone immediately north of the town of Buchans (e.g., Calon and Green, 1987).

The structurally underlying Lloyds River Complex is an ophiolitic sliver comprised of gabbro, anorthosite, sheeted dykes and pillow lava, which are geochemically distinct from the Annieopsquotch ophiolite belt, and yielded an age of 473 Ma (Zagorevski et al., subm.). It is interpreted to have originated in a back-arc basin to the Buchans arc (Zagorevski et al., subm.). The Lloyds River Complex is separated from the Annieopsquotch ophiolite belt by the Otter Brook Shear Zone (Fig. 5.1). The Otter Brook Shear Zone is a northwest-dipping amphibolite to greenschist grade shear zone characterized by mylonite, mica schist, and phyllonite with strong northeast-trending foliations and north-northeast-plunging lineations (Fig. 5.3b; Zagorevski and van Staal, 2002). It records an important phase of sinistral oblique underthusting of the Lloyds River Complex beneath the Annieopsquotch ophiolite belt (Zagorevski and van Staal, 2002).

The Otter Pond Complex is defined herein as a distinct suite of plutonic rocks and associated highly deformed felsic volcanic and metasedimentary rocks, which is spatially associated with the Otter Brook Shear Zone. The volcano-sedimentary rocks (rhyolite, amphibolite, garnet-mica schist, and graphitic schist) are contained within strands of the Otter Brook Shear Zone, whereas the plutonic rocks intrude both within the shear zone and within surrounding units (Fig. 5.1). The plutonic rocks of the Otter Pond Complex have been subdivided into a mafic suite, which comprises generally hornblende porphyritic to oikocrystic gabbros, diorites, and associated mafic dykes, and a granodiorite suite. The mafic suite predominantly intruded the Annieopsquotch ophiolite, both as a c. 2 by 2 km sized, medium-grained pluton (Fig. 5.1), and as meter wide, (very) fine-grained dykes. Otter Pond mafic dykes have also been observed to intrude sheeted dykes of the Star Lake and King George IV ophiolites (Fig. 5.1). The main body of the granodiorite suite intruded the southeastern margin of the Annieopsquotch ophiolite, forming an elongate body (c. 5 by 0.7 km) parallel to the Otter Brook Shear Zone (Fig. 5.1). In addition, the granodiorite suite occurs as meter-scale sheets intruding amphibolites of the Otter Brook Shear Zone and as subordinate aphanitic, locally flow banded dykes that intrude the Annieopsquotch ophiolite and Lloyds River Complex. The granodiorite is chemically similar to the aphanitic dykes and rhyolite of the volcano-sedimentary sequence (see below), suggesting together they form part of a consanguineous suite of shallow plutonic-volcanic bodies. These relationships suggest the Otter Pond Complex formed by intrusion and local extrusion and sedimentation along the Otter Brook Shear Zone during thrusting of the Lloyds River Complex underneath the Annieopsquotch ophiolite belt.

The Lloyds River Complex is separated from the structurally underlying Buchans Group (473 Ma; Dunning et al., 1987) and Red Indian Lake Group (464 Ma; Zagorevski et al., subm.) by a series of southeast-directed, ductile-brittle thrusts in the Buchans area (Calon and Green, 1987; Thurlow and Swanson, 1987; Thurlow et al., 1992); similar kinematic relationships have been found elsewhere along strike (Zagorevski et al., 2003). Geochemical and isotopic data suggest the Buchans Group (and its northeastern equivalent, the Robert's Arm Group; Bostock, 1988) represents a volcanic arc that was formed on continental basement (Swinden et al., 1997; Zagorevski et al., subm.). It is postulated to have formed on a sliver of continental crust that rifted off of the Dashwoods microcontinent and was emplaced outboard of the Annieopsquotch ophiolite belt and Lloyds River Complex by trench-parallel strike-slip movement (Zagorevski et al., subm.). Rifting of the Buchans arc at 464 Ma produced an ensimatic back arc basin and younger arc phase, both preserved in the Red Indian Lake Group, which was subsequently thrust beneath the Buchans Group (Zagorevski et al., subm.). The Red Indian Lake Group is bounded to the southeast by the Red Indian Line, which separates it from the peri-Gondwanan arc-back arc complexes of the Exploits Subzone (Figs. 5.1, 5.2; van Staal et al., 1998; Zagorevski et al., subm.).

5.4. Plutonic rocks within the Annieopsquotch Accretionary Tract

Several phases of plutonic rocks intrude into the Annieopsquotch Accretionary Tract and its boundaries, and are concentrated around the Lloyds River Fault Zone and the Otter Brook Shear Zone. In this section, I will discuss their geological relationships, whole-rock geochemistry and Nd-isotope geochemistry. Analytical techniques are described in Appendix 2, and detection limits and sample locations are given in Rogers (2004). Whole-rock geochemical data are listed in Table 5.1, and Nd-isotopic data in Table 5.2.

5.4.1. Pierre's Pond suite

Along the northwestern and southeastern shear zones of the Lloyds River Fault Zone, mylonitic amphibolites of ophiolitic origin are intimately interlayered with centimeter- to meter-wide veins and sheets of foliated diorite and subordinate tonalite. In general, the amphibolites and intrusive rocks are heavily deformed. However, near Star Lake (Fig. 5.1), such tonalite-diorite sheets have intruded outside of the Lloyds River Fault Zone, directly into ophiolitic gabbro of the Star Lake ophiolite (Fig. 5.4). The diorite is composed of aligned hornblende and plagioclase with accessory quartz, biotite, titanite, and oxides, whereas the tonalite is composed of plagioclase, quartz, biotite, hornblende with accessory titanite and oxides. There is a marked contrast in deformation between the narrow zones of sheared intrusive rocks, which have foliations striking predominantly parallel to the southeastern shear zone, and the largely unfoliated host ophiolitic gabbro, which displays a partial greenschist-facies metamorphic overprint (randomly oriented clinozoisite-actinolite-chlorite) of an earlier static amphibolite-facies metamorphism. The amphibolite-facies assemblage in turn largely replaced the original igneous assemblage of clinopyroxene and plagioclase. These relationships suggest that the diorite and tonalite sheets localized deformation during intrusion, the heat of the intrusions and associated fluids producing a contact greenschist-facies metamorphism in the surrounding host gabbro (Chapter 6). Given that the diorites and tonalites also intrude Lloyds River Fault Zone amphibolites, this suggests they intruded the Lloyds River Fault Zone syn-kinematically. I interpret these sheets as well-exposed, small-scale examples of less well-exposed larger bodies of mixed diorite and tonalite that have intruded the northwestern portion of the Lloyds River Fault Zone and the Star Lake ophiolite at Star Lake (Fig. 5.1), and were defined as the Pierre's Pond suite by Whalen et al. (1997).

Geochemically, the Pierre's Pond suite is composed of both arc rocks, characterized by enrichment in LILE and Th over Nb, and non-arc rocks, which lack Th enrichment with respect to Nb (Whalen et al., 1997). The arc-like rocks were further subdivided into La-rich and La-poor groups. I analyzed several small-scale, syn-kinematic diorite and tonalite sheets on Star Lake. The tonalite analyses are similar to equivalent rocks of the Pierre's Pond suite of Whalen et al. (1997; Fig. 5.5a), with the exception of the higher K_2O content in samples VL01J225A and 238C (see Table 5.1). This is likely related to alkali metasomatism, expressed by replacement of plagioclase by irregular patches of muscovite. The large negative Nb and Ti anomalies, and the enrichment in Th and LILE (Cs, Rb, Ba) relative to the REE of the tonalites are typical of arc tonalite (Fig. 5.5a). La/Yb_N (chondrite normalized) spans a large range (8 – 71), suggesting the tonalites in the Lloyds River Fault Zone resemble both the La-rich and La-poor arc-like groups of Whalen et al. (1997). The diorites show depletion in Nb, Zr and Ti, albeit less than the analysed tonalites, and enrichment in LILE and Th. La/Yb_N ranges from 3 to 7, typical of the La-poor arc-like group of the Pierre's Pond suite (Fig. 5.5b). Sample VL01J210B deviates from this pattern by its low Th/Nb ratio (Fig. 5.5b), indicative of a non-arc setting, similar to the non-arc group defined in the Pierre's Pond suite by Whalen et al. (1997). A dominantly arc origin for the tonalites and diorites is consistent with the La-Y-Nb (diorites; Cabanis and Lecolle, 1989) and Rb vs Y+Nb (tonalites; Pearce et al., 1984) tectonic discrimination diagrams

(Fig. 5.6). One diorite sample was analyzed for Nd-isotopes, and yielded an ε_{Nd} value of –5.1 (Table 5.2), similar to values previously obtained for the Pierre's Pond suite (average –5.0; Whalen et al., 1997, and unpublished data). Both geochemical and isotopic data thus support the interpretation that the syn-kinematic sheets belong to the Pierre's Pond suite.

5.4.2. Portage Lake monzogabbro

The Portage Lake monzogabbro is herein defined as a large sheet (~30 by 5 km) of foliated, generally medium-grained, K-feldspar porphyritic, hornblende monzogabbro to monzonite, which occupies a central position within the Lloyds River Fault Zone, between the central and southeastern shear zones (Fig. 5.1). Accessory phases include biotite, epidote, and titanite. K-feldspar phenocrysts typically have large aspect ratios (up to ~10), giving the Portage Lake monzogabbro a very distinct character (Fig. 5.7). It comprises an early, fine-grained facies, which is generally equigranular, and occurs as decimeter-sized enclaves in the later coarser grained porphyritic facies. In general, the Portage lake monzogabbro has a solid-state fabric parallel to the foliations of Lloyds River Fault Zone amphibolites. In low strain zones, however, a foliation subparallel to the Lloyds River Fault Zone is defined by the K-feldspar phenocrysts, which are locally tiled (Fig. 5.7). The phenocrysts are enclosed in a low strain matrix and lack pressure shadows or deformed tails, suggesting the K-feldspar foliation originated by flow in the magmatic state. A magmatic fabric parallel to the Lloyds River Fault Zone, along with age constraints (see below), implies the Portage Lake monzogabbro intruded syn-kinematically into the Lloyds River Fault Zone. This is consistent with the presence of foliated amphibolite enclaves in a correlative monzodiorite immediately west of the Annieopsquotch ophiolite (Fig. 5.1). This pluton is generally highly deformed with foliation parallel to the Lloyds River Fault Zone amphibolites, and has a flaser gabbro-like appearance with hornblende augen up to 1 cm in length within a plagioclase-K-feldspar-quartz matrix.

The Portage Lake monzogabbro is primitive, with low SiO_2 (44.6-53.5%), high $MgO+Fe_2O_3^*$ (11.7-19.6%), and has a remarkably high alkali content (3.9-7.0%), with the majority of the alkalis being K_2O (average K_2O / Na_2O = 1.6). The abundance of K-feldspar within the monzogabbro indicates these high K_2O contents are a primary feature. The high K_2O defines the Portage Lake monzogabbro as absarokite (SiO_2 <52%) to shoshonite (SiO_2 >52%) (cf. Morrison, 1980). Such compositions are extremely rare within the Appalachians; to my knowledge, only one other shoshonitic pluton has been reported (Pavlides et al., 1994). Harker diagrams show well-defined trends suggestive of fractionation of olivine, clinopyroxene, plagioclase, ilmenite, and apatite. The Portage Lake monzogabbro is LREE-rich, with somewhat depleted HREE, leading to high La/Yb_N (19-24). Its trace element patterns reveal depletion in Nb, Ti, and Zr, and marked enrichment in LILE (Cs, Rb, Ba, Th, K, Pb), indicating a strong subduction component in their petrogenesis (Fig. 5.5c). This is consistent with the La-Y-Nb discrimination diagram (Fig. 5.6a). ε_{Nd} values of the Portage Lake monzogabbro range from –3.4 to –4.9 (Table 5.2), suggesting crustal assimilation or recycling of an old crustal component into the mantle source. Its primitive composition, combined with an incompatible element content higher than average upper continental crust and fractionation trends, suggest limited crustal assimilation. I therefore interpret the Portage Lake monzogabbro to be derived from a mantle source strongly enriched in alkalis and LREE by hydrous fluids and/or melts derived from a subducted slab and overlying sediments. This is in keeping with petrogenetic models for shoshonites elsewhere (e.g., Sun and Stern 2001; Chung et al., 2001).

5.4.3. Otter Pond Complex

Otter Pond mafic suite

The Otter Pond mafic suite comprises variably deformed predominantly gabbroic-dioritic bodies that occur along the Otter Brook Shear Zone and intrude the Annieopsquotch, Star Lake, and King George IV ophiolites, as well as the Lloyds River Complex (Fig. 5.1). The suite is generally distinct because of its hornblende porphyritic to oikocrystic nature, with the oikocrysts locally having a diameter of 1 cm. In thin section, brown, igneous, tschermakitic amphibole oikocrysts enclose crystals of calcic plagioclase, pyroxene, and oxides. Deformed equivalents along the Otter Brook Shear Zone locally preserve the igneous poikilitic to porphyritic texture as porphyroclastic hornblende aggregates in schists and mylonites.

Non-cumulate mafic bodies of this suite have basaltic to andesitic compositions (SiO_2 = 47.1-56.3 wt%, MgO+ Fe_2O_3* =14.2-21.1%), with moderate LREE enrichment (La/Yb_N = 2-8, average 5). LILE were likely remobilized in a post-magmatic stage, but they are consistently enriched. Nb is strongly depleted (average Nb/Th =0.8), while Zr, Hf, and Ti are slightly depleted (Fig. 5.5d). The presence of amphibole oiko- and phenocrysts, calcic plagioclase, and oxides in associated cumulates indicate high water activity and oxygen fugacity. Chemistry and mineralogy of the Otter Pond mafic suite thus indicate formation in an arc environment, supported by their position in the La-Y-Nb diagram (Fig. 5.6). ε_{Nd} values of –0.9 and –1.8 for a gabbro and a mafic dyke, respectively (Table 5.2), indicate assimilation or recycling of an old crustal component into the mantle source of the suite.

Otter Pond granodiorite suite

The Otter pond granodiorite suite comprises several granodioritic to tonalitic bodies that intrude the Annieopsquotch ophiolite and Lloyds River Complex, as well as subordinate rhyolites. Accessory mineral phases include chloritized hornblende, chloritized biotite and titanite. Several smaller, highly deformed, fine-grained granodioritic intrusions locally cut Otter Brook Shear Zone mylonites, and have a strong foliation parallel to those within the surrounding Otter Brook Shear Zone tectonites (Fig. 5.8). The dykes cut the Lloyds River Complex, Annieopsquotch ophiolite, and Otter Pond mafic suite, and hence also stitch the boundary between Annieopsquotch ophiolite belt and Lloyds River Complex (Otter Brook Shear Zone). These relationships suggest the Otter Pond granodiorite suite intruded the Otter Brook Shear Zone syn-kinematically (Fig. 5.8). The suite must also postdate intrusion of the Otter Pond mafic suite. The felsic intrusions likely intruded at very shallow levels, as evidenced by the generally fine-grained nature of the larger bodies and flow-banding in the associated aphanitic dykes. Chemically similar rhyolitic tuff and flows (Fig. 5.5e), interlayered with graphitic sediment and mica schist, occur along the Otter Brook Shear Zone and are interpreted to represent the extrusive equivalents of the shallow level intrusions.

The Otter Pond granodiorite suite is characterized by high SiO_2 (68.0-73.2%) and alkali (3.7-6.2%) content, and low to moderate MgO+Fe_2O_3* (3.0-10.1%). LREE and LILE are enriched (La/Yb_N=6-9, average 7), while HFSE (Nb, Ti) are depleted (Fig. 5.5e). These features suggest formation in an arc environment, consistent with their position in the Rb vs Y+Nb discrimination diagram (Fig. 5.6b). The rhyolite has a similar composition (Fig. 5.5e), and yielded an ε_{Nd} value of –6.8 (Table 5.2).

5.5. Geochronology

5.5.1. Analytical procedures

Laser $^{40}Ar/^{39}Ar$ step-heating analysis was carried out at the Geological Survey of Canada, with data collection protocols after Villeneuve and MacIntyre (1997) and Villeneuve et al. (2000) and error analysis following Scaillet (2000) and Roddick (1988). Analytical data are presented in Table 5.3 and plotted in Fig 5.9. U-Pb TIMS and SHRIMP II analyses were conducted at the GSC. U-Pb TIMS analytical methods are outlined in Parrish et al. (1987) and Davis et al. (1997), with treatment of analytical errors after Roddick et al. (1987). SHRIMP II analyses were conducted using analytical procedures described by Stern (1997), with standards and U-Pb calibration methods following Stern and Amelin (2003). U-Pb TIMS and SHRIMP analyses are presented in Tables 5.4 and 5.5, respectively, and are plotted in concordia diagrams with errors at the 2σ level (Fig. 5.10). Further details on the $^{40}Ar/^{39}Ar$ and U-Pb TIMS and SHRIMP analytical techniques are presented in Appendix 2. All of the geochronology sample locations are indicated in Fig. 5.1 and Tables 5.3, 5.4, and 5.5.

5.5.2. $^{40}Ar/^{39}Ar$ geochronology

$^{40}Ar/^{39}Ar$ analyses were carried out on hornblende separates from two amphibolites that mark the Lloyds River Fault Zone (sample # 1 and 2 in Fig. 5.1) to provide a minimum age of deformation along the Lloyds River Fault Zone. Sample VL01J261A is a strongly foliated amphibolite taken from a zone of amphibolites that defines the southeastern shear zone along the northwestern margin of the Annieopsquotch ophiolite (Fig. 5.1). Both aliquots of sample VL01J261A (z7152; #1) have fairly consistent Ca/K ratios, and yield a well-defined plateau, comprising 97.4% of the total gas and defining the age of the sample to be 468±6 Ma (Table 5.3, Fig. 5.9a). Sample VL02J368A (z7586; #2) was taken from a foliated amphibolite that marks the southeastern shear zone along the northwestern margin of the Star Lake ophiolite (Fig. 5.1). It has a nearly constant Ca/K ratio throughout most of the heating process, with the exception of the last steps of the two aliquots, which may indicate degassing of a second, contaminating phase. The two aliquots yield a plateau region, comprising 98.2% of the gas, which defines the age of the sample to be 471±5 (Table 5.3, Fig. 5.9b), in agreement with the age of VL01J261A. I therefore conclude that the age of c. 470 Ma is geologically significant, and represents the age at which the amphibolites cooled below the hornblende closure temperature for argon (c. 550°; Harrison, 1981), providing a minimum age for ductile deformation of the Lloyds River Fault Zone.

5.5.3. U/Pb geochronology

VL01J120 (z7508) – Portage Lake monzogabbro

A sample was collected from the main body of the Portage Lake monzogabbro, north of Lloyds Lake (#3 in Fig. 5.1). It contained abundant high-quality zircons, which were grouped into different fractions based on size and morphology (Table 5.4). Three of the analyzed fractions are near-concordant (-0.1% to 0.5 % discordant), while fraction 5 is slightly discordant (0.8%), suggesting it has been affected by minor lead loss (Fig. 5.10a). There is no evidence for inheritance in the sample. A weighted average of the $^{207}Pb/^{206}Pb$ ages of all four analyses is 462±2 Ma (MSWD = 0.9, probability = 0.45). This date is interpreted to be the crystallization age of the Portage Lake monzogabbro, and provides an age for syn-kinematic intrusion within the Lloyds River Fault Zone.

VL01J016 (z7153) – Portage Lake monzodiorite

A sample of the highly strained monzodiorite immediately west of the Annieopsquotch ophiolite, immediately south of the northwestern shear zone (#4 in Fig. 5.1), contains abundant zircon ranging in morphology from euhedral stubby prismatic grains to anhedral fragments (Table 5.4). All of the zircon fractions analyzed are somewhat discordant (0.5%-1.2%), and define a discordia, interpreted to result from recent lead loss (Fig. 5.10b). No cores have been observed, and there is no isotopic evidence for inheritance. A weighted average of the $^{207}Pb/^{206}Pb$ ages of all four analyses is 464±2 Ma (MSWD=0.5, probability=0.68; Fig. 5.10b), which is interpreted to be the crystallization age of the monzodiorite. This age provides a maximum age for the deformation of the monzodiorite within the Lloyds River Fault Zone.

Four titanite fractions are 0.4% to 3.8% discordant, and one fraction is slightly reversely discordant (-1.9%; Fig. 5.10b). The titanite analyses, which have large associated errors, define an array with $^{207}Pb/^{206}Pb$ ages ranging between 465 Ma and 426 Ma. This range could indicate the presence of distinct age populations within the multi-grain fractions, lead loss during a younger event, or a combination thereof. Given that the host rock crystallized at 464 Ma (see above), and that the adjacent amphibolite to granulite-facies Cormacks Lake Complex was juxtaposed along the Lloyds River Fault Zone during rapid Early Silurian exhumation (Pehrsson et al., 2003), I postulate that the titanite population reflects a mixture of titanite formed during initial cooling of the host rock following crystallization, and grains that were reset or crystallized during the c. 430 Ma uplift of the adjacent Cormacks Lake Complex.

VL02J238D (z7524) – Pierre's Pond suite diorite

A sample from a highly strained syn-kinematic diorite sheet intruding ophiolitic cumulates on the shore of Star Lake (#5 in Fig. 1) yielded small (50-100 µm), colorless to light brown zircons, which range from subhedral prismatic crystals to anhedral grain fragments with concoidal fractures. Cracks and inclusions are common, as are dark blurry cores, which likely represent inherited material. SEM imaging of the grains showed bright domains in the cores of many grains, with rims characterized by oscillatory zoning, suggesting magmatic overgrowth of inherited zircons. Some zircons are core-free, however, and are interpreted as entirely magmatic grains. A Concordia age, calculated from the SHRIMP analyses of magmatic grains (n=18), is 458.6±3.2 Ma (MSWD of concordance and equivalence = 1.6, probability = 0.014) (Fig. 5.10c, Table 5.5). This age of 459±3 Ma is interpreted as the crystallization age of the diorite, and marks the age of syn-kinematic intrusion of the Pierre's Pond suite within the Lloyds River Fault Zone. One inherited core was analyzed and yielded an age of 1961 Ma (Table 5.5, not plotted).

VL01A258 – Otter Pond Granodiorite suite

A sample was collected from an elongate (500 by 70m), sheared, fine-grained granodiorite intrusion that stitches the Otter Brook Shear Zone southeast of the Annieopsquotch ophiolite (#6 in Fig. 5.1). Two fractions of small, euhedral, prismatic zircons and two fractions of small, euhedral, equant zircons were analyzed. Fraction A1 is concordant and fractions A2 and B1 are slightly discordant (0.9 and –2.0%, respectively) (Table 5.4). A weighted average of the $^{206}Pb/^{238}U$ ages of these three analyses is 468±2 (MSWD = 2.1, probability = 0.11), which is interpreted to be the crystallization age of the granodiorite (Fig. 5.10d). This age provides a minimum age of juxtaposition of the Annieopsquotch ophiolite belt and the Lloyds River Complex, and hence a minimum age of formation of the Otter Brook Shear Zone. Zircon fraction B2 (n=74) is concordant at 473±1 Ma ($^{206}Pb/^{238}U$). This fraction has a distinct morphology, and its age is statistically distinct from the 468±2 Ma crystallization age of the rock (MSWD=26, probability=0.000). Since the sample is from a narrow intrusive sheet (~2 x 0.15 km) that intruded at shallow levels, the granodiorite probably crystallized over a short time perdiod. In addition, the four fractions do not define a linear trend, indicating the two populations cannot be explained by Pb-loss. Therefore, fraction B2 is interpreted to comprise inherited zircons.

5.6. Discussion

5.6.1. Assembly of the Annieopsquotch Accretionary Tract

The data presented above impose strong time- and dynamic constraints on the evolution of the Annieopsquotch Accretionary Tract. The earliest tectonic activity related to assembly of the Annieopsquotch Accretionary Tract is recorded by c. 470 Ma cooling ages of hornblende from amphibolites deformed within the Lloyds River Fault Zone. This provides a minimum age on ductile deformation related to accretion of the Annieopsquotch ophiolite belt to the Dashwoods microcontinent, and suggests the belt was accreted to the Dashwoods microcontinent within 10 Ma after its formation (480 Ma; Dunning and Krogh, 1985). The Otter Pond granodiorite suite intruded both the Annieopsquotch ophiolite belt and the structurally underlying Lloyds River Complex, and hence its age of 468±2 Ma represents a minimum age for emplacement of the Annieopsquotch ophiolite belt above the Lloyds River Complex. The Lloyds River Complex was thus accreted within 5 Ma of its formation (473 Ma; Zagorevski et al., subm.). The overlap in ages of thrusting on the Lloyds River Fault Zone (bracketed between ~480-470 Ma) and Otter Brook Shear Zone (~473-468 Ma) suggests that both shear zones were active around the same time, and may have been genetically related, implying that that ophiolites of both the Annieopsquotch ophiolite belt and Lloyds River Complex were accreted to the Dashwoods microcontinent simultaneously. This is consistent with the similar kinematic histories recorded in the Lloyds River Fault Zone and Otter Brook Shear Zone (Chapter 6; Zagorevski and van Staal, 2002).

The 473±1 Ma inherited zircon fraction in the Otter Pond granodiorite is the same age as the Lloyds River Complex (473Ma; Zagorevski et al., subm.), which it cuts, and the structurally underlying Buchans Group (473 Ma; Dunning et al., 1987). Zircons are rare within the ophiolitic Lloyds River Complex, and it is isotopically juvenile. In contrast, the ensialic Buchans contains abundant felsic volcanic rocks and has a non-juvenile ε_{Nd} signature typical of crustal contamination (e.g., Swinden et al., 1997). The Buchans group is thus a more likely source for the inherited zircon, and can in part account for the markedly negative ε_{Nd} of the Otter Pond granodiorite suite (-6.8). I thus infer that the granodiorite assimilated rocks of the Buchans Group during its ascent, and/or was in part generated by partial melting of the Buchans Group and its basement. If correct, this implies that the Buchans Group was also juxtaposed with the Lloyds River Complex by 468 Ma. This is consistent with structural relationships west of the town of Buchans, where the Buchans Group is interpreted to have been overthrust by a hot thrust sheet comprising c. 467 Ma plutonic rocks of the Notre Dame Arc along the Hungry Mountain Thrust (Thurlow, 1981; Whalen et al., 1987). Geochronological and structural data thus indicate a significant part of the Annieopsquotch Accretionary Tract was assembled and accreted to the Dashwoods by 468 Ma, within 10 Ma (Annieopsquotch ophiolite belt) and 5 Ma (Lloyds River Complex, Buchans Group) after their intra-oceanic generation.

Convergence between intra-oceanic components of the Annieopsquotch Accretionary Tract and the Dashwoods microcontinent likely resulted from continued collision between Laurentia and the Dashwoods microcontinent with its Notre Dame Arc. This collision had started by at least 475 Ma (Waldron and van Staal, 2001), probably initially along promontories, propagating compression to the eastern side of the Dashwoods microcontinent, initiating west-directed subduction (Chapter 3). Extension in the upper plate resulted in retreat of the subduction zone to form the progressively eastward younging units of the Annieopsquotch Accretionary Tract. However, continued Dashwoods-Laurentia collision caused the newly formed basins to collapse, and led to underthrusting of the Annieopsquotch ophiolite belt, Lloyds River Complex and Buchans Group underneath Dashwoods.

The subsequent tectonic history of the Annieopsquotch Accretionary Tract is recorded by formation of the arc-back arc complexes of the Red Indian Lake Group at 464 Ma, which must have occupied a position somewhat outboard of the composite Dashwoods microcontinent (Zagorevski et al., subm.). The Lloyds River Fault Zone was still active during this time, marked by the syn-kinematic intrusion of the Portage Lake monzogabbro (464-462 Ma) and Pierre's Pond suite diorite (459 Ma). Final assembly of the Annieopsquotch Accretionary Tract occurred when the Red Indian Lake Group was accreted to composite Dashwoods microcontinent as a result of the collision with the peri-Gondwanan Victoria arc (van Staal et al., 1998; Zagorevski et al., 2004). The age of this collision is constrained to lie between 454 Ma (the age of the latest volcanism of the Victoria arc; Zagorevski et al., 2004) and 450 Ma (presence of Laurentia-derived detritus in Upper Caradoc-Ashgill sedimentary cover of the Victoria arc; e.g., McNicoll et al., 2001). Accretion-related ductile motion on the Lloyds River Fault Zone and Otter Brook Shear Zone had ceased by the Early Silurian, indicated by the little-deformed Lloyds Lake granite (427±3 Ma, Whalen et al., in prep.) and Boogie Lake suite (435 +6/-3 Ma; Dunning et al., 1990), which stitch the Lloyds River Fault Zone and Otter Brook Shear Zone, respectively.

5.6.2. Source of magmatism in the Annieopsquotch Accretionary Tract

Link with the Notre Dame Arc?

The plutonic rocks that intrude into the Lloyds River Fault Zone and Otter Brook Shear Zone have dominantly arc signatures, and show Nd-isotopic compositions indicative of involvement of an old crustal component in their petrogenesis. The plutons within the Annieopsquotch Accretionary Tract share these characteristics with and are coeval with plutons of the second, slab break-off related phase of the adjacent Notre Dame Arc (469-458 Ma; Whalen et al., 2003; van Staal et al., 2003). Notre Dame Arc pluton ε_{Nd} values range from 2.5 to −13.5 (Whalen et al., 1997), and, like the Pierre's Pond suite, they contain inherited Proterozoic zircon (Whalen et al., 1987; Dunning et al., 1989; McNicoll, unpublished data). This suggests an overall consanguineous relationship between magmatism in the Annieopsquotch Accretionary Tract and the Notre Dame Arc. This is consistent with the geochronological data presented above, which indicate that the Annieopsquotch ophiolite belt, Lloyds River Complex and Buchans Group were already accreted to the Dashwoods microcontinent prior to this magmatic phase.

The role of crustal assimilation

Despite the overall similarities, several notable differences exist between the plutons within the Annieopsquotch Accretionary Tract and the Notre Dame Arc. First, the absarokitic to shoshonitic composition of the Portage Lake monzogabbro is unique. Only one other occurrence has been reported within the Appalachians, suggesting conditions required for shoshonite generation (highly metasomatized mantle source) and preservation (limited crustal assimilation) were met only within the Annieopsquotch Accretionary Tract. Second, the plutonic rocks within the Annieopsquotch Accretionary Tract are volumetrically dominated by mafic compositions, with subordinate intermediate-felsic rocks (average Mg# 56), whic contrasts with the dominantly evolved nature of the Notre Dame Arc (average Mg# 45; Fig. 5.11). In addition, the Otter Pond mafic suite and Portage Lake monzogabbro are as primitive or more primitive than the most primitive Notre Dame Arc suites. The cause of the more mafic nature of the plutons within the Annieopsquotch Accretionary Tract is unlikely to be source-related, as they are thought to be consanguineous with the Notre Dame Arc plutons, and the Portage Lake monzogabbro was likely sourced by mantle of, or mantle derived from, the Dashwoods microcontinent (i.e., the same mantle source by which the Notre Dame Arc was underlain; see below). In contrast, I suggest the dominantly mafic character of the Portage Lake monzogabbro, Otter Pond mafic suite and part of the Pierre's Pond suite is caused by the tectonic environment in which they were emplaced. First, the Annieopsquotch Accretionary Tract likely formed thin crust that was dominantly composed of ophiolites. Second, the close spatial association between the plutons and the Lloyds River Fault Zone plus Otter Brook Shear Zone indicates the plutons ascended along active large-scale shear zones, significantly facilitating transport, thereby limiting crustal assimilation.

The bimodal distribution of plutons within the Annieopsquotch Accretionary Tract, with dominant mafic and subordinate evolved phases, reflects different petrogenetic processes between the Portage Lake monzogabbro and the Otter Pond mafic suite on the one hand, and the Otter Pond granodiorite and Pierre's Pond suite tonalites on the other. The Pierre's Pond diorites appear to have characteristics of both groups. The Otter Pond mafic suite and Portage Lake monzogabbro have high compatible element contents (MgO, Cr, Ni: up to 9.9%, 413 ppm, and 102 ppm, and 8.5%, 201 ppm, and 65 ppm for both suites, respectively), suggesting limited crustal assimilation and preservation of a significant mantle-derived component. In contrast, the magnitude of the negative ε_{Nd} values (up to −6.8) and the evolved nature of the Otter Pond granodiorite suite and Pierre's Pond suite tonalites, as well as the presence of inherited Paleoproterozoic zircons in the Pierre's Pond Suite diorite, suggest that partial melting and assimilation of continental crust was a major process in formation of these plutons. However, the crustal component of the plutons within the Annieopsquotch Accretionary Tract cannot be the derived from crust of the Dashwoods microcontinent, as both field- and seismic data indicate that the Annieopsquotch Accretionary Tract structurally underlies Dashwoods (Fig. 5.2). The 473 Ma inherited zircons in the Otter Pond granodiorite and structural relationships in the Buchans area are consistent with accretion of the Buchans Group, and by inference, its continental basement, to the Dashwoods microcontinent prior to magmatism in the Annieopsquotch Accretionary Tract. I thus infer that the Annieopsquotch Accretionary Tract was underlain by the continental basement of the Buchans Group during generation of the plutonic rocks in the Annieopsquotch Accretionary Tract.

This is consistent with seismic interpretations, which suggest that the thrust slices that contain the Buchans Group are present underneath the entire Annieopsquotch Accretionary Tract, and cut-out the Annieopsquotch ophiolite belt at depth (Fig. 5.2; van der Velden et al., 2004).

The source of the Portage Lake monzogabbro

The strong enrichment in LREE and LILE and negative ε_{Nd} of the Portage Lake monzogabbro, combined with its primitive nature, require a mantle source extensively enriched by an old crustal component. Given the marked absence of sediments within the Annieopsquotch Accretionary Tract, it is unlikely that the enrichment is caused solely by subduction of continent-derived material. In contrast, I propose that the Portage Lake monzogabbro taps old subcontinental lithospheric mantle of the Dashwoods microcontinent or its derivative, the basement to the Buchans arc. This is analogous to recent shoshonites and associated high-K magmas in the eastern Sunda arc and Taiwan, which were produced by melting of enriched subcontinental lithosphere following arc-continent collision (Varne, 1985; Wang et al., 2004). In the Sunda arc, there is a spatial relationship between K-enrichment, concurrent with decreasing ε_{Nd}, and proximity to the advancing Australian plate. Arc-continent collision has caused the arc to tap a dominantly subcontinental Australian mantle source in the east yielding shoshonites, whereas to the west, where the collision has not yet occurred, the high-K signature decreases and calc-alkaline and transitional arc tholeiites erupt (Varne, 1985). The intrusion of the Portage Lake monzogabbro occurred c. 5 Ma after the Buchans arc-Dashwoods microcontinent collision, suggesting it was generated in a tectonic setting very similar to the Sunda and Taiwan shoshonites. Limited crustal assimilation within the Annieopsquotch Accretionary Tract allowed the lithospheric mantle signature to be largely retained, leading to the unique geochemical character of the Portage Lake monzogabbro.

5.6.3. Accretionary tectonics

The Annieopsquotch Accretionary Tract records a complicated history of generation and accretion of several intra-oceanic elements within a short time span. Two geochemically and geochronologically distinct suprasubduction zone ophiolites, the Annieopsquotch ophiolite belt and the Lloyds River Complex, were formed within a time span of 7 Ma (Zagorevski et al., subm.) above a west-dipping subduction zone. The formation of the Lloyds River Complex was related to rifting of the coeval Buchans arc off of the Dashwoods microcontinent (Zagorevski et al., subm.). The Buchans arc in turn rifted shortly (9 Ma) after its formation to yield the Red Indian Lake arc and associated back arc (Zagorevski et al., subm.). The Red Indian Lake arc retained its intra-oceanic position for c. 10 Ma, when it collided with the Peri-Gondwanan Victoria Lake arc along the Red Indian Line. The accretion of the units to the Dashwoods microcontinent was coeval with the intrusion of several plutons. The observed complexities, notably the rapid generation and migration of arc-back arc igneous complexes and the intrusion of plutons into accretionary complexes, are reminiscent of the current southwest Pacific (e.g., Hall 2002) as well as other Paleozoic (e.g., Kunlun; Xiao et al., 2003) and Meso-Cenozoic orogens (e.g., Kamchatka; Konstantinovskaia, 2001), and illustrate the dynamic nature of accretionary margins.

However, the virtual absence of sediments and the importance of recycled continental basement of the Annieopsquotch Accretionary Tract (basement of Buchans and Red Indian Lake arcs) contrast with other major accretionary orogens, which are dominated by large, dominantly sedimentary accretionary complexes, intruded by arc plutons as a result of progressive retreat of the subducting slab (e.g., Sengör and Natal'in, 1996). These arc plutons are generally isotopically juvenile, signaling an important depleted mantle component in their petrogenesis (Chen et al., 2000, and references therein). Such accretionary orogens show little evidence of arc rifting or presence of rifted continental slivers, and are characterized by long-lived subduction-accretion in the fore-arc, leading to the formation of large sedimentary prisms (Sengör and Natal'in, 1996), similar to the Aleutian accretionary complex (Moore et al., 1991). In contrast, the Annieopsquotch Accretionary Tract results from repeated rifting and rapid accretion of slivers of the Dashwoods microcontinent, their overlying arcs and intervening basins. The short life span of these basins, as well as the submarine nature of the Buchans and Red Indian Lake arcs, limited sediment influx, and hence fore-arc accretion. Plutons intruding the Annieopsquotch Accretionary Tract formed in response to slab break-off, and tapped not only a sub-arc mantle source, but also an enriched lithospheric mantle and crustal source, leading to isotopically evolved signatures. The Annieopsquotch Accretionary Tract thus records a greater ratio of recycled crustal material over newly added mantle-derived material than most other accretionary orogens.

5.7. Conclusion

The Annieopsquotch Accretionary Tract in Newfoundland is a well-preserved example of an Early Paleozoic accretionary complex, which formed by the accretion of several arc sequences and oceanic crust to the composite Laurentian margin. It preserves the record of circa 30 million years of west-directed subduction beneath Laurentia, providing a unique view of the tectonic proceses during the Early-Middle Ordovician closure of Iapetus. This record is poorly preserved esewhere in the Northern Appalachians, maily due to the presence of extensive Siluro-Devonian cover sequences (van Staal et al., 1998). Assembly of the Annieopsquotch Accretionary Tract is recorded by shear zones that separate distinct units, and syn-kinematic plutonic suites within those shear zones. Age constraints suggest that the various units of the Annieopsquotch Accretionary Tract formed and were accreted to the Laurentian margin within 5 to 10 million years of their formation.

Growth of the Appalachian Laurentian margin occurred maily due to the repeated accretion of oceanic crust and the addition of melts generated in both lithospheric and sub-arc mantle. However, recycling of continental crust, in the form of continental slivers that formed basement to the arc sequences, was an important process within the Annieopsquotch Accretionary Tract. The involvement of this basement, combined with an enriched lithospheric mantle, caused the syn-kinematic plutons in the Annieopsquotch Accretionary Tract to be isotopically evolved. Sediment influx during formation of the Annieopsquotch Accretionary Tract was apparently minor, significantly limiting the role of fore-arc accretion.

The data presented in this paper indicate that tectono-magmatic processes in Iapetus operated over very short time scales. In addition, it presents a record of dynamic interaction between extension due to subduction rollback and evidenced by the formation of marginal basins and arc-trench migration, and episodic compression in the abandoned back-arc region, leading to the rapid closure and accretion of the remnant arc phases and marginal basins.

The role of strike-slip tectonics, particularly the movement of fore-arc continental slivers, was probably significant during the tectonic evolution of the Annieopsquotch Accretionary Tract, although its exact role in the development of the Annieopsquotch Accretionary Tract remains to be established. The tectonic complexities along the Early Paleozoic Laurentian margin were thus similar to those operating at present in the Southwest Pacific. In general, the nature of accretionary tectonics thus appears to have remained unchanged throughout the Phanerozoic.

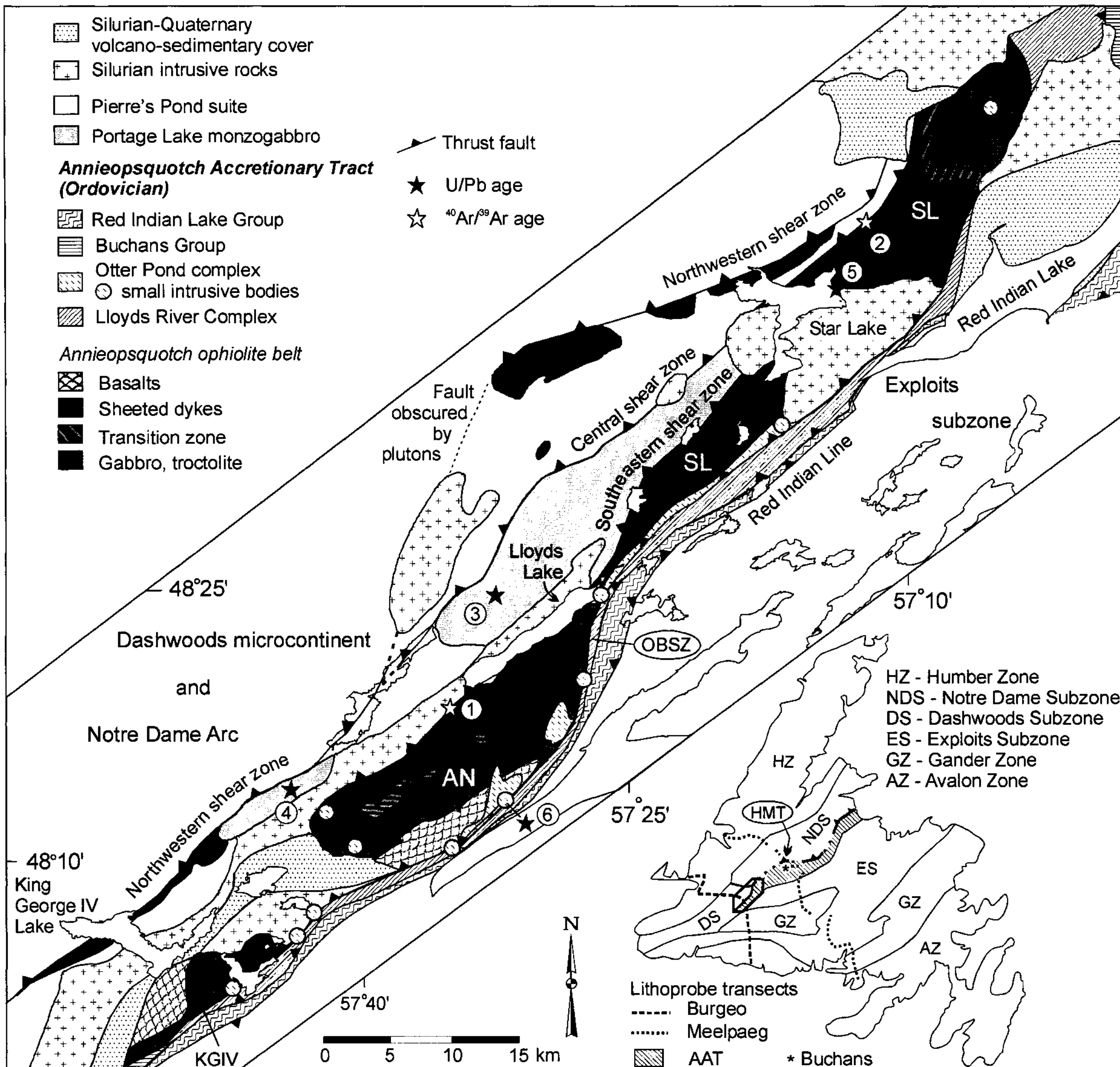

①	468±6 Ma; $^{40}Ar/^{39}Ar$ hornblende amphibolite LRFZ	④	464±2 Ma; U/Pb TIMS zircon Portage Lake monzodiorite
②	471±5 Ma; $^{40}Ar/^{39}Ar$ hornblende amphibolite LRFZ	⑤	459±3 Ma; U/Pb SHRIMP Pierre's Pond suite
③	462±2 Ma; U/Pb TIMS zircon Portage Lake monzogabbro	⑥	468±2 Ma; U/Pb TIMS zircon Otter Pond granodiorite

Figure 5.1: Simplified geological map of the Annieopsquotch Accretionary Tract, with approximate locations of samples dated in this study indicated by numbered filled stars (U/Pb) and open stars ($^{40}Ar/^{39}Ar$). Inset shows tectonostratigraphic zones of the Newfoundland Appalachians, extent of the Annieopsquotch Accretionary Tract (AAT), and the locations of the study area, Lithoprobe seismic transects and town of Buchans. AN=Annieopsquotch ophiolite; HMT=Hungry Mountain Thrust; KGIV=King George IV ophiolite; OBSZ=Otter Brook shear zone; SL=Star Lake ophiolite. Modified from Lissenberg et al. (in press) and van Staal et al. (in press a,b,c).

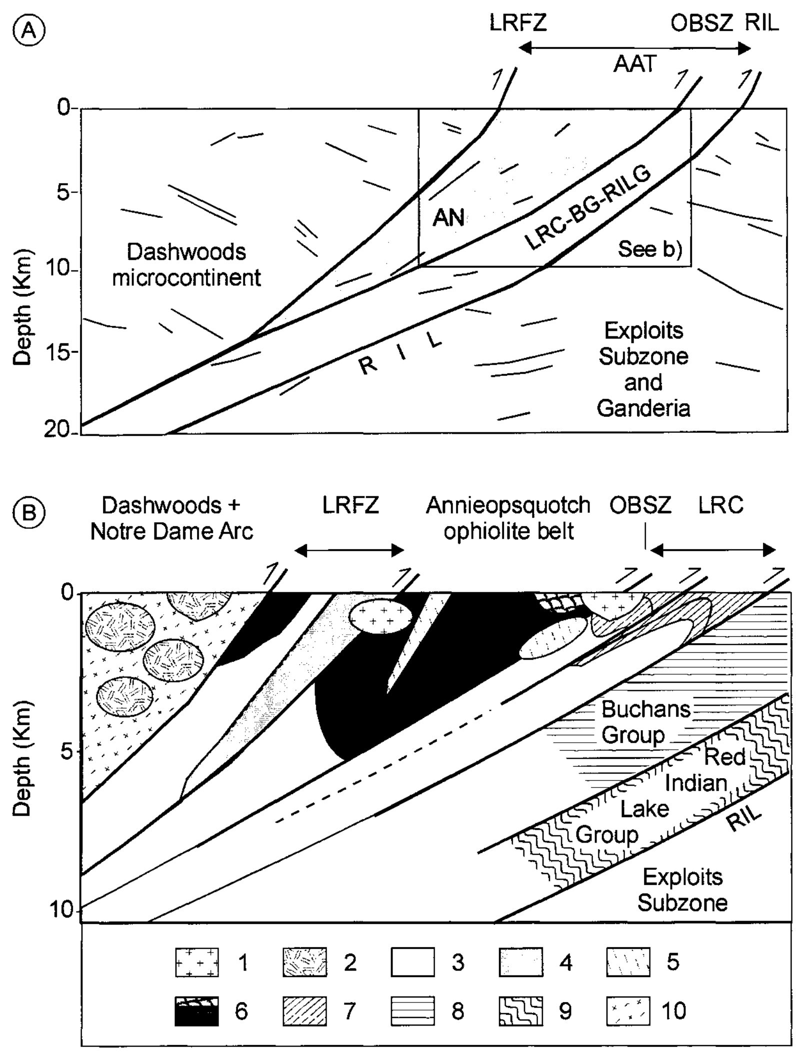

Figure 5.2: Schematic cross-sections of the study area (no vertical exaggeration). a) Cross-section based on Lithoprobe seismic reflection profile along the Burgeo transect, modified from van der Velden et al. (2004). b) Schematic composite cross-section interpolated between Burgeo and Meelpaeg transects showing structural relationships and stratigraphy of different components of the Annieopsquotch Accretionary Tract, as well as plutonic rocks described in this chapter (see text for discussion). 1=Silurian plutons (Lloyds Lake granite & Boogie Lake suite); 2=Notre Dame Arc plutons; 3= Pierre's Pond suite; 4= Portage Lake monzogabbro; 5=Otter Pond Complex; 6=Annieopsquotch ophiolite; 7=Lloyds River Complex; 8=Buchans Group; 9=Red Indian Lake Group; 10=Dashwoods. AAT=Annieopsquotch Accretionaty Tract; AN=Annieopsquotch ophiolite; LRC-BG-RILG=Lloyds River Complex + Buchans Group + Red Indian Lake Group; LRFZ=Lloyds River Fault zone; OBSZ=Otter Brook shear zone; RIL=Red Indian Line.

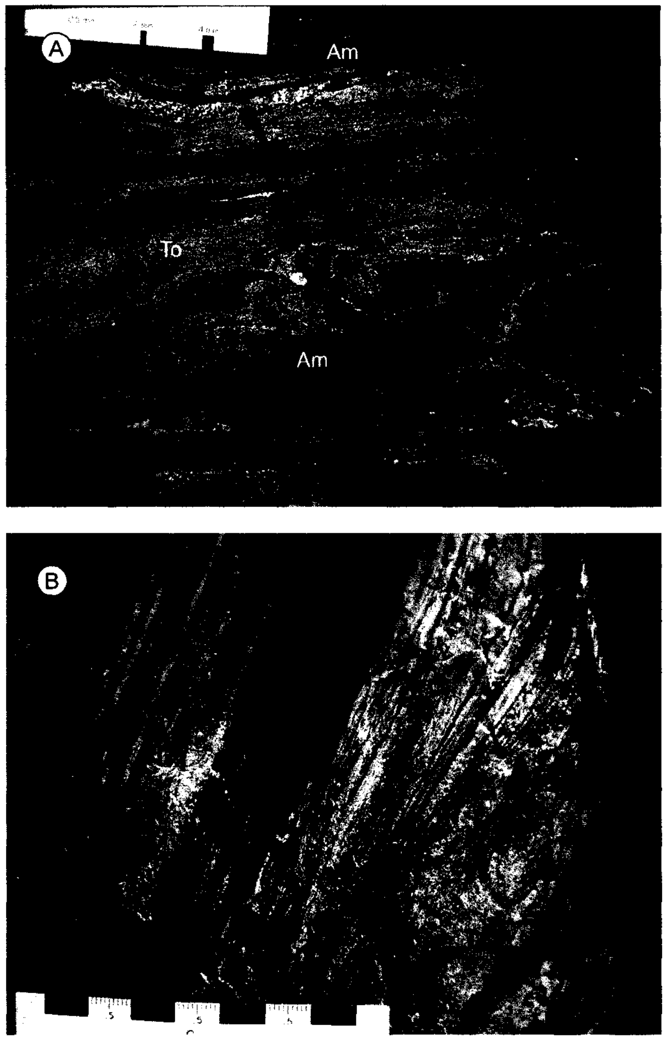

Figure 5.3: Field photographs illustrating the Lloyds River Fault Zone and Otter Brook Shear Zone. a) Highly strained tectonites of the Lloyds River Fault Zone composed of amphibolites (Am) and intrusive sheets of tonalite (To). b) Highly strained volcanic rocks of the Otter Pond Complex that mark the Otter Brook Shear Zone. View towards NE. Scale card divisions are 1 cm.

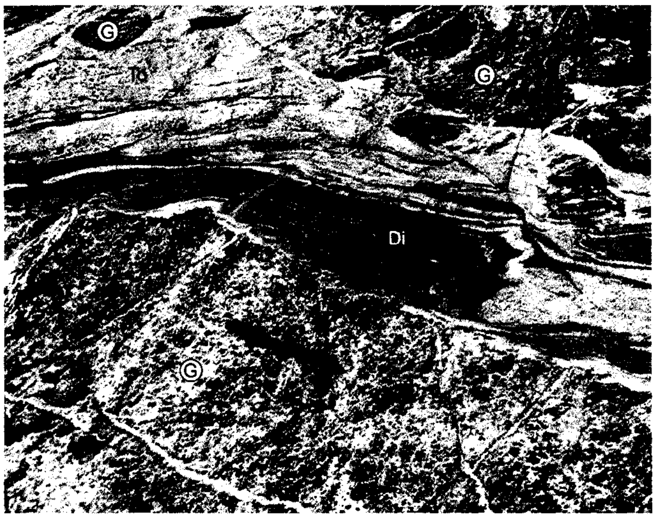

Figure 5.4: Sheet of highly deformed diorite (Di) and tonalite (To), correlated with the Pierre's Pond Suite, intrude unfoliated gabbros (G) of the Star Lake ophiolite on an island in Star Lake. Note gabbro enclaves in tonalite and large deformation contrast between host gabbro and intrusive rocks. Pen is 15 cm long.

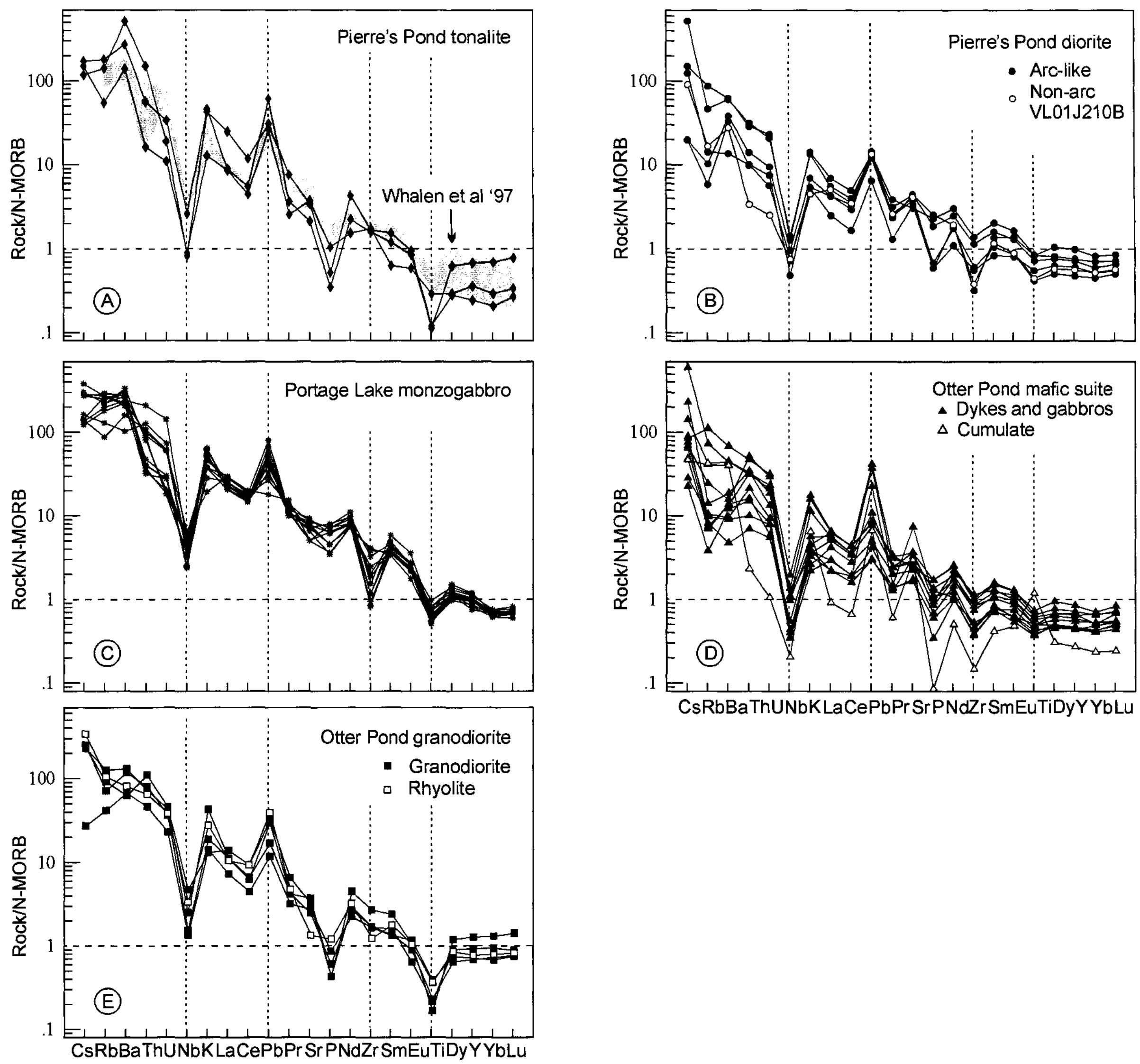

Figure 5.5: Trace element patterns of syn-kinematic plutonic rocks in the Annieopsquotch Accretionary Tract. a) Pierre's Pond Suite tonalites. b) Pierre's Pond Suite diorites. c) Portage Lake monzogabbro; d) Otter Pond mafic suite and associated cumulate. e) Otter Pond granodiorite and associated rhyolite. Normalizing values from Sun and McDonough (1989).

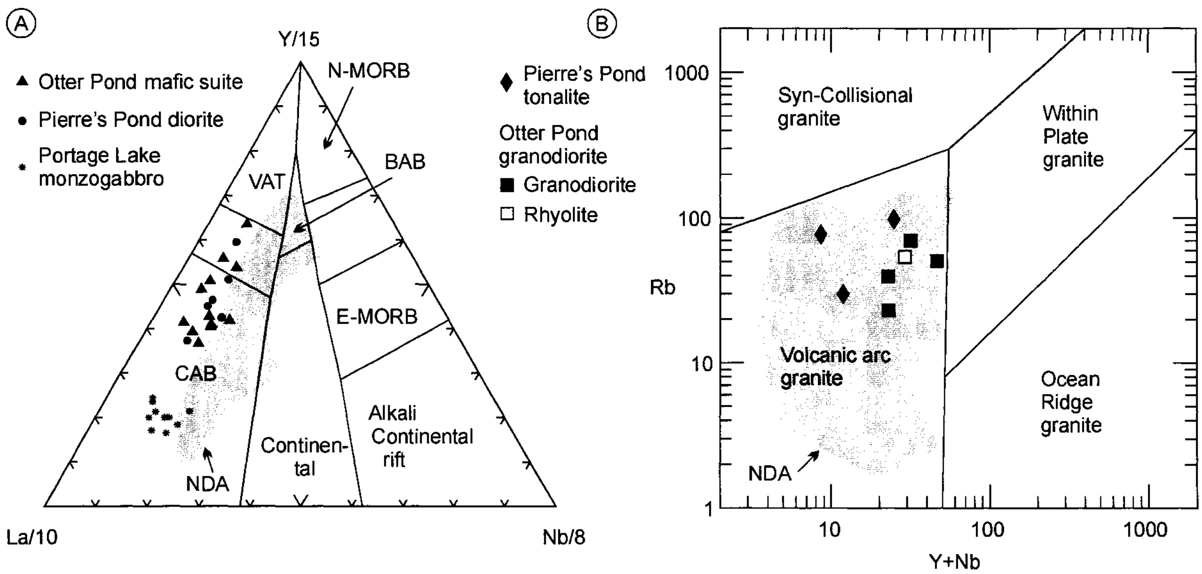

Figure 5.6: Tectonic discrimination diagrams for plutons within the Annieopsquotch Accretionary Tract compared with plutons of the Notre Dame Arc (shaded area; NDA). a) La-Y-Nb diagram of Cabanis and Lecolle (1989) illustrating the arc affinity of the mafic plutons (Portage Lake monzogabbro, Pierre's Pond suite diorites, Otter Pond mafic suite). BAB=back-arc basin basalt; CAB=calc-alkaline basalt; E-MORB=enriched mid-ocean ridge basalt; N-MORB=normal mid-ocean ridge basalt; VAT=volcanic arc tholeiite; b) Rb vs Nb+Y diagram of Pearce et al. (1984) indicating the granitoid plutons in the (Pierre's Pond suite tonalites, Otter Pond granodiorites and rhyolite) are of arc affinity. NDA data from Whalen et al. (1997) and unpublished data.

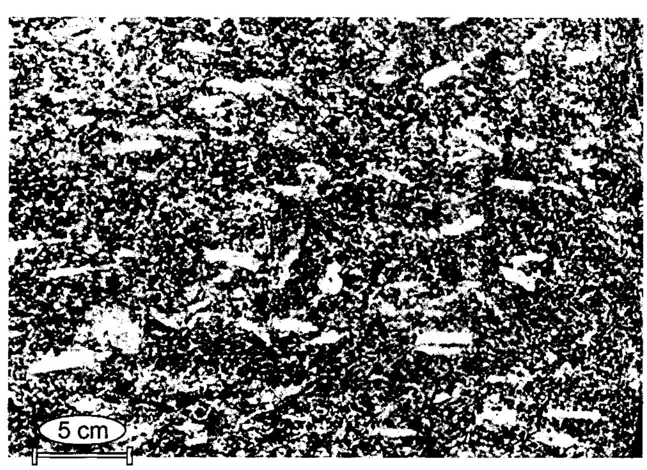

Figure 5.7: K-feldspar phenocrysts define a foliation in the Portage Lake monzogabbro. Low strain in the matrix suggests the monzogabbro was deformed in part in the magmatic state.

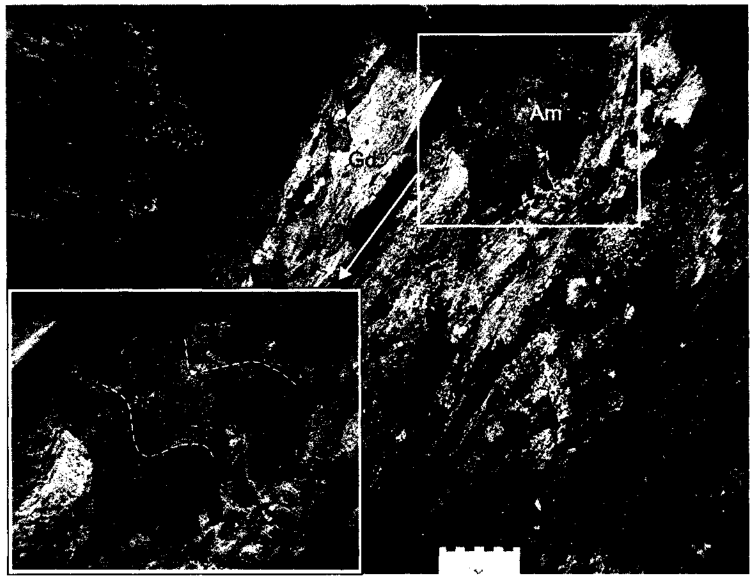

Figure 5.8: Small plug of Otter Pond granodiorite (Gd) contains enclaves of folded mylonitic amphibolite (Am) of the Otter Brook Shear Zone, and is itself highly deformed, suggesting it intruded the Otter Brook Shear Zone synkinematically. View towards NE. Scale card divisions are 1 cm.

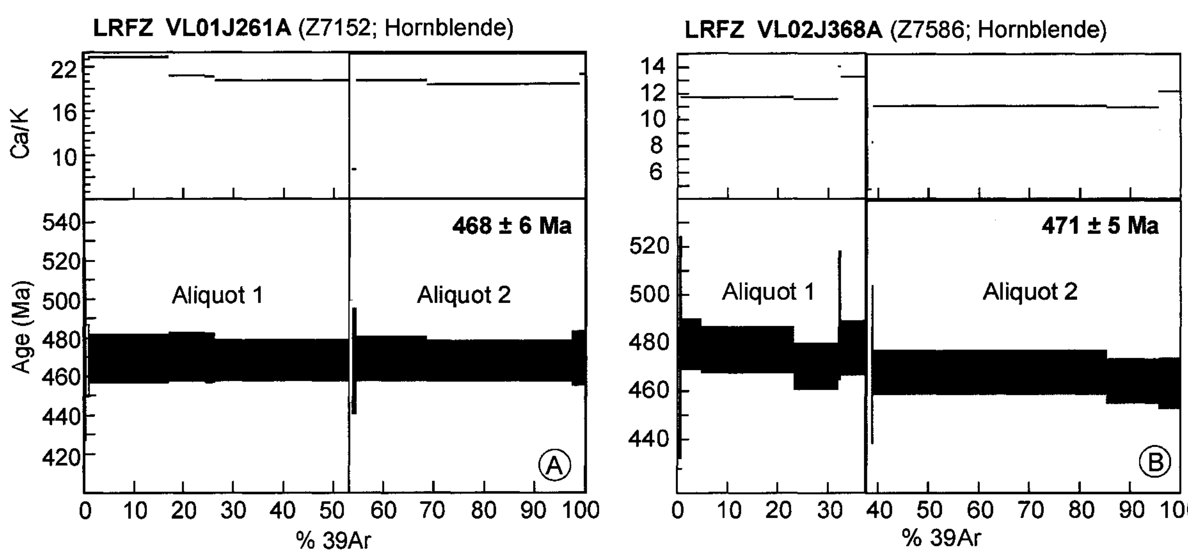

Figure 5.9: Results of $^{40}Ar/^{39}Ar$ hornblende geochronology. a) Age spectrum of ophiolite-derived amphibolite VL01J261A in the Lloyds River Fault Zone near the Annieopsquotch ophiolite. b) Age spectrum of ophiolite-derived amphibolite VL02J368 in the Lloyds River Fault Zone near the Star Lake ophiolite.

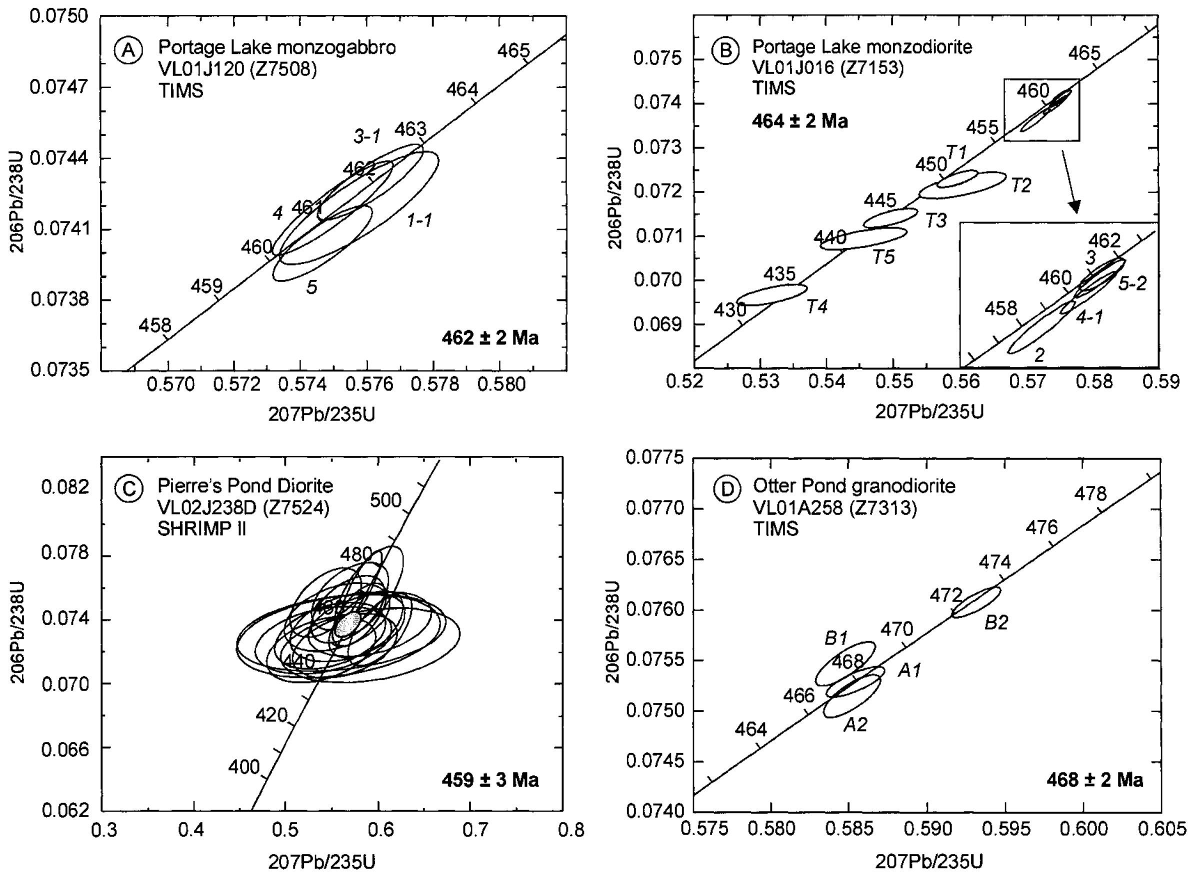

Figure 5.10: Concordia diagrams and ages of the Portage Lake monzogabbro (a; #3 in Fig. 1), Portage Lake monzodiorite (b; #4 in Fig. 1), Pierre's Pond suite (c; #5 in Fig. 1) and Otter Pond granodiorite (d; #6 in Fig. 1). Italic numbers refer to fraction numbers listed in Table 5.4. Grey ellipse in diagram of VL02J238D is calculated Concordia age following the method of Ludwig (1998).

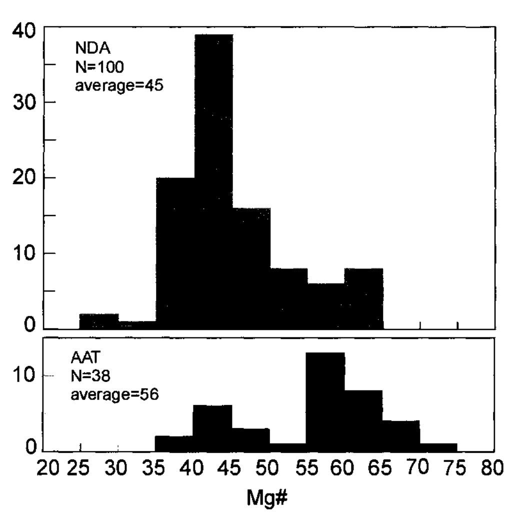

Figure 5.11: Histograms comparing the Mg# of plutonic rocks of the Notre Dame Arc (NDA) and plutonic rocks within the Annieopsquotch Accretionary Tract. Cumulates have been omitted. Mg#=100*Mg/Mg+Fe^{2+}, assuming Fe^{3+}/Fe^{2+}=0.1. NDA data from Whalen et al. (1997) and unpublished data.

Table 5.1: Whole-rock geochemical data from syn-kinematic plutonic rocks

sample	VL01 084	VL01A 050	VL01A 051	VL01A 349b	VL01J 035c	VL01J 036b	VL01J 209b	VL02A 193b	VL02J 307	VL02J 323a	VL02J 339c	VL02J 400	VL02A 278d
Unit	OPm	OPm	OPm	OPm	OPm	OPm	OPm	OPm	OPm	OPm	OPm	OPm	OPm
SiO_2	56.28	55.45	40.00	51.94	51.94	48.90	48.97	47.09	48.75	52.33	53.56	51.91	50.34
TiO_2	0.62	0.53	1.52	0.84	0.63	0.73	0.56	0.64	0.94	0.49	0.47	0.79	0.80
Al_2O_3	15.75	9.88	18.10	16.27	15.51	16.37	17.51	15.56	16.93	13.95	14.32	14.70	17.87
Fe_2O_3*	8.50	9.25	16.20	9.94	9.72	9.75	8.88	12.01	9.43	10.40	8.98	9.25	11.80
MnO	0.16	0.22	0.18	0.17	0.18	0.19	0.15	0.20	0.15	0.17	0.15	0.16	0.21
MgO	5.67	9.91	6.07	6.01	7.75	8.16	8.62	9.11	6.40	7.72	8.01	8.35	5.27
CaO	5.96	12.52	12.70	8.64	9.67	12.18	10.67	12.10	10.31	10.67	11.74	8.58	9.45
Na_2O	3.91	1.83	0.92	4.09	2.84	2.39	2.87	2.10	2.48	3.25	2.36	2.31	3.47
K_2O	0.33	0.28	0.47	1.16	0.41	0.26	0.24	0.29	1.28	0.19	0.16	0.83	0.30
P_2O_5	0.11	0.04	0.01	0.20	0.10	0.12	0.15	0.13	0.20	0.08	0.07	0.16	0.23
LOI	3.40	1.18	5.19	1.24	1.62	1.15	1.80	0.72	2.80	0.81	0.91	2.70	0.87
Total	100.68	101.09	98.60	100.51	100.39	100.19	100.42	100.02	99.76	100.10	100.80	99.85	100.64
Trace elements (ppm)													
Ba	119	88	256	282	100	87	58	30	435	61	77	286	43
Cr	121	413	31	117	328	299	315	304	171	145	338	397	52
Cs	1.61	0.34	0.33	4.18	0.49	0.46	0.54	0.63	0.60	0.20	0.16	1.00	0.94
Cu	43.8	19.0	55.0	105.4	79.2	150.1	25.5	27.5	63.6	5.7	10.0	11.3	18.1
Hf	2.26	1.25	0.37	1.94	1.67	1.44	0.84	0.90	2.20	1.00	0.90	2.30	1.90
Nb	2.27	0.93	0.48	3.20	2.59	2.58	0.82	1.28	4.60	1.02	0.80	2.50	3.64
Ni	45	102	10	64	100	96	141	66	31	42	69	93	14
Pb	2.6	1.3	2.0	2.5	3.3	2.3	0.9	6.8	12.6	1.5	0.9	11.3	9
Rb	7.9	3.9	23.0	40.9	13.7	4.2	5.5	4.6	62.6	5.9	2.1	23.9	5
Sc	32.1	59.2	42.0	34.6	38.4	41.5	34.4	48.0	32.0	52.5	41.3	29.0	43
Sr	232	159	273	217	268	332	292	669	328	203	148	253	863
Th	4.20	1.96	0.28	4.02	6.22	3.90	1.21	0.84	5.70	2.58	1.83	3.80	3.11
V	202	252	639	299	238	253	230	318	287	315	240	228	297
U	0.89	0.28	0.05	0.63	1.40	1.10	0.37	0.26	1.50	0.44	0.38	1.00	1.34
Y	18.4	13.1	7.6	20.2	15.4	16.7	12.6	12.4	23.9	12.5	12.2	18.9	16.0
Zn	67.1	59.2	97.0	65.3	74.4	67.4	56.6	72.3	273.0	55.0	48.5	69.0	89.0
Zr	85.1	39.3	11.0	71.6	62.3	55.4	27.6	32.8	76.5	34.5	28.8	62.6	69.6
La	16.1	7.3	2.3	15.8	14.4	12.8	5.6	5.5	16.4	10.5	7.5	13.7	16.8
Ce	32.3	14.6	5.0	33.0	26.8	25.5	12.1	14.3	32.7	21.0	14.6	26.9	33.4
Pr	4.13	1.80	0.80	4.49	3.25	3.21	1.68	1.97	4.28	2.67	1.87	3.17	4.18
Nd	16.1	7.2	3.7	18.3	12.8	13.0	7.9	9.0	18.7	10.7	7.6	14.4	17.5
Sm	3.48	1.86	1.10	4.00	2.74	2.94	2.00	2.13	4.20	2.25	1.98	3.30	3.79
Eu	1.02	0.65	0.49	1.31	0.89	1	0.77	0.64	1.32	0.62	0.55	1.16	1.03
Gd	3.18	2.22	1.3	3.76	2.84	2.97	2.16	2.37	4.5	2.19	1.98	3.59	3.57
Tb	0.50	0.35	0.22	0.59	0.44	0.46	0.34	0.37	0.6	0.38	0.33	0.50	0.54
Dy	3.13	2.27	1.4	3.53	2.62	2.93	2.08	2.27	4.33	2.21	2.27	3.11	2.94
Ho	0.66	0.48	0.3	0.76	0.59	0.6	0.46	0.48	0.81	0.49	0.51	0.65	0.58
Er	2.02	1.38	0.81	2.08	1.62	1.66	1.42	1.46	2.03	1.45	1.47	1.84	1.69
Tm	0.3	0.22	0.11	0.33	0.25	0.25	0.2	0.22	0.38	0.24	0.23	0.27	0.24
Yb	2.04	1.32	0.72	2.01	1.63	1.61	1.26	1.25	2.17	1.31	1.5	1.55	1.56
Lu	0.32	0.22	0.11	0.33	0.25	0.24	0.2	0.2	0.38	0.23	0.24	0.31	0.24
Mg#	59	70	45	57	63	65	68	62	60	62	66	66	49
La/Yb_N	5.7	4.0	2.3	5.6	6.3	5.7	3.2	3.2	5.4	5.7	3.6	6.3	7.7

Notes: OPm=Otter Pond mafic suite; Mg#=Mg/(Mg+Fe^{2+}), assuming Fe^{3+}/Fe^{2+}=0.1; b.d.=below detection limit

Table 5.1 (continued)

sample	VL01A 118	VL01A 258b	VL01A 267	VL01A 354b	VL01A 081	VL01J 225a	VL01J 229a	VL01J 238c	VL01J 227b	VL01J 231a	VL01J 229b	VL01J 232	VL01J 238b
Unit	OPgd	OPgd	OPgd	OPgd	OPr	PPSt	PPSt	PPSt	PPSd	PPSd	PPSd	PPSd	PPSd
SiO_2	72.06	72.75	68.04	73.20	70.18	72.25	67.03	74.62	50.08	48.90	48.54	52.07	48.98
TiO_2	0.29	0.27	0.49	0.21	0.46	0.15	0.36	0.14	1.07	0.57	0.93	0.54	1.08
Al_2O_3	14.11	13.76	15.24	14.02	11.76	14.38	16.60	13.84	18.48	17.61	16.74	17.36	16.24
Fe2O3*	2.65	2.47	4.21	2.09	7.40	1.58	3.63	1.47	11.22	10.92	10.50	9.85	10.18
MnO	0.09	0.09	0.08	0.03	0.32	0.02	0.04	0.05	0.24	0.18	0.18	0.18	0.18
MgO	0.80	0.90	1.23	0.91	2.76	0.58	1.22	0.52	3.69	7.06	7.30	6.10	8.11
CaO	1.95	1.65	3.94	2.73	1.98	3.12	5.25	1.75	9.13	11.84	11.53	10.70	10.74
Na_2O	4.69	3.13	4.39	4.51	1.68	3.10	3.61	3.89	4.18	1.59	2.49	2.38	2.77
K_2O	1.35	3.07	1.01	0.94	1.97	3.02	0.91	3.24	0.51	0.40	0.99	0.33	1.04
P_2O_5	0.07	0.05	0.10	0.05	0.14	0.06	0.12	0.04	0.30	0.07	0.22	0.08	0.27
LOI	2.49	1.60	1.64	1.14	1.35	0.83	0.91	0.64	0.54	0.86	1.03	0.74	1.02
Total	100.54	99.83	100.37	99.83	100.02	99.10	99.68	100.21	99.44	99.99	100.44	100.33	100.62
Trace elements (ppm)													
Ba	735	818	419	392	503	3185	864	1686	242	176	384	210	395
Cr	1	21	1	34	98	7	8	7	11	67	124	63	308
Cs	1.74	1.60	0.19	1.64	2.35	0.81	1.03	1.18	0.14	0.64	3.69	0.14	1.06
Cu	7.9	3.8	9.2	33.3	67.9	27.4	11.7	21.8	48.9	82.7	75.4	58.3	74.7
Hf	3.30	3.40	2.99	5.00	2.50	2.85	2.73	3.34	0.75	1.08	1.98	1.38	2.58
Nb	3.55	5.80	3.12	10.89	7.72	1.89	2.04	6.02	2.27	1.71	3.35	1.77	3.02
Ni	b.d.	b.d.	b.d.	5	51	b.d.	5	b.d.	6	37	73	30	101
Pb	5.0	8.8	3.5	9.5	11.6	9.0	7.8	18.0	3.7	3.7	4.0	4.4	4.1
Rb	39.8	69.9	23.2	50.8	58.0	77.7	30.1	99.0	5.8	9.4	26.2	3.3	49.2
Sc	7.5	7.0	10.7	5.3	16.7	2.1	5.3	3.7	37.9	43.0	38.8	36.5	36.2
Sr	221	334	244	285	120	304	329	188	406	377	402	347	279
Th	9.56	8.60	5.50	13.06	7.73	17.69	1.92	6.64	1.71	0.41	3.79	1.20	3.48
V	27	15	55	24	89	24	45	16	195	286	268	243	221
U	1.70	2.00	1.07	2.13	1.79	0.88	0.51	1.56	0.45	0.12	0.99	0.27	1.10
Y	19.2	25.8	19.9	35.6	21.5	6.7	9.9	18.7	21.4	15.9	20.2	13.4	27.8
Zn	62.5	36.0	32.3	25.8	57.2	11.2	27.7	18.3	96.0	60.7	67.0	59.6	69.8
Zr	124.6	122.9	122.2	198.5	90.7	120.7	126.2	115.8	23.8	28.5	85.6	45.2	103.6
La	27.6	27.5	18.0	34.5	25.9	61.0	21.1	21.9	10.8	10.7	14.0	12.9	17.5
Ce	49.5	46.6	33.2	69.2	69.2	87.3	32.9	40.8	22.4	25.3	30.1	26.5	37.4
Pr	5.58	5.48	4.18	8.60	6.22	9.88	3.34	4.74	3.14	3.47	4.20	3.33	5.17
Nd	19.7	21.8	16.3	32.4	23.3	30.7	11.1	16.0	14.3	14.3	18.3	13.1	22.4
Sm	3.54	4.20	3.48	6.25	4.64	3.98	1.63	3.08	3.62	3.11	4.24	2.79	5.42
Eu	0.91	0.65	1.19	1.07	1.06	0.95	0.59	0.85	1.41	0.92	1.34	0.89	1.69
Gd	3.12	3.95	3.35	5.67	4.19	2.4	1.47	2.51	3.83	2.8	3.95	2.5	5.4
Tb	0.48	0.6	0.54	0.9	0.65	0.27	0.21	0.41	0.6	0.42	0.59	0.40	0.84
Dy	2.91	4.09	3.38	5.4	3.87	1.25	1.31	2.79	3.74	2.65	3.52	2.32	4.82
Ho	0.65	0.82	0.76	1.14	0.81	0.23	0.3	0.62	0.82	0.58	0.73	0.48	1.00
Er	1.97	2.47	2.11	3.55	2.51	0.61	0.89	1.84	2.28	1.6	2.02	1.45	2.76
Tm	0.31	0.42	0.33	0.58	0.35	0.09	0.14	0.3	0.34	0.25	0.31	0.22	0.41
Yb	2.2	2.86	2.06	3.96	2.40	0.62	0.88	2.08	2.18	1.61	1.84	1.39	2.53
Lu	0.35	0.4	0.34	0.64	0.37	0.12	0.15	0.35	0.33	0.25	0.3	0.23	0.39
Mg#	40	44	39	49	45	44	42	44	42	58	60	57	63
La/Yb_N	9.0	6.9	6.3	6.3	7.7	70.6	17.2	7.6	3.6	4.8	5.4	6.7	5.0

Notes: OPgd=Otter Pond granodiorite; OPr=Otter Pond rhyolite; PPSt=Pierre's Pond Suite tonalite; PPSd= Piere's Pond Suite diorite

Table 5.1 (continued)

sample	VL01J 260b	VL01J 118	VL01J 120	VL01J 016A	WXNF 108	WXNF 117	WXNF 199	WXNF 216	WXNF 222	WXNF 223	WXNF 224	WXNF 225	WXNF 227
Unit	PPSd	PLM	PLM	PLM	PLM	PLM	PLM	PLM	PLM	PLM	PLM	PLM	PLM
SiO_2	49.17	44.60	49.82	51.74	49.06	53.46	50.00	53.30	48.90	48.00	53.10	47.40	43.95
TiO_2	0.71	0.86	0.76	0.70	0.80	0.64	0.91	0.78	0.94	1.03	0.67	1.01	1.22
Al_2O_3	15.85	16.88	16.28	16.93	16.50	16.70	15.50	16.30	16.30	16.00	16.70	15.60	15.25
Fe2O3*	9.69	10.52	9.16	10.53	9.60	7.84	8.78	7.51	9.40	10.01	7.48	9.91	11.15
MnO	0.17	0.19	0.16	0.19	0.17	0.17	0.16	0.15	0.17	0.17	0.15	0.17	0.19
MgO	8.91	7.71	5.83	4.61	5.49	4.11	5.82	4.25	6.29	6.21	4.26	6.36	8.47
CaO	12.87	12.05	9.76	8.64	9.28	7.76	9.68	7.71	10.47	10.79	7.87	10.83	12.57
Na_2O	2.08	1.49	1.98	2.98	2.08	2.39	1.90	2.40	2.50	3.00	2.60	1.70	1.10
K_2O	0.39	2.73	3.83	2.03	3.69	4.49	3.99	4.64	2.67	1.39	4.34	3.55	2.76
P_2O_5	0.07	0.90	0.74	0.42	0.71	0.52	0.73	0.53	0.84	0.83	0.53	0.82	0.93
LOI	0.85	1.56	0.99	1.18	0.90	1.10	0.60	0.50	0.40	0.60	0.80	0.40	0.60
Total	100.76	99.49	99.31	99.94	98.62	99.95	97.49	97.56	98.18	97.32	98.02	97.14	97.43
Trace elements (ppm)													
Ba	87	1690	1782	646	2092	1720	1900	1700	1400	1000	1400	1600	1300
Cr	342	167	117	73	103	61	105	81	116	116	80	125	201
Cs	0.88	2.10	1.95	1.13	0.00	0.00	1.90	1.90	0.86	0.98	1.00	2.00	2.65
Cu	83.1	94.2	86.3	85.7	75.5	59.5	99.0	49.0	32.0	48.0	51.0	108.0	165.0
Hf	1.19	2.76	1.86	1.89	3.12	4.53	1.80	7.20	2.20	6.30	4.10	3.30	2.45
Nb	1.14	11.88	5.90	7.73	11.42	8.15	5.70	9.60	5.50	15.00	7.40	11.00	14.00
Ni	89	80	42	20	33	22	39	28	41	41	29	42	65
Pb	2.0	5.4	12.2	16.5	14.3	19.5	14	17	10	9	15	12	8
Rb	8.1	123.8	136.4	72.2	121.0	163.9	140	160	100	49	150	150	150
Sc	44.2	41.3	32.3	30.0	36.7	25.1	32	22	32	33	23	33	45
Sr	307	450	450	450	829	710	701	642	759	768	671	788	644
Th	1.22	4.45	5.72	15.14	9.63	10.44	4.8	11.0	3.8	13.0	12.0	4.9	4.1
V	253	324	290	217	295	224	259	193	278	276	197	280	332
U	0.36	0.85	1.41	3.45	0.00	0.00	1.30	2.80	1.30	2.90	2.90	1.30	0.95
Y	17.1	33.1	28.0	27.6	22.9	21.1	27.0	26.0	28.0	31.0	27.0	29.0	32.0
Zn	50.3	70.1	62.8	85.0	63	59	70	65	77	80	68	79	95
Zr	41.5	112.8	61.2	69.4	86	137	62	280	85	240	180	150	84
La	6.3	73.4	53.0	64.4	62.7	58.4	51.0	57.0	51.0	73.0	57.0	63.0	61.0
Ce	12.6	149.6	110.4	118.1	127.0	120.0	109.0	116.0	109.0	143.0	115.0	132.0	135.5
Pr	1.74	20.12	14.72	14.24	15.55	14.14	14.00	13.00	14.00	18.00	14.00	16.00	17.00
Nd	8.1	79.9	59.4	53.2	59.9	56.9	56.0	54.0	58.0	70.0	53.0	66.0	69.5
Sm	2.23	15.21	11.23	9.33	10.77	10.23	10.00	9.50	11.00	12.00	9.30	12.00	13.00
Eu	0.83	3.62	2.78	2.24	2.62	2.40	2.40	2.30	2.70	2.70	2.20	2.70	2.60
Gd	2.66	11.11	8.36	7.51	8.37	7.56	8.00	7.20	8.50	9.50	7.30	9.10	10.00
Tb	0.45	1.38	1.03	0.99	0.99	0.93	1.00	0.97	1.10	1.30	0.96	1.20	1.30
Dy	2.9	6.8	5.33	5.29	5.29	5.12	5.10	4.80	5.20	5.90	4.80	5.50	6.30
Ho	0.61	1.19	0.99	1.03	0.88	0.96	0.92	0.89	0.96	1.10	0.89	1.00	1.10
Er	1.82	2.83	2.44	2.71	2.34	2.50	2.10	2.10	2.20	2.50	2.20	2.40	2.60
Tm	0.27	0.38	0.34	0.35	0.30	0.35	0.30	0.31	0.31	0.36	0.31	0.33	0.35
Yb	1.61	2.16	1.98	2.26	1.86	2.06	1.90	2.10	2.00	2.30	2.10	2.10	2.20
Lu	0.26	0.319	0.327	0.348	0.27	0.31	0.30	0.33	0.31	0.37	0.33	0.32	0.35
Mg#	67	61	58	49	55	53	59	55	59	57	55	58	62
La/Yb_N	2.8	24.4	19.2	20.4	24.1	20.3	19.3	19.5	18.3	22.8	19.5	21.5	19.9

Notes: PPSd= Piere's Pond Suite diorite; PLM=Portage Lake monzogabbro

Table 5.2: Nd isotopic data of syn-kinematic plutonic rocks

Sample	Unit	Nd	Sm	(143/144)m	(147/144)m	(143/144)i	CHURi	Age	$(\varepsilon_{Nd})t$
VL010084	Opm	15.59	3.35	0.512389 ±17	0.1299	0.5120	0.512035	468 Ma	-0.9
VL01J036b	Opm	12.79	2.96	0.512371 ±9	0.1399	0.5119	0.512035	468 Ma	-1.8
VL01A081	OPr	20.83	4.21	0.512063 ±20	0.1222	0.5117	0.512035	468 Ma	-6.8
VL01J232	PPSd	12.89	2.67	0.512163 ±10	0.1254	0.5118	0.512050	457 Ma	-5.1
VL01J118	PLM	76.07	14.52	0.512145 ±9	0.1154	0.5118	0.512043	462 Ma	-4.8
WXNF117	PLM	50.34	9.25	0.512191 ±17	0.1111	0.5119	0.512043	462 Ma	-3.7
WXNF216	PLM	48.37	8.82	0.512127 ±6	0.1102	0.5118	0.512043	462 Ma	-4.9
WXNF227	PLM	64.94	12.41	0.512190 ±16	0.1155	0.5118	0.512043	462 Ma	-4.0
VL01J016a	PLM	50.35	9.21	0.512204 ±9	0.1106	0.5119	0.512041	464 Ma	-3.4

Note: Abbreviations as in Table 1

Table 5.3: Ar/Ar data of LRFZ amphibolites

#[1]	Power[2]	Vol. ^{39}Ar x10^{-11} cc	^{36}Ar/^{39}Ar	^{37}Ar/^{39}Ar	^{38}Ar/^{39}Ar	^{40}Ar/^{39}Ar	%^{40}Ar ATM	*^{40}Ar/^{39}Ar	f_{39}[3] (%)	Apparent Age Ma[4]
1	VL01J261A Hornblende; J[5]=.01475990 (Z7152; UTM[6] 21456448/5355510)									
	Aliquot A									
	2.4	0.0302	0.2626 ± 0.0409	3.431 ± 0.305	3.117 ± 0.156	98.109 ± 8.397	79.2	20.406 ± 12.397	0.1	474.98 ± 253.96
	3.0	0.1817	0.0695 ± 0.0076	4.184 ± 0.124	0.789 ± 0.034	40.890 ± 1.485	50.3	20.319 ± 2.258	0.3	473.20 ± 46.26
	3.9	0.3846	0.0183 ± 0.0026	4.007 ± 0.109	0.246 ± 0.014	25.460 ± 0.760	21.3	20.040 ± 0.892	0.7	467.48 ± 18.32
	4.6	9.4429	0.0017 ± 0.0002	12.122 ± 0.101	0.811 ± 0.012	20.596 ± 0.108	2.4	20.095 ± 0.611	16.1	468.60 ± 12.55
	5.5	4.2294	0.0000 ± 0.0008	10.835 ± 0.089	0.674 ± 0.013	20.143 ± 0.117	0	20.133 ± 0.615	7.2	469.39 ± 12.63
	6.5	1.1513	0.0023 ± 0.0009	10.766 ± 0.127	0.699 ± 0.015	20.772 ± 0.268	3.2	20.098 ± 0.627	2	468.66 ± 12.87
	12.0	15.7649	0.0004 ± 0.0002	10.450 ± 0.068	0.703 ± 0.011	20.183 ± 0.049	0.7	20.048 ± 0.521	26.8	467.63 ± 10.72
	Aliquot B									
	2.4	0.0444	0.1593 ± 0.0376	2.713 ± 0.249	2.498 ± 0.221	66.774 ± 7.281	70.6	19.614 ± 10.358	0.1	458.70 ± 214.13
	3.0	0.3066	0.0593 ± 0.0042	2.738 ± 0.081	0.528 ± 0.021	37.793 ± 0.902	46.4	20.268 ± 1.275	0.5	472.14 ± 26.13
	3.9	0.5000	0.0148 ± 0.0039	4.185 ± 0.157	0.264 ± 0.015	24.419 ± 0.824	18	20.024 ± 1.315	0.9	467.15 ± 27.02
	4.6	8.2369	0.0021 ± 0.0002	10.501 ± 0.127	0.788 ± 0.014	20.706 ± 0.209	3	20.087 ± 0.561	14	468.43 ± 11.52
	5.5	16.8504	0.0009 ± 0.0001	10.210 ± 0.071	0.644 ± 0.011	20.289 ± 0.048	1.3	20.028 ± 0.509	28.7	467.22 ± 10.46
	6.5	0.8522	0.0014 ± 0.0012	10.212 ± 0.170	0.635 ± 0.020	20.520 ± 0.378	2.1	20.092 ± 0.687	1.5	468.54 ± 14.12
	12.0	0.7505	0.0020 ± 0.0012	10.912 ± 0.174	0.676 ± 0.015	20.688 ± 0.343	2.8	20.100 ± 0.684	1.3	468.71 ± 14.05
2	VL02J368A Hornblende; J=.02315970 (Z7586; UTM 21485040/5386911)									
	Aliquot A									
	3.0	0.6315	0.0292 ± 0.0039	5.318 ± 0.262	0.575 ± 0.018	27.344 ± 0.585	32.0	18.592 ± 0.810	0.4	646.01 ± 23.65
	3.5	0.3993	0.0187 ± 0.0066	2.549 ± 0.145	0.180 ± 0.015	18.590 ± 0.766	29.5	13.106 ± 1.433	0.3	478.20 ± 45.93
	4.2	6.1586	0.0020 ± 0.0005	6.141 ± 0.112	0.687 ± 0.013	13.728 ± 0.069	4.2	13.151 ± 0.331	4	479.67 ± 10.62
	4.6	28.9861	0.0014 ± 0.0001	6.112 ± 0.102	0.740 ± 0.011	13.491 ± 0.028	3.1	13.077 ± 0.305	18.6	477.28 ± 9.79
	5.0	13.6688	0.0008 ± 0.0002	6.032 ± 0.103	0.731 ± 0.011	13.105 ± 0.046	1.8	12.865 ± 0.304	8.8	470.46 ± 9.78
	6.0	0.8274	0.0015 ± 0.0035	7.339 ± 0.262	0.739 ± 0.023	13.782 ± 0.297	1.9	13.527 ± 0.844	0.5	491.66 ± 26.85
	12.0	8.0812	0.0010 ± 0.0004	6.913 ± 0.128	0.732 ± 0.012	13.373 ± 0.060	2.0	13.101 ± 0.355	5.2	478.06 ± 11.39
	Aliquot B									
	3.9	1.4655	0.0264 ± 0.0020	2.459 ± 0.125	0.412 ± 0.016	25.172 ± 0.353	31.1	17.334 ± 0.469	0.9	608.89 ± 13.99
	4.6	0.5851	0.0017 ± 0.0048	4.325 ± 0.166	0.420 ± 0.019	12.991 ± 0.469	0.8	12.890 ± 1.022	0.4	471.28 ± 32.88
	5.0	72.2574	0.0012 ± 0.0001	5.758 ± 0.101	0.727 ± 0.011	13.154 ± 0.025	2.8	12.785 ± 0.287	46.3	467.90 ± 9.24
	6.0	16.1870	0.0000 ± 0.0002	5.689 ± 0.103	0.722 ± 0.011	12.652 ± 0.039	-0.1	12.671 ± 0.289	10.4	464.21 ± 9.33
	12.0	6.7885	0.0006 ± 0.0004	6.326 ± 0.119	0.703 ± 0.012	12.800 ± 0.055	1.2	12.644 ± 0.326	4.4	463.34 ± 10.54

[1] Number refers to text and Figure 5.1
[2] As measured by laser in % of full nominal power (10W)
[3] Fraction 39Ar as percent of total run
[4] Errors are analytical only and do not reflect error in irradiation parameter J
[5] Nominal J, referenced to PP-20=1072 Ma (Roddick, 1983)
[6] UTM in NAD83
All uncertainties quoted at 2s level

Table 5.4: U-Pb TIMS analytical data of syn-kinematic plutons

#[1]	Fraction[2]	Description[3]	Wt. ug	U ppm	Pb[4] ppm	206Pb[5]/204Pb	Pb[6] pg	Isotopic Ratios[7] 208Pb/206Pb	207Pb/235U	±1SE Abs	206Pb/238U	±1SE Abs	Corr.[8] Coeff.	207Pb/206Pb	±1SE Abs	Ages (Ma)[9] 206Pb/238U	±2SE	207Pb/235U	±2SE	207Pb/206Pb	±2SE	% Disc
3	VL01J120 (Z7508; UTM[10] 21458004/5362821); Portage Lake monzogabbro																					
	1-1(Z;5)	Co, Clr, An, Frag, Dia, 250	33	251	21	5398	7	0.27	0.57578	0.00120	0.07419	0.00012	0.847	0.05628	0.00006	461.4	1.4	461.7	1.5	463.6	5.0	0.5
	3-1(Z;2)	Clr, El, Pr, Dia, 300	35	270	23	6599	7	0.27	0.57612	0.00080	0.07430	0.00008	0.857	0.05623	0.00004	462.0	1.0	462.0	1.0	461.6	3.2	-0.1
	4(Z;12)	Clr, El, Pr, Dia, 150	30	280	23	7031	5	0.26	0.57498	0.00091	0.07419	0.00010	0.914	0.05621	0.00004	461.3	1.2	461.2	1.2	460.8	2.9	-0.1
	5(Z;2)	Co, Clr, Mf, Dia, 300	29	178	15	6677	3	0.26	0.57467	0.00074	0.07404	0.00008	0.830	0.05629	0.00004	460.4	0.9	461.0	1.0	464.0	3.2	0.8
4	VL01J016 (Z7153; UTM 21446038/5349989); Monzodiorite																					
	2(Z;21)	Co, Clr, Eu, St, Dia, 150	34	689	52	8442	13	0.13	0.57143	0.00111	0.07364	0.00013	0.947	0.05628	0.00004	458.1	1.5	458.9	1.4	463.3	2.8	1.2
	3(Z;34)	Co, Clr, Eu, St, Dia, 100	27	486	38	5842	10	0.18	0.57538	0.00075	0.07416	0.00008	0.828	0.05627	0.00004	461.1	1.0	461.5	1.0	463.2	3.2	0.5
	4-1(Z;1)	Br, An, Frag, Dia, 75	17	2303	157	76503	2	0.02	0.57450	0.00093	0.07398	0.00011	0.960	0.05632	0.00003	460.1	1.3	460.9	1.2	465.0	2.0	1.1
	5-2(Z;10)	Co, Clr, An, Frag, Dia, 100	76	271	22	16974	6	0.21	0.57524	0.00083	0.07412	0.00009	0.946	0.05629	0.00003	460.9	1.1	461.4	1.1	463.8	2.1	0.7
	T1(T;11)	Br, Sh, Tab, fln, M75, 350	187	748	53	785	821	0.07	0.55973	0.00154	0.07231	0.00010	0.746	0.05614	0.00011	450.1	1.2	451.3	2.0	458.0	8.7	1.8
	T2(T;18)	Br, An, fln, M75, 200	131	650	45	403	989	0.06	0.56048	0.00329	0.07216	0.00015	0.677	0.05633	0.00027	449.2	1.8	451.8	4.3	465.4	20.8	3.6
	T3(T;26)	Br, Sh, fln, M75, 200	111	453	31	612	374	0.07	0.54962	0.00203	0.07142	0.00011	0.709	0.05581	0.00016	444.7	1.3	444.7	2.7	444.9	12.5	0.1
	T4(T;16)	Br, Sh, Mf, fln, M75, 200	47	432	32	381	244	0.16	0.53173	0.00268	0.06967	0.00012	0.662	0.05535	0.00023	434.2	1.4	433.0	3.6	426.4	18.3	-1.9
	T5(T;24)	Co, An, fln, M75, 200	68	285	20	358	250	0.10	0.54559	0.00325	0.07095	0.00012	0.666	0.05577	0.00028	441.9	1.5	442.1	4.3	443.4	21.9	0.4
6	VL01A258 (Z7313; UTM 21458607/5348154); Otter Pond granodiorite																					
	A1(Z;59)	Co, Clr, rln, St, NM0, 75	22	223	18	5266	4	0.19	0.58544	0.00094	0.07529	0.00007	0.771	0.05640	0.00006	467.9	0.9	468.0	1.2	468.0	4.7	0.0
	A2(Z;65)	Co, Clr, rln, St, NM0, 75	26	199	16	3385	7	0.19	0.58521	0.00092	0.07515	0.00011	0.761	0.05648	0.00006	467.1	1.3	467.8	1.2	471.3	4.6	0.9
	B1(Z;75)	Co, Clr, rln, Eq, NM0, 70	26	261	21	5627	4	0.18	0.58479	0.00096	0.07547	0.00011	0.786	0.05620	0.00006	469.0	1.3	467.5	1.2	460.2	4.5	-2.0
	B2(Z;74)	Co, Clr, fln, Eq, NM0, 70	33	125	10	3966	5	0.18	0.59314	0.00078	0.07608	0.00008	0.808	0.05655	0.00004	472.7	0.9	472.9	1.0	473.9	3.4	0.3

Notes:

[1] Number refers to text and Figure 5.1

[2] Z=zircon fraction; T=titanite fraction. All zircon fractions are abraded following the method of Krogh (1982). Number in brackets refers to the number of grains in the analysis.

[3] Zircon descriptions: Co=Colorless, Br=brown, Clr=Clear, fln=Few Inclusions, rln=Rare Inclusions, Eu=Euhedral, Sh=Subhedral, An=Anhedral, Pr=Prismatic, St=Stubby Prism Mf=multifaceted, Tab=Tabular, Fr=Fragments, Dia=Diamagnetic, NM0=NonMag @1.8A 0°SS, M75=Magnetic @ 0.75A 10°SS; Number refers to average size of zircons in um.

[4] Radiogenic Pb

[5] Measured ratio, corrected for spike and fractionation

[6] Total common Pb in analysis corrected for fractionation and spike

[7] Corrected for blank Pb and U and common Pb, errors quoted are 1 sigma absolute; procedural blank values for this study ranged from 0.1- 0.2 pg U and 2-4 pg Pb for zircon analyses and 1-2 pg U and 8-9 pg Pb for titanite analyses; Pb blank isotopic composition is based on the analysis of procedural blanks; corrections for common Pb were made using Stacey-Kramers compositions.

[8] Correlation Coefficient

[9] Corrected for blank and common Pb, errors quoted are 2 sigma in Ma

[10] UTM in NAD83

Table 5.5: U-Pb SHRIMP analytical data of Pierre's Pond suite diorite

#[1]	Spot name[2]	U (ppm)	Th (ppm)	Th/U	Pb* (ppm)	^{204}Pb (ppb)	$^{204}Pb/^{206}Pb$	$\pm\ ^{204}Pb/^{206}Pb$	$f(206)^{204}$	$^{208}Pb/^{206}Pb$	$\pm\ ^{208}Pb/^{206}Pb$	$^{207}Pb/^{235}U$	$\pm ^{207}Pb/^{235}U$	$^{206}Pb/^{238}U$	$\pm ^{206}Pb/^{238}U$	Corr Coeff	$^{207}Pb/^{206}Pb$	$\pm ^{207}Pb/^{206}Pb$	Ages (Ma)[3] $^{206}Pb/^{238}U$	$\pm ^{206}Pb/^{238}U$	$^{207}Pb/^{206}Pb$	$\pm ^{207}Pb/^{206}Pb$	Ages (Ma)[4] $^{206}Pb/^{238}U$	$\pm ^{206}Pb/^{238}U$
5	VL02J238D (Z7524; UTM[5] 21481714/5381618): Diorite Star Lake																							
	7524-18.1	333	237	0.734	27	7	0.000352	0.000135	0.0061	0.2288	0.0071	0.5419	0.0241	0.0722	0.0008	0.378	0.0545	0.0023	449	5	390	96	449	5
	7524-4.1	292	156	0.551	23	7	0.000362	0.000111	0.0063	0.1897	0.0061	0.5674	0.0231	0.0724	0.0008	0.394	0.0569	0.0022	451	5	486	86	450	5
	7524-3.1	171	52	0.314	12	7	0.000612	0.000227	0.0106	0.1115	0.0096	0.5953	0.0398	0.0724	0.0010	0.315	0.0596	0.0038	451	6	589	145	450	5
	7524-8.1*	138	59	0.440	10	3	0.000291	0.000161	0.0050	0.1304	0.0068	0.5443	0.0302	0.0728	0.0009	0.332	0.0543	0.0029	453	5	382	123	454	5
	7524-5.1	180	64	0.367	13	9	0.000766	0.000266	0.0133	0.1267	0.0112	0.5606	0.0454	0.0730	0.0011	0.300	0.0557	0.0043	454	6	440	183	455	6
	7524-26.1	451	199	0.455	34	9	0.000331	0.000134	0.0057	0.1344	0.0058	0.5512	0.0245	0.0730	0.0009	0.379	0.0548	0.0023	454	5	402	96	455	5
	7524-12.1	114	42	0.375	9	6	0.000845	0.000270	0.0146	0.1272	0.0123	0.5637	0.0467	0.0732	0.0010	0.283	0.0558	0.0045	455	6	446	189	455	6
	7524-28.1*	104	46	0.451	8	0	0.000010	0.000010	0.0002	0.1420	0.0072	0.6058	0.0143	0.0734	0.0009	0.629	0.0599	0.0011	457	6	598	40	455	6
	7524-16.1*	155	53	0.351	11	2	0.000198	0.000137	0.0034	0.1104	0.0100	0.5708	0.0254	0.0736	0.0009	0.389	0.0563	0.0023	458	5	463	94	457	5
	7524-6.1	358	266	0.769	30	5	0.000239	0.000155	0.0041	0.2538	0.0127	0.5948	0.0273	0.0737	0.0008	0.361	0.0585	0.0025	459	5	549	97	457	5
	7524-9.1	365	31	0.087	25	2	0.000081	0.000076	0.0014	0.0311	0.0033	0.5902	0.0165	0.0737	0.0009	0.521	0.0581	0.0014	459	5	532	53	458	5
	7524-27.1	417	199	0.494	32	10	0.000367	0.000096	0.0064	0.1458	0.0064	0.5589	0.0233	0.0742	0.0009	0.397	0.0546	0.0021	461	5	397	89	462	5
	7524-14.1*	530	317	0.619	42	1	0.000038	0.000048	0.0007	0.1885	0.0031	0.5828	0.0119	0.0743	0.0008	0.624	0.0569	0.0009	462	5	486	36	462	5
	7524-17.1	414	234	0.583	33	7	0.000275	0.000076	0.0048	0.1805	0.0057	0.5704	0.0162	0.0747	0.0009	0.516	0.0554	0.0014	464	5	428	56	465	5
	7524-2.1*	577	435	0.779	48	10	0.000264	0.000074	0.0046	0.2417	0.0043	0.5470	0.0158	0.0751	0.0009	0.512	0.0528	0.0013	467	5	321	58	469	5
	7524-1.1	884	61	0.072	62	6	0.000097	0.000054	0.0017	0.0234	0.0022	0.5732	0.0171	0.0755	0.0009	0.492	0.0551	0.0014	469	5	415	60	470	5
	7524-20.1*	488	403	0.853	42	2	0.000064	0.000044	0.0011	0.2679	0.0039	0.5938	0.0152	0.0758	0.0011	0.675	0.0568	0.0011	471	7	483	43	471	7
	7524-21.1*	743	544	0.757	63	2	0.000048	0.000021	0.0008	0.2401	0.0021	0.5846	0.0094	0.0760	0.0009	0.844	0.0558	0.0005	472	6	443	19	473	6
	7524-27.1*	29	20	0.699	11	1	0.000089	0.000164	0.0015	0.2057	0.0074	5.7170	0.1636	0.3445	0.0047	0.580	0.1204	0.0028	1908	23	1961	43	1902	22

Notes (see Stern, 1997):

Uncertainties reported at 1s (absolute) and are calculated by numerical propagation of all known sources of error

$f206^{204}$ refers to mole fraction of total ^{206}Pb that is due to common Pb, calculated using the ^{204}Pb-method; common Pb composition used is the surface blank

[1] Number refers to text and Figure 5.1

[2] analyses marked by asterisk on GSC mount# 295, unmarked analyses from mount #312

[3] 204-corrected ages

[4] 207-corrected ages (Stern, 1997)

[5] UTM in NAD83

CHAPTER VI

Feedback between deformation and magmatism in the Lloyds River Fault Zone, an example of episodic fault reactivation in an accretionary setting, Newfoundland Appalachians

6.1. Introduction

Magma extraction, transfer, and emplacement in orogenic belts are often associated with large-scale shear zones, resulting in an intimate interplay between deformation and magmatism. However, the genetic relationships between deformation and pluton emplacement remain controversial: was deformation localized in melt-rich zones as a consequence of the rheological contrasts between the pluton and the host rock (e.g., Hollister and Crawford, 1986; Brown and Solar, 1998), or were magmas emplaced along active shear zones, as these provide efficient pathways for pluton ascent and emplacement (e.g., McCaffrey, 1992; Moyen et al., 2003; Rosenberg, 2004)? This argument persists because criteria to unequivocally distinguish between the two endmembers are sparse, the positive feedback between deformation and magmatism may make reconstruction of the original relationships difficult, and because both mechanisms may operate within the same area (e.g., Vauchez et al., 1997).

The Lloyds River Fault Zone is a fundamental boundary in the Newfoundland Appalachians that formed during the Ordovician Taconic orogeny. It forms part of a major fault system that extends for at least 200 km and accommodated convergence between suprasubduction zone, intra-oceanic elements formed above a west-dipping subduction zone in Iapetus and the peri-Laurentian Dashwoods microcontinent situated further to the west (Fig. 6.1; Waldron and van Staal, 2001). Specifically, it marked the site of subduction of an infant arc terrane preserved as the Annieopsquotch ophiolite belt, in analogous fashion to subduction of the fore-arc in Taiwan (e.g., Chemenda et al., 2001). The Lloyds River Fault Zone is marked by several amphibolite-grade shear zones that contain two suites of plutonic rocks. An extensive mapping program in conjunction with high-precision U/Pb and $^{40}Ar/^{39}Ar$ geochronological data has provided a well-defined geological framework for southwest to central Newfoundland. The Lloyds River Fault Zone therefore presents an excellent opportunity to study the feedback mechanisms between shear zones and syntectonic magmatism.

This chapter describes the structural characteristics of the Lloyds River Fault Zone, its relationship to spatially associated plutonic rocks, and the implications of geothermobarometry of both Lloyds River Fault Zone tectonites and plutonic rocks. I integrate these with U/Pb and $^{40}Ar/^{39}Ar$ geochronological data presented elsewhere (Chapter 5), and derive a model for the evolution of the Lloyds River Fault Zone. I will argue that the Lloyds River Fault Zone originated prior to 471 Ma under upper amphibolite-facies conditions. Age and metamorphic constraints suggest the fault zone cooled significantly before two distinct episodes of intrusion of plutonic rocks. These intrusions triggered repeated high-temperature reactivation of the Lloyds River Fault Zone and led to local contact metamorphism of the host rocks. Intrusion of offshoots of the plutons outside the fault zone localized deformation, forming new small scale shear zones. I conclude that the Lloyds River Fault Zone channeled magma transport and facilitated pluton emplacement, but pluton emplacement in turn played an active role in strain localization.

6.2. Geological Framework

The Appalachian mountain chain formed as a result of the Cambrian-Silurian closure of the Iapetus Ocean (including seaways and marginal basins), and resulted in the juxtaposition of Laurentia with various peri-Gondwanan continental blocks. In Newfoundland, the Appalachians have been subdivided into numerous zones with distinct tectonostratigraphic characteristics (Williams, 1979; Fig. 6.1). The Dunnage Zone preserves the remnants of rock assemblages formed within the oceanic realm of Iapetus, and is subdivided into the Exploits Subzone, which comprises rocks of peri-Gondwanan affinity, and the Dashwoods and Notre Dame subzones, which contain peri-Laurentian rocks (Williams et al., 1988; Fig. 6.1). The two subzones are separated by the fundamental suture zone of the Newfoundland Appalachians, the Red Indian Line. Both the Notre Dame and Dashwoods subzones are dominated by the Late Cambrian to Silurian (488-429 Ma, Whalen et al., 1987; Dubé et al., 1996) Notre Dame Arc, which was built on Laurentian continental basement (Whalen et al., 1997), obducted ophiolites of the Lushs Bight and Baie Verte oceanic tracts (Swinden et al., 1997), and arc-back arc complexes and ophiolites of the Annieopsquotch Accretionary Tract (van Staal et al., 1998; Chapter 5). Tectonic emplacement of Lushs Bight and correlative ophiolitic rocks occurred in the Late Cambrian (Swinden et al., 1997), immediately proceeding metamorphism and early Tremadoc magmatism associated with the Notre Dame Arc. However, the Humber zone, which represents the Laurentian Grenville basement and its passive margin cover sequence, records the persistence of passive margin sedimentation until 475 Ma (Waldron and van Staal, 2001). This disparity between early orogenesis and continuous passive margin development, combined with paleomagnetic arguments (Cawood et al., 2001) suggests the Notre Dame Arc was built on a microcontinent, referred to as Dashwoods, which was separated from the Laurentian margin by an oceanic basin termed the Humber Seaway (Waldron and van Staal, 2001). Closure of the Humber Seaway by east-directed subduction underneath the Dashwoods microcontinent in the early Ordovician initiated the Taconic collision between Dashwoods and the Laurentian margin by at least 475 Ma (Waldron and van Staal, 2001).

The most outboard unit of the Notre Dame Subzone is the Annieopsquotch Accretionary Tract, which comprises a series of east vergent thrust slices dominantly composed of ophiolites and arc-back arc complexes (Fig. 6.1; van Staal et al., 1998; Zagorevski et al., 2003; Chapter 5). Units of the Annieopsquotch Accretionary Tract were formed between 480-464 Ma above a west-dipping subduction zone outboard of the Dashwoods microcontinent, and were accreted to Dashwoods between 471 and 450 Ma (Chapter 5; Zagorevski et al., 2003). The largest, structurally highest unit of the Annieopsquotch Accretionary Tract is the Annieopsquotch ophiolite belt, a c. 200 km long, narrow belt that comprises three nearly complete ophiolites; the King George IV, Annieopsquotch, and Star Lake ophiolites (Figure 1a). It originated at 481-478 Ma (Dunning and Krogh, 1985) during initiation of intra-oceanic subduction outboard of the Dashwoods microcontinent (Chapter 3). The Annieopsquotch Accretionary Tract is bounded to the southeast by the Red Indian Line, which juxtaposes it with peri-Gondwanan arc-back arc sequences, and to the northwest by the Lloyds River Fault Zone, which separates it from the Notre Dame Arc and its Dashwoods basement. The Lloyds River Fault Zone thus constitutes a fundamental tectonic boundary that accommodated the transfer of intra-oceanic complexes to the composite Laurentian margin.

Plutonic rocks within the Lloyds River Fault Zone comprise two suites, defined as the Pierre's Pond suite and Portage Lake monzogabbro (Fig. 6.1; Whalen et al., 1997; Chapter 5). They are coeval with the second, voluminous pulse of the Notre Dame Arc (468-456 Ma; Dunning et al., 1989; Whalen et al., 1997, 2003), and are dominated by arc-like compositions, suggesting an overall consanguineous relationship (Chapter 5). This magmatic episode generated large volumes of both arc- and non-arc plutons throughout the Dashwoods and Notre Dame subzones in a short time span, and occurred c. 10 Ma after the collision between the Dashwoods microcontinent and Laurentia. Consequently, this magmatism was attributed to slab break-off of the oceanic portion of the Laurentian plate following closure of the Humber seaway (van Staal et al., 2003; Whalen et al., 2003).

6.3. The Lloyds River Fault Zone

6.3.1. Field description

The Lloyds River Fault Zone separates large ophiolite massifs of the Annieopsquotch ophiolite belt from the Dashwoods microcontinent and its Notre Dame Arc suprastructure to the northwest. It is dominated by intrusive rocks of the Pierre's Pond suite and Portage Lake monzogabbro, but contains significant amounts of amphibolites and less metamorphosed gabbros, which are relics of the Annieopsquotch ophiolite belt (Chapter 3). The Lloyds River Fault Zone is 10-15 km wide north of Lloyds Lake, but narrows considerably to the northeast and southwest, where the intrusive rocks are less abundant (Fig. 6.1). While deformation is distributed over the entire width of the zone, three major high-strain zones have been recognized, herein referred to as the southeastern, central and northwestern shear zones (Fig. 6.1). These shear zones are separated by relatively low-strain domains dominated by variably deformed and metamorphosed plutonic rocks. On the Lithoprobe seismic reflection profile, the Lloyds River Fault Zone appears as a northwest-dipping reflector that can be traced to c. 15 km depth (Fig. 6.2; van der Velden et al., 2004). At depth, the Lloyds River Fault Zone appears to be cut off by the Otter Brook Shear Zone, which emplaced the Annieopsquotch ophiolite belt over the slightly younger Lloyds River Complex of the Annieopsquotch Accretionary Tract (Chapter 5).

The southeastern shear zone delineates the northwestern margin of the main bodies of the Annieopsquotch and Star Lake ophiolites, and is marked by a zone at least several hundred meters thick of numerous, strongly foliated, narrow (c. 0.1-1 m) amphibolitic shear zones. These shear zones grade over short distances (c. 0.1 m) into less deformed and metamorphosed ophiolitic rocks, which in many places largely retain their igneous mineralogy. $^{40}Ar/^{39}Ar$ hornblende ages suggest the amphibolites formed and cooled below c. 550°C by c. 470 Ma (Chapter 5). Locally, the amphibolites are intruded by variably deformed veins and sheets of (quartz) diorite and associated tonalite. Where such intrusions occur, the amphibolites and intrusive rocks are generally strongly deformed, and intrusive veins are folded and deformed with the amphibolites (Fig. 6.3). The age (c. 459 Ma), arc-like geochemical signature, negative εNd, and the presence of inherited Paleoproterozoic zircons of the intrusions (Chapter 5) contrast with the host amphibolite, whose protolith is older (c. 480 Ma; Dunning and Krogh, 1985) and has a MORB-like, isotopically juvenile character (Chapter 3). These characteristics, as well as field constraints, indicate the diorite-tonalite sheets are small-scale offshoots of the Pierre's Pond suite (Chapter 5), the main members of which occur between the northwestern shear zone and central shear zone (Fig. 6.1). Around Star Lake, Pierre's Pond diorite-tonalite sheets are particularly abundant, and intruded outside the Lloyds River Fault Zone, directly into coarse- to very coarse-grained layered gabbro and pyroxenite cumulates of the Star Lake ophiolite (Fig. 6.4). The sheets are generally 30-100 cm wide, commonly have steep dips, and generally strike northeast-southwest. The diorites are highly strained, with strong foliations generally parallel to the margins of the sheets, and commonly contain intrafolially folded and boudinaged tonalite veins (Figures 6.4a, 6.5). The highly strained character of the diorites and tonalites is in sharp contrast with the generally undeformed nature of the host gabbros (Fig. 6.4b); only in a few outcrops are the host gabbros foliated as well. The host gabbros display relics of primary clinopyroxene ($En_{45-52}Fs_{7-8}Wo_{40-47}$) and plagioclase ($An_{84-98}$), that are partially replaced first by amphibolite-facies assemblages (hornblende rims around clinopyroxene) and then by randomly oriented greenschist-facies minerals such as actinolite, clinozoisite and chlorite (Table 6.1). This greenschist-grade metamorphic overprint is present only in the gabbros that occur near the intrusive sheets, and is absent in the rest of the Star Lake ophiolite. The undeformed nature, random orientation of the greenschist-facies minerals, and the preserved primary mineralogy suggest the metamorphic episode that affected the gabbros was static and relatively short lived. These relationships suggest the diorites and tonalites intruded into the gabbros, localizing deformation in the intrusive rocks, and triggering greenschist-facies contact metamorphism in the host gabbros. Since the diorite sheets also intrude into already deformed Lloyds River Fault Zone amphibolites, this strongly suggests that the diorites and tonalites intruded syn-kinematically into the Lloyds River Fault Zone after it had already accommodated movement at amphibolite-facies conditions. This is corroborated by (1) a U/Pb zircon SHRIMP age of 459±3 Ma for a diorite from a syn-kinematic sheet (Chapter 5), which is younger than the $^{40}Ar/^{39}Ar$ age of the Lloyds River Fault Zone amphibolites, and (2) evidence of magmatic deformation in the intrusive rocks (see below).

The central shear zone predominantly marks the boundary between the Portage Lake monzogabbro and the Pierre's Pond suite (Fig. 6.1). The Portage Lake monzogabbro is a variably deformed, elongate (c. 30x5 km), heterogeneous intrusive body that comprises an early fine-grained facies followed by a voluminous phase of K-feldspar phyric monzogabbro to monzodiorite. The monzogabbro is generally weakly deformed in the interior of the pluton. The K-feldspar phenocrysts characteristically have large aspect ratios (5-15), generally define a foliation, and are occasionally tiled (Fig. 6.6). In the weakly deformed part of the pluton, the phenocrysts have not recrystallized, occur within a little-deformed matrix and frequently define a shape fabric subparallel to the Lloyds River Fault Zone (see below). This suggests that the Portage Lake monzogabbro intruded syn-kinematically into the Lloyds River Fault Zone. This is consistent with the presence of a foliated amphibolite enclave within the Portage Lake monzogabbro, presumably derived from nearby Lloyds River Fault Zone amphibolites, with microstructures (see below), and with the high aspect ratio of the pluton. The northwestern margin of the pluton, along the central shear zone, is marked by an amphibolite-grade high strain zone of unknown thickness, which is dissected by several narrow (c. 25 cm wide) chlorite+epidote-bearing shear zones. This indicates that deformation localized along the pluton margin at lower temperatures.

The northwestern shear zone runs from King George IV Lake to northeast of Star Lake, and separates elongated bodies of variably metamorphosed ophiolitic gabbros and pyroxenites from the Dashwoods microcontinent and its Notre Dame Arc (Fig. 6.1). The northwestern shear zone is mostly marked by amphibolitesand amphibolitized gabbro. The amphibolites are best exposed northeast of King George IV Lake, where they form a mylonite zone that is at least 100 m thick. Locally the amphibolites contain clinopyroxene, which has straight, clean grain boundaries against hornblende and plagioclase, commonly with 120° angles, and has a composition distinct (i.e. higher Wo content) from primary clinopyroxene of Annieopsquotch gabbros. This indicates the clinopyroxene is of metamorphic origin. The amphibolites are intimately interlayered with veins and centimeter- to meter-wide sheets of highly deformed diorite and tonalite (Fig. 6.7). Based on geochemical data of the larger sheets the diorites and tonalites are correlated with the Pierre's Pond suite. Rare ultramafic rocks, enclosed within the amphibolites, were generally transformed into olivine-tremolite, talc-tremolite-chlorite and serpentine-talc assemblages.

West of Star Lake, ophiolitic gabbros along the northwestern shear zone are transformed into chloritic phyllonites with abundant quartz veins. This suggests that deformation on this part of the northwestern shear zone continued, or that it was reactivated, at lower temperature conditions. Since this contact also juxtaposes the Pierre's Pond suite with contrasting plutonic rocks of the Notre Dame Arc, its formation postdates the intrusion of the Pierre's Pond suite. The northwestern shear zone cannot be traced along its full length; north of Lloyds Lake it disappears within a large foliated tonalite body of the Notre Dame Arc and is cut by a large body of Silurian gabbro (Fig. 6.1). It is inferred that the northwestern shear zone was intruded by the voluminous Middle Ordovician tonalite phase of the Notre Dame Arc (Dunning et al., 1989), which distributed deformation over large areas (Fig. 6.1).

6.3.2. Kinematic interpretations

The foliation of the Lloyds River Fault Zone tectonites generally dips steeply to the northwest (Fig. 6.8a). Southeast-dipping foliations occur locally, but are restricted to a ~1 km long section of the northwestern shear zone northeast of King George IV Lake. Lineations on the northwest-dipping planes commonly plunge c. 40° to 60° to the north or northeast, while they plunge ~40° to 60° to the south on southeast-dipping planes (Fig. 6.8a). Considering the geometrical constraints imposed by the regional-scale, linear outcrop pattern of the faults (Fig. 6.1), as well as seismic interpretations (van der Velden et al., 2004), these data are most consistent with an overall northwest-dipping, shear zone-related foliation that is locally internally folded into steeply southeast-dipping orientations by tight, asymmetric macroscopic folds. The presence of macroscopic folds within the shear zones is consistent with their local occurrence on micro-and mesoscopic scale.

Shear sense indicators are best developed within the northwestern shear zone, where deformed diorite and tonalite are intimately interlayered with amphibolites, producing a gneissic layering. I excluded the section with southeast-dipping foliations from kinematic analysis. The obliquity of the instantaneous extension direction determined from late-kinematic stretched veins, and locally also by shear bands and asymmetrical boudinage, indicates that the Annieopsquotch ophiolite belt was thrust beneath the Dashwoods microcontinent (Fig. 6.7). This is in keeping with (1) the Z-asymmetry of intrafolial folds on vertical faces and the S-asymmetry of such folds on horizontal faces (Fig. 6.9, 6.10). The interlimb angle of these folds commonly changes rapidly along curviplanar axial surfaces (Figs. 6.9, 6.10), suggesting that they are drag folds with fold axes at a high angle to the lineation; (2) shear bands observed in amphibolites of the southeastern shear zone, which also indicate underthrusting of the Annieopsquotch ophiolite belt (Fig. 6.9). The north to northeast plunge of the lineations on the northwest-dipping foliation planes, combined with underthrusting of the Annieopsquotch ophiolite belt, suggests the Lloyds River Fault Zone also accommodated a sinistral strike slip component. Alternatively, the moderate to steep pitch of the stretching lineation could have formed in an oblique transpression zone with triclinic symmetry that mainly accommodated strike slip shear (Lin et al., 1998). However, a significant dip slip component is required to account for the great depth to which the Annieopsquotch ophiolite belt was transported (at least 33 km; exposed rocks represent a paleodepth of c. 18 km (see below) and the belt extends to c. 15 km depth (van der Velden et al., 2004)). Foliations within the Portage Lake monzogabbro (magmatic and solid-state) and Pierre's Pond suite (solid-state) dip to the northwest, similar to the foliation in the amphibolites (Fig. 6.8b). Foliations in the small diorite-tonalite sheets in the southeastern shear zone near Star Lake dominantly strike northeast-southwest, conform the general trend of the Lloyds River Fault Zone, but dip both northwest and southeast because they are generally parallel to the margins of the intrusions, which have somewhat variable orientations (Fig. 6.8c). The shear zones are generally steep, as are lineations defined by amphibole, suggesting a dominantly dip-slip motion (assuming monoclinic flow).

Sinistral oblique underthrusting of the Annieopsquotch ophiolite belt interpreted along the Lloyds River Fault Zone is consistent on a regional scale with (1) relationships along strike, where the northeasterly extension of the Lloyds River Fault Zone shows similar thrusting motion. The Hungry Mountain thrust (Fig. 6.1) records overthrusting of the Annieopsquotch Accretionary Tract by a hot amphibolite-facies thrust sheet comprising Notre Dame Arc diorites and tonalites (Thurlow, 1981; Thurlow et al., 1992; Calon and Green, 1987; Whalen et al., 1987). These tonalites contain numerous mafic to ultramafic enclaves which are interpreted as relics of the Annieopsquotch ophiolite belt (Whalen et al., 1997); (2) sinistral-oblique reverse motion documented for the Otter Brook Shear Zone (Zagorevski and van Staal, 2002), which bounds the Annieopsquotch ophiolite belt to the southeast, and is in part coeval with the Lloyds River Fault Zone (Chapter 5); (3) the Lithoprobe seismic reflection profile, which shows that the Annieopsquotch ophiolite belt extends underneath Dashwoods to c. 15 km depth (Fig. 6.2).

6.3.3. Microstructures

Tectonites of the Lloyds River Fault Zone preserve a variety of microstructures. Amphibolites are generally characterized by fine-grained hornblende and plagioclase. Locally, partially to completely recrystallizated aggregates of small metamorphic plagioclase (0.1-0.3 mm) have pseudomorphed igneous plagioclase laths. Most amphibolites have a single foliation defined by well developed shape and lattice preferred orientations of hornblende and to a lesser extent elongate plagioclase aggregates (Fig. 6.11a). Highly strained amphibolites are generally marked by strong grain size reduction and elongation (hornblende with aspect ratios up to 15; Fig 11a) compared to less strained rocks. Relic large plagioclase crystals behaved as rigid objects wrapped by the foliation. Locally the amphibolites show a crenulation cleavage, with the younger schistosity axial planar to open to tight microfolds developed in the older hornblende schistosity. Euhedral hornblende crystals (generally 0.5-1 mm) have overgrown both foliations, suggesting shear zone development, folding and development of a transposition foliation took place under amphibolite-facies conditions, consistent with them forming part of a progressive deformation that is preferentially localized in the shear zones. Hornblende porphyroclasts in the relatively low strain domains show subgrains and tails comprising fine grained aggregates of new grains (Fig. 6.11b), suggesting that rotation recrystallization (Urai et al., 1986) together with new grain growth contributed to the foliation development in the shear zones. Some amphibolites in contact with intrusive sheets experienced high degrees of deformation. These amphibolites have a strong foliation, defined by long axes of amphiboles, which is locally folded with intrusive tonalite (Fig. 6.11c). While most amphibolites retain their shape-preferred orientation, feldspars within some samples have been partly to completely recrystallized into polygonal aggregates with 120° grain boundaries. This suggests that temperatures remained high in these rocks or that they experienced reheating after deformation had ceased.

The Portage Lake monzogabbro preserves a range of deformation states from near-magmatic to completely recrystallized in the solid state. Samples with limited solid-state deformation preserve aligned K-feldspar phenocrysts (up to 2 cm long) with high aspect ratios (up to 6) that are recrystallized only along their margins. Internally, the phenocrysts are undeformed, preserve Carlsbad twins, lack microcline twinning, and enclose euhedral hornblende. The phenocrysts are set in a hornblende+feldspar+biotite matrix that lacks shape-preferred orientations, and preserves euhedral hornblende crystals (Fig. 6.11d). These features suggest K-feldspar fabric development during deformation in the magmatic state (Vernon, 2000). Extensive solid-state deformation has led to complete recrystallization of phenocrysts into fine-grained K-feldspar aggregates in most samples.

The diorites and tonalites that have intruded the ophiolitic gabbros around Star Lake generally show large degrees of solid-state deformation characterized by strong shape-preferred orientations, grain size reduction, formation of S-C fabrics, and foliation that wraps around large, partially recrystallized relic igneous plagioclase crystals that are now best described as porphyroclasts. Foliations in these rocks are generally defined by aligned biotite and hornblende, and to a lesser extent elongate plagioclase ± quartz aggregates. In some samples this foliation is overprinted by shear bands mainly defined by chlorite and/or epidote. Nevertheless, evidence for deformation occurring while the rock was still partially in a magmatic state appears to be locally preserved in the syn-kinematic intrusions. Tightly to isoclinally folded tonalite veins in strongly foliated diorite (Fig. 6.11e) contain elongate plagioclase grains that can be traced around the fold hinges, yet have locally preserved oscillatory zoning, and show only little to moderate recrystallization only along their grain boundaries, despite showing abundant deformation twinning (Fig. 6.11f). Quartz grains are generally equidimensional with minor subgrain formation and recrystallization. This contrast with the hornblende-plagioclase fabric in the host diorite, which displays a strong hornblende-defined fabric tracing the fold hinges. The preservation of primary igneous textures such as oscillatory zoning within aligned plagioclase displaying little internal strain besides twinning, suggest that fabric formation in the folded tonalite veins did not occur entirely by solid-state deformation, but probably started in the magmatic state.

6.4. Pressure-temperature conditions

6.4.1. Analytical techniques

Mineral compositions were analyzed by electron microprobe at the Geological Survey of Canada (Ottawa) using a wavelength-dispersive Cameca SX-50, a mixture of natural and synthetic standards, and ZAF matrix correction procedures described by Armstrong (1988). Accelerating voltage and beam current were 20 kV and 10nA, respectively, and counting time was 15 seconds. Olivine and pyroxene were analyzed with a focused beam, plagioclase and amphibole with a 10µm beam spot. Compositions are listed in Tables 6.1 (amphibole), 6.2 (plagioclase), and 6.3 (clinopyroxene and olivine).

6.4.2. Geothermobarometry

Temperature constraints on accretion of the Annieopsquotch ophiolite belt are provided by the amphibolites that mark the southeastern shear zone and northwestern shear zone (Fig. 6.1). The amphibolites are commonly composed of magnesiohornblende and plagioclase (typically $An_{45\text{-}55}$; Tables 6.1 and 6.2) that define the main foliation of the shear zones. Grain boundaries are generally straight, clean, and lack evidence for reaction or alteration, suggesting they were in equilibrium. In some samples, plagioclase displays reverse zoning, with highly saussuritized cores with anorthite contents up to 69 to fresh rims with anorthite contents of c. 50. This may result from partial reequilibration of primary high-An cumulus crystals during metamorphism. In other samples, normal zoning is marked by cores of oligoclase (An_{14}) with epidote inclusions rimmed by zoned plagioclase ($An_{47\text{-}56}$), and actinolite cores rimmed by magnesiohornblende with increasing Al content towards the rim. I interpret the oligoclase and actinolite cores as prograde mineral compositions, recording early greenschist-facies metamorphism partially overprinted by amphibolite-facies assemblages.

Hornblende-plagioclase thermometry (edenite+albite=richterite+anorthite; Holland and Blundy, 1994) using rim compositions of three amphibolites indicates temperatures of 778°C to 826°C, with an average of 806°C (assuming P=5 kbar). The different temperatures result from small compositional variations in plagioclase (±4 mole % An) and amphibole (±0.09 Al^T and ±0.04 Na), but fall within the uncertainty of the thermometer (±40°C; Holland and Blundy, 1994). Despite the high temperatures, (metamorphic) clinopyroxene is absent in all but one of the amphibolites. This likely results from (1) the quartz undersaturated nature of the rocks, which increases the stability field of hornblende such that the cpx-in reaction lies at c. 800°C at P>2 kbar and fO_2=QFM (Spear, 1981); (2) the high Mg# of the amphibole (average 76), which suppresses the appearance of pyroxene to higher temperatures (Spear, 1981); and (3) high P_{H2O} within the shear zone, which has a stabilizing effect on hornblende.

Additional constraints on the temperatures recorded by the amphibolites are provided by a metadunite, composed of olivine and a small amount of acicular tremolite, which is enclosed within metagabbros of the northwestern shear zone. Olivine ($Fo_{86\text{-}87}$; Table 6.3) in the metadunite is unzoned to very weakly zoned, and, whereas tremolite shows increasing Al-contents towards the rim, its Mg# remains essentially constant (Mg#=0.94-0.96; Table 6.1). Fe-Mg exchange between the olivine and tremolite, calculated using WinTWQ (Berman, 1988, 1991; Mader and Berman, 1992) indicates temperatures between 740-780°C. These temperatures support the upper amphibolte-facies temperatures derived from the amphibolites.

Pressure constraints are provided by a clinopyroxene-bearing amphibolite from the northwestern shear zone. It is composed of magnesiohornblende-diopside ($En_{38\text{-}42}Wo_{49\text{-}50}Fs_{9\text{-}13}$; Table 6.3)-calcic plagioclase ($An_{85\text{-}94}$). Pressure conditions during this event are estimated by intersecting the hornblende-plagioclase thermometer (Holland and Blundy, 1994) with reactions between hornblende, plagioclase and clinopyroxene calculated using WinTWQ. I used the reaction 5 Fe-tschermakite + 8 diopside + 2 albite = 8 anorthite + 3 Fe-tremolite + 2 pargasite, since this reaction: (1) has the largest ΔV, and is thus most pressure sensitive; (2) has diopside as the only pyroxene end member, and should be more robust since the activity of diopside is much larger than that of hedenbergite in the pyroxenes analyzed; (3) has pargasite as an amphibole end member, which is thermodynamically better characterized than the Fe-pargasite endmember used in other reactions. The intersection between the hornblende-plagioclase-clinopyroxene reaction described above and the hornblende-plagioclase thermometer suggest the amphibolite was equilibrated at ~790° and 6 kbar (Fig. 6.12). The uncertainty of P as a result of compositional heterogeneity and analytical uncertainty was estimated by varying mineral compositions: varying Mg/Fe contents of clinopyroxene+amphibole and An content of plagioclase by 4 mole % indicates the uncertainty is ~1.5 kbar.

High temperature conditions similar to those of the amphibolites are recorded within samples of the Portage Lake monzogabbro and Pierre's Pond suite that have been deformed in the solid state. Amphiboles in the Portage Lake monzogabbro have Si contents around 1.5 and A-site occupancy around 0.5, defining the amphiboles as edenite, tschermakite, magnesiohornblende, and magnesiohastingsite (cf. Leake et al., 1997). Some amphiboles are subtly zoned from edenitic cores to magnesiohastingsite or magnesiohornblende rims. Plagioclase is ~An_{45} in cores, and An_{40} in rims and small matrix grains. K-feldspar is generally Or_{88-90}, but small grains and rims have orthoclase contents up to 94. This suggests minor reequilibration of hornblende, plagioclase and K-feldspar occurred. Therefore, core compositions have been used for geothermometry. Hornblende-plagioclase thermometry of core compositions yielded temperatures between 757-781°C, with an average of 770°C (assuming P=5 kbar). Rim compositions yielded temperatures within error (±40°C) of the core composition temperatures. Two-feldspar thermometry (Fuhrmann and Lindsley, 1988) yields lower temperatures, due to low orthoclase activity in plagioclase and low anorthite activity in K-feldspar, suggesting that these feldspars reequilibrated at lower temperatures. These lower temperatures can be explained by up to 4 mole % K-Na exchange between the two feldspars. I note that reequilibration of 4 mole % Na changes the results of the hornblende-plagioclase temperatures by only 10°, well within the uncertainty involved in the thermometer (±40°C; Holland and Blundy, 1994).

Hornblende from the Pierre's Pond suite diorites is weakly zoned magnesiohornblende to tschermakite, and plagioclase compositions are An_{48-50} in cores, ranging to An_{44} in rims (Tables 6.1-6.2) The Holland and Blundy (1994) geothermometer, using core compositions, indicates the diorites were deformed at temperatures of 735-765°C (average 748°C, assuming P=5 kbar). Rim compositions yielded temperatures within error (±40°C) to slightly lower temperatures (~700°C). Deformation in the Portage Lake monzogabbro and Pierre's Pond suite continued at lower temperature, indicated by actinolite and albite rims on some grains and the formation of cleavage planes marked by greenschist-facies minerals (chlorite+epidote) in some samples.

6.5. Synthesis and discussion

6.5.1. Structural evolution of the Lloyds River Fault Zone

The data presented in this chapter, combined with the geochronological data presented in Chapter 5, allow the structural evolution of the Lloyds River Fault Zone to be reconstructed in some detail. The structures and mineral compositions of the amphibolites indicate that the Lloyds River Fault Zone records undertrusting of the Annieopsquotch ophiolite belt beneath the Dashwoods microcontinent at temperatures of c. 800°C and at 6 kbar. Underthrusting is consistent with both interpretations of seismic data and structural relationships along strike to the northwest of the study area (Dean and Strong, 1977; Thurlow et al., 1992; van der Velden et al., 2004), and was thus a regional tectonic phenomenon. Formation of the Lloyds River Fault Zone during convergence between the Annieopsquotch ophiolite belt and the Dashwoods microcontinent probably started in response to a plate reorganization following the collision between the Dashwoods microcontinent and the Laurentian margin, which had started by at least by c. 475 Ma (Waldron and van Staal, 2001; van Staal et al., 2003; Chapter 5). Such a tectonic scenario is consistent with the $^{40}Ar/^{39}Ar$ ages, which suggest that underthrusting must have started prior to c. 471 Ma, when the rocks cooled below ~550°C (Chapter 5).

Both the preservation of high-temperature fabrics and old cooling ages within Lloyds River Fault Zone amphibolites indicate that, after 471 Ma, movement on the fault zone was either localized under lower temperature conditions (<550°C) in narrow shear zone segments currently not preserved as a result of assimilation into syn-kinematic intrusions, or that movements had ceased all together. However, a renewed phase of high temperature deformation must have taken place at least locally at c. 462 Ma when the Portage Lake monzogabbro intruded into the Lloyds River Fault Zone, which significantly weakened the shear zone. Deformation was initially localized within the weak, not yet completely solidified pluton, leading to the magmatic alignment of K-feldspar phenocrysts subparallel to Lloyds River Fault Zone, before an episode of solid-state deformation. The high temperatures recorded by the metamorphic mineral assemblages in the core of the pluton (c. 770°C), and the local preservation of magmatic fabrics, suggest this episode was relatively short lived. Solid-state deformation continued along the pluton margin at lower temperatures, forming a narrow zone of epidote-chlorite mylonite.

At c. 459 Ma, the diorites and subordinate tonalites of the Pierre's Pond suite intruded into the Lloyds River Fault Zone. On a large scale, this magmatism is expressed by the elongated diorite-tonalite sheet that occurs between the northwestern shear zone and central shear zone. On a small scale, the Pierre's Pond suite formed decameter- to meter-sized intrusive sheets and veins within the amphibolites, and intruded the underformed ophiolitic gabbros near Star Lake (Chapter 5). Like the Portage Lake monzogabbro, the intrusive rocks localized deformation. Most amphibolites experienced a renewed episode of deformation to form the amphibolite-diorite-tonalite tectonites. Where the diorites and tonalites intruded directly into gabbros, they were highly deformed while the gabbros underwent mainly static contact metamorphism. This is indicated by the large deformation contrast between the highly strained diorites and the undeformed, contact metamorphosed host gabbros, as well as the microstructures indicative of magmatic deformation. The greenschist grade of the contact metamorphism and preservation of high temperatures in the diorites (~750°C) suggests the regional ambient temperature of the Lloyds River Fault Zone during intrusion was relatively low. Locally, deformation in the Pierre's Pond suite continued at greenschist-facies conditions, indicated by growth of epidote+chlorite along cleavage planes.

In summary, the Lloyds River Fault Zone thus records the high-temperature sinistral oblique accretion of the Annieopsquotch ophiolite belt to the Dashwoods block, and subsequent periodic high-temperature reactivation triggered by the intrusion of plutons. Reactivation occurred along the majority of the Lloyds River Fault Zone within the study area, and led to the formation of most of the Lloyds River Fault Zone mylonites. Intrusion of the plutons locally caused an increase in the geothermal gradient, but on a regional scale temperatures were already significantly lower (<550°C) than the c. 800°C accompanying the initial accretionary event prior to 471 Ma.

Final movements in the Lloyds River Fault Zone are marked by chloritic phyllonites that occur along part of the northwestern shear zone. The segment where this brittle-ductile deformation has been observed coincides with the part of the northwestern shear zone that appears to be connected to the Little Grand Lake Fault, which separates the Dashwoods and Notre Dame subzones (Brem et al., 2003) (see inset Fig. 6.1). The Little Grand Lake Fault was reactivated, presumably in the Silurian, at shallow crustal levels after Early-Middle Ordovician ductile movement (Brem et al., 2003). Consequently, I infer that part of the northwestern shear zone and the Little Grand Lake Fault were reactivated together. Finally, the Lloyds River Fault Zone was stitched by Early Silurian plutons.

6.5.2. Heat source during initial accretion

Rocks in accretionary complexes are generally subject to high-P, low-T metamorphism since isotherms are depressed by subduction of cool lithosphere. While the Annieopsquotch ophiolite belt occurs in an accretionary setting, and marks the subduction of infant arc lithosphere, it was metamorphosed at high T (~800°C) and at moderate pressures (~6 kbar) during its initial accretion to the Dashwoods microcontinent. A likely explanation for these elevated temperatures lies in the fact that Dashwoods was basement to the Notre Dame Arc after 488 Ma (Dubé et al., 1996), and hence was characterized by a high geothermal gradient when it was thrust over the Annieopsquotch ophiolite belt. An inverted geothermal gradient beneath the overriding Dashwoods led to high-temperature metamorphism along the Lloyds River Fault Zone, which, prior to the intrusion of the Portage Lake monzogabbro and Pierre's Pond suite, was likely significantly narrower that its current width. The temperature gradient underneath the thrust was likely sharp and the thermal pulse short-lived, which may explain the preservation of seafloor-spreading related features within the interior of the Annieopsquotch ophiolite (Dunning, 1987; Chapter 4) and the preserved prograde zoning in some amphibolites. This scenario is consistent with relationships along the Hungry Mountain thrust, which forms part of Lloyds River Fault Zone-related faults further to the north and accommodated overthrusting of the Buchans Group by a hot sheet comprising plutonic rocks of the Hungry Mountain Complex (Thurlow, 1981). Thrusting led to an inverted metamorphic gradient with amphibolite-facies metamorphism immediately beneath the thrust to (sub)greenschist-facies metamorphism at structurally deeper levels (Thurlow, 1981). Hence thrusting must have occurred shortly after crystallization of the Hungry Mountain Complex (467±8 Ma; Whalen et al., 1987). Thrusting was probably coeval with movements in the Lloyds River Fault Zone, but due to the large error on the age of the Hungry Mountain Complex the initiation of thrusting is at present not as well constrained as in the Lloyds River Fault Zone.

6.5.3. Feedback between deformation and magmatism

While part of the amphibolites were metamorphosed and deformed synchronously with intrusion of the c. 459 Ma Pierre's Pond suite, as is evidenced by the amphibolite-diorite-tonalite tectonites that mark segments of the northwestern shear zone and southeastern shear zone (Figs. 6.3, 6.8, 6.10, 6.11b), several arguments presented below suggest that the Lloyds River Fault Zone was already active when the Portage Lake monzogabbro and Pierre's Pond suite intruded: (1) The cooling age of the amphibolite bounding the Star Lake ophiolite (471±5 Ma) and the crystallization age of the Portage Lake monzogabbro (462±2Ma) and Pierre's Pond suite (459±3 Ma) can be distinguished at the 2σ level. While the cooling age of the amphibolite bounding the Annieopsquotch ophiolite (468±6 Ma) overlaps with the age of the Portage Lake monzogabbro, the probability of overlap is very low (0.001). This suggest that this amphibolite preserves the age of initial underthrusting, rather than a thermal pulse associated with the intrusion of the Portage Lake monzogabbro; (2) The Pierre's Pond suite and the c. 468 Ma Otter Pond suite, which both intrude the Annieopsquotch ophiolite, have geochemical and isotopic signatures as, well as inherited zircon, that require a component of crustal assimilation in their petrogenesis (Chapter 5). Hence, the Annieopsquotch ophiolite belt was already accreted to Dashwoods prior to this magmatism; (3) The Portage Lake monzogabbro has a high aspect ratio, consistent with intrusion along a preexisting structural anisotropy.

Hence, I conclude that the Lloyds River Fault Zone was already active prior to intrusion of the Portage Lake monzogabbro and Pierre's Pond suite, and served as a guide for the ascending magmas. However, the presence of melt sparked renewed high-temperature deformation, recorded in the magmatic fabrics of both plutonic suites, and caused thermal softening of the fault zone, leading to high-temperature solid-state deformation. This deformation was localized mostly within the plutonic rocks themselves and the immediately adjacent amphibolites; the preservation of the older Ar/Ar ages indicate that amphibolites further removed from the plutons were not deformed during this episode. Continued solid-state deformation within the plutons, but not in the amphibolites, is consistent with the rheologically weaker nature of the hot quartz-biotite bearing plutons relative to the already cooled amphibolites (cf. Pavlis, 1996).

In the Lloyds River Fault Zone, establishment of the shear zone thus preceded magmatism, but a positive feedback occurred between deformation and magmatism. Similar relationships have been documented elsewhere (e.g., Davidson et al., 1992; de Saint Blanquat et al., 1998; Moyen et al., 2003). In the periphery of the Lloyds River Fault Zone, however, magmatism appears to have triggered formation of new shear zones; the small-scale diorite-tonalite offshoots of the Pierre's Pond suite sheets around Star Lake are highly deformed at amphibolite-facies conditions, while their host gabbros remain undeformed and are subject to greenschist-grade contact metamorphism, suggesting deformation nucleated within the intrusive rocks. Thus while the main pluton intruded into a shear zone, its offshoots intruded outside the shear zone and initiated the formation of new small-scale shear zones. Deformation, magmatism and metamorphism were thus intimately related, and, while deformation generally preceded intrusion, locally magmatism preceded deformation. Both endmembers may thus operate simultaneously within a single fault system.

Whereas a positive feedback between shear zones and magma ascent is generally accepted, there has been debate as to whether shear zones provide space for pluton emplacement (e.g., Hutton, 1990; Karlstrom, 1989; Paterson, 1989; Tikoff and Teyssier, 1992). In the Lloyds River Fault Zone, there is a positive relationship between the presence of plutons and shear zone width; the Lloyds River Fault Zone is wide in its center, where the Portage Lake monzogabbro and Pierre's Pond suite are most abundant, but is considerably narrower to the northeast and southwest, where the Portage Lake monzogabbro is absent and Pierre's Pond suite less abundant (Figure 1). Whereas it could be argued that the along-strike thinning of the Pierre's Pond suite is in part due to translation during deformation, the absence of the Portage Lake monzogabbro in the narrower segments suggests at least part of the observed variability is primary. The Pierre's Pond suite contains several map-scale blocks of ophiolitic gabbros, suggesting emplacement at least in part occurred by stoping. However, it is striking that the plutons are thickest in the segment where the generally northeast striking Lloyds River Fault Zone curves to the south (Fig. 6.1), which may suggest they were preferentially emplaced in a dilational jog created during sinistral oblique movement (cf. Hutton, 1988). Whereas we do not have enough data to reconstruct in detail the relative importance of stoping, floor subsidence, and roof uplift within the Lloyds River Fault Zone, the fault zone thus may have played an active role in creating space for pluton emplacement.

6.6. Conclusion

The Lloyds River Fault Zone comprises amphibolites that accommodated sinistral-oblique underthrusting of the Annieopsquotch ophiolite belt beneath the Dashwoods microcontinent, and two suites of plutonic rocks. The amphibolites formed during initial accretion (>471 Ma) of the ophiolites at high temperatures (c. 800°C) and pressures of c. 6 kbar. The Lloyds River Fault Zone was intruded syn-kinematically by the c. 462 Ma Portage Lake monzogabbro and c. 459 Ma Pierre's Pond suite. Intrusion localized deformation in the plutonic rocks, initially in the magmatic state but also at high-temperatures in the solid-state during cooling (c. 770-750°C). The current configuration of the Lloyds River Fault Zone thus results from a positive feedback between deformation and magmatism. However, offshoots of the Pierre's Pond suite that intruded unfoliated gabbro initiated formation of small-scale shear zones. This illustrates that channeling of plutons into shear zones and nucleation of shear zones in melt-rich zones may occur simultaneously within the same fault system. Since accretionary complexes are commonly intruded by plutons as a result of hinge retreat, this type of structural evolution may characterize many accretionary margins, indicating that plutons may significantly facilitate the transfer of oceanic material to continents.

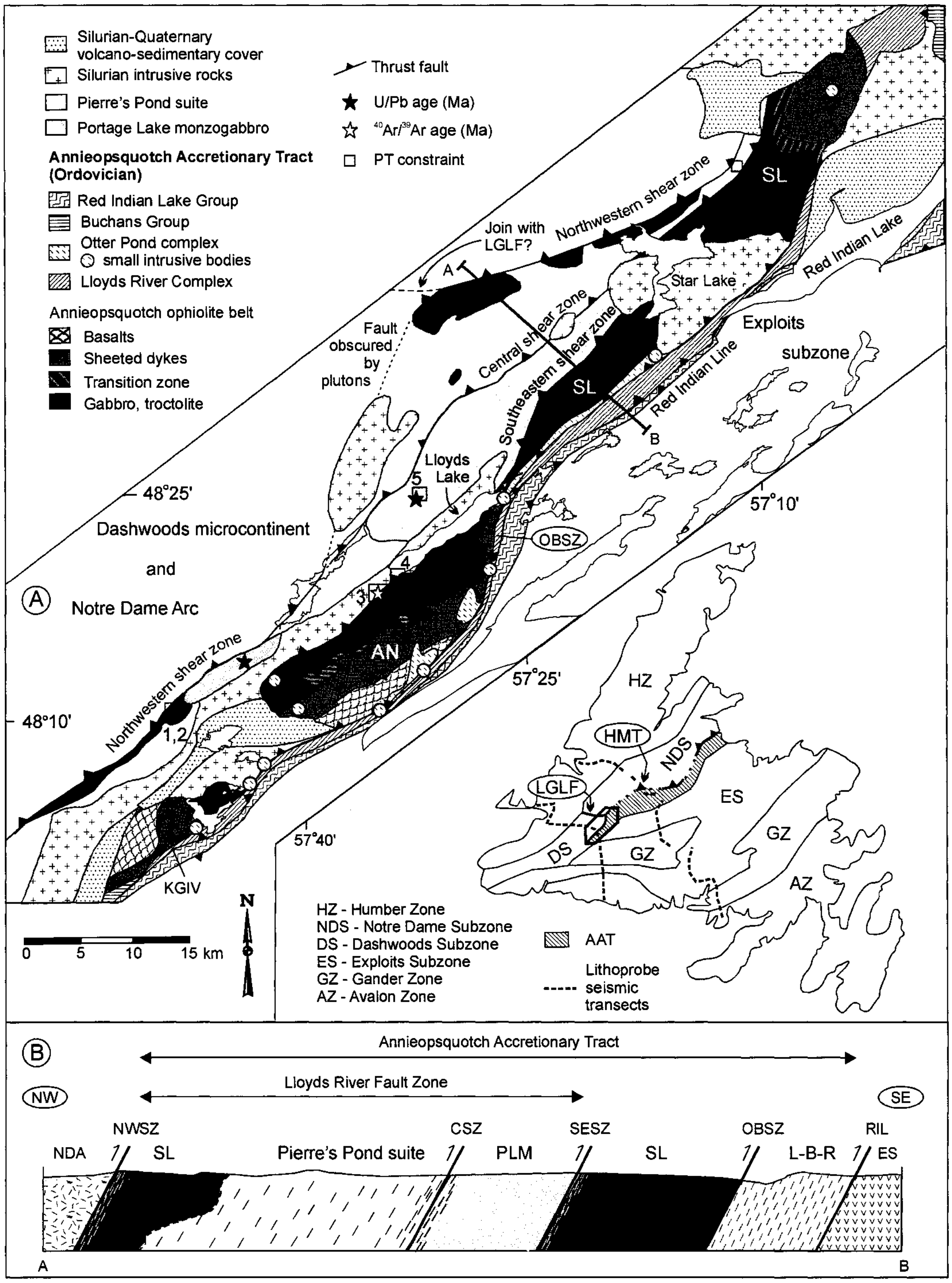

Figure 6.1: a) Simplified geological map of the Annieopsquotch Accretionary Tract (AAT), modified from Lissenberg et al. (in press) and van Staal et al. (in press a,b,c), showing the Lloyds River Fault Zone and the locations of samples used for geothermobarometry (numbers correspond to Tables 6.1-6.3). Inset shows location of the study area, Hungry Mountain Thrust (HMT), Little Grand Lake Fault (LGLF) and Lithoprobe seismic reflection profiles, as well as the extent of the Annieopsquotch Accretionary Tract. Ages discussed in this chapter are marked by black (U/Pb) and white (Ar/Ar) stars (from Chapter 5). b) Cross section through the Annieopsquotch Accretionary Tract (no vertical exaggeration). An=Annieopsquotch ophiolite; CSZ=central shear zone; ES=Exploits Subzone; KGIV=King George IV ophiolite; L-B-R=Lloyds River Complex+Buchans Group+Red Indian Lake Group; NDA=Notre Dame Arc; NWSZ=northwestern shear zone; OBSZ=Otter Brook shear zone; PLM=Portage Lake monzogabbro; RIL=Red Indian Line; SESZ=southeastern shear zone; SL=Star Lake ophiolite

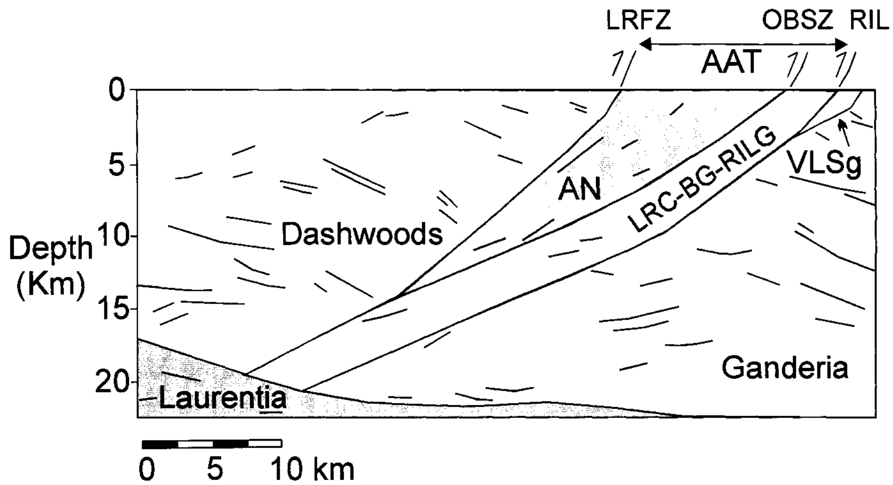

Figure 6.2: Schematic results of the Burgeo Lithoprobe seismic transect through southwestern Newfoundland, modified from van der Velden et al. (2004). Lines mark orientations of major reflectors. See Fig. 6.1 for location. AAT=Annieopsquotch Accretionary Tract; AN=Annieopsquotch ophiolite; LRC-BG-RILG=Lloyds River Complex, Buchans Group and Red Indian Lake Group; LRFZ= Lloyds River Fault Zone; OBSZ=Otter Brook Shear Zone; RIL=Red Indian Line; VLSg=Victoria Lake Supergroup.

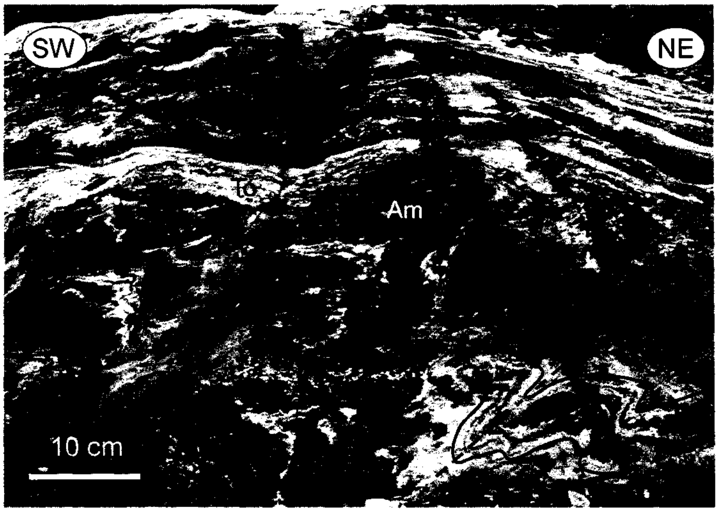

Figure 6.3: Highly strained amphibolite-tonalite mylonite of the southeastern shear zone (top) grades into less well foliated amphibolite-tonalite tectonite (bottom). Note presence of folds in bottom right corner. Am=amphibolite; To=tonalite.

Figure 6.4: a) Typical occurrence of Pierre's Pond intrusive sheets around Star Lake. Deformation is localized in decameter- to meter-wide diorites (D) and subordinate tonalites (T) that intrude gabbro (G) with igneous layering of the Star Lake ophiolite. Diorites contain relatively undeformed gabbro boudins, and tonalite veins are stretched and folded. b) Close-up of the contact between ophiolitic gabbro and intrusive mylonitized diorite and tonalite (DTM) that grades into less deformed diorite (D). The large deformation contrast between the host gabbro and the diorite-tonalite mylonite suggests deformation localized in the diorites during syn-kinematic intrusion in the Lloyds River Fault Zone. Static greenschist-facies metamorphism in the gabbros is thought to result from contact metamorphism by the intrusive rocks.

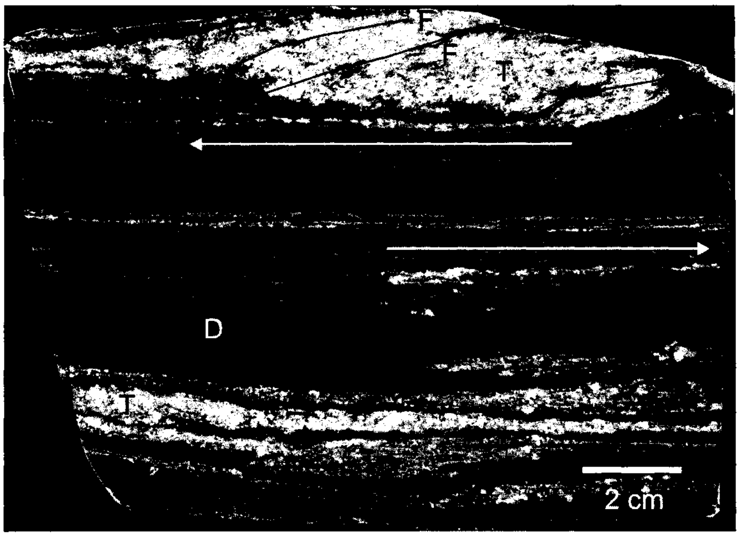

Figure 6.5: Polished hand sample of mylonitic Pierre's Pond suite diorite and tonalite from Star Lake, illustrating highly strained character of the diorite (D) and tonalite (T). Note folding (F) and stretching (arrows) of tonalite veins within the foliation planes.

Figure 6.6: Foliation defined by K-feldspar phenocrysts with high aspect ratios in the Portage Lake monzogabbro. Note tiling of the phenocrysts (circled) and the low strain recorded in the matrix, indicative of deformation in the magmatic state.

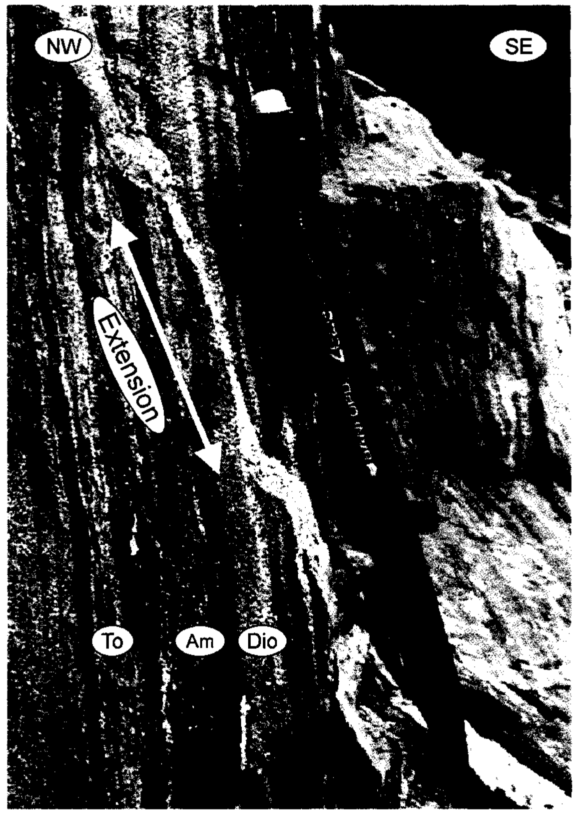

Figure 6.7: Typical gneissic tectonite of the northwestern shear zone, comprised of amphibolite (Am), diorite (Dio) and tonalite (To). Stretching of late-kinematic felsic vein suggests the Annieopsquotch ophiolite belt, to the southeast, was moving down with respect to the Dashwoods microcontinent to the northwest. Vertical face, looking NE.

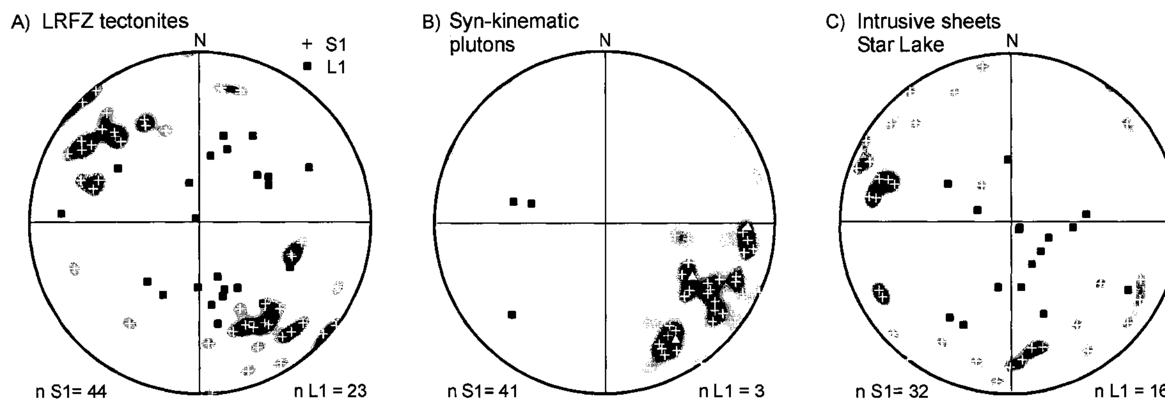

Figure 6.8: Lower hemisphere equal area plots of structures of the Lloyds River Fault Zone. a) Foliation (crosses) and lineation (squares) of Lloyds River Fault Zone tectonites. b) Foliation and lineation in syn-kinematic intrusive sheets. Magmatic foliation of the Portage Lake monzogabbro is indicated by triangles. c) Foliation and lineation of diorite-tonalite hosted shear zones around Star Lake.

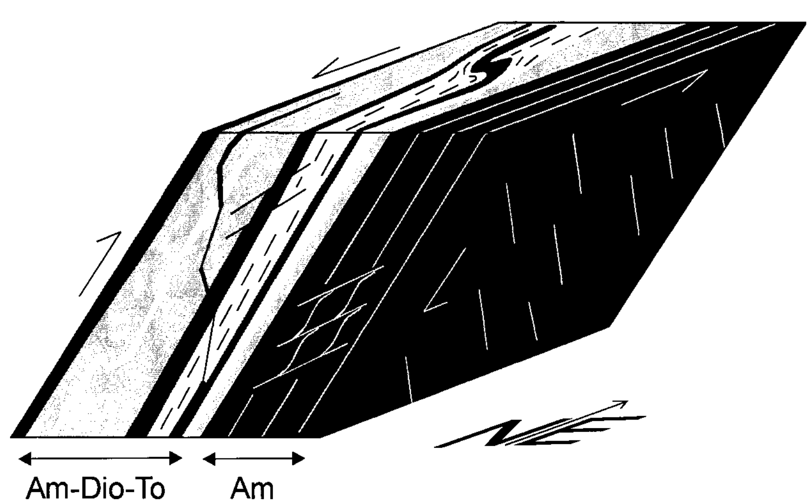

Figure 6.9: Schematic block diagram summarizing the various structures observed within amphibolites (Am; dark grey) and amphibolite-diorite-tonalite (Am-Dio-To; dark grey, light grey and white, respectively) tectonites of the Lloyds River Fault Zone. Stretched late-kinematic vein is indicated in black.

Figure 6.10: Intrafolial fold in amphibolite (Am)-tonalite (To) tectonite of the northwestern shear zone changes from tight (in center) to open (in top left corner), suggesting it formed by sinistral drag. Horizontal plane.

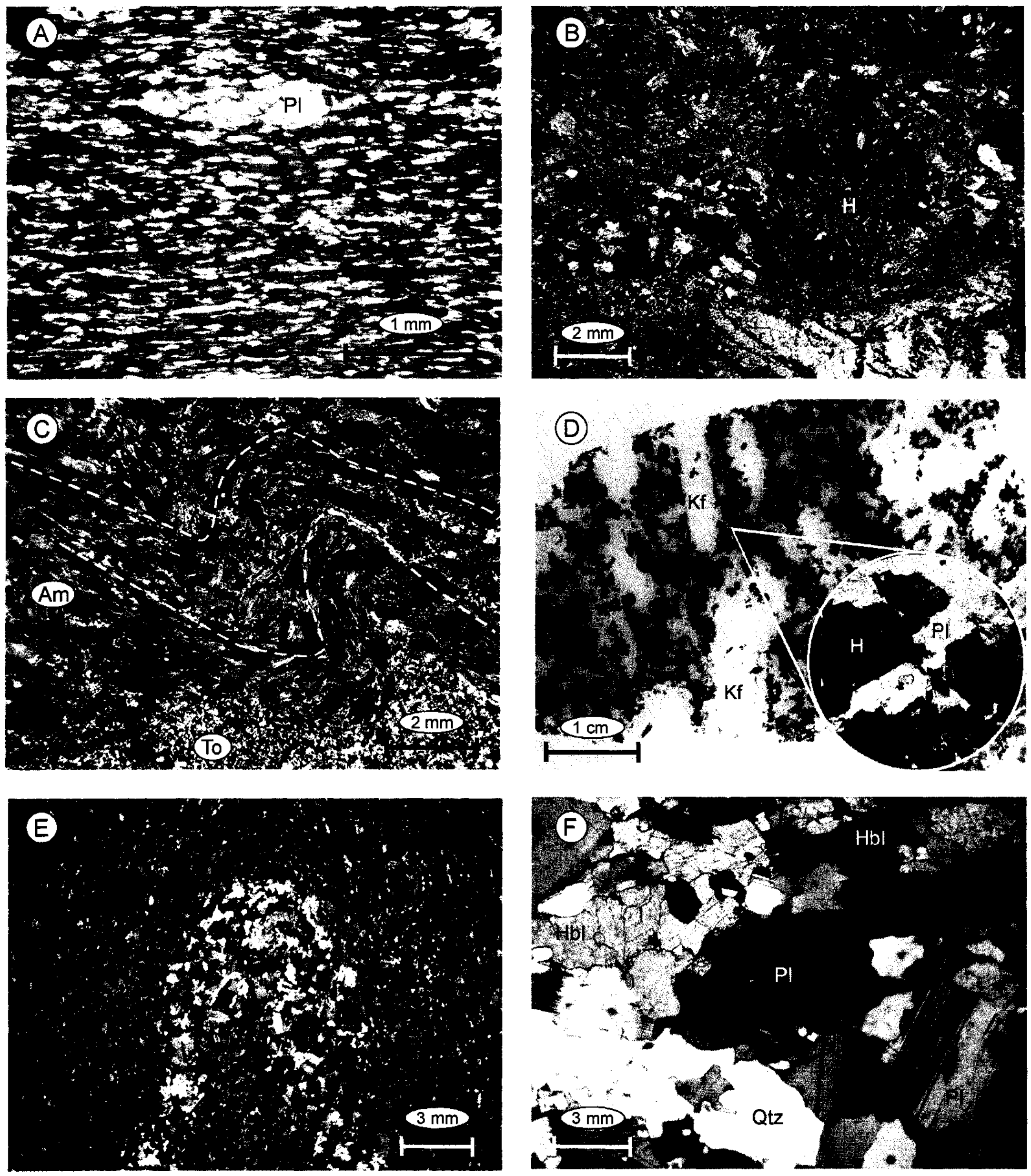

Figure 6.11: Photomicrographs of microstructures in amphibolites and syn-kinematic plutons of the Lloyds River Fault Zone. a) Highly strained amphibolite shows extreme grain size reduction and stretching, yielding highly elongate hornblende and plagioclase. A relic large plagioclase grain (Pl) serves as relatively rigid object, and is recrystallized into small grains. Plane polarized light. b) Hornblende porphyroclast (H) with tail of recrystallized hornblende grains. Crossed polars c). Folded amphibolite (Am)-tonalite (To) tectonite. Crossed polars. d) The Portage Lake monzogabbro shows parallel K-feldspar phenocrysts (Kf) that define a foliation (vertical) within a matrix that lacks shape-preferred orientations, and preserves euhedral hornblende (inset). Plane polarized light. e) Folded tonalite vein in diorite. Crossed polars. f) Close-up of tonalite vein of (e), showing oscillatory zoning in plagioclase (Pl) and limited solid-state deformation within the plagioclase (Pl)-quartz (Qtz)-hornblende (Hbl) matrix. Crossed polars.

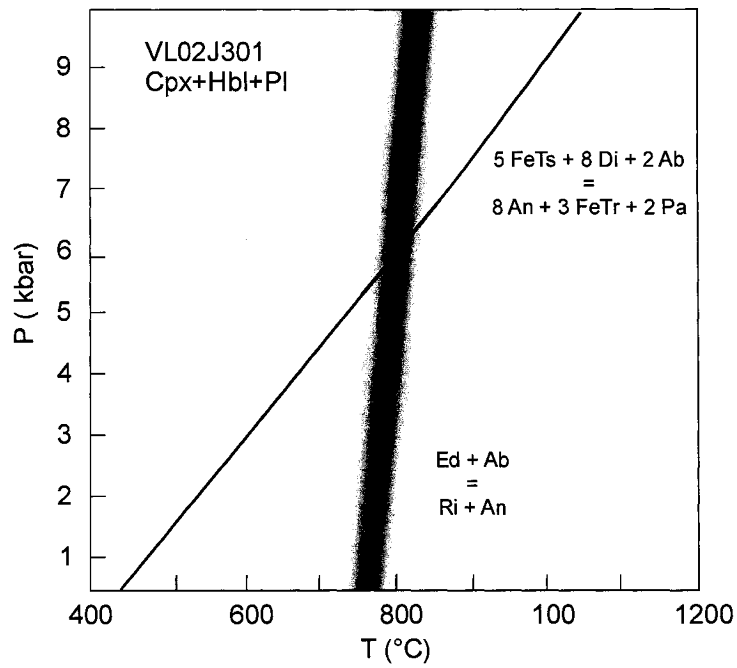

Figure 6.12: Diagram illustrating PT conditions calculated from amphibolite VL02J301. Grey field represents uncertainty of the amphibole-plagioclase thermometer.

Table 6.1: Amphibole compositions of the Lloyds River Fault Zone

	Gabbro Star Lake		Amphibolites														Portage Lake Monzogabbro							
Sample[1]	238-7	225-3	178-1	178-3	178-3	178-3	178-4	178-7	261-1	261-2	261-3	261-4	301-1	301-1	301-1	301-1	223-1	223-1	223-1	223-1	223-2	223-2	223-3	223-3
			Rim	Core	Int	Rim	Rim	Rim	Rim	Rim	Rim	Rim	Core	Int	Int	Rim	Core	Int	Int	Rim	Core	Rim	Core	Rim
Location[2]			4	4	4	4	4	4	3	3	3	3	2	2	2	2	5	5	5	5	5	5	5	5
SiO_2	56.02	56.53	43.67	51.11	53.29	44.82	45.41	45.87	45.80	46.55	46.98	46.67	47.18	46.60	47.16	47.06	43.27	44.14	43.77	43.56	42.87	41.60	43.32	43.54
AL_2O_3	1.27	0.81	8.65	3.89	3.82	8.29	8.31	7.90	8.19	7.62	7.30	7.54	8.55	8.38	8.19	8.36	9.68	8.58	8.96	9.79	9.55	10.18	9.00	8.73
TiO_2	0.00	0.00	0.95	0.37	0.38	0.82	0.79	0.69	0.93	0.98	0.92	0.89	0.74	0.79	0.68	0.67	1.05	0.91	0.92	0.61	0.88	1.33	0.98	0.96
Cr_2O_3	0.04	0.03	0.00	0.09	0.00	0.00	0.06	0.02	0.03	0.03	0.10	0.31	0.01	0.13	0.14	0.16	0.03	0.03	0.08	0.06	0.09	0.01	0.05	0.01
FeO	5.84	5.37	16.58	13.59	12.51	16.53	15.99	16.59	14.96	14.34	14.05	13.54	11.47	11.46	11.23	11.69	16.17	15.65	16.47	16.55	16.20	17.53	16.86	16.25
NiO	0.12	0.09	0.05	0.02	0.04	0.10	0.00	0.03	0.05	0.17	0.07	0.05	0.06	0.11	0.00	0.01	0.07	0.01	0.00	0.00	0.08	0.04	0.00	0.00
MnO	0.18	0.19	0.35	0.35	0.30	0.50	0.31	0.22	0.27	0.38	0.31	0.27	0.20	0.16	0.17	0.22	0.38	0.22	0.34	0.38	0.41	0.36	0.39	0.33
MgO	21.29	21.59	11.47	15.49	13.83	11.83	12.45	12.99	12.89	13.85	13.97	14.44	13.47	13.50	13.61	13.49	11.00	11.74	11.50	10.82	11.00	10.32	11.12	11.31
CaO	12.94	9.88	11.50	12.30	11.21	11.96	11.81	11.32	12.02	12.11	12.16	12.14	12.12	12.35	12.44	12.36	11.86	11.99	11.89	11.93	12.18	11.71	11.86	11.71
BaO	0.00	0.00	0.20	0.00	0.00	0.28	0.00	0.00	0.13	0.17	0.00	0.00	0.09	0.06	0.07	0.00	0.00	0.05	0.03	0.01	0.00	0.03	0.00	0.08
Na_2O	0.00	0.00	0.88	0.36	0.42	0.97	0.96	0.62	0.95	0.86	0.85	0.82	0.92	0.96	0.86	1.02	1.21	1.19	1.12	1.02	1.31	1.20	1.19	1.16
K_2O	0.02	0.03	0.59	0.17	0.14	0.53	0.47	0.35	0.67	0.64	0.49	0.55	0.34	0.28	0.29	0.23	1.07	0.95	0.97	0.97	1.03	1.44	1.03	1.04
ZnO	0.05	0.06	0.00	0.05	0.00	0.02	0.00	0.10	0.00	0.00	0.00	0.00	0.09	0.05	0.00	0.01	0.04	0.02	0.00	0.08	0.04	0.06	0.00	0.00
V_2O_3	0.00	0.00	0.06	0.02	0.00	0.09	0.42	0.36	0.00	0.00	0.10	0.06	0.07	0.05	0.10	0.12	0.00	0.10	0.05	0.05	0.08	0.11	0.04	0.06
P_2O_5	0.10	0.03	0.01	0.06	0.00	0.05	0.00	0.05	0.00	0.00	0.09	0.00	0.07	0.00	0.00	0.00	0.00	0.00	0.00	0.00	0.04	0.16	0.06	0.00
F	0.29	0.00	0.00	0.00	0.00	0.00	0.00	0.00	0.00	0.00	0.00	0.00	0.13	0.07	0.00	0.16	0.18	0.55	0.27	0.12	0.37	0.00	0.49	0.12
Cl	0.04	0.02	0.14	0.04	0.05	0.15	0.14	0.14	0.09	0.08	0.11	0.04	0.03	0.03	0.01	0.01	0.06	0.04	0.07	0.06	0.03	0.11	0.04	0.05
Total	98.21	94.62	95.10	97.91	95.99	96.94	97.10	97.25	96.98	97.80	97.50	97.31	95.55	94.98	94.95	95.57	95.8	95.6	96.1	95.9	95.8	96.1	95.9	95.2
Name[3]	Act	Act	Mg-H	Act	Mg-H	Mg-H	Mg-H	Mg-H	Mg-H	Mg-H	Mg-H	Mg-H	Mg-H	Mg-H	Mg-H	Mg-H	Mg-H	Mg-H	Mg-H	Mg-H	Ed	M-Hs	Mg-H	Mg-H
T (°C)[4]			794			805	817	818	778	818	806	826				795	757				772		781	

[1]Grey shading marks compositions used for PT calculation;
[2]Location refers to Fig. 6.1;
[3]Act=actinolite; Ed=edenite; Mg-H=magnesiohornblende; M-Hs=magnesiohastingsite Tre=tremolite;
[4]T is temperature calculated from Holland and Blundy (1994) except for metadunite, which is calculated using WinTWQ

Table 6.1 (continued)

	Pierre's Pond suite								Metadunite								
Sample	365-1	365-1	365-1	365-2	365-2	365-2	365-3	365-3	452-1	452-1	452-1	452-1	452-2	452-2	452-2	452-4	452-4
Location	6	6	6	6	6	6	6	6	1	1	1	1	1	1	1	1	1
	Core	Int	Rim	Core	Int	Rim	Core	Rim	Core	Int	Int	Rim	Core	Int	Rim	Core	Rim
SiO_2	45.19	45.27	45.71	45.10	45.17	45.61	45.74	45.58	58.70	58.65	58.42	56.43	58.78	57.83	56.93	56.23	57.27
AL_2O_3	9.22	9.13	9.07	9.30	9.13	8.88	9.03	8.99	0.27	0.27	0.51	1.00	0.35	0.42	1.41	1.53	1.38
TiO_2	1.06	1.01	0.91	0.93	0.97	1.00	1.07	0.98	0.06	0.01	0.10	0.10	0.08	0.07	0.08	0.11	0.18
Cr_2O_3	0.03	0.01	0.00	0.05	0.07	0.06	0.04	0.00	0.07	0.00	0.11	0.00	0.04	0.01	0.08	0.10	0.00
FeO	15.96	16.04	15.87	15.68	15.64	15.34	15.78	15.30	2.65	2.66	2.65	2.88	2.26	2.70	2.82	2.52	2.52
NiO	0.00	0.08	0.00	0.00	0.00	0.10	0.00	0.04	0.05	0.11	0.14	0.11	0.04	0.05	0.09	0.14	0.16
MnO	0.35	0.37	0.43	0.39	0.42	0.35	0.43	0.44	0.04	0.08	0.14	0.06	0.07	0.15	0.11	0.11	0.11
MgO	11.36	11.76	11.67	11.73	11.62	12.00	11.69	11.54	23.57	23.46	23.54	23.59	23.58	23.45	23.27	22.93	23.08
CaO	12.30	12.42	12.28	11.97	12.24	12.48	12.32	12.20	12.61	12.60	12.49	11.83	12.87	12.58	12.08	12.11	12.61
BaO	0.04	0.00	0.00	0.00	0.05	0.09	0.14	0.01	0.03	0.00	0.00	0.08	0.00	0.05	0.00	0.07	0.11
Na_2O	1.09	0.96	1.00	1.04	1.09	0.99	1.16	0.96	0.09	0.06	0.11	0.24	0.10	0.11	0.30	0.44	0.29
K_2O	1.12	0.95	0.99	1.02	1.02	0.95	1.06	0.98	0.00	0.02	0.00	0.01	0.01	0.00	0.02	0.02	0.01
ZnO	0.00	0.04	0.05	0.05	0.00	0.06	0.01	0.00	0.00	0.00	0.00	0.00	0.10	0.01	0.00	0.00	0.01
V_2O_3	0.08	0.03	0.04	0.03	0.15	0.11	0.00	0.10	0.00	0.00	0.00	0.00	0.04	0.17	0.00	0.03	0.00
P_2O_5	0.00	0.08	0.07	0.07	0.00	0.00	0.00	0.00	0.00	0.01	0.03	0.00	0.00	0.13	0.00	0.00	0.00
F	0.41	0.16	0.28	0.00	0.25	0.00	0.00	0.38	0.00	0.00	0.00	0.37	0.00	0.07	0.00	0.00	0.00
Cl	0.10	0.11	0.12	0.15	0.10	0.10	0.15	0.09	0.00	0.00	0.05	0.03	0.00	0.00	0.00	0.01	0.01
Total	98.3	98.4	98.5	97.5	97.9	98.1	98.6	97.6	98.1	97.9	98.3	96.7	98.3	97.8	97.2	96.4	97.7
Name	Mg-H	Mg-H	Mg-H	Mg-H	Mg-H	Mg-H	Mg-H	Mg-H	Tre	Tre	Tre	Tre	Tre	Tre	Tre	Tre	Tre
T (°C)	735			765			746		780				765			740	

Table 6.2: Plagioclase compositions of the Lloyds River Fault Zone

	Amphibolites																
Sample[1]	178-1	178-3	178-3	178-4	178-7	178-7	178-7	261-1	261-1	261-2	261-2	261-2	261-3	261-4	261-4	261-4	301-1
	Rim	Core	Rim	Rim	Core	Int	Rim	Core	Rim	Core	Int	Rim	Rim	Core	Int	Rim	Rim
Location[2]	4	4	4	4	4	4	4	3	3	3	3	3	3	3	3	3	2
SiO_2	56.3	55.8	55.0	55.3	55.1	55.4	53.8	56.2	56.5	53.8	55.8	56.1	55.8	50.7	53.4	55.1	45.8
Al_2O_3	27.3	27.8	27.4	27.7	27.6	27.8	28.3	27.6	27.8	29.1	27.5	28.2	28.0	31.1	29.0	27.4	32.7
CaO	8.7	9.2	9.2	9.5	9.3	9.4	9.9	9.6	9.6	11.9	9.8	9.9	9.9	13.8	11.5	10.0	16.6
Na_2O	6.0	5.7	5.9	5.6	5.8	5.8	5.2	5.6	5.8	4.6	5.7	5.4	5.5	3.3	4.6	5.3	1.0
K_2O	0.2	0.1	0.1	0.1	0.1	0.1	0.1	0.1	0.1	0.1	0.1	0.1	0.1	0.1	0.1	0.1	0.8
FeO	0.0	0.2	0.9	0.1	0.1	0.1	0.1	0.1	0.1	0.1	0.1	0.1	0.2	0.2	0.2	0.0	0.1
SrO	0.0	0.0	0.0	0.0	0.1	0.0	0.1	0.0	0.1	0.0	0.1	0.1	0.0	0.0	0.0	0.0	0.0
BaO	0.1	0.1	0.0	0.0	0.2	0.3	0.1	0.2	0.0	0.0	0.2	0.1	0.0	0.0	0.0	0.0	0.2
Total	98.6	98.8	98.6	98.4	98.2	98.9	97.6	99.3	99.9	99.5	99.1	99.9	99.6	99.1	98.8	97.9	97.2
An	44	47	46	48	47	47	51	48	48	59	48	50	49	69	58	51	86

[1]Grey shading marks compositions used for PT calculation;
[2]Location refers to Fig. 6.1

	Portage Lake Monzogabbro						Pierre's Pond suite							
Sample	223-1	223-1	223-2	223-2	223-3	223-3	365-1	365-1	365-1	365-2	365-2	365-3	365-3	365-3
	Core	Rim	Core	Rim	Core	Rim	Core	Int	Rim	Core	Rim	Core	Int	Rim
Location	5	5	5	5	5	5	6	6	6	6	6	6	6	6
SiO_2	56.2	56.2	55.7	57.0	57.2	57.2	55.5	55.2	55.7	55.4	68.9	54.8	55.7	54.4
Al_2O_3	26.9	26.9	26.8	26.5	26.7	26.1	28.6	28.6	28.4	28.1	19.7	28.7	28.6	29.8
CaO	9.0	8.8	8.9	8.6	8.8	8.4	10.2	10.1	10.1	10.1	0.3	10.3	10.4	8.4
Na_2O	6.1	6.3	6.2	6.4	6.4	6.3	5.7	5.9	5.9	5.5	11.6	5.5	5.7	4.9
K_2O	0.1	0.1	0.1	0.1	0.1	0.1	0.1	0.2	0.1	0.2	0.1	0.1	0.1	1.5
FeO	0.1	0.1	0.0	0.1	0.0	0.2	0.2	0.2	0.3	0.3	0.4	0.2	0.2	0.3
SrO	0.3	0.2	0.2	0.2	0.2	0.2	0.1	0.1	0.1	0.1	0.0	0.2	0.2	0.0
BaO	0.1	0.0	0.0	0.0	0.1	0.1	0.1	0.0	0.1	0.0	0.0	0.1	0.0	0.0
Total	98.8	98.5	98.1	98.8	99.6	98.6	100.6	100.2	100.6	99.7	100.9	99.9	101.0	99.3
An	44	44	44	42	43	42	49	48	48	50	1	50	50	44

Table 6.3: Olivine and clinopyroxene compositions of the Lloyds River Fault Zone

	olivine (metadunite)										clinopyroxene (amphibolite)	
Sample[1]	452-1	452-1	452-1	452-2	452-2	452-2	452-4	452-4	452-4	452-4	301-1	301-1
	Core	Core	Core		Rim	Rim		Core	Int	Rim	Core	Rim
Location[2]	1	1	1	1	1	1	1	1	1	1	2	2
SiO_2	40.25	40.41	40.75	39.80	39.76	39.44	39.76	39.69	39.94	39.70	51.87	53.05
AL_2O_3	0.07	0.07	0.04	0.04	0.05	0.01	0.03	0.03	0.06	0.06	1.52	1.16
TiO_2	0.06	0.07	0.03	0.00	0.00	0.01	0.02	0.03	0.04	0.04	0.12	0.14
CaO	0.02	0.00	0.00	0.00	0.02	0.00	0.00	0.00	0.02	0.00	23.84	23.78
MgO	46.09	45.91	46.24	46.00	46.29	45.88	46.24	46.03	46.10	46.31	13.35	13.62
FeO	12.73	12.70	12.85	12.58	13.16	13.03	12.46	12.77	12.96	12.84	7.30	6.82
Na_2O	0.01	0.03	0.00	0.02	0.01	0.00	0.01	0.04	0.03	0.00	0.27	0.25
K_2O	0.03	0.00	0.00	0.00	0.00	0.00	0.02	0.01	0.00	0.00	0.00	0.02
MnO	0.10	0.20	0.19	0.20	0.17	0.23	0.19	0.08	0.14	0.26	0.15	0.31
Cr_2O_3	0.00	0.03	0.04	0.01	0.00	0.05	0.00	0.12	0.00	0.00	0.05	0.04
NiO	0.32	0.29	0.37	0.45	0.31	0.39	0.34	0.27	0.36	0.25	0.00	0.00
V_2O_3	0.07	0.00	0.00	0.00	0.03	0.03	0.00	0.00	0.00	0.07	0.05	0.09
Total	99.76	99.71	100.51	99.10	99.82	99.05	99.07	99.07	99.65	99.52	100.27	99.28
Fo	86.6	86.6	86.5	86.7	86.2	86.3	86.9	86.5	86.4	86.5		-
En	-	-	-	-	-	-	-	-	-	-	39	39
Fs	-	-	-	-	-	-	-	-	-	-	12	12
Wo	-	-	-	-	-	-	-	-	-	-	49	49

[1]Grey shading marks compositions used for PT calculation

[2]Location refers to Fig. 6.1

CHAPTER VII
Summary and Conclusions

The Annieopsquotch Accretionary Tract marks an episode of transfer of a series of arc-back arc complexes and ophiolites from Iapetus Ocean to the overriding composite Laurentian margin during the Ordovician Taconic Orogeny. Due to its good exposure and limited cover sequences it provides a unique opportunity to study Paleozoic accretionary tectonics, and address outstanding questions regarding processes involved in continental growth. The Annieopsquotch ophiolite belt is the oldest and structurally highest component of the Annieopsquotch Accretionary Tract, and thus constrains its early evolution. Whole rock geochemical data indicate that all of the different massifs of the Annieopsquotch ophiolite belt have similar compositions and record similar magmatic histories, and likely constitute a single accreted oceanic terrane. Geochemical data presented in this thesis show that all of the ophiolite massifs within the belt have a suprasubduction zone (SSZ) signature, in contrast with previous interpretations (Dunning, 1987; Swinden et al., 1997) that the Annieopsquotch ophiolite belt was dominated by NMORB compositions. Field relationships imply that the Annieopsquotch ophiolite belt was generated in three phases. The first phase, of unknown age, encompasses troctolites and olivine gabbros formed from boninitic melts. The absence of an associated coeval intra-oceanic arc suggests the boninites were generated during initiation of subduction outboard of the Dashwoods microcontinent by shallow melting of a previously depleted mantle source. Subduction likely initiated in response to initial collision between the Dashwoods microcontinent and the Laurentian margin. The southeast-vergent configuration of the Annieopsquotch Accretionary Tract, with southeast-younging units, indicates the subduction zone was west-dipping. The second magmatic phase comprises the tholeiitic SSZ gabbro-sheeted dyke-basalt sequence. These rocks were formed at 480 Ma when more fertile mantle melted by a combination of decompression and fluid fluxing, thought to be the result of continued rollback of the subducting slab. The SSZ signature decreases upwards within the basalts. The final magmatic episode is marked by off-axis dykes that cut the entire ophiolite. These data constrain the timing of initiation of west-directed subduction outboard of the composite Laurentian margin. This subduction zone was responsible for formation of the entire Annieopsquotch Accretionary Tract, and thus played a significant role in Early Ordovician Appalachian orogenesis.

The Annieopsquotch ophiolite belt and structurally underlying complexes were accreted to the composite Laurentian margin along the sinistral-oblique Lloyds River Fault Zone and Otter Brook Shear Zone, both of which were intruded by syn-kinematic, arc-like, isotopically evolved plutonic suites. $^{40}Ar/^{39}Ar$ hornblende ages of amphibolites from the Lloyds River Fault Zone indicate that the Annieopsquotch ophiolite belt was thrust beneath the composite Laurentian margin prior to ~470 Ma. Syn-kinematic plutons (468±2, 462±2 and 459±3 Ma) localizated deformation in the plutonic rocks, initially in the magmatic state but also at high-temperatures (~770-750°C) in the solid state during cooling. The current configuration of the Lloyds River Fault Zone thus results from a positive feedback between deformation and magmatism, and indicates that the accretion of oceanic complexes was facilitated by pluton emplacement. Age constraints indicate that accretion of the various units to the Dashwoods microcontinent occurred within c. 5-10 Ma of their formation. The rapid formation and accretion of the units of the Annieopsquotch Accretionary Tract, emplacement of plutons in accreted complexes, and strike slip movements suggest accretionary processes in the

Paleozoic were similarly complex to those currently operating in the southwest Pacific. In contrast, recycling of continental crust, in the form of continental slivers that formed basement to the arc sequences, was an important process within the Annieopsquotch Accretionary Tract. Melting and assimilation of this basement, as well as melting of lithospheric manle, was responsible for the isotopically evolved signature of the syn-kinematic plutons. Sediment influx during formation of the Annieopsquotch Accretionary Tract was very minor, significantly limiting the role of fore-arc accretion. Growth of the Appalachian Laurentian margin occurred by (1) repeated accretion of oceanic crust and (2) the addition of melts generated in both lithospheric and sub-arc mantle.

Whether lower oceanic crust forms by remobilization of cumulates from a melt lens situated near the base of the sheeted dyke complex, or whether it froms by *in-situ* intrusion of mantle-derived magmas, has been a matter of considerable debate. The internal structure of rocks from the gabbro zone of the Annieopsquotch ophiolite shows that the lower ophiolitic crust is dominated by 10-30 m thick sills, which can be recognized to within 400 m of the sheeted dyke complex. The sills are composed of gabbroic cumulates whose calculated parental magmas generally become more evolved upwards, and which exhibit compositions very similar to those of the overlying basaltic sheeted dykes and lavas. These data suggest to a model in which mantle derived magmas intrude into and fractionate within a lower crustal sill complex. Fractionated melts are expelled through dyke- or channel-like conduits, and then move up-section where they may 1) form new sills; 2) pond at the gabbro/sheeted dyke interface to form an axial melt lens; or 3) erupt at the surface. The evidence from the Annieopsquotch ophiolite implies that a persistent axial melt lens was not a significant site for aggregation, homogenization and differentiation of mantle-derived melts. Rather, it seems that most of the fractional crystallization in the system occurred within the intra-crustal sill complex, and that this intra-conduit differentiation dominates the compositional evolution of the lavas. If sill complexes also characterize some types of mid-ocean ridges, then they may play an important role in MORB evolution.

APPENDIX I
The origin of mafic-ultramafic bodies in the northern Dashwoods Subzone

A1.1. Introduction

Abundant mafic-ultramafic bodies within the Notre Dame and Dashwoods subzones range in size from 100 m^2 to 30 km^2. Contact relationships of most are uncertain. Dunning and Chorlton (1985) interpreted all mafic-ultramafic enclaves as remnants of the Annieopsquotch ophiolite belt, which by their definition included the Long Range Complex, while Currie and van Berkel (1989) suggested some mafic bodies represent Silurian plutons.

Mafic-ultramafic bodies have been studied in the northern part of the Dashwoods Subzone and in the Lloyds River Fault Zone. Samples of the Long Range Complex have been studied for comparison. Major occurrences are summarized in Table A1.1 and Fig. A1.1. Based on compositional differences, as well as metamorphic grade, the studied bodies can be divided into two types.

The first type is dominantly gabbroic in composition, and rocks are generally fresh and rarely display penetrative fabrics. Ultramafic rocks are unknown from these bodies, and they are relatively large in size. The biggest of these is the Puddle Pond complex (c. 10 by 3 km), which occurs along the boundary between the Dashwoods Subzone and the Annieopsquotch Accretionary Tract (#1 in Fig. A1.1). This complex is dominated by a layered cumulate sequence, that grades from troctolite through olivine gabbro to gabbro (Fig. A1.2a,b). Hornblende-bearing gabbro dominates the southwestern part of the complex. In addition, it contains olivine norite and associated troctolite, the position of which within the sequence is uncertain. Pegmatitic patches, with grain size up to 10 cm, are common within gabbroic rocks. The complex is cut by granite of presumed Silurian age. The cumulate rocks are characterized by ubiquitous presence of generally fresh, subhedral plagioclase. Olivine occurs in nearly all cumulates as sub- to anhedral grains, and is partly altered to serpentine or iddingsite. In more evolved cumulates, clinopyroxene is modally abundant, and is generally partly altered to green amphibole. Igneous brown amphibole is ubiquitous as rims around cumulus plagioclase, olivine and pyroxene, and locally forms interstitial grains. Minor orange-brown biotite is locally associated with brown hornblende. The presence of igneous hornblende and biotite suggests the magmas that generated the Puddle Pond complex were hydrous. Both on a macro- and microscopic scale, the gabbroic rocks are dissected by small fractures, which are lined with chlorite and green amphibole. A second large gabbroic body, the John's Brook Lake gabbro, occurs c. 20 km northwest of the Annieopsquotch ophiolite (# 2 in Fig. A1.1). It comprises undeformed to weakly deformed gabbro, with local igneous layering and pegmatitic patches, as well as hornblende gabbro. Contact relationships are not exposed, although it is cut by granite of presumed Silurian age. Several smaller gabbroic bodies are associated with the John's Brook Lake gabbro, and have similar characteristics (Fig. A1.1).

The second type recognized in the mafic-ultramafic bodies is dominated by variably metamorphosed ultramafic rocks (lherzolite, harzburgite, wehrlite, dunite, pyroxenite; Fig. A1.2c, d). They are commonly associated with (meta)gabbro, which appears to be both intrusive into, and interlayered with, the ultramafic rocks. Their size is generally restricted (< 1 km). The body near Whaleback Pond (#3 in Fig. A1.1) comprises websterite intruded by deformed lherzolite (Fig. A1.2c), as well as dunite, wehrlite and minor metagabbro. The ultramafic rocks are composed of variably serpentinized olivine, clinopyroxene, orthopyroxene and tremolite. The metagabbro is highly deformed, giving the rock a flaser gabbro-like appearance. It is composed of hornblende, which locally forms cm-sized augen, and plagioclase. The body appears to be enclosed in tonalites of the Notre Dame Arc, although direct contact relationships were not observed. West of Silver Pond, scattered outcrops within an area of c. 1 by 1 km consist of (meta)harzburgite and minor dunite with associated gabbro (#4 in Fig. A1.1). A smaller associated body occurs just to the east of it. These rocks are dominated by subhedral to euhedral partly serpentinized olivine enclosed in largely chloritized pyroxene oikocrysts. Minor plagioclase occurs interstitially. Tremolite is common, and magnesite and chromite occur as accessory phases. The ultramafic rocks are cut by granite of presumed Silurian age. On the southeast shore of Lake of the Hills, harzburgite and metapyroxenite (tremolite+chlorite+talc) occur amidst outcrops of Notre Dame Arc plutons (#5 in Fig. A1.1). On the southeast shore of Padille Pond, several outcrops of variably metamorphosed lherzolite occur (#6 in Fig. A1.1). The lherzolite is composed of olivine (mostly altered to iddingsite and serpentine) enclosed by blurry clinopyroxene oikocrysts. A more metamorphosed variety is characterized by tremolite in a matrix of serpentine, magnesite and chlorite. Contact relationships are not directly exposed, but the body is surrounded by Middle Ordovician tonalites of the Notre Dame Arc. North of Lloyds River, a single outcrop of dunite occurs, which is enclosed in gabbro (#7 in Fig. A1.1). The dunite is composed of olivine and tremolite, and is partly serpentinized. The ultramafic bodies have been interpreted as ophiolitic fragments of the Annieopsquotch ophiolite belt (Dunning and Chorlton, 1985).

A1.2. Geochronology

I have dated two of the gabbroic bodies, the Puddle Pond complex and the John's Brook Lake gabbro, to test whether their age is compatible with an ophiolitic origin.

A sample of a gabbroic pegmatite from within the layered troctolite-olivine gabbro-gabbro sequence of the Puddle Pond complex (#1 in Fig. A1.1) contained zircons with varying morphologies, including colorless to brown anhedral fragments with concoidal fractures and colorless to light brown prisms with aspect ratios of 2.5-5 (Table A1.2, Figs. A1.4a,b). A Concordia age calculated utilizing all four analyses is 432.4±1.0 Ma (MSWD of concordance and equivalence=1.6; probability=0.14; Fig. A1.3a), which is interpreted to be the crystallization age of the gabbro.

A pegmatitic gabbro of the John's Brook Lake gabbro (#2 in Fig. A1.1), yielded zircons with both prismatic and anhedral habits (Table A1.2, Figs. A1.4c,d). A total of four fractions were analyzed, one of which (fraction 5-2) yielded slightly older $^{206}Pb/^{238}U$ and $^{207}Pb/^{206}U$ ages, suggesting the presence of a small amount of inherited material. The other three fractions, which are 0.6-1.5% discordant, were used to calculate a Concordia age of 429.9±1.2 Ma (MSWD of concordance and equivalence=1.3; probability=0.26; Fig. A1.3b). This age is interpreted to be the crystallization age of the gabbro.

A1.3. Discussion

The Silurian ages of c. 432 and c. 430 Ma rule out the possibility that the gabbroic bodies are part of the Annieopsquotch ophiolite belt as inferred by Dunning and Herd (1980) and Dunning and Chorlton (1985). Their fresh nature, hydrous character and ages indicate they are part of the Silurian magmatic event that affected the Notre Dame and Dashwoods subzones between c. 438-427 Ma (cf.

Currie and van Berkel, 1989). This magmatic episode has been attributed to slab break-off of the oceanic part of the Ganderian plate following its collision with the composite Laurentian margin (van Staal et al., 2003; Whalen et al., 2003). Silurian magmatism is dominated volumetrically by granites and rhyolites, but some mafic plutons have been described within the region (the Main Gut and Boogie Lake suites; Currie and van Berkel, 1989; Dunning et al., 1990). These have been dated at 431±2 and 435 +6/-3 Ma, respectively (Dunning et al., 1990), in agreement with the ages presented herein. These new data suggest that Silurian mafic plutons are both more widespread and volumetrically important than previously recognized. In addition, the examples of Silurian mafic magmatism that I have dated include layered cumulate sequences that are absent in the Boogie Lake and Main Gut suites.

The dominantly ultramafic bodies are of a different origin, since (1) the gabbroic bodies are relatively fresh, whereas the ultramafic bodies are metamorphosed, and (2) in general, ultramafic rocks, especially lherzolites, are not expected in plutons intruding continental crust. The occurrence of ultramafic cumulates and intrusive lherzolite strongly suggests an oceanic lower crustal affinity for these rocks. An ophiolitic origin is also consistent with their metamorphosed nature; both the Lushs Bight oceanic tract and Annieopsquotch ophiolite belt are metamorphosed at greenschist to amphibolite-facies conditions. Petrogenetic grids for ultramafic rocks indicate tremolite is stable above temperatures of c. 500°C, and is commonly associated with chlorite, olivine and talc (Jenkins, 1981). The presence of tremolite in most ultramafic rocks thus indicates they were metamorphosed at amphibolite-facies conditions. The associated gabbros generally show amphibolite- to greenschist-facies mineral assemblages.

The ultramafic bodies occur on either side of the Lloyds River Fault Zone, the fundamental boundary that separates the Dashwoods Subzone from the Annieopsquotch Accretionary Tract (Fig. A1.1). The bodies at Whaleback Pond and Silver Pond, like those at Dennis Pond, Three Ponds, and North Fischells Brook (#8-10 in Fig. A1.1), occur within the Dashwoods Subzone, suggesting a correlation between the two. The latter occur as enclaves in a migmatitic mélange that resembles the Mischief mélange (Fox and van Berkel, 1988), and they occur along strike of the Long Range Complex, suggesting that these ultramafic bodies are relics of the Lushs Bight oceanic tract. This correlation is consistent with the similar metamorphic assemblages observed in the Long Range complex and the ultramafic bodies described herein (Table A1.1). I thus infer all ultramafic bodies in the Dashwoods Subzone to be relics of the Lushs Bight oceanic tract. Their widespread occurrence indicates that the original extent of the Lushs Bight oceanic tract was much larger than currently preserved. I speculate that these ultramafic bodies are relics of a once continuous sheet of oceanic crust that was emplaced over the Dashwoods microcontinent. Subsequent burial and intrusion by Ordovician and Silurian plutons has largely masked the ophiolitic cover, however, and left only scattered ultramafic bodies in most of the Dashwoods and Notre Dame subzones.

The ultramafic bodies (Lloyds River, Padille Pond, Lake of the Hills) that occur within the Lloyds River Fault Zone are part of the Annieopsquotch Accretionary Tract, suggesting a genetic link with the Annieopsquotch ophiolite belt. Ultramafic lithologies are sparse in the Annieopsquotch ophiolite belt, but do occur within the Star Lake ophiolite and in the large ophiolitic massif to the west of it. The ultramafic rocks are confined to a thrust slice of the Annieopsquotch ophiolite belt that is bounded by the northwestern splay of the Lloyds River Fault Zone, and is separated from the main ophiolitic bodies by plutonic rocks that intruded the Lloyds River Fault Zone syn-kinematically (Fig. A1.1; Chapter 6). The higher abundance of ultramafic rocks within this thrust slice is consistent with the orientation of the pseudostratigraphy of the Annieopsquotch ophiolite, which suggests ultramafic lithologies should become abundant to the northwest. The olivine-tremolite assemblages observed within the ultramafic rocks are consistent with the metamorphic grade recorded by amphibolites of the Lloyds River Fault Zone. I thus infer the ultramafic rocks within the Lloyds River Fault Zone represent stratigraphically deeper crustal levels of the Annieopsquotch ophiolite belt.

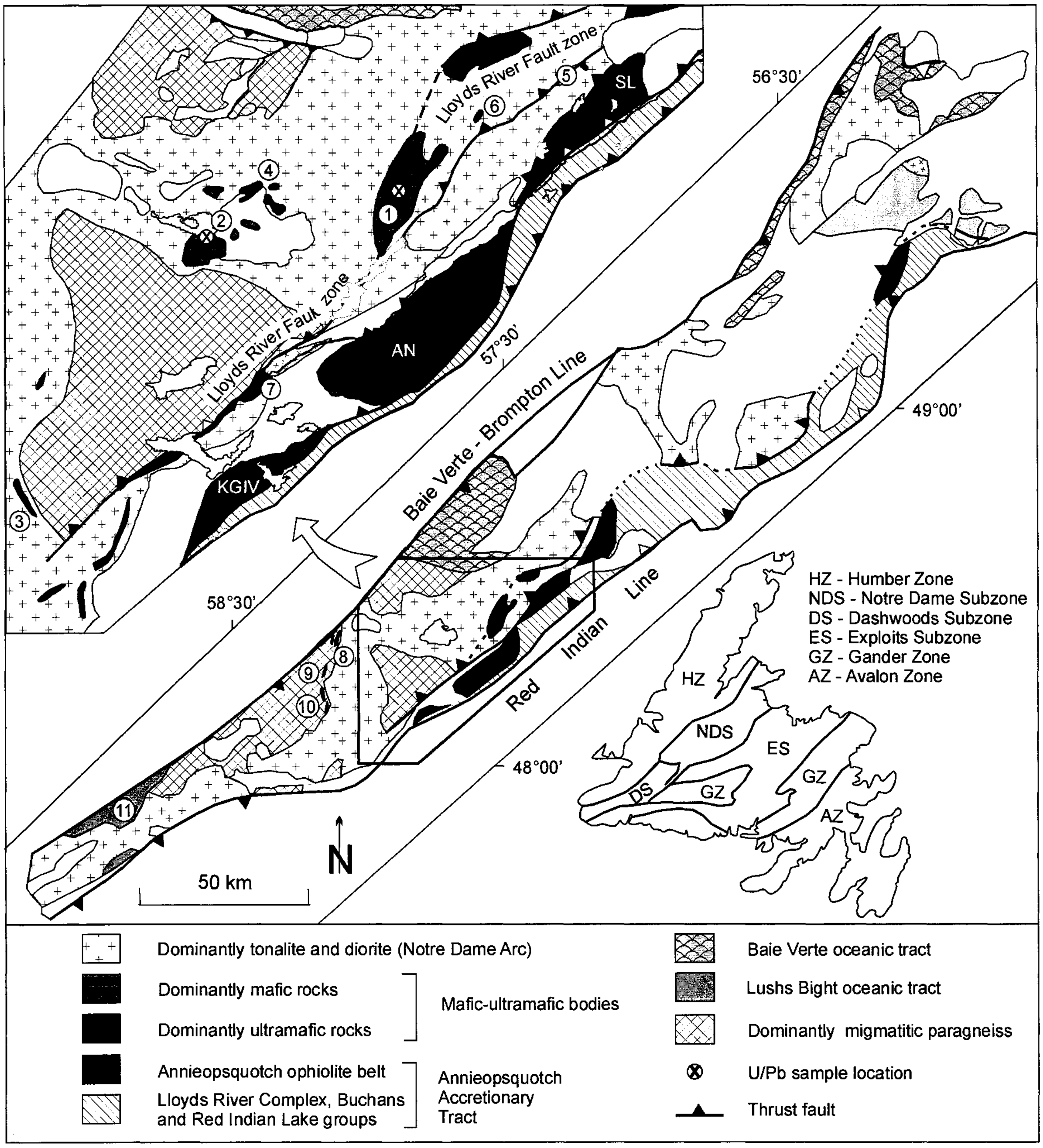

Figure A1.1: Simplified geological map showing the distribution of pre-Silurian elements in the Dashwoods and Notre Dame Subzones and the distribution of mafic-ultramafic bodies discussed herein. Inset shows close-up of study area. 1=Puddle Pond Complex; 2=John's Brook Lake gabbro; 3=Whaleback Pond; 4=Silver Pond; 5=Lake of the Hills; 6=Padille Pond; 7=Lloyds River; 8=Dennis Pond; 9=Three Ponds; 10=North Fischells Brook; 11=Long Range Complex. AN=Annieopsquotch ophiolite; KGIV=King George IV ophiolite; SL=Star Lake ophiolite. Modified from Colman-Sadd et al. (1990), Lissenberg et al. (in press) and van Staal et al. (in press a,b,c).

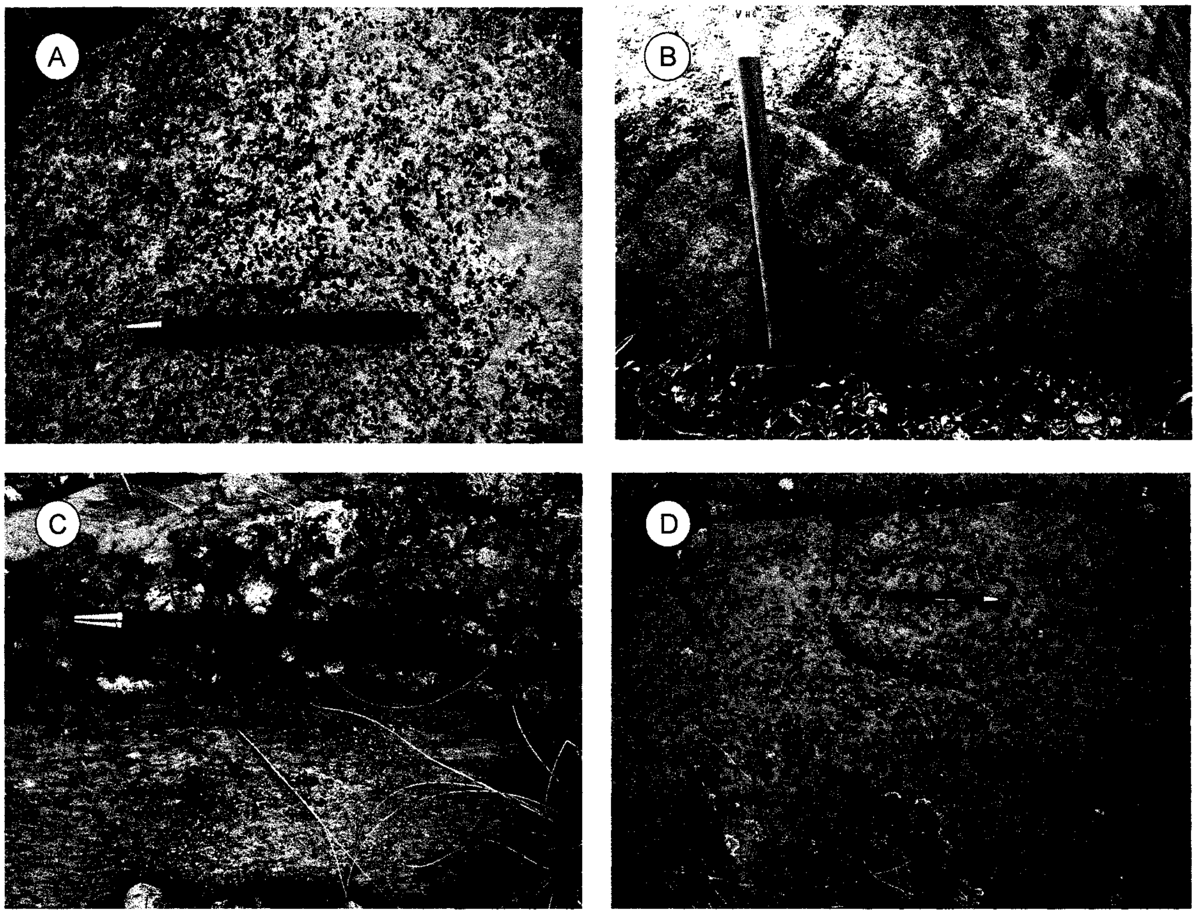

Figure A1.2: Field photographs of mafic bodies within the Notre Dame and Dashwoods subzones. a) Layered troctolite cumulates from the Puddle Pond Complex. b) Layered gabbro from the Puddle Pond Complex. c) Fine-grained lherzolite intrudes very coarse-grained websterite in body near Whaleback Pond. Note the deformed nature of lherzolite. d) Wehrlite cumulate in body near Whaleback Pond.

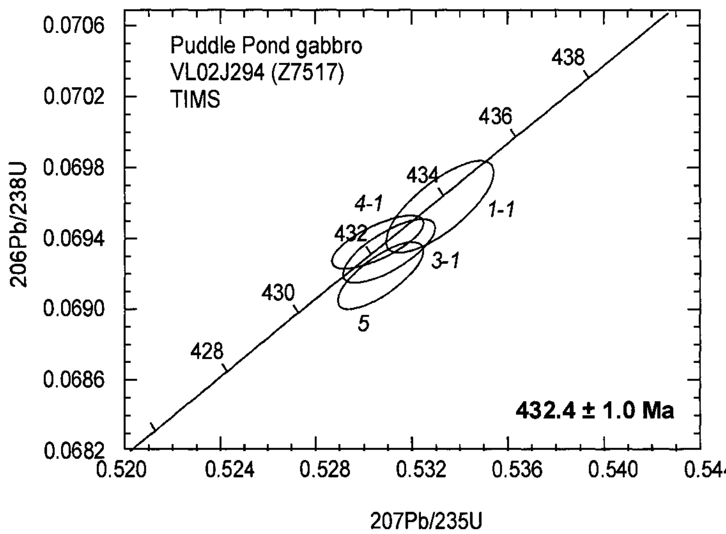

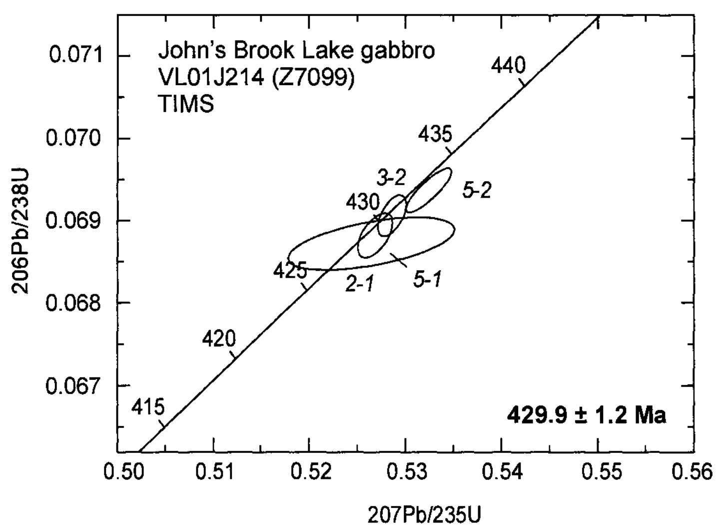

Figure A1.3: Concordia diagrams for the Puddle Pond Complex and the John's Brook Lake gabbro.

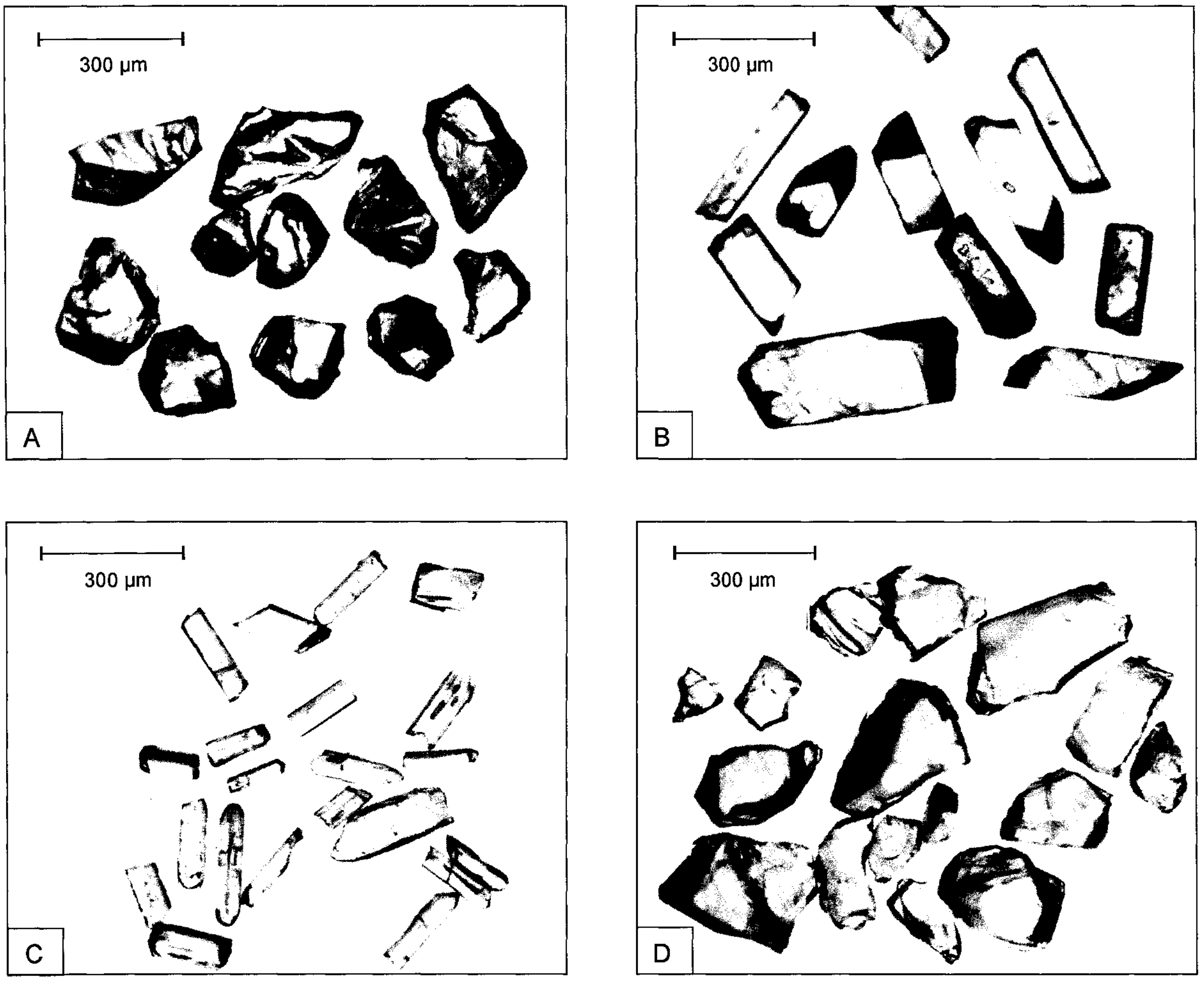

Fig. A1.4: Photomicrographs of zircon fractions of dated samples. a) Fraction I of the Puddle Pond complex; b) Fraction IV of the Puddle Pond complex; c) Fraction II of the John's Brook Lake gabbro; d) Fraction V of the John's Brook Lake gabbro

Table A1.1: Occurrences of major mafic-ultramafic bodies in the northern Dashwoods Subzone

#[1]	Location	Lithology	Mineralogy[2]	Exposed contact relationships	Source
1	Puddle Pond	Troctolite, ol-gabbro, gabbro, hbl-gabbro, ol-norite	Varying amounts of *Ol+Pl+Cpx+Hbl+Opx+/-Bt*	Cut by granite of presumed Silurian age	This study; Dunning and Herd (1980)
2	John's Brook Lake	Gabbro, hbl-gabbro	*Cpx+Pl+Hbl*	Cut by granite of presumed Silurian age	This study; Dunning and Chorlton (1985)
3	Whaleback Pond	Lherzolite, dunite, websterite, wehrlite, metagabbro	Relic Ol+Cpx+opx; Tr+Chl+Srp+Car; *Hbl+Pl*	Surrounded by c. 460 Ma Notre Dame Arc plutons	This study
4	W of Silver Pond	Dunite, wehrlite, harzburgite, pyroxenite, gabbro.	Relic Ol+Cpx+Opx+Cr; Tr+Chl+Srp+Car; Am+Chl	Cut by granite of presumed Silurian age	This study, Dunning and Herd (1980)
5	Lake of the Hills	Metapyroxenite, harzburgite	Tr+Chl+Tlc	Surrounded by c. 460 Ma Notre Dame Arc plutons	This study, Dunning and Chorlton (1985), Dunning et al. (1982)
6	Padille Pond	Lherzolite, harzburgite	relic Ol+Cpx; Srp+Car+Tr+Chl	Surrounded by c. 460 Ma Notre Dame Arc plutons	This study, Dunning and Herd (1980)
7	Lloyds River	Dunite	Ol+Tr	Enclosed in gabbros	This study
8	Dennis Pond	Serpentinite, metagabbro	Ol+Srp+Tlc+Car+Cr+Chl; *Hbl+Ep+Zo+Chl*	Enclaves in metasediments	Fox and van Berkel (1988)
9	Three Ponds	Serpentinite, metagabbro	Srp+Tlc+Chl+Car; *Hbl+Ep+Zo+Qtz*	Enclaves in metasediments	Fox and van Berkel (1988)
10	North Fischells Brook	Serpentinite, metagabbro	Srp+Chl+Tr+Tlc; *Pl+Hbl+Qtz*	Enclaves in metasediments	Fox and van Berkel (1988)
11	Long Range Complex	Harzburgite, lherzolite, pyroxenite, gabbro	Ol+Opx+Tlc+Tr	Overlies Mischief melange	This study; Hall and van Staal (1999)

[1] Nubmers refer to locations in Figure 1

[2] Mineralogy of ultramafic rocks in normal font, mafic rocks in *italics*Abbreviations (after Kretz, 1983): am=amphibole, bt=biotite, car=carbonate, chl=chlorite, cpx=clinopyroxene, cr=chromite, ep=epidote, hbl=hornblende, ol=olivine, opx=orthopyroxene, pl=plagioclase, qtz=quartz, srp=serpentine, tlc=talc, tr=tremolite, zo=zoisite

Table A1.2: U-Pb TIMS analytical data data of gabbroic bodies within the Dashwoods Subzone

Fraction[1]	Description[2]	Wt. ug	U ppm	Pb[3] ppm	206Pb/204Pb[4]	Pb[5] pg	Isotopic Ratios[6] 208Pb/206Pb	207Pb/235U	±1SE Abs	206Pb/238U	±1SE Abs	Corr.[7] Coeff.	207Pb/206Pb	±1SE Abs	Ages (Ma)[8] 206Pb/238U	±2SE	207Pb/235U	±2SE	207Pb/206Pb	±2SE	% Disc
VL02J294 (Z7517; UTM[9] 21454561/5366499); Puddle Pond Complex gabbro																					
1-1 (Z; 4)	Co, Clr, An, Fr, Dia, 300	30	134	10	2787	6	0.21	0.53316	0.00113	0.06958	0.00013	0.756	0.05557	0.00008	433.6	1.6	433.9	1.5	435.4	6.3	0.4
3-1 (Z; 5)	Co, Clr, Eu, Pr, Dia, 250	29	118	9	3328	4	0.18	0.53057	0.00096	0.06938	0.00007	0.726	0.05547	0.00007	432.4	0.9	432.2	1.3	431.1	5.6	-0.3
4-1 (Z; 2)	Br, Clr, Pr, Eu, Dia, 300	33	112	9	3985	0	0.27	0.53104	0.00096	0.06933	0.00009	0.732	0.05555	0.00007	432.1	1.1	432.5	1.3	434.5	5.4	0.6
5 (Z; 16)	Br, fln, Eu, Pr, Dia, 150	30	173	13	3965	6	0.24	0.53069	0.00089	0.06919	0.00009	0.752	0.05563	0.00006	431.3	1.1	432.3	1.2	437.5	5.0	1.5
VL01J214 (Z7099; UTM 21435635/5359962); John's Brook Lake gabbro																					
2-1 (Z; 16)	Co, Clr, Eu, Pr, Dia, 200	39	60	5	343	28	0.25	0.52649	0.00433	0.06872	0.00016	0.548	0.05556	0.00040	428.5	1.9	429.5	5.8	434.9	31.8	1.5
3-2 (Z; 2)	Co, Clr, Eu, Pr, Dia, 350	35	215	17	10894	3	0.24	0.52861	0.00074	0.06906	0.00012	0.562	0.05552	0.00009	430.5	1.5	430.9	1.0	433.1	6.8	0.6
5-1 (Z; 11)	Co, Clr, An, Frag, Dia, 30(	84	104	8	3892	10	0.19	0.52684	0.00091	0.06882	0.00013	0.570	0.05552	0.00010	429.0	1.6	429.7	1.2	433.2	7.6	1.0
5-2 (Z; 4)	Co, Clr, An, Frag, Dia, 30(	57	159	12	2568	15	0.23	0.53243	0.00119	0.06937	0.00013	0.858	0.05567	0.00006	432.3	1.6	433.4	1.6	439.2	5.1	1.6

[1] Z=zircon fraction; All zircon fractions are abraded following the method of Krogh (1982). Number in brackets refers to the number of grains in the analysis.
[2] Zircon descriptions: Co=Colorless, Br=brown, Clr=Clear, fln=Few Inclusions, Eu=Euhedral, An=Anhedral, Pr=Prismatic, Fr=Fragments, Dia=Diamagnetic, Number refers to average size of zircons in um.
[3] Radiogenic Pb
[4] Measured ratio, corrected for spike and fractionation
[5] Total common Pb in analysis corrected for fractionation and spike
[6] Corrected for blank Pb and U and common Pb, errors quoted are 1 sigma absolute; procedural blank values for this study ranged from 0.1- 0.2 pg U and 2-4 pg Pb for zircon analyses; Pb blank isotopic composition is based on the analysis of procedural blanks; corrections for common Pb were made using Stacey-Kramers compositions.
[7] Correlation Coefficient
[8] Corrected for blank and common Pb, errors quoted are 2 sigma in Ma
[9] UTM in NAD83

APPENDIX II
Analytical procedures

A2.1. Whole rock geochemistry

The VL01 series were analyzed at the Ontario Geological Survey laboratory (Sudbury, Canada), with some exceptions (see below). Major elements and selected trace elements were analyzed by XRF using a Rigaku RIX-3000 WD-XRF; trace element analyses were measured on a Perkin-Elmer ELAN 5000 ICP-MS. Precision and accuracy are described by Richardson et al. (1996). Major elements and selected trace elements of the VL02 series, as well as VL01A081 and 354B, were analyzed by XRF on fused glass beads at McGill (Montreal, Canada), using a PHILIPS PW2440 4kW automated XRF, with accuracy within 1%. Trace elements were analysed at the Ontario Geological Survey. Samples VL01A048, 258B, 260 and VL02J308, 318, 319, 326c, 380a, 391, 392, 393 and 400 were analysed at ACME (Vancouver, Canada). Major and selected trace elements were measured using a Jarrel Ash Atom Comp Model 975 ICP-ES. The majority of the trace elements were measured using a Perkin Elmer Elan 6000 ICP-MS; Pb and Ni were analysed on a Perkin Elmer Optima DV3000 ICP-ES. Precision and accuracy was generally within 1% for major elements and within 10% for trace elements. The WXNF series (except 108 and 117), as well as VL01A051, was analyzed at the Geological Survey of Canada (Ottawa) by XRF (major elements) and ICP-MS (trace elements), with precision for trace elements generally within 10%. WXNF108 and 117 were analyzed by XRF on fused glass disks (major elements) and pressed powder pellets (trace elements) at X-ray Assay Laboratories (Toronto, Canada). REE and selected trace elements were analyzed by ICP-MS at Memorial University of Newfoundland, with precision and accuracy described in Jenner et al. (1990).

Detection limits of the various geochemical laboratories is listed in Table A2.1. For further details about analytical procedures the reader is referred to Rogers (2004).

A2.2. Nd isotope geochemistry

Samples VL010084, VL01A081, WXNF117 and WXNF227 were analyzed at Carleton University (Ottawa, Canada). Samples were spiked with a mixed ^{148}Nd-^{149}Sm spike prior to dissolution. Concentrations are precise to +1%, but ^{147}Sm/^{144}Nd ratios are reproducible to 0.5%. Samples were analyzed on a Finnigan MAT 261 thermal ionization mass spectrometer (TIMS). Isotope ratios are normalized to ^{146}Nd/^{144}Nd = 0.72190. Analyses of the USGS standard BCR-1 yield Nd = 29.02 ppm, Sm = 6.68 ppm, and ^{143}Nd/^{144}Nd = 0.512668 ± 0.000020 (n=4). 32 runs of the La Jolla standard average ^{143}Nd/^{144}Nd = 0.511875 ± 0.000018.

Samples VL01J036b and VL01J232 were analyzed at Geospec (Edmonton, Canada). The isotopic composition of Nd was determined in multi-dynamic mode by TIMS. The ^{143}Nd /^{144}Nd ratio of samples is presented relative to a value of 0.512107 for the Geological Survey of Japan Nd isotopic standard JNdi-1 (Tanaka et al., 2000), which is equivalent to a value of 0.511850 for the La Jolla Nd isotopic standard. For Nd, the long-term average value for JNdi-1 is 0.512110 ± 0.000012 (1sd), equivalent to a value of 0.511853 for the La Jolla Nd isotopic standard, and within the generally accepted window of La Jolla values (0.511850 ± 0.000010). For Sm, the long-term average value for

$^{149}Sm/^{154}Sm$ determined from a Sm standard solution was 0.60759 ± 0.00009 (1sd), identical within quoted uncertainty to the value determined by Wasserburg et al. (1981) of 0.60750 ± 0.00002.

Samples VL01J118 and WXNF216 were analyzed at the Geological Survey of Canada. Sm-Nd isotopic ratios were measured using a Nu Plasma multicollector ICP-MS. $^{143}Nd/^{144}Nd$ isotopic ratios are reported relative to the value of 0.51186 in the LaJolla Nd standard. Nine spiked and unspiked analyses of BCR-1 yielded the weighted average values $^{143}Nd/^{144}Nd$= 0.512636 ± 0.000009.

More details about analytical procedures can be found in Rogers (2004).

A2.3. $^{40}Ar/^{39}Ar$ geochronology

Selected samples were processed for $^{40}Ar/^{39}Ar$ analysis of hornblende phenocrysts by standard mineral separation techniques, including hand-picking of clear, unaltered crystals in the size range 0.5 to 1 mm. Individual mineral separates were loaded into aluminum foil packets along with PP-20 hornblende (Hb3gr equivalent) with an apparent age of 1072 Ma (Roddick 1983) to act as flux monitor. The sample packets were arranged radially inside an aluminum can. The samples were then irradiated for 12 hours at the research reactor of McMaster University in a fast neutron flux of approximately $3x10^{16}$ neutrons/cm^2.

Laser $^{40}Ar/^{39}Ar$ step-heating analysis was carried out at the Geological Survey of Canada (Ottawa, Ontario). Upon return from the reactor, samples were split into several aliquots and loaded into individual 1.5 mm-diameter holes in a copper planchet. The planchet was then placed in the extraction line and the system evacuated. Heating of individual sample aliquots in steps of increasing temperature was achieved using a Merchantek MIR10 10W CO_2 laser equipped with a 2 mm x 2 mm flat-field lens. The released Ar gas was cleaned over getters for ten minutes, and then analyzed isotopically using the secondary electron multiplier system of a VG3600 gas source mass spectrometer; details of data collection protocols can be found in Villeneuve and MacIntyre (1997) and Villeneuve et al. (2000). Error analysis on individual steps follows numerical error analysis routines outlined in Scaillet (2000); error analysis on grouped data follows algebraic methods of Roddick (1988).

Neutron flux gradients throughout the sample canister were evaluated by analyzing the hornblende flux monitors included with each sample packet and interpolating a linear fit against calculated J-factor and sample position. The error on individual J-factor values is conservatively estimated at ±0.6% (2σ). Because the error associated with the J-factor is systematic and not related to individual analyses, correction for this uncertainty is not applied until calculation of dates from isotopic correlation diagrams (Roddick 1988). No evidence for excess ^{40}Ar was observed in either of the samples and, therefore, all regressions are assumed to pass through the $^{40}Ar/^{36}Ar$ value for atmospheric air (295.5). All errors are quoted at the 2σ level of uncertainty.

A2.4. U/Pb geochronology

U-Pb TIMS analytical methods utilized are outlined in Parrish et al. (1987) and Davis et al. (1997). Heavy mineral concentrates were prepared using standard crushing, grinding, Wilfley™ table, and heavy liquid techniques. Mineral separates were sorted by magnetic susceptibility using a Frantz™ isodynamic separator. Single and multigrain zircon fractions analyzed were very strongly air abraded following the method of Krogh (1982). Multigrain fractions of titanite were also lightly air abraded. Treatment of analytical errors follows Roddick et al. (1987) with errors on the ages reported at the 2σ level.

SHRIMP II analyses were conducted at the Geological Survey of Canada (GSC) using analytical procedures described by Stern (1997), with standards and U-Pb calibration methods following Stern and Amelin (2003). Zircons from the samples were cast in 2.5 cm diameter epoxy mounts (GSC mount #295 for sample VL02J185 (z7644) and GSC mount #'s 295 and 312 for sample VL02J238D (z7524)) along with fragments of the GSC laboratory standard zircon (z6266, with $^{206}Pb/^{238}U$ age = 559 Ma). The mid-sections of the zircons were exposed using 9, 6, and 1 μm diamond compound, and the internal features of the zircons were characterized with backscatter electrons (BSE) and cathodoluminescence (CL) utilizing a Cambridge Instruments scanning electron microscope (SEM). Mount surfaces were evaporatively coated with 10 nm of high purity Au. Analyses were conducted using an $^{16}O^-$ primary beam, projected onto the zircons at 10 kV. The sputtered area used for analysis was ca. 25 μm in diameter with a beam current of ca. 5 nA and 6 nA for z7644 and z7524, respectively. The count rates of ten isotopes of Zr^+, U^+, Th^+, and Pb^+ in zircon were sequentially measured over 6 scans with a single electron multiplier and a pulse counting system with deadtime of 35 ns. Off-line data processing was accomplished using customized in-house software. The 1σ external errors of $^{206}Pb/^{238}U$ ratios reported in Table 5.5 incorporate a ±1.0 % error in calibrating the standard zircon (see Stern and Amelin 2003). No fractionation correction was applied to the Pb-isotope data; common Pb correction utilized the measured $^{204}Pb/^{206}Pb$ and compositions modelled after Cumming and Richards (1975). The $^{206}Pb/^{238}U$ ages for the analyses have been corrected for common Pb using both the 204- and 207-methods (Stern 1997), but there is generally no significant difference in the results. Isoplot v. 2.49 (Ludwig 2001) was used to generate concordia plots and calculate weighted means.

A Concordia age (Ludwig 1998) is calculated for the samples analyzed by SHRIMP. A Concordia age incorporates errors on the decay constants and includes both an evaluation of concordance and an evaluation of equivalence of the data (how well the data fit the assumption that they are repeated measurements of the same point). The calculated Concordia ages and errors quoted in the text are at 2σ with decay constant errors included.

Table A2.1: Detection limits of various geochemical laboratories

	Major elements (%)					Trace elements (ppm)				
	OGS	McGill	ACME	GSC		OGS 2001	OGS 2002	McGill	ACME	GSC
SiO_2	0.01	0.006	0.02	0.5	Ba	5	0.6	n.a.	5	10
TiO_2	0.01	0.004	0.01	0.02	Cr	1	8	n.a.	n.a.	10
Al_2O_3	0.01	0.012	0.03	0.4	Cs	0.01	0.007	n.a.	0.1	0.02
Fe_2O_3	0.01	0.003	0.04	0.1	Ga	1	0.1	1	0.5	0.1
MnO	0.01	0.003	0.01	0.01	Hf	0.1	0.1	n.a.	0.5	0.05
MgO	0.01	0.01	0.01	0.1	Nb	0.08	0.09	1	0.5	0.05
CaO	0.01	0.002	0.01	0.1	Ni	5	0.8	3	2	10
Na_2O	0.01	0.008	0.01	0.5	Pb	0.1	0.4	1	5	2
K_2O	0.01	0.003	0.04	0.05	Rb	0.2	0.05	1	0.5	0.05
P_2O_5	0.01	0.004	0.01	0.02	Sc	0.5	0.6	10	10	0.5
Cr_2O_3	n.a.	0.002	0	0.02	Sr	2	0.5	n.a.	0.5	5
					Th	0.05	0.06	1	0.1	0.02
					U	0.01	0.007	1	0.1	0.02
					V	4	1	10	5	5
					Y	0.2	0.02	1	0.1	0.02
					Zr	6	4	1	0.5	0.5
					La	0.2	0.02	n.a.	0.5	0.1
					Ce	0.3	0.07	n.a.	0.5	0.1
					Pr	0.03	0.006	n.a.	0.02	0.02
					Nd	0.2	0.03	n.a.	0.4	0.1
					Sm	0.03	0.01	n.a.	0.1	0.02
					Eu	0.004	0.005	n.a.	0.05	0.02
					Gd	0.03	0.009	n.a.	0.05	0.02
					Tb	0.001	0.003	n.a.	0.01	0.02
					Dy	0.01	0.008	n.a.	0.05	0.02
					Ho	0.002	0.003	n.a.	0.05	0.02
					Er	0.006	0.008	n.a.	0.05	0.02
					Tm	0.005	0.003	n.a.	0.05	0.02
					Yb	0.01	0.01	n.a.	0.05	0.05
					Lu	0.001	0.003	n.a.	0.01	0.02

n.a.=not analysed

REFERENCES

Alabaster, T., and Story, B.C., 1990, Modified Gulf of California model for South Geogia, north Scotia Ridge, and implications for the Rocas Verdes back-arc basin, southern Andes: Geology, v. 18, p. 497-500.

Armstrong, J.T., 1988, Quantitative analysis of silicates and oxide minerals: Comparison of Monte-carlo, ZAF and Phi-Rho-Z procedures, *in:* Newbury, D.E. (Ed.), Microbeam Analysis-1988, San Francisco Press, San Francisco, p. 239-246.

Barnes, S.J., 1986, The effect of trapped liquid crystallization on cumulus mineral compositions in layered intrusions: Contributions to Mineralogy and Petrology, v. 93, p. 524-531.

Bédard, J.H., 1990, Cumulate recycling and crustal evolution in the Bay of Island ophiolite: Journal of Geology, v. 99, p. 225-249.

Bédard, J.H., 1993, Oceanic crust as a reactive filter: synkinematic intrusion, hybridization, and assimilation in an ophiolitic magma chamber, western Newfoundland: Geology, v. 21, p. 77-80.

Bédard, J.H., 1994, A procedure for calculating the equilibrium distribution of trace elements among the minerals of cumulate rocks, and the concentration of trace elements in the coexisting liquids: Chemical Geology, v. 118, p.143-153.

Bédard, J.H., 1999, Petrogenesis of boninites from the Betts Cove ophiolite, Newfoundland, Canada: Identification of subducted source components: Journal of Petrology, v. 40, p. 1853-1889.

Bédard, J.H., in press, Partitioning coefficients between olivine and silicate melts, Lithos.

Bédard, J.H., and Hébert, R., 1996, The lower crust of the Bay of Islands ophiolite, Canada: Petrology, mineralogy, and the importance of syntexis in magmatic differentiation in ophiolites and at ocean ridges: Journal of Geophysical Research, v. 101, p. 25,105-25,124.

Bédard, J.H., Lauzière, K., Tremblay, A., and Sangster, A., 1998, Evidence for forearc seafloor spreading from the Betts Cove ophiolite, Newfoundland: oceanic crust of boninitic affinity: Tectonophysics, v. 284, p. 233-245.

Bédard, J.H., Berclaz, A., Hébert, R., and Varfalvy, V., 2000a, Syntexis and the genesis of the oceanic crust, *in:* Dilek, Y., et al. (Eds.), Ophiolites and Oceanic Crust: New Insights from Field Studies and the Ocean Drilling Program: Special Paper, Geological Society of America, v. 349, p. 105-119.

Bédard, J.H., Lauzière, K., Tremblay, A., Sangster, A., Douma, S.L., and Dec, T., 2000b, Betts Cove ophiolite and its cover rocks, Newfoundland: Geological Survey of Canada Bulletin, v. 550, 76 pp.

Bédard, J.H., Pagé, P., and Lissenberg, J., 2003, Melt transfer mechanisms in the lower ophiolitic crust: Examples from the Bay of Islands, Thetford-Mines, Betts Cove and Annieopsquotch: EOS, Transactions of the AGU, v. 84, p. F1540.

Benn, K., and Allard, B., 1989, Preferred mineral orientations related to magmatic flow in ophiolite layered gabbros: Journal of Petrology, v. 30, p. 925-946.

Berman, R.G., 1988, Internally-consistent thermodynamic data for stoichiometric minerals in the system Na_2O-K_2O-CaO-MgO-FeO-Fe_2O_3-Al_2O_3-SiO_2-TiO_2-H_2O-CO_2: Journal of Petrology, v. 29, p. 445-522.

Berman, R.G., 1991, Thermobarometry using multiequilibrium calculations: a new technique with petrologic applications: Canadian Mineralogist, v. 29, p. 833-855.

Bird, D.K., Manning, C.E., and Rose, N.M., 1988, Hydrothermal alteration of Tertiary layered gabbros, East Greenland: American Journal of Science, v. 288, p. 405-457.

Bohnenstiehl, D.R., and Carbotte, S.M., 2001, Faulting patterns near 19°30'S on the East Pacific Rise: Fault formation and growth at a superfast spreading center: Geochemistry Geophysics Geosystems, v. 2, doi:10.1029/2001GC000156.

Bostock, H.H., 1988, Geology and petrochemistry of the Ordovician volcano-plutonic Robert's Arm group, Notre Dame Bay, Newfoundland: Geological Survey of Canada Bulletin, v. 369, 84 pp.

Boudier, F., Nicolas, A., and Ildefonse, B., 1996, Magma chambers in the Oman ophiolite: Fed from the top and the bottom: Earth and Planetary Science Letters, v. 144, p. 239–250.

Brem, A.G., Lin, S., and van Staal, C.R., 2003, Structural relationships south of Grand Lake, Newfoundland: Current Research, Newfoundland Department of Mines and Energy, Geological Survey Report, v. 03-1, p. 1-13.

Brenan, J.M., Shaw, H.F., Phinney, D.L., and Ryerson, F.J., 1994, Rutile-aqueous fluid partitioning of Nb, Ta, Hf, Zr, U and Th: Implications for high field strength element depletions in island-arc basalts: Earth and Planetary Science Letters, v. 128, p. 327-339

Brown, M., and Solar, G.S., 1998, Shear-zone systems and melts: feedback relations and self-organization in orogenic belts: Journal of Structural Geology, v. 20, p. 211-227.

Cabanis, B., and Lecolle, M., 1989, Le diagramme La/ 10-Y/ 15-Nb/ 8; un outil pour la discrimination des series volcaniques et la mise en evidence des processus de melange et/ou de contamination crustale : Comptes Rendus de l'Academie des Sciences, Serie 2, Mecanique, Physique, Chimie, Sciences de l'Univers, Sciences de la Terre, v. 309-20, p. 2023-2029.

Calon, T.J., and Green, F.K., 1987, Preliminary results of a detailed structural analysis of the Buchans Mine area, *in* Kirkham, R.V., ed., Buchans Geology, Newfoundland: Geological Survey of Canada Paper, v. 86, no. 24, p. 273-288.

Cannat, M., Mével, C., and Stakes, D., 1991, Normal ductile shearzones at an oceanic spreading ridge: Tectonic evolution of Site 735 gabbros (Southwest Indian ocean), *in*: Von Herzen, R.P., et al. (Eds.), Proceedings of the ODP, Scientific Results, v. 118, Ocean Drilling Program, College Station, TX, p. 415-429.

Cawood, P.A., van Gool, J.A.M., and Dunning, G.R., 1996, Geological development of eastern Humber and western Dunnage zone: Corner Brook – Glover Island region: Canadian Journal of Earth Sciences, v. 33, p.182-198.

Cawood, P.A., McCausland, P.J.A., and Dunning, G.R., 2001, Opening Iapetus; constraints from the Laurentian margin in Newfoundland: Geological Society of America Bulletin, v. 113, p. 443-453.

Chemenda, A.I., Yang, R.-K., Stephan, J.-F., Konstantinovskaya, E.A., and Ivanov G.M., 2001, New results from physical modelling of arc-continent collision in Taiwan: evolutionary model: Tectonophysics, v. 333, p. 159-178.

Chen, B., Jahn, B, Wilde, S., and Xu, B., 2000, Two contrasting Paleozoic magmatic belts in northern Inner Mongolia, China: petrogenesis and tectonic implications: Tectonophysics, v. 328, p. 57-182.

Chen, Y.J., 2001, Thermal effects of gabbro accretion from a deeper second melt lens at the fast spreading East Pacific Rise: Journal of Geophysical Research, v. 106, p. 8,581–8,588.

Cherkaoui, A.S.M., Wilcock, W.S.D., Dunn, R.A., and Toomey, D.R., 2003, A numerical model of hydrothermal cooling and crustal accretion at a fast spreading mid-ocean ridge: Geochemistry Geophysics Geosystems v. 4, p. 8616, doi:10.1029/2001GC000215.

Christeson, G.L., Kent, G.M., Purdy, G.M., and Detrick, R.S., 1996, Extrusive thickness variability at the East Pacific Rise, 9°-10°N: Constraints from seismic techniques: Journal of Geophysical Research, v. 101, p. 2859-2873.

Chung, S.-L., Wang, K-L., Crawford, A.J., Kamenetsky, V.S., Chen, H.-H., Lan, C.-Y., and Chen, C.H., 2001, High-Mg potassic rocks from Taiwan: implications for the genesis of orogenic potassic lavas: Lithos, v. 59, p. 153-170.

Class, C., Miller, D.M. Goldstein, S.L., and Langmuir, C.H., 2000, Distinguishing melt and fluid subduction components in Umnak Volcanics, Aleutian Arc: Geochemistry, Geophysics, Geosystems, v. 1, paper 1999GC000010.

Clemens, J.D., and Mawer, C.K., 1992, Granitic magma transport by fracture propagation: Tectonophysics, v. 204, p. 339-360.

Colman-Sadd, S.P., Hayes, J.P., and Knight, I., 1990, Geology of the Island of Newfoundland: Geological Survey Branch, Dept. of Mines and Energy, Government of Newfoundland and Labrador, scale 1:1.000.000.

Coogan, L.A., Gillis, K.M., MacLeod, C.J., Thompson, G.M., and Hékinian, R., 2002a, Petrology and geochemistry of the lower ocean crust formed at the East Pacific Rise and exposed at Hess Deep: A synthesis and new results: Geochemistry Geophysics Geosystems, v. 3, doi:10.1029/2001GC000230.

Coogan, L.A., Thompson, G., and MacLeod, C.J., 2002b, A textural and geochemical investigation of high level gabbros from the Oman ophiolite: implications for the role of the axial magma chamber at fast-spreading ridges: Lithos, v. 63, p. 67-82.

Coogan, L.A., Banks, G.J., Gillis, K.M., MacLeod, C.J., and Pearce, J.A., 2003, Hidden melting signatures in the Troodos ophiolite plutonic suite: evidence for widespread generation of depleted melts and intra-crustal melt aggregation: Contributions to Mineralogy and Petrology, v. 144, p. 484-505.

Cook, J., and Gordon, J.E., 1964, A mechanism for the control of crack propagation in all-brittle systems: Proceedings of the Royal Society of London Serie A, v. 282, p. 508-520.

Crawford, A.J., Beccaluva, L., and Serri, G., 1981, Tectono-magmatic evolution of the West Philippine-Mariana region and the origin of boninites: Earth and Planetary Science Letters, v. 54, p. 346-356.

Crawford, A.J., Falloon, T.J., and Green, D.H., 1989, Classification, petrogenesis and tectonic setting of boninites, *in* Crawford, A.J., ed., Boninites and related rocks: London, Unwin Hyman, p. 1-49.

Crawford, W.C., and Webb, S. C., 2002, Variations in the distribution of magma in the lower crust and at the Moho beneath the East Pacific Rise at 9°–10°N: Earth and Planetary Science Letters, v. 203, p. 117–130.

Crawford, W.C., Webb, S. C., and Hildebrand, J.A., 1999, Constraints on melt in the lower crust and Moho at the East Pacific Rise, 9°48'N, using seafloor compliance measurements: Journal of Geophysical Research, v. 104, p. 2923-2939.

Cumming, G.L., and Richards, J.R., 1975, Ore lead in a continuously changing Earth: Earth and Planetary Science Letters, v. 28, p. 55-171.

Currie, K.L., and van Berkel, J.T., 1989, Geochemistry of post-tectonic mafic intrusions in the Central Gneiss terrane of southwestern Newfoundland: Atlantic Geology, v. 25, p. 181-190.

Danyushevsky, L.V., Sobolev, A.V., and Falloon, T.J., 1995, North Tongan high-Ca boninite petrogenesis: the role of the Samoan plume and subduction zone-transform fault transition: Journal of Geodynamics, v. 20, p. 219-241.

Davidson, C., Hollister L.S., and Schmid, S.M., 1992, Role of melt in the formation of a deep-crustal compressive shear zone: The Maclaren Glacier metamorphic belt, south central Alaska: Tectonics, v. 11, p. 348-359.

Davis, W.J., McNicoll, V.J., Bellerive, D.R., Santowski, K., and Scott, D.J., 1997, Modified chemical procedures for the extraction and purification of uranium from titanite, allanite and rutile in the Geochronology Laboratory, Geological Survey of Canada: Radiogenic Age and Isotopic Studies, Report 10, Geological Survey of Canada, Current Research, v. 1997-F, p. 33-35.

De Saint Blanquat, M., Tikoff, B., Teyssier, C., and Vigneresse, J.L., 1998, Transpressional kinematics and magmatic arcs, *in:* Holdsworth, R.E., R.A. Stachan, and J.F. Dewey (eds.): Continental transpressional and transtensional tectonic: Geological Society of London Special Publications, v. 135, p. 327-340.

Dean, P.L., and Strong, D.F., 1977, Folded faults in Notre Dame bay, central Newfoundland: American Journal of Science, v. 277, p. 97-108.

Dick, H.J.B., Lin, J., and Schouten, H., 2003, An ultraslow-spreading class of ocean ridge: Nature, v. 426, p. 405-412.

Dubé, B., Dunning, G.R., Lauziere, K., and Roddick, J.C., 1996, New insights into the Appalachian orogen from geology and geochronology along the Cape Ray fault zone, southwest Newfoundland: Geological Society of America Bulletin, v. 108, p.101-116.

Dunn, R.A., Toomey D.R., and Solomon, S.C., 2000, Three-dimensional seismic structure and physical properties of the crust and shallow mantle beneath the East Pacific Rise at 9°30'N: Journal of Geophysical Research, v. 105, p. 23,537–23,555.

Dunning, G.R., 1984, The geology, geochemistry, geochronology and regional setting of the Annieopsquotch Complex and related rocks of Southwest Newfoundland: Ph.D. thesis, Memorial University of Newfoundland, St. John's, 1984.

Dunning, G.R., 1987, Geology of the Annieopsquotch Complex, southwest Newfoundland: Canadian Journal of Earth Sciences, v. 24, p. 1162-1174.

Dunning, G.R., and Herd, R.K., 1980, The Annieopsquotch ophiolite belt, southwest Newfoundland, and its regional relationships: Current Research, Geological Survey of Canada, Paper 80-1A, p. 227-234.

Dunning, G.R., and Chorlton, L.B., 1985, The Annieopsquotch ophiolite belt of southwest Newfoundland: Geology and tectonic significance: Geological Society of America Bulletin, v. 96, p. 1466-1476.

Dunning, G.R., and Krogh, T.E., 1985, Geochronology of ophiolites in the Newfoundland Appalachians: Canadian Journal of Earth Sciences, v. 22, p. 1659-1670.

Dunning, G.R., Carter, P.J., and Best, M.A., 1982, Geology of Star Lake (west half), southwest Newfoundland: Current Research, Geological Survey of Canada, Paper 82-1B, p. 21-26.

Dunning, G.R., Kean, B.F.,Thurlow, J.G., and Swinden, H.S., 1987, Geochronology of the Buchans, Roberts Arm, and Victoria Lake groups and Mansfield Cove complex, Newfoundland: Canadian Journal of Earth Sciences, v. 24, p. 1175-1184.

Dunning, G.R., Wilton, D.H.C., and Herd, R.K., 1989, Geology, geochemistry and geochronology of a taconic batholith, southwestern Newfoundland: Transactions of the Royal Society of Edinburgh, 80, p.159-168.

Dunning, G.R., O'Brien, S.J., Colman-Sadd, S.P., Blackwood, R.F., Dickson, W.L., O'Neill, P.P., and Krogh, T.E., 1990, Silurian orogeny in the Newfoundland Appalachians: Journal of Geology, v. 98, p. 895-913.

Einaudi, F., Godard, M., Pezard, P., Cochemé, J.-J., Coulon, C., Brewer, T., and Harvey, P., 2003, Magmatic cycles and formation of the upper oceanic crust at spreading centers: Geochemical study of a continuous extrusive sequence in the Oman ophiolite: Geochemistry Geophysics Geosystems, v. 4, doi 10.1029/2002GC000362.

Elliott, C.G., Dunning, G.R., and Williams, P.F., 1991, New U/Pb zircon age constraints on the timing of deformation in north-central Newfoundland and its implications for Early Paleozoic Appalachian orogenesis: Geological Society of America Bulletin, v. 103, p. 125-135.

Ewart, A., Bryan, W.B., Chappell, B.W., and Rudnick, R.L., 1994, Regional geochemistry of the Lau-Tonga arc and backarc systems, *in* Hawkins, J., et al., eds., Proceedings of the Ocean Drilling Program Scientific Results, v. 135, College Station, TX, p. 385-425.

Falloon, T.J., and Crawford, A.J., 1991, The petrogenesis of high-calcium boninite lavas derdged from the northern Tonga ridge: Earth Planetary Science Letters, v.102, p. 375-394.

Fox, D. and van Berkel, J.T., 1988, Mafic-ultramafic occurrences in metasedimentary rocks of southwestern Newfoundland: Current Research, Geological Survey of Canada, Paper 88-1B, p. 41-48.

Fuhrman, M.L., and Lindsley, D.H., 1988, Ternary-feldspar modeling and thermometry: American Mineralogist, v. 73, p. 201-216.

Garmany, J., 1989, Accumulations of melt at the base of young oceanic crust: Nature, v. 340, p. 628-632.

Hall, C.E., Gurnis, M., Sdrolias, M., Lavier, L.L., and Müller, R.D., 2003, Catastrophic initiation of subduction following forced convergence across fracture zones: Earth Planetary Science Letters, v. 212, p. 15-30.

Hall, L.A.F., and van Staal, C.R. 1999, Geology of the southern end of the Long Range mountains (Dashwoods Subzone), Newfoundland: Geological Survey of Canada Open File 3727, 1:50.000.

Hall, R., 2002, Cenozoic geological and plate tectonic evolution of SE Asia and the SW Pacific: computer-based reconstructions, model and animations: J. Asian Earth Sci., v. 20, p. 353-431.

Harding, A.J., Orcutt, J.A., Kappus, M.E., Vera, E.E., Mutter, J.C., Buhl, P., Detrick, R.S., and Brocher, T. M., 1989, Structure of young oceanic crust at 13°N on the East Pacific Rise from expanding spread profiles: Journal of Geophysical Research, v. 94, p. 12,163-12,196.

Harper, G.D., 1985, Tectonics of slow spreading mid-ocean ridges and consequences of a variable depth to the brittle/ductile transition: Tectonics, v. 4, p. 395-409.

Harrison, T.M., 1981, Diffusion of ^{40}Ar in Hornblende: Contributions to Mineralogy and Petrology 78, p.324-331.

Hawkesworth, C.J., Hergt, J.M., Ellam, R.M., and McDermott, F., 1991, Element fluxes associated with subduction related magmatism: Philosophical Transactions of the Royal Society of London, v. 335, p. 392-405.

Hawkins, J.W., and Allan, J.F., 1994, Petrologic evolution of Lau basin sites 834 through 839, *in* Hawkins, J., et al., eds., Proceedings of the Ocean Drilling Program Scientific Results, v. 135, College Station, TX, p. 427-470.

Henstock, T.J., Woods, A.W., and White, R.S., 1993, The accretion of oceanic crust by episodic sill intrusion: Journal of Geophysical Research, v. 98, p. 4143-4161.

Hergt, J.M., and Hawkesworth, C.J., 1994a Major element, trace element, and isotope (Pb, Sr, and Nd) geochemistry of site 839 basalts and basaltic andesites: implications for arc volcanism, *in* Hawkins, J., et al., eds., Proceedings of the Ocean Drilling Program Scientific Results, v. 135, College Station, TX, p. 505-517.

Hergt, J.M., and Nilsson Farley, K., 1994b, Major element, trace element, and isotope (Pb, Sr, and Nd) variations in site 834 basalts: implications for the initiation of backarc opening, *in* Hawkins, J., et al., eds., Proceedings of the ODP, Scientific Results, v. 135, College Station, TX, p. 471-485.

Hickey, R.L., and Frey, F.A., 1982, Geochemical characteristics of boninite series volcanics: implications for their source: Geochimica et Cosmochimica Acta, v. 46, p. 2099-2115.

Holland, T., and Blundy, J., 1994, Non-ideal interactions in calcic amphiboles and their bearing on amphibole-plagioclase thermometry: Contributions to Mineralogy and Petrology, v. 116, p. 433-447.

Hollister, L.S., and Crawford, M.L., 1986, Melt-enhanced deformation: A major tectonic process: Geology, v. 14, p. 558-561.

Hutton, D.H.W., 1988, Granite emplacement mechanisms and tectonic controls: inferences from deformation studies: Transactions of the Royal Society of Edinburgh, v. 79, p. 245-255.

Jenkins, D.M., 1981, Expirimental phase relations of hydrous peridotites modeled in the system H2O-CaO-MgO-Al2O3-SiO2: Contributions to Mineralogy and Petrology, v. 77, p. 166-176.

Jenner, G.A., Dunning, G.R., Malpas, J., Brown, M., and Brace, T., 1991, Bay of Islands and Little Port Complexes revisited: Age, geochemical and isotopic evidence confirm supra-subduction zone origin: Canadian Journal of Earth Sciences, v. 28, 1635-1652.

Karlstrom, K.E., 1989, Toward a syntectonic paradigm for granitoids, EOS, Transactions of the American Geophysical Union, v. 70, p. 762.

Karson, J.A., 1998, Internal structure of oceanic lithosphere: A perspective from tectonic windows, *in*: Buck, W. R., et al. (Eds.), Faulting and Magmatism at Mid-Ocean Ridges: Geophysical Monograph Series, v. 106, AGU, Washington, D.C., p.177-218.

Karson, J.A., 1999, Geological investigation of a lineated massif at the Kane Transform Fault: implications for oceanic core complexes: Philosophical Transactions of the Royal Society of London, v.357, p. 713-740.

Karson, J.A., Hurst, S.D., Lee, C.E., Rivizzigno, P.A., Curewitz, D., Morris, A.R., and Hess Deep '99 Scientific Party, 2002a, Structure of uppermost fast-spread oceanic crust exposed at the Hess Deep Rift: Implications for subaxial processes at the East Pacific Rise: Geochemistry Geophysics Geosystems, v. 3, doi 10.1029/2001GC000155.

Karson, J.A., Tivey, M.A., and Delaney, J.R., 2002b, Internal structure of uppermost oceanic crust along the Western Blanco Transform Scarp: Implications for subaxial accretion and deformation at the Juan de Fuca Ridge: Journal of Geophysical Research, v. 107, 2181, doi:10.1029/2000JB000051.

Kelemen, P.B., and Aharonov, E., 1998, Periodic formation of magma fractures and generation of layered gabbros in the lower crust beneath oceanic spreading ridges, *in:* Buck, W. R., et al. (Eds.), Faulting and Magmatism at Mid-Ocean Ridges: Geophysical Monograph Series, v. 106, AGU, Washington, D.C., p. 267–289.

Kelemen, P.B., Koga, K., and Shimizu, N., 1997, Geochemistry of gabbro sills in the crust/mantle transition zone of the Oman ophiolite: Implications for the origin of the oceanic lower crust: Earth and Planetary Science Letters, v. 146, p. 475–488.

Kelemen, P.B., Johnson, K.T.M., Kinzler, R.J., and Irving, A.J., 1990, High-field-strength element depletions in arc basalts due to mantle-magma interaction: Nature, v. 345, p. 521-524.

Keller, R.A., Fisk, M.R. Smellie, J.L., Strelin, J.A., and Lawver, L.A., 2002, Geochemistry of back arc basin volcanism in Bransfield Strait, Antarctica; subducted contributions and along-axis variations: Journal of Geophysical Research, v. 107, no. 8, 10.1029/2001JB000444.

Kent, G.M., Harding, A.J. and Orcutt, J.A., 1993, Distribution of magma beneath the East Pacific Rise between the Clipperton Transform and the 9°17'N Deval from forward modeling of common depth point data: Journal of Geophysical Research, v. 98, p. 13,945-13,969.

Keppler, H., 1996, Constraints from partitioning experiments on the composition of subduction-zone fluids: Nature, v. 380, p. 237-240.

Koepke, J., Feig, S.T., and Snow, J.E., 2004a, A new model for the late-stage magmatic evolution of oceanic gabbros: EGU Geophysical Research Abstracts, v. 6, A-3057.

Koepke, J., Feig, S.T., Snow, J., Freise, M., 2004b, Petrogenesis of oceanic plagiogranites by partial melting of gabbros: an experimental study: Contributions to Mineralogy and Petrology, v. 146, p. 414-432.

Konstantinovskaia, E.A., 2001, Arc-continent collision and subduction reversal in the Cenozoic evolution of the Northwest Pacific: an example from Kamchatka (NE Russia): Tectonophysics, v. 333, p.75-94.

Korenaga, J., and Kelemen, P. B., 1997, Origin of gabbro sills in the Moho transition zone of the Oman ophiolite: Implications for magma transport in the lower oceanic crust: Journal of Geophysical Research, v. 102, p. 27,729-27,749.

Kretz, R., 1983, Symbols for rock-forming minerals: American Mineralogist, v. 68, p. 277-279.

Krogh, T.E., 1982, Improved accuracy of U-Pb ages by creation of more concordant systems using an air abrasion technique: Geochimica et Cosmochimica Acta, v. 46, p.637-649.

Kurth, M., Sassen, A., Suhr, G., and Mezger, K., 1998, Precise ages and isotopic constraints for the Lewis Hills (Bay of Island Ophiolite): Preservation of an arc-spreading ridge intersection: Geology, v. 26, p. 1127-1130.

Lagabrielle, Y., Bideau, D., Cannat, M., Karson, J.A., and Mével, C., 1998, Ultramafic-mafic plutonic rock suites exposed along the Mid-Atlantic Ridge (10°N-30°N). Symmetrical-asymmetrical distribution and implications for seafloor spreading processes, *in*: Buck, W. R., et al. (Eds.), Faulting and Magmatism at Mid-Ocean Ridges: Geophysical Monograph Series, v. 106, AGU, Washington, D.C., p.153-176.

Leake, B.E., et al., 1997, Nomenclature of the amphiboles: report of the subcommittee on amphiboles of the international mineralogical association, commission on new minerals and mineral names: Canadian Mineralogist, v. 35, p. 219-246.

Lécuyer, C., and Reynard, B., 1996, High temperature alteration of oceanic gabbros by seawater (Hess Deep, Ocean Drilling Program Leg 147): Evidence from oxygen isotopes and elemental fluxes: Journal of Geophysical Research, v. 101, p. 15,883-15,897.

Lin, S., Jiang, D., and Williams, P.F., 1998, Transpression (or transtension) zones of triclinic symmetry: natural example and theoretical modeling, *in:* Holdsworth, R.E., R.A. Stachan, and J.F. Dewey (eds.), Continental transpressional and transtensional tectonic: Geological Society of London Special Publications, v. 135, p. 41-57.

Lissenberg, C.J., Zagorevski, A., Whalen, J.B., and van Staal, C.R., in press, Geology, Star Lake, Newfoundland (NTS 12A/11): Geological Survey of Canada Open File 1669, scale 1:50.000.

Ludwig, K.R., 1998, On the treatment of concordant uranium-lead ages: Geochimica et Cosmochimica Acta, v. 62, p. 665-676.
Ludwig, K.R., 2001, User's manual for Isoplot/Ex rev. 2.49: a Geochronological Toolkit for Microsoft Excel: Special Publication, 1a, Berkeley Geochronology Center, Berkeley, 55 pp.
MacLennan, J., Hulme, T., and Singh, S.C., 2004, Thermal models of oceanic crustal accretion: Linking geophysical, geological and petrological observations, Geochemistry Geophysics Geosystems, v. 5, doi 10.1029/2003GC000605.
Macpherson, C.G., and Hall, R., 2001, Tectonic setting of Eocene boninite magmatism in the Izu-Bonin-Mariana forearc: Earth and Planetary Science Letters, v. 186, p. 215-230.
Mader, U.K., and Berman, R.G., 1992, Amphibole thermobarometry: a thermodynamic approach. Current Research, Part E, Geological Survey of Canada, Paper 92-1E, p. 393-400.
Manning, C.E., Weston, P.E., and Mahon, K.I., 1996, Rapid high temperature metamorphism of the East Pacific Rise gabbros from Hess Deep: Earth and Planetary Science Letters, v. 144, p. 123–132.
McCaffrey, K.J.W., 1992, Igneous emplacement in a transpressive shear zone: Ox Mountains igneous complex: Journal of the Geological Society of London, v. 149, p. 221-235.
McCollom, T.M., and Shock, E.L., 1998, Fluid-rock interactions in the lower oceanic crust: Thermodynamic models of hydrothermal alteration: Journal of Geophysical Research, v. 103, p. 547–575.
McNicoll, V.J., van Staal, C.R., and Waldron, J.W.F., 2001, Accretionary history of the northern Appalachians: SHRIMP study of Ordovician-Silurian syn-tectonic sediments in the Canadian Appalachians: Geological Association of Canada – Mineralogical Society of Canada Joint Annual Meeting, Abstracts Volume 26, p. 100-101.
Meyer, A., 1980, Primitive arc volcanism and a boninite series: examples from western pacific island arcs, *in* Hayes, D.E., ed., The tectonic and geological evolution of South Asian seas and islands, Washington, AGU Geophysical Monograph, p. 269-282.
Miller, B.V., Samson, S.D., and D'Lemos, R.S., 1999, Time span of plutonism, fabric development, and cooling in a Neoproterozoic magmatic arc segment: U-Pb age constraints from syn-tectonic plutons, Sark, Channel Islands, UK: Tectonophysics, v. 312, p. 79-95.
Monzier, M., Danyushevsky, L.V., Crawford, A.J., Bellon, H., and Cotton, J., 1993, High-Mg andesites from the southern termination of the New Hebrides island arc (SW Pacific): Journal of Volcanology and Geothermal Research, v. 57, p.193-217.
Moore, J.C., Diebold, J., Fisher, M.A., Sample, J., Brocher, T., Talwani, M., Ewing, J., von Huene, R., Rowe, C., Stone, D., Stevens, C., and Sawyer, D., 1991, EDGE deep seismic reflection transect of the eastern Aleutian arc-trench layered lower crust reveals underplating and continental growth: Geology, v. 19, p. 420-424.
Morrison, G.W., 1980, Characteristics and tectonic setting of the shoshonite rock association: Lithos, v. 13, p. 97-108.
Moyen, J.-F., Nédélec, A., Martin, H., and Jayananda, M., 2003, Syntectonic granite emplacement at different structural levels: the Closepet granite, South India: Journal of Structural Geology, v. 25, p. 611-631.

Müller, R.D., Gaina, C., Roest, W.R., and Lundbek Hansen, D., 2001 A recipe for microcontinent formation: Geology, v. 29, p. 203–206.

Natland, J.H., and Dick, H.J.B., 1996, Melt migration through high level gabbroic cumulates of the East Pacific Rise at Hes Deep: the origin of magma lenses and the deep crustal structure of fast-spreading ridges, *in:* Mével, C., Gillis, K.M., Allan, J.F., and Meyer, P.S. (Eds.), Proceedings of the ODP, Scientific Results, v. 147, Ocean Drilling Program, College Station, TX, p. 21-58.

Natland, J.H., and Dick, H.J.B., 2001, Formation of the lower ocean crust and the crystallization of gabbroic cumulates at a very slow spreading ridge: Journal of Volcanology and Geothermal Research, v. 110, p. 191-233.

Natland, J.H., Meyer, P.S., Dick, H.J.B., Bloomer, S.H., et al., 1991, Magmatic oxides and sulfides in gabbroic rocks from Hole 735B and the later development of the liquid line of descent, *in:* Von Herzen, R.P., et al. (Eds.), Proceedings of the ODP, Scientific Results, v. 118, Ocean Drilling Program, College Station, TX, p. 75-111.

Nicolas, A., 1992, Kinematics in magmatic rocks with special reference to gabbros: Journal of Petrology, v. 33, p. 891-915.

Nicolas, A., Boudier, F., Ildefonse, B., and Ball, E., 2000, Accretion of Oman and United Arab Emirates ophiolite – Discussion of a new structural map: Marine Geophysical Researches, v. 21, p. 147-179.

Nicolas, A., Mainprice, D., and Boudier, F., 2003, High-temperature seawater circulation throughout crust of oceanic ridges: A model derived from the Oman ophiolites: Journal of Geophysical Research, v. 108, p. 2371, doi 10.1029/2002JB002094.

Pallister, J.S., and Hopson, C.A., 1981, Samail ophiolite plutonic suite: Field relations, phase variation and layering and a model of a spreading ridge magma chamber: Journal of Geophysical Research, v. 86, p. 2593-2644.

Parrish, R.R., Roddick, J.C., Loveridge, W.D., and Sullivan, R.W., 1987, Uranium-lead analytical techniques at the Geochronology Laboratory: Geological Survey of Canada, Radiogenic age and isotope studies, Report 1, Geological Survey of Canada, paper 87-2, p. 3-7.

Paterson, S.R., 1989, Are syntectonic granites truly syn-tectonic? EOS, Transactions of the American Geophysical Union, v. 70, p. 763.

Pavlides, L., Arth, J.G., Sutter, J.F., Stern, T.W., and Cortesini, H., 1994, Early Paleozoic alkalic and calc-alkalic plutonism and associated contact metamorphism, central Virginia Piedmont: U. S. Geological Survey Professional Paper. U. S. Geological Survey. Reston, VA, United States, 147 pp.

Pavlis, T.L., 1996, Fabric development in syn-tectonic intrusive sheets as a consequence of melt-dominated flow and thermal softening of the crust: Tectonophysics, v. 253, p. 1-31.

Pearce, J.A., 1983, Role of sub-continental lithosphere in magma genesis at active continental margins, *in* C.J. Hawkesworth, et al., ed., Continental basalts and mantle xenoliths, Shiva Publishing, Nantwich, Cheshire, p. 230-249.

Pearce, J.A., and Parkinson, I.J, 1993, Trace element models for mantle melting: Application to volcanic arc petrogenesis, *in* Prichard, H.M., et al., eds., Magmatic Processes and Plate Tectonics, Geological Society of London Special Publication, v. 76, p. 373-403

Pearce, J.A., Harris, N.B.W., and Tindle, A.G., 1984, Trace element discrimination diagrams for the tectonic interpretation of granitic rocks: Journal of Petrology, v. 25, p. 956-983.

Pearce, J.A., van der Laan, S.R., Arculus, R.J., Murton, B.J., Ishii, T., Peate, D.W., and Parkinson, I.J., 1992, Boninite and Harzburgite from leg 125 (Bonin-Mariana forearc): A case study of magma genesis during the initial stages of subduction, *in* Fryer, P., et al., eds., Proceedings of the ODP, Scientific results, v. 125, p. 623-659.

Pehrsson, S.J., van Staal, C.R., Herd, R.K., McNicoll, V., 2003, The Cormacks Lake complex, Dashwoods Subzone: A window into the deeper levels of the Notre Dame arc: Current Research, Newfoundland Department of energy and Mines, Geological Survey Report, v. 03-1, p. 115-125.

Phipps Morgan, J., and Chen, Y. J.,1993, The genesis of oceanic crust: Magma injection, hydrothermal circulation, and crustal flow: Journal of Geophysical Research, v. 98, p. 6283–6297.

Quick, J.E., and Denlinger, R.P., 1993, Ductile deformation and the origin of layered gabbro in ophiolites: Journal of Geophysical Research, v. 98, p. 14,015-14,027.

Reynolds, J.R., and Langmuir, C.H., 2000, Identification and implications of off-axis lava flows around the East Pacific Rise: Geochemistry, Geophysics, Geosystems, v. 1, paper number 1999GC000033.

Richardson, W.P., Stein, S., Stein, C.A., and Zuber, M.T., 1995, Geoid data and thermal structure of the oceanic lithosphere: Geophysical Research Letters, v. 22, p. 1913-1916.

Roddick, J.C., 1983, High-precision intercalibration of ^{40}Ar-^{39}Ar standards: Geochimica et Cosmochimica Acta, v. 47, p. 887-898.

Roddick, J.C., 1988, The assessment of errors in ^{40}Ar/^{39}Ar dating: Radiogenic Age and Isotopic Studies, Report 2, Geological Survey of Canada, Paper 88-2, p. 7–16.

Roddick, J.C., Cliff, R.A. and Rex, D.C., 1980, The evolution of excess argon in alpine biotites - a ^{40}Ar/^{39}Ar analysis: Earth and Planetary Science Letters, v. 48, p. 185–208.

Roddick, J.C., Loveridge, W.D. and Parrish, R.R., 1987, Precise U-Pb dating of zircon at the sub-nanogram Pb level: Chemical Geology, v. 66, p. 111-121.

Roeder, P.L., and Emslie, R.F., 1970, Olivine-liquid equilibrium: Contributions to Mineralogy and Petrology, v. 29, p. 275-289.

Rogers, N., 2004, Geochemical database, Red Indian Line project, Central Newfoundland: Geological Survey of Canada Open File 4605.

Rosenberg, C.L., 2004, Shear zones and magma scent: A model based on a review of the Tertiary magmatism in the Alps: Tectonics, v. 23, TC3002, doi:10.1029/2003TC001526.

Ryan, M.P., 1994, Neutral-buoyancy controlled magma transport and storage in mid-ocean ridge magma resevoirs and their sheeted dyke complex: a summary of basic relationships, *in:* Ryan, M. P. (Ed.), Magmatic Systems, Academic, San Diego (CA), p. 97-138.

Saunders, A.D., Fornari, D.J., and Morrison, M.A., 1982, The composition and emplacement of basaltic magmas produced during the development of continental-margin basins: the Gulf of California, Mexico: Journal of the Geological Society of London, v. 139, p. 335-346.

Saunders, A.D., Norry, M.J., and Tarney, J., 1991, Fluid influence on the trace element compositions of subduction zone magmas: Philosophical Transactions of the Royal Society of London, v. 335, p. 377-392.

Scaillet, S., 2000, Numerical error analysis in ^{40}Ar/^{39}Ar dating: Chemical Geology, v. 162, p. 269–298.

Sengör, A.M.C., and Natal'in, B.A., 1996, Turkic-type orogeny and its role in the making of the continental crust: Annual Reviews of Earth and Planetary Sciences, v. 24, p. 263-337.

Singh, S.C., Kent, G.M., Collier, J.S., Harding, A.J., and Orcutt, J.A., 1998, Melt to mush variations in crustal magma properties along the ridge crest at the Southern East Pacific Rise: Nature, v. 394, p. 874-878.

Sinton, J.M., and R.S. Detrick, 1992, Mid-ocean ridge magma chambers: Journal of Geophysical Research, v. 97, 197-216.

Smewing, J.D., 1981, Mixing characteristics and compositional differences in mantle-derived melts beneath spreading axes: evidence from cyclically layered rocks in the ophiolite of North Oman: Journal of Geophysical Research, v. 86, p. 2645-2660.

Solobev, A.V., and Danyushevsky, L.V., 1994, Petrology and geochemistry of boninites from the northern termination of the Tonga trench: Constraints on the generation conditions of primary high-Ca boninite magmas, Journal of Petrology, v. 35, no. 5, p. 1183-1211.

Spear, F.S., 1981, An experimental study of hornblende stability and compositional variability in amphibolite: American Journal of Science, v. 281, p. 697-734.

Stakes, D.S., and Taylor, H.P., 1992, The northern Samail Ophiolite: An oxygen isotope, microprobe, and field study: Journal of Geophysical Research, v. 97, p. 7,043-7,080.

Stern, R.A., 1997, The GSC sensitive high resolution ion microprobe (SHRIMP): analytical techniques of zircon U-Pb-Th age determinations and performance evaluation: Radiogenic age and isotope studies, Report 10, Geological Survey of Canada, Current Research, v. 1997-F, p. 1-31.

Stern, R.A., and Amelin, Y., 2003, Assessment of errors in SIMS zircon U-Pb geochronology using a natural zircon standard and NIST SRM 610 glass: Chemical Geology, v. 197, p. 111-146.

Stern, R.J., and Bloomer, S.H., 1992, Subduction zone infancy: examples from the Eocene Izu-Bonin Mariana and Jurassic California arcs: Geological Society of America Bulletin, v. 104, p.1621-1636.

Sun, C-H., and Stern, R.J., 2001, Genesis of Mariana shoshonites: Contribution of the subduction component: Journal of Geophysical Research, v. 106-B1, p. 589-608.

Sun, S-S., and McDonough, W.F., 1989, Chemical and isotopic systematics of oceanic basalts: implications for mantle compositions and processes, *in:* Saunders, A.D., and Norry, M.J. (Eds.), Magmatism in the ocean basins: Geological Society of London Special Publications, v. 42, p. 313-345.

Swinden, H.S., Jenner, G.A., and Szybinski, Z.A., 1997, Magmatic and tectonic evolution of the Cambrian-Ordovician Laurentian margin of Iapetus: Geochemical and isotopic constraints from the Notre Dame subzone, Newfoundland: *in* Sinha, A.K., Whalen, J.B., and Hogan, J.P., eds., The Nature of Magmatism in the Appalachian Orogen, Boulder, Colorado, Geological Society of America Memoir, v. 191, p. 337-365.

Szybinski, Z.A., 1995, Paleotectonic and structural setting of the western Notre Dame bay area, Newfoundland Appalachians (Ph.D. thesis]: St. John's, Memorial University of Newfoundland, 195 p.

Szybinski, A., House, S., and Jenner, G.A., 1995, Stratigraphy and structure of the Glover group, Grand Lake – Little Grand Lake area, Newfoundland: Current Research, Geological Survey of Canada, v. 1995E, p. 245-251.

Tatsumi, Y., Hamilton, D.L., and Nesbitt, R.W., 1986, Chemical characteristics of fluid phase released from a subducted lithosphere and origin of arc magmas: evidence from high-pressure experiments and natural rocks: Journal of Volcanology and Geothermal Research, v. 29, p. 293-309.

Thurlow, J.G., 1981, The Buchans group: Its stratigraphic and structural setting, *In*: Swanson, E.A., Strong, D.F., and Thurlow, J.G., eds., The Buchans orebodies; fifty years of geology and mining: Special Paper - Geological Association of Canada, v. 22, p. 79-90.

Thurlow, J.G., and Swanson, E.A., 1981, Geology and ore deposits of the Buchans area, central Newfoundland, *In*: Swanson, E.A., Strong, D.F., and Thurlow, J.G., eds., The Buchans orebodies; fifty years of geology and mining: Special Paper - Geological Association of Canada, v.. 22, p. 113-142.

Thurlow, J.G., and Swanson, E.A., 1987, Stratigraphy and structure of the Buchans Group, *In:* Kirkham, R.V., ed., Buchans Geology, Newfoundland: Geological Survey of Canada Paper 86-24, p. 35-46.

Thurlow, J.G., Spencer, C.P., Boerner, D.E., Reed, L.E., and Wright, J.A., 1992, Geological interpretation of a high resolution reflection seismic survey at the Buchans mine, Newfoundland: Canadian Journal of Earth Sciences, v. 29, p. 2022-2037.

Tikoff, B., and Teyssier C., 1992, Crustal-scale, en-echelon "P-shear" tensional bridges: A possible solution to the batholithic room problem: Geology, v. 20, p. 927-930.

van der Velden, A.J., van Staal, C.R., and Cook, F.A. 2004., Paleosubduction of Ganderia beneath Laurentia: a reprocessed lithoprobe seismic reflection survey of the Newfoundland Appalachians: Geological Society of America Bulletin (in press).

van Staal, C.R., Dewey, J.F., Mac Niocaill, C., and McKerrow, W.S., 1998, The Cambrian-Silurian tectonic evolution of the northern Appalachians and British Caledonides: history of a complex, west and southwest Pacific type segment of lapetus, *in* Blundell, D.J., et al., eds., Lyell: the Past is the Key to the Present: Geological Society of London Special Publication, v.143, p. 199-242.

van Staal, C.R., Whalen, J.B. Pehrsson, S.J., and McNicoll, V.J., 2003, Tectonic evolution of the Notre Dame magmatic arc, Newfoundland Appalachians, Eos Transactions of the American Geophysical Union, v. 84, no. 46, Fall Meeting Supplement, Abstract V41A-06.

van Staal, C.R., Lissenberg, C.J., Rogers, N., Zagorevski, A., Bédard, J.H., Jenner, G., McNicoll, V., Valverde-Vaquero, P., Waldron, J., and Whalen, J.B., 2004, The Northern Appalachian Orogen – From Rifting and Ocean Opening to Accretion of Oceanic Terranes and Collisional Events. The LITHOPROBE Celebratory Conference: From Parameters to Processes - Revealing the Evolution of a Continent, available online at http://www.lithoprobe.ca/about/events/CC-Abs-Vol-CD-reduced size.pdf.

van Staal, C.R., Lissenberg, C.J., Pehrsson, S., Zagorevski, A., Valverde-Vaquero, P., Herd, R.K., McNicoll, V., and Whalen, J.B., in press a, Geology, Puddle Pond, Newfoundland (NTS 12A/05): Geological Survey of Canada Open File 1664, scale 1:50.000.

van Staal, C.R., Zagorevski, A., Valverde-Vaquero, P., Rogers. N., Lissenberg, C.J., in press b, Geology, Victoria Lake, Newfoundland (NTS 12A/06): Geological Survey of Canada Open File 1667, scale 1:50.000.

van Staal, C.R., P. Valverde-Vaquero, A. Zagorevski, S. Boutsma, S. Pehrsson, M. van Noorden, and V. McNicoll, in press c, Geology, King George IV Lake, Newfoundland (NTS 12A/04), Geological Survey of Canada Open File 1665, scale 1:50.000.

Varne, R., 1985, Ancient subcontinental mantle: a source for K-rich orogenic volcanics: Geology, v. 13, p. 405-408.

Vauchez, A., Pacheco Neves, S., and Tommasi, A., 1997, Transcurrent shear zones and magma emplacement in Neoproterozoic belts of Brazil, *In:* Bouchez, J.L., et al., eds, Granite: From segregation of melt to emplacement fabrics: Kluwer, Dordrecht, p. 275-293.

Vera, E.E., Mutter, J.C., Buhl, P., Orcutt, J.A., Harding, A.J., Kappus, M.E., Detrick, R.S., and Brocher, T. M., 1990, The structure of 0 to 0.2-m.y.-old oceanic crust at 9°N on the East Pacific Rise from expanded spread profiles: Journal of Geophysical Research, v. 95, p. 15,529-15,556.

Vernon, R.H., 2000, Review of microstructural evidence of magmatic and solid-state flow, Electronic Geosciences, v. 5:2.

Villeneuve, M.E., and MacIntyre, D.G., 1997, Laser $^{40}Ar/^{39}Ar$ ages of the Babine porphyries and Newman Volcanics, Fulton Lake map area, west-central British Columbia: Radiogenic Age and Isotopic Studies, Report 10, Geological Survey of Canada, Current Research, v. 1997-F, p.131–139.

Villeneuve, M.E., Sandeman, H.A., and Davis, W.J., 2000, A method for the intercalibration of U-Th-Pb and $^{40}Ar/^{39}Ar$ ages in the Phanerozoic: Geochimica et Cosmochimica Acta, v. 64, p. 4017-4030.

Wager, L.R., Brown, G.M., and Wadsworth, W.J., 1960, Types of igneous cumulates, Journal of Petrology, v. 1, p. 73-85.

Waldron, J.W.F., and van Staal, C.R., 2001, Taconian orogeny and the accretion of the Dashwoods block: A peri-Laurentian microcontinent in the Iapetus ocean: Geology, v. 29, p. 811-814.

Wang, K.-L., Chung, S.-L., O'Reilly, S.Y., Sun, S.-S., Shinjo, R., and Chen, C.-H., 2004, Geochemical constraints for the genesis of post-collisional magmatism and the geodynamic evolution of the northern Taiwan region: Journal of Petrology,v. 45, p. 975-1011.

Whalen, J.B., 1989, The Topsails igneous suite, western Newfoundland: an Early Silurian subduction-related magmatic suite? Canadian Journal of Earth Sciences, v. 26, p. 2421-2434.

Whalen, J.B., 1993, Geology, Star Lake, Newfoundland (NTS 12A/11), Geological Survey of Canada Open File 2735, scale 1:50.000.

Whalen, J.B., Currie, K.L., and van Breemen, O., 1987, Episodic Ordovician-Silurian plutonism in the Topsails igneous terrane, western Newfoundland: Transactions of the Royal Society of Edinburgh, v. 78, p. 17-28.

Whalen, J.B., Jenner, G.A., Longstaffe, F.J., Gariepy, C., and Fryer, B.J., 1997, Implications of granitoid geochemical and isotopic (Nd, O, Pb) data from the Cambrian-Ordovician Notre Dame arc for rthe evolution of the Central Mobile belt, Newfoundland Appalachians, *in* Sinha, A.K., et al., eds., The Nature of Magmatism in the Appalachian Orogen: Boulder, Colorado, Geological Society of America Memoir, v. 191, p. 367-395.

Whalen, J.B., McNicoll, V.J., van Staal, C.R., and Pehrsson, S.J., 2003, Plutonic rock geochemical and isotopic evidence for a transition from arc (c.489-435 Ma) to within-plate (c. 430 Ma) magmatism within the Notre Dame arc: Geological Society of America Abstracts with Programs, v. 35-3, p. 33.

Williams, H., 1979, Appalachian orogen in Canada: Canadian Journal of Earth Sciences, v. 16, p. 792-807.

Williams, H., 1995, Temporal and spatial divisions, *in* Geology of the Appalachian-Caledonian Orogen in Canada and Greenland: Ottawa, Geological Survey of Canada, Geology of Canada, vol. 6, p. 23-44.

Williams, H., and Hatcher, R.D., 1983, Appalachian suspect terranes, *in* Hatcher, R.D., Williams, H., and Zietz, I., eds., The tectonics and geophysics of mountain chains, Geological Society of America Memoir, v. 158, p. 33-53.

Williams, H., Colman-Sadd, S.P., and Swinden, H.S., 1988, Tectonic-stratigraphic subdivision of central Newfoundland: Current Research, Geological Survey of Canada Paper 88-1B, p. 91-98.

Wilson, J.T., 1966, Did the Atlantic close and then re-open? Nature, v. 266, p. 676-681.

Xiao, W.-J., Han, F., Windley, B.F., Yuan, C., Zhou, H., and Li, J., 2003, Multiple accretionary orogenesis and episodic continental growth of continents: Insights from the western Kunlun range, central Asia: International Geology Review, v. 45, p. 303-328.

Zagorevski, A., and van Staal, C.R., 2002, Structures associated with the Red Indian Line in southwestern Newfoundland: Current Research, Newfoundland Department of Energy and Mines, Geological Survey Report, v. 02-1, p. 211-218.

Zagorevski, A., Lissenberg, C.J., van Staal, C.R., McNicoll, V., and Rogers, N., 2003, Tectonic history of the Annieopsquotch Accretionary Tract: Geological Society of America Abstracts with Programs, v. 35, no. 3, p. 34.

Zagorevski, A., van Staal, C. R., McNicoll, V., and Rogers, N., 2004, Pats Pond and Wigwam Brook Groups: Record of Episodic per-Gondwanan Upper Cambrian-Caradoc Island Arc Activity in the Exploits Subzone of Central Newfoundland: Geological Society of America Abstracts with Programs, v. 36-2, p. 129.

Zagorevski, A., Rogers, N., van Staal, C.R., McNicoll, V., Lissenberg, C.J., Valverde-Vaquero, P., Lower to Middle Ordovician evolution of peri-Laurentian arc and back-arc complexes in Iapetus: Constraints from the Annieopsquotch Accretionary Tract, Central Newfoundland: Submitted to GSA Bulletin.